


Summer 8-19-2016

Stability and Kinetics of DNA Pseudoknots: Formation of T*A•T Base-Triplets and Their Targeting Reactions

Calliste Steffensmeier
University of Nebraska Medical Center

Tell us how you used this information in this [short survey](#).

Follow this and additional works at: <https://digitalcommons.unmc.edu/etd>

 Part of the [Nucleic Acids, Nucleotides, and Nucleosides Commons](#), [Other Pharmacy and Pharmaceutical Sciences Commons](#), and the [Physical Chemistry Commons](#)

Recommended Citation

Steffensmeier, Calliste, "Stability and Kinetics of DNA Pseudoknots: Formation of T*A•T Base-Triplets and Their Targeting Reactions" (2016). *Theses & Dissertations*. 130.
<https://digitalcommons.unmc.edu/etd/130>

This Dissertation is brought to you for free and open access by the Graduate Studies at DigitalCommons@UNMC. It has been accepted for inclusion in Theses & Dissertations by an authorized administrator of DigitalCommons@UNMC. For more information, please contact digitalcommons@unmc.edu.

**STABILITY AND KINETICS OF DNA PSEUDOKNOTS:
FORMATION OF T•A•T BASE-TRIPLETS AND THEIR
TARGETING REACTIONS**

By

Calliste Fran Steffensmeier

A DISSERTATION

Presented to the Faculty of
the University of Nebraska Graduate College
in Partial Fulfillment of the Requirements
for the Degree of Doctor of Philosophy

Pharmaceutical Sciences
Graduate Program

Under the Supervision of Professor Luis A. Marky

University of Nebraska Medical Center
Omaha, Nebraska

July, 2016

Supervisory Committee:

Gloria E. Borgstahl, Ph.D.

Sorin Luca, Ph.D.

Joseph A. Vetro, Ph.D.

Jonathan L. Vennerstrom, Ph.D.

To my Family and Friends who believed in me when I did not myself.

In memory of my Dad, one of my biggest supporters.

ACKNOWLEDGEMENTS

I would like to thank my advisor Dr. Luis A. Marky for giving me the opportunity to work in his lab. He has provided me with a solid foundation to build my future upon, but he has also given me much more than that during the time in his lab. He was always concerned for my health and well-being. I owe a lot to him for his understanding and support during a very difficult and trying time in my life. I thank him for his patience, understanding and the opportunity to fulfil this goal. Without his guidance, this dissertation would not have been possible.

I would also like to thank my supervisory committee members: Dr. Gloria Borgstahl, Dr. Sorin Luca, Dr. Jonathan Vennerstrom, and Dr. Joseph Vetro for being a part of my committee and for their input, guidance, and support throughout my studies. Especially Gloria and Sorin, for our many discussions and their concern for my health and overall well-being.

I would also like to acknowledge the current and past members of the lab. I thank them for their friendship and discussions throughout my time here. I also thank them for taking the time to help me learn the techniques of the lab and troubleshoot problems I encountered.

I would like to thank the staff and faculty of the department, especially Katina Winters, Michelle Parks, and Elaine Payne for all of their hard work. Also, none of this work would be possible without the funding from NSF, the GAANN fellowship, and the UNMC Fellowship.

I would like to thank my family and friends, without their support this would not have been possible. Thank you for believing in me during the time I did not myself. I

always had them to rely on during the difficult times when I was struggling whether it be school related or during personal matters. I specifically would like to acknowledge my husband, Steven, for always being there for me. He's always been supportive of my goals staying up late with me to get papers and presentations done and even taking time to drive me to lab when I couldn't, so I could get experiments done. Without him, this would have not been possible. I would also like to thank Alyssa Hudnall, Michelle Antes, and Megan Hangartner. You guys have always been there for me through the thick and thin and I am very grateful that you have not let distance come between us. Your friendship means the world to me and without your support this would not have been possible. I would also like to thank Damian Daszynski, Laura Weber, and Lee Sleightholm your guys' friendship and humor has made graduate school more enjoyable. Finally, I would like to acknowledge my Dad. It was his belief in me that first made me apply to graduate school. He always believed I could achieve anything I put my mind to and again he was right. Even though he didn't make it to see the completion of this dissertation, he will always remain one of my biggest supporters in my heart.

STABILITY AND KINETICS OF DNA PSEUDOKNOTS: FORMATION OF T*A•T
BASE-TRIPLETS AND THEIR TARGETING REACTIONS

Calliste Fran Steffensmeier, Ph.D.

University of Nebraska, 2016

Advisor: Luis A. Marky, Ph.D.

Pseudoknots have been found to play important roles in the biology of RNA. These stem-loop motifs are considered to be very compact and the targeting of their loops with complementary strands is accompanied with lower favorable free energy terms. We used a combination of UV melting, calorimetric (DSC and PPC) and kinetic (SPR) techniques to investigate: 1) Local base-triplet formation in pseudoknot secondary structures and the effect of buffer conditions; 2) energetic contributions for the association of pseudoknots with their complementary strands, including the kinetic rates as a function of targeting strand length; and 3) characterization of the preQ₁ riboswitch DNA analog in its unbound and ligand bound states.

Specifically, we investigated a set of DNA pseudoknots with sequence: d(TCTCTT_nAAAAAAAAAGAGAT₅TTTTTTT), where the length of the “T_n” loop was varied with n = 5, 7, 9, and 11. The favorable folding of each pseudoknot resulted from a favorable enthalpy-entropy compensation; related to favorable stacking and unfavorable uptakes of ions and water molecules. The increase in the length of the loop yielded higher T_{MS}, 53°C to 59°C, folding enthalpies ranging from -60 to -110 kcal/mol, resulting in a significant stabilization of the pseudoknots, ΔG° = -8.5 to -16.6 kcal/mol. This is consistent with the formation of one to two TAT/TAT base-triplet stacks in the pseudoknots with longer loops. Furthermore, the PPC results yielded folding volume changes, ΔV_s, ranging from 18 to 23 ml/mol, indicating a higher volume of the folded pseudoknots, due to the observed uptake of water (Δn_w of -11 to -24 mol H₂O/mol) and ions (Δn_{ion} of -2.5 to -4.1 mol Na⁺/mol) measured from osmotic stress and salt-dependence experiments, respectively. Furthermore, the folding thermodynamic profiles in different buffer conditions (10 mM Sodium Phosphate, 10 mM Sodium Cacodylate and 10 mM Sodium Cacodylate with 10 MgCl₂) for the pseudoknot with the larger loop (*PsK-11dT*) and its dU

substituted loop (*PsK-11dU*) and its RNA counterpart (*PsK-11RNA*) stabilities follow the order: $PsK-11dU < PsK-11dT < PsK-11RNA$, regardless of the buffer used. The magnitude of each thermodynamic profile depends heavily on the buffer used, this means it's important to consider the conditions used when carrying out these types of experiments. It is also very important to consider a suitable buffer for comparative purposes.

We use isothermal titration calorimetry and DSC to determine thermodynamic profiles for the association of pseudoknots with partially complementary strands to form duplex products, we obtained favorable reaction free energies. However, the targeting of pseudoknots containing local base-triplets is less favorable due to a larger free energy term that must be overcome to form the duplex product.

The SPR data indicated that the rate of association, k_{on} , decreases while the rate of dissociation, k_{off} , increases as the length of the targeting strand increases, which yielded increasing $K_{D\ app}$. This means the affinity of the target strand to the pseudoknot decreases as the length of the target strand increases for each pseudoknot. A similar trend was obtained when dissociation constant, $K_{D\ DSC}$, were measured from the Hess cycles created with the DSC data. However, the $K_{D\ DSC}$ were much smaller than the $K_{D\ app}$, the reason for the apparent discrepancy is that SPR is measuring both the initial association and initial dissociation rates of steady state equilibrium states while DSC are true equilibrium states involving the entire molecules.

The unfolding thermodynamic data of the DNA $preQ_1$ riboswitch analog appears to form multiple secondary structures in its unbound state. These structures could include: either the formation of dimers due to complementarity of the loops (kissing hairpins) or of the flanking ends (duplex), a hairpin, and a duplex with mismatches and wobble base-pairs. In the bound state there are structural changes, which are most noticeable under low salt conditions, indicating under high salt conditions a $PreQ_1$ could already be in a pseudoknot-like structure. However, more studies need to be done to confirm this finding.

TABLE OF CONTENTS

DEDICATION	i
ACKNOWLEDGMENTS	ii
ABSTRACT	iv
TABLE OF CONTENTS	vi
LIST OF TABLES	ix
LIST OF FIGURES	xi
LIST OF ABBREVIATIONS	xvi
CHAPTER 1: INTRODUCTION	1
CHAPTER 2: EXPERIMENTAL PROTOCOLS	
2.1. Materials	16
2.2. Methods	19
2.2.1. Temperature-Dependent UV Spectroscopy	19
2.2.2. Differential Scanning Calorimetry	27
2.2.3. Temperature-dependent Fluorescence Spectroscopy	31
2.2.4. Circular Dichroism	33
2.2.5. Pressure Perturbation Calorimetry	37
2.2.6. Isothermal Titration Calorimetry	39
2.2.7. Surface Plasmon Resonance	40
CHAPTER 3: STABILITY OF PSEUDOKNOTS CONTAINING TAT AND C ⁺ GC BASE-TRIPLETS: EFFECT OF STEM-LOOP COMPLEMENTARITY	
3.1. Summary	45
3.2. Introduction	46
3.3. Materials and Methods	48
3.4. Results	52
3.5. Conclusions	76

CHAPTER 4. INFLUENCE OF BUFFER OF ON THERMODYNAMIC STABILITY
OF DNA, dU AND RNA PSEUDOKNOTS

4.1. Summary	78
4.2. Introduction	79
4.3. Materials and Methods	80
4.4. Results	84
4.5. Conclusions	101

CHAPTER 5. CONTRIBUTIONS OF THE LOOPS ON THE TARGETING OF DNA
PSEUDOKNOTS

5.1. Summary	103
5.2. Introduction	104
5.3. Materials and Methods	106
5.4. Results	111
5.5. Conclusions	120

CHAPTER 6. KINETIC CHARETERIZATION OF DNA PSEUDOKNOT
TARGETING BY SURFACE PLASMON RESONANCE

6.1. Summary	122
6.2. Introduction	123
6.3. Materials and Methods	125
6.4. Results	127
6.5. Conclusions	165

CHAPTER 7. THERMODYNAMIC CHARACTERIZATION OF PREQ₁
RIBOSWITCH IN BOUND AND UNBOUND STATES

7.1. Summary	167
7.2. Introduction	168
7.3. Materials and Methods	170
7.4. Results	173

7.5. Conclusions	183
------------------	-----

CHAPTER 8. CONCLUSIONS AND FUTURE STUDIES

8.1. Local triplex formation in pseudoknot secondary structures and the effect of buffer conditions on DNA, dU, and RNA pseudoknots	185
8.2. Energetic contributions for the association of pseudoknots with their complementary strands, including the kinetic rates as a function of targeting strand length	188
8.3. Characterization of the PreQ1 riboswitch DNA analog in its unbound and ligand bound states	190

REFERENCES	192
------------	-----

LIST OF TABLES

CHAPTER 2:

Table 1.	Extinction Coefficients of Oligonucleotides	17-18
----------	---	-------

CHAPTER 3:

Table 1.	Thermodynamic Folding Profiles for DNA Pseudoknots and Controls	57
Table 2.	Thermodynamic Folding Profiles of Pseudoknots with a Flipped AT Base	68
Table 3.	Thermodynamic Folding Profiles of Pseudoknots with a C ⁺ GC Triplets	75

CHAPTER 4:

Table 1.	Thermodynamic Folding Profiles for <i>PsK-11dT</i>	90
Table 2.	Thermodynamic Folding Profiles for <i>PsK-11dU</i>	93
Table 3.	Thermodynamic Folding Profiles for <i>PsK-11RNA</i>	96
Table 4.	Ion and Water Uptake for Pseudoknots	100

CHAPTER 5:

Table 1.	Unfolding Thermodynamic profiles	115
Table 2.	Thermodynamic Profiles for the Targeting Reactions: Formation of Duplex Products	119

CHAPTER 6:

Table 1.	Kinetic Rates and Equilibrium Constants for <i>PsK-5</i> Targeting Reactions	132
Table 2.	Kinetic Rates and Equilibrium Constants for <i>PsK-9</i> Targeting Reactions	138
Table 3.	Kinetic Rates and Equilibrium Constants for <i>PsK-11</i> Targeting Reactions	149
Table 4.	Unfolding Thermodynamic Profiles for <i>PsK-5</i> , Target Strands, and Duplex Products.	155
Table 5.	DSC and SPR Equilibrium Constants for <i>PsK-5</i> Targeting Reactions	156
Table 6.	Thermodynamic Profiles for <i>PsK-9</i> and Duplex Products	159
Table 7.	DSC and SPR Equilibrium Constants for <i>PsK-9</i> Targeting Reactions	160
Table 8.	Thermodynamic Profiles for <i>PsK-11</i> and Duplex Products	163

Table 9.	DSC and SPR Equilibrium Constants for <i>PsK-11</i> Targeting Reactions	164
----------	--	-----

CHAPTER 7:

Table 1.	Folding Thermodynamic Profiles for DNA PreQ ₁ and Control Molecules	178
Table 2.	Folding Thermodynamic Profiles for DNA PreQ ₁ in Bound State	182

LIST OF FIGURES

CHAPTER 1:

Figure 1.	Watson-Crick base-pairing between DNA	3
Figure 2.	Structure of DNA and RNA	4
Figure 3.	The Structures of 2-aminopurine and naturally occurring purines of DNA	6
Figure 4.	Structure of Pseudoknots	7
Figure 5.	Hydrogen bonds involved in the formation of a Pyrimidine motif triplex	10

CHAPTER 2:

Figure 1.	Temperature Dependent Melting Curves A) Typical Absorbance <i>vs</i> Temperature Curves B) Plot of α <i>vs</i> Temperature	21
Figure 2.	UV Melting Curve for a Pseudoknot	22
Figure 3.	Typical DSC Melting Curve	30
Figure 4.	CD Spectra of Nucleic Acid Molecules A) Typical CD Spectra of DNA Pseudoknot B) Typical CD Spectra of RNA Pseudoknot	36
Figure 5.	How SPR Works A) Principle of SPR Experiment B) Typical Binding Curve and Equations	44

CHAPTER 3:

Figure 1.	Sequences, structures and designations of molecules investigated	50
Figure 2.	UV Melting Curves and Concentration Dependence A) UV Melt of Pseudoknots B) UV Melt of Control Molecules C) Concentration Dependence Pseudoknots D) Concentration Dependence Control Molecules	53
Figure 3.	DSC Melting Curves of Pseudoknots and Controls A) DSC unfolding of pseudoknots B) DSC unfolding of control molecules	56
Figure 4.	T_M -dependence on Salt concentration a) T_M dependence on salt concentration b) Δn_{Na^+} as a function of loop size	59

Figure 5.	T_M -dependence on water activity a) T_M -dependence on water activity b) Δn_w as a function of loop size	61
Figure 6.	PPC Curves of Pseudoknots	63
Figure 7.	UV Melting Curves and Concentration Dependence A) UV Melts of Flipped AT Pseudoknots B) Concentration Dependence of Flipped AT Pseudoknots	66
Figure 8.	DSC Melting Curves of Flipped AT Pseudoknots A) DSC unfolding of <i>PsK-9-6TA</i> B) DSC unfolding of <i>PsK-11-6TA</i>	67
Figure 9.	Fluorescence Spectra and Melting Curves of 2-AP <i>PsKs</i> A) Wavelength spectra of 2-AP modified pseudoknots B) Temperature melts of 2-AP modified pseudoknots	70
Figure 10.	DSC Melting Curves of 1 CGC Substituted Pseudoknots A) DSC unfolding of <i>PsK-5-1CGC</i> B) DSC unfolding of <i>PsK-9-1CGC</i>	73
Figure 11.	DSC Melting Curves of 2 CGC Substituted Pseudoknots A) DSC unfolding of <i>PsK-5-2CGC</i> B) DSC unfolding of <i>PsK-9-2CGC</i>	74
CHAPTER 4:		
Figure 1.	Sequences, Structures, and Designations of Molecules	81
Figure 2.	UV Melting Curves and Concentration Dependence A) UV Melts of <i>PsK-11dT</i> , <i>PsK-11dU</i> , and <i>PsK-11RNA</i> B) Concentration Dependence Pseudoknots	85
Figure 3.	Circular Dichroism Spectra of Pseudoknots	87
Figure 4.	DSC Melting Curves of <i>PsK-11dT</i>	89
Figure 5.	DSC Melting Curves of <i>PsK-11dU</i>	92
Figure 6.	DSC Melting Curves of <i>PsK-11RNA</i>	95
Figure 7.	T_M -dependence on Salt concentration and Water Activity A) T_M dependence on salt concentration B) T_M dependence on water activity	99

CHAPTER 5:

Figure 1.	Reactions Investigated	109
Figure 2.	Hess Cycle	110
Figure 3.	Targeting Reactions	112
	A) ITC injections of <i>PsK-5</i> into <i>CS-5</i>	
	B) ITC injections of <i>PsK-9</i> into <i>CS-9</i>	
Figure 4.	Melting Curves for Pseudoknots	114
	A) UV Melting Curves	
	B) T_M vs. $\ln C_T$	
	C) DSC Melting Curves	
Figure 5.	DSC Curves for PsKs, CS, and Duplexes	117
	A) <i>PsK-5</i> targeting reaction	
	B) <i>PsK-9</i> targeting reaction	

CHAPTER 6:

Figure 1.	Targeting Reactions of PsK-5 with Complementary Strands	130
Figure 2.	Sensograms and Steady State Fitting <i>PsK-5 + CS-5 Short</i>	131
	A) Sensogram for <i>CS-5 Short</i> binding	
	B) Steady State Fitting	
Figure 3.	Sensograms and Steady State Fitting <i>PsK-5 + CS-5 Mid</i>	133
	A) Sensogram for <i>CS-5 Mid</i> binding	
	B) Steady State Fitting	
Figure 4.	Sensograms and Steady State Fitting <i>PsK-5 + CS-5 Full</i>	134
	A) Sensogram for <i>CS-5 Full</i> binding	
	B) Steady State Fitting	
Figure 5.	Targeting Reactions of PsK-9 with Complementary Strands	136
Figure 6.	Sensograms and Steady State Fitting <i>PsK-9 + CS-9 Short</i>	137
	A) Sensogram for <i>CS-9 Short</i> binding	
	B) Steady State Fitting	
Figure 7.	Sensograms and Steady State Fitting <i>PsK-9 + CS-9 Mid</i>	139
	A) Sensogram for <i>CS-9 Mid</i> binding	
	B) Steady State Fitting	
Figure 8.	Sensograms and Steady State Fitting <i>PsK-9 + CS-9 Full</i>	142

	A) Sensogram for <i>CS-9 Full</i> binding	
	B) Steady State Fitting	
Figure 9.	Targeting Reactions of PsK-11 with Complementary Strands	146
Figure 10.	Sensograms and Steady State Fitting <i>PsK-11 + CS-11 Short</i>	147
	A) Sensogram for <i>CS-11 Short</i> binding at 20°C	
	B) Steady State Fitting at 20°C	
Figure 11.	Sensograms and Steady State Fitting <i>PsK-11 + CS-11 Short</i>	148
	A) Sensogram for <i>CS-11 Short</i> binding at 25°C	
	B) Steady State Fitting at 25°C	
Figure 12.	Sensograms and Steady State Fitting <i>PsK-11 + CS-11 Mid</i>	150
	A) Sensogram for <i>CS-11 Mid</i> binding at 20°C	
	B) Steady State Fitting at 20°C	
Figure 13.	Sensograms and Steady State Fitting <i>PsK-11 + CS-11 Mid</i>	151
	A) Sensogram for <i>CS-11 Mid</i> binding at 25°C	
	B) Steady State Fitting at 25°C	
Figure 14.	DSC Unfolding of <i>PsK-5</i> and Its Reaction Products	154
	A) <i>PsK-5</i> and <i>CS-5 Short</i> Reaction	
	B) <i>PsK-5</i> and <i>CS-5 Mid</i> Reaction	
	C) <i>PsK-5</i> and <i>CS-5 Full</i> Reaction	
Figure 15.	DSC Unfolding of <i>PsK-9</i> and Its Reaction Products	158
	A) <i>PsK-9</i> and <i>CS-9 Short</i> Reaction	
	B) <i>PsK-9</i> and <i>CS-9 Mid</i> Reaction	
	C) <i>PsK-9</i> and <i>CS-9 Full</i> Reaction	
Figure 16.	DSC Unfolding of <i>PsK-11</i> and Its Reaction Products	162
	A) <i>PsK-11</i> and <i>CS-11 Short</i> Reaction	
	B) <i>PsK-11</i> and <i>CS-11 Mid</i> Reaction	
CHAPTER 7:		
Figure 1.	Sequences, Structures, and Designation of Molecules	171
Figure 2.	UV Melting Curves and T_M Dependence on Concentration	174
	A) UV Melting of <i>PreQ₁</i> and controls	
	B) T_M vs. $\ln C_T$	
Figure 3.	Unfolding of <i>PreQ₁</i> and Control Molecules in Unbound State	177
	A) DSC unfolding of <i>PreQ₁</i>	
	B) DSC unfolding of <i>PreQ₁ HP</i>	
	C) DSC unfolding of <i>PreQ₁ T₅</i>	
Figure 4.	Possible Structures of <i>PreQ₁</i> Based on Sequence	179

Figure 5.	Unfolding of <i>PreQ1</i> and Control Molecules in Bound State	181
	A) DSC unfolding of <i>PreQ1</i>	
	B) DSC unfolding of <i>PreQ1 HP</i>	
	C) DSC unfolding of <i>PreQ1 T5</i>	

ABBREVIATIONS

2AP	2-aminopurine
SSC	sodium citrate
A	adenine
a_w	activity of water
CD	circular dichroism
C	cytosine
DNA	deoxyribonucleic acid
DSC	differential scanning calorimetry
dU	deoxyuridine
G	guanine
HP	hairpin
IDT	Integrated DNA Technologies
ITC	isothermal titration calorimetry
K	equilibrium constant
K_d	dissociation constant
k_{on}	association rate
k_{off}	dissociation rate
mRNA	messenger RNA
miRNA	microRNA
NaCac	sodium cacodylate
NaPi	sodium phosphate

ODNs	oligonucleotides
Osm	osmolality
PPC	pressure perturbation calorimetry
Q	queuosine
RISC	RNA-induced silencing complex
RNA	ribonucleic acid
RNAi	RNA interference
RU	resonance unit
siRNA	small interfering RNA
SPR	surface plasmon resonance
T	thymine
UV	ultraviolet

CHAPTER ONE

1.1 INTRODUCTION

The discovery of deoxyribonucleic acid (DNA) spans back all the way to the early 1870s when Friedrich Miescher was researching the components of leukocytes and discovered an interesting new molecule. He first believed it was a new protein but soon realized it was a completely new molecule in which he termed “nuclein” which would later be known as nucleic acids (1). It wasn't until the 1920s that Phoebus Levene identifies the building blocks of DNA to include four bases: adenine (A), cytosine (C), guanine (G), and thymine (T). However, at this time it was still believed that proteins were the carriers of genetic information because there were 20 amino acids and only four different nucleotides. In 1944, Oswald T. Avery, Colin MacLeod, and Maclyn McCarty suggests that DNA may function as the genetic material, however it won't come until later when this was accepted (2). Erwin Chargaff makes an important finding in the early 1950s about the base composition of DNA having fixed ratios: the same number of A's as T's and the same number of C's as G's, later known as Chargaff's rule. In 1952, Alfred Hershey and Martha Chase used viruses to confirm DNA as the genetic material by demonstrating that during viral infection DNA enters the bacteria while the viral proteins do not and that this DNA can be found in offspring virus particles (3). Rosalind Franklin and Maurice Wilkins play a huge role in the determination of the structure of DNA by the use of fiber diffraction to demonstrate that DNA has a regularly repeating helical structure. A molecular model for DNA structure was created by Watson and Crick in 1953 by putting all of this information together to determine DNA forms a double helix

structure with Watson-Crick base-pairing with the sugar phosphate backbone containing deoxyribose (4), Figure 1.

The structure of DNA and ribonucleic acid (RNA) are quite similar. They are both composed of the sugar phosphate backbone, however, the main chemical difference is that RNA contains an extra hydroxyl group at the 2' position of the sugar. Another difference is RNA is composed of the base uracil instead of thymine which lacks a methyl group. In nature DNA usually exists in a double-stranded helical state, while RNA is found in a single-stranded state of shorter lengths, Figure 2. Along with the composition of DNA and RNA there are also structural differences between the molecules as well. DNA is typically found in the B-form and RNA in the A-form. What this means is when in the B-form the double helical axis runs through the center of the Watson-Crick base-pairs and there is a well-defined major and minor groove. The A-form, however, contains a hole along the molecular axis because the base-pairs are no longer centered and the minor groove is flat and broad, while the major groove is very deep and narrow. The reason for the A and B form has to deal with what is known as sugar puckering. B-form adopts a C2' endo conformation giving a distance of 7Å between the adjacent phosphate residues along the chain. In A-form the C3' endo conformation gives only a distance of 5.9Å between the adjacent phosphates, showing the sugar group is an elastic element in the backbone and permits conformational changes in the backbone of nucleic acids (5). The final element in flexibility is found in the orientation of the bases to the sugar, which can be found in either the syn or anti conformations. It has been found that in B-DNA the bases are only found in the anti-conformation but can be found in syn conformation in other DNA conformations (5).

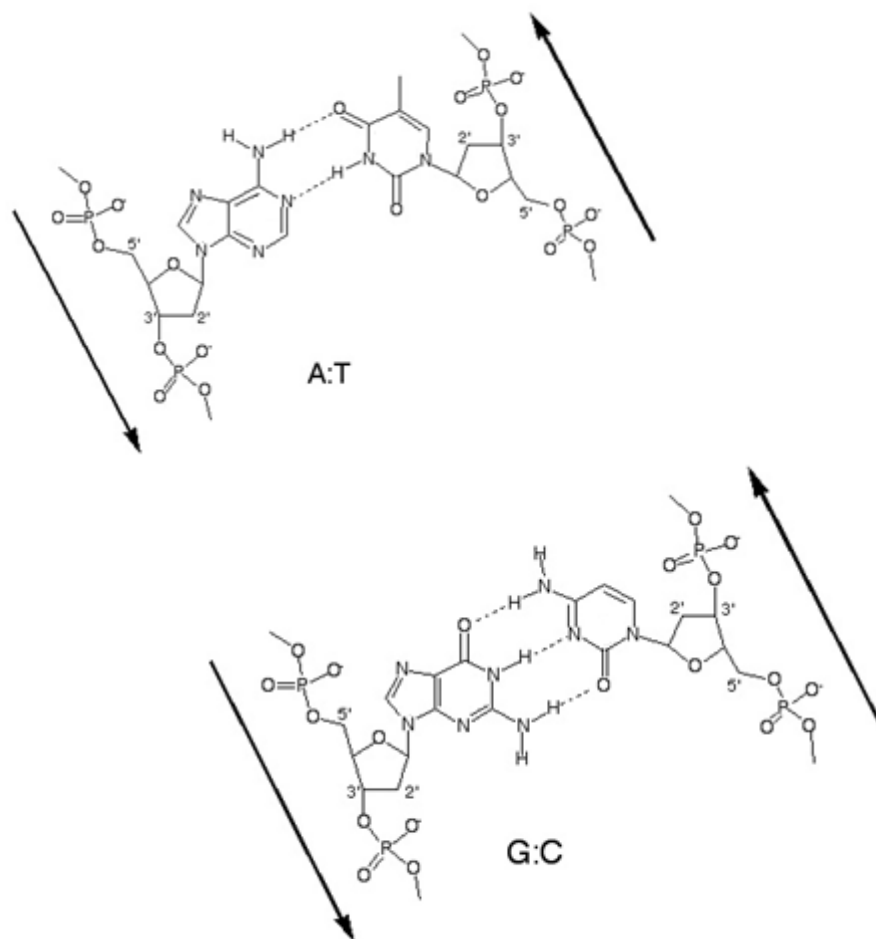
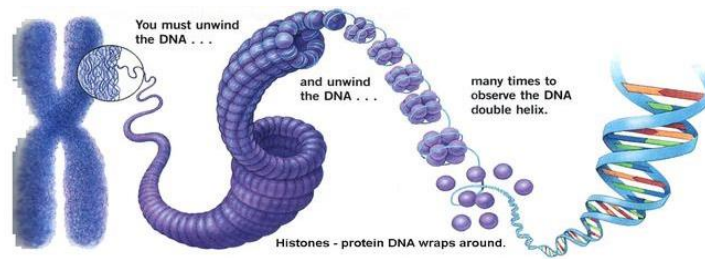


Figure 1. Watson-Crick base-pairing between DNA.

A)



B)

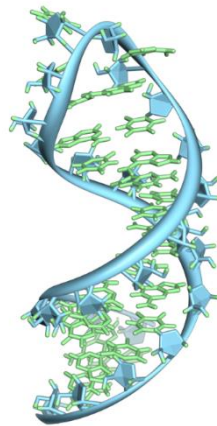


Figure 2. Structure of DNA and RNA. A) Image from Chapter 7. DNA, Genes and Chromosomes page 165. B) Image from PDB: 1YSV. (6)

More recently, modified bases have been used to study the physical properties of the local environment of DNA. One important technique to study these properties is fluorescence, however, DNA itself does not fluoresce, so the development of a synthetic fluorescent base known as 2-aminopurine (2AP) can be substituted for a canonical base in a DNA molecule. For example, in the fluorescent analog of the purine bases; its amino group is in the 2 position rather than 6 in adenine, Figure 3 (7). Due to the fact that it can be substituted for either an adenine or guanine, it can still form hydrogen bonds with both thymine and cytosine, respectively (8). As the DNA molecules undergo conformational changes the observed fluorescence intensity will give insight in what is occurring during this transition. 2AP has been used widely as a probe to investigate the local environment and dynamics of nucleic acids (9-15), and their interaction with protein and other ligands (16-19).

Since the discovery of the double helix structure of DNA a variety of other structures have been found that nucleic acids can form. These include but aren't limited to: hairpins, triplexes, quadruplexes, cruciforms and pseudoknots (5). The formation of these secondary structures depends on Van der Waals forces, electrostatic dipole forces between bases, and solvation effects (20). The formation and biological functions of these structures are well documented (5), (21-36). In particular, pseudoknots are an interesting and diverse RNA structural motif which contain two or more stem-loop motifs with intercalated stems, Figure 4. They are diverse due to variation in their stem sequence, the fluctuation of loop length and sequence, as well as, their interactions among themselves. Pseudoknots have been found to be involved in a variety of biological functions

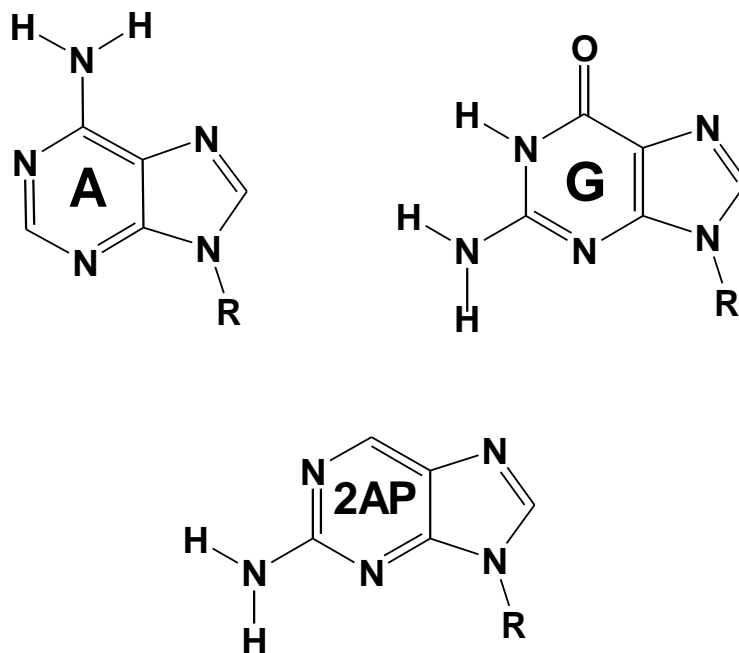
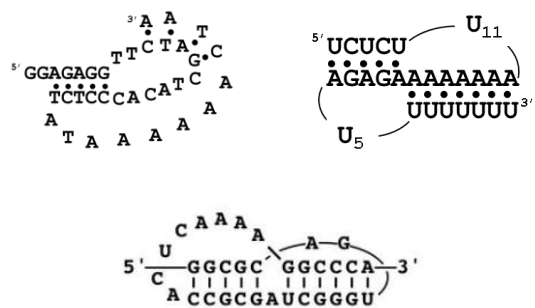


Figure 3. The structures of 2-aminopurine and the naturally occurring purines of DNA.

A)



B)

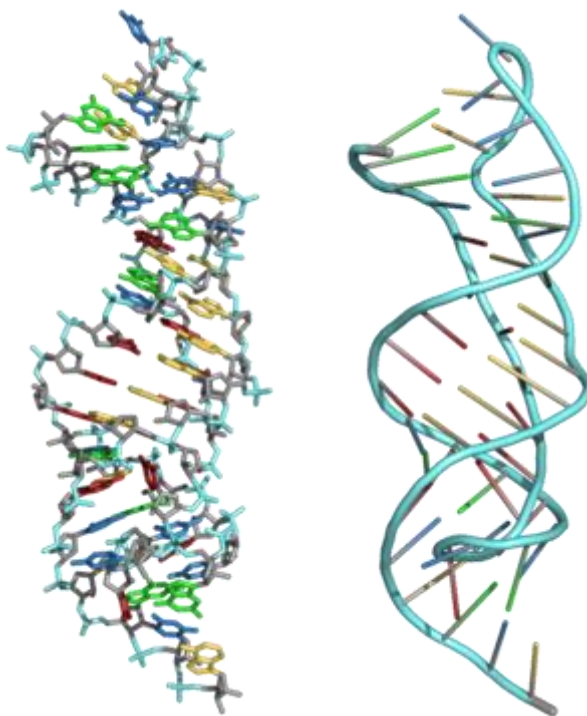


Figure 4. Structure of Pseudoknots. A) Different structures of pseudoknots. B) Structure of Human Telomerase RNA pseudoknot PDB 1YMO. (37)

including: telomerase (38), (37), self-splicing introns (39), forming the catalytic core of various ribozymes (40-42), ribosomal frameshifting (43), (44), and riboswitches (45).

The human telomerase contains a 451 nucleotide RNA, a catalytic protein (hTERT) and other proteins. There is a pseudoknot structure at the 5' end that is essential for the telomerase activity although little is known on the exact mechanism (37). Also, the HDV ribozyme self-cleaves to produce the single-genome RNA of hepatitis delta virus with the folding into a double-pseudoknot structure (46). Another example is the *glmS* ribozyme where there is a pseudoknot located in the 3' non-core region that enhances the self-cleavage activity (47).

In ribosomal frameshifting, a common mechanism found in viruses, the production of two proteins is possible from the same mRNA. One example is HIV₁ polyprotein gag-pol which requires efficient -1 frameshifting for the expression of gag and pol gene products (48). The -1 ribosomal frameshifting event brings the overlapping gag-pol out-of-phase allowing for the two products to be translated separately (49). There are three things that are needed for an effective frameshift event to occur: a slippery sequence, a spacer sequence, and a stem-loop secondary structure often found to be a pseudoknot and in HIV₁ this is the case (43,) (50). The importance of the pseudoknot is to stall the ribosome allowing for the tRNA to re-pair with the mRNA in the -1 position (50). The high efficiency of frameshifting could be due to the formation of a local base-triplet stack within the pseudoknot to increase the stability of the terminal stem and its interaction with the ribosome (44).

The stability of a triplex depends again on the hydrogen bonding between the third strand and the purine bases of the duplex, base-stacking, and solvation effects (24),

(44), (51). There are two classes of triplexes which depends on the third strand's composition and orientation. The pyrimidine motif consists of pyrimidine bases that bind the purine duplex bases in the parallel orientation and the purine motif where purine bases bind the purine duplex bases in the anti-parallel orientation, Figure 5.

Riboswitches are noncoding RNA elements that control gene expression and monitor the cellular environment (52). They are composed of a highly conserved aptamer domain and an expression platform which can function as a genetic on/off switch in response to ligands (53). Riboswitches are cis-acting mRNA sequences that provide a well-designed solution to the problem of bacterial gene regulation. By directly sensing small molecules via an aptamer domain, riboswitches can adapt quickly to fluctuations in intracellular ligand concentration to establish a feedback loop that controls the production or import of metabolites, or the response to second messengers (54). Several ligands have been identified that are recognized by multiple, structurally unrelated riboswitch classes; this group includes: SAM, cyclic-di-GMP, TPP, and preQ₁ (55), (56). Riboswitches can control gene expression in a variety of ways including: transcription and translation attenuation or antisense regulation (52). TPP, preQ₁, and SAM-I riboswitches rely on a mechanism where the ribosomal binding site is sequestered within the core of the conserved aptamer domain of the riboswitch to control translation (52).

The riboswitch of interest due to its size and structure is preQ₁. The preQ₁ riboswitch is responsive to preQ₁ which is the final metabolite on the biosynthetic pathway that produces the hypermodified nucleotide queuosine (Q). Q is an important modification that enhances translational accuracy (57-59) by incorporating Q at the wobble position of specific anticodons in several eukaryotic and bacterial tRNAs (58).

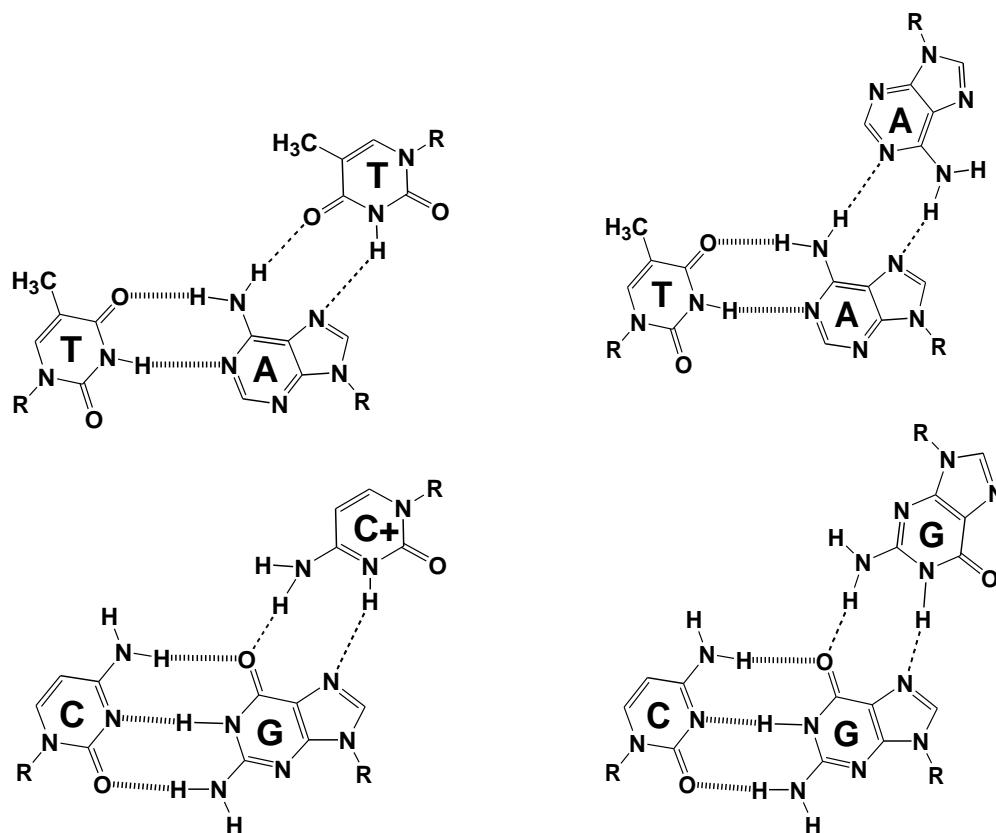


Figure 5. Hydrogen bonds involved in the formation of a Pyrimidine motif triplex.

Watson-Crick hydrogen bonds are shown with thicker dashes, and Hoogsteen hydrogen bonds are shown with dashed lines.

Q deficiency in bacteria can lead to reduced growth in the stationary phase (59) and reduced virulence (60). To meet regulatory needs, riboswitches responsive to preQ₁ evolved into three distinct riboswitch classes. The preQ₁-I aptamer is distributed widely and is 34 nucleotides (61). The preQ₁-II riboswitch is 80 nucleotides (62), while the preQ₁-III is 120 nucleotides and much more complex in structure (63).

It is also important to understand the stability of nucleic acid secondary structures because it will help in the development of gene regulation. The use of drugs to target these structures to control their biological regulation in the treatment of genetic disorders will ultimately further our understanding of the genome (64-67). Most traditional small molecule DNA-binding drugs, have failed due to low selectivity to a particularly gene of interest which needs high specificity and tight affinity. However, DNA can provide both of these factors needed by forming either a duplex or triplex product providing strategies for the control of gene expression. Based on the number of base-pairs in the human genome, only 17 bases are needed to target a specific gene because statistically a 17 base sequence can only appear once with the genome containing 6.4×10^9 base-pairs (68).

There are three main approaches for using oligonucleotides as modulators of gene expression: antisense, antigene and RNA interference (RNAi) strategies all of which target specific nucleic acid sequences. In the antisense and antigene strategies, formation of stable duplex or triplex molecules is needed which is provided by the energy in base-pair and base-triplet stack formation, respectively. RNAi also depends on the formation of base-pairs and base-pair stacks but is enhanced by protein binding.

If there is a particular protein of interest, in the antisense strategy an oligonucleotide binds to the mRNA, forming a DNA/RNA hybrid duplex that inhibits translation (27),

(29). This strategy has long been the main method used to control genes at the post-transcriptional level (26) (69). The DNA/RNA hybrid duplex that is formed between the antisense oligonucleotide and the target mRNA interferes directly with protein synthesis, resulting in reduced expression of the protein of interest. This inhibition can be caused by the inability of the correct assembly of the translation machinery or an RNase H mediated cleavage of the RNA strand in this hybrid (28). However, this strategy is limited by the secondary and tertiary structure of mRNA. If an oligonucleotide targets a region of mRNA, it will need to unfold the original secondary/tertiary structure of this RNA. In terms of thermodynamics, this means the binding reaction needs to provide enough energy to overcome this potential barrier. Unpaired bases are needed to drive the reaction forward because the strand must be able to invade and disrupt the secondary structure to form a larger number of base-pair stacks in the duplex products.

In the antigene strategy, a triplex is formed when an oligonucleotide binds to the major groove of a DNA duplex (70), (71). This triplex formation is sequence specific and forms through Hoogsteen base-pairing (70), (71). In general, the affinity in the stable formation of a triplex is provided by base stacking contributions, hydrogen bonding between the third strand bases and purine bases of the duplex, and electrostatic and hydration contributions (24), (51), (72). For instance, in order to prevent the transcription of a gene using an antigene strategy, a triplex with a ΔG° of nearly $-20 \text{ kcal}\cdot\text{mol}^{-1}$ can potentially compete with the binding of proteins that activate the transcriptional machinery (29), (73), (74). This approach is feasible and has advantages over other strategies due to their only being a few copies of a gene and an abundance of mRNA making it more efficient to target the gene directly (31), (75). However, there are

limitations to this approach due to the nuclear DNA being highly packed and the targeting DNA also needing to cross both the cellular and nuclear membranes (76).

A simplified model for RNAi includes: natural occurring interfering RNAs are cleaved from the transcriptional product through the function of a series of proteins into siRNA or miRNA and transported to the cytoplasm (77-81). In the second step, the dsRNA assembles with proteins, forming an RNA-induced silencing complex (RISC) (82-86) and one of the strands is removed from this complex (87-89), allowing the other complementary strand to bind to the mRNA target (86), (90), (91). The binding of RISC to the target will suppress, or silence, the expression by either degrading the target mRNA (92); or repressing the translation of mRNA if siRNA/mRNA duplex contains mismatches (93-95).

In this investigation we have studied a variety of DNA pseudoknots, hairpin loops, duplexes and related oligonucleotides using calorimetric and spectroscopic techniques. Specifically, we used a combination of temperature-dependent UV, fluorescence, circular dichroism (CD) spectroscopy, and differential scanning calorimetry (DSC) techniques to characterize the melting behavior, and to determine the energetics, hydration and electrostatic contributions involved in the following systems: (i) the formation of various DNA structures, (ii) the interactions of DNA structures with their complementary single stranded oligonucleotides and (iii) the interaction of preQ₁ riboswitch with and without its ligand. Isothermal titration calorimetry (ITC) was also used to directly characterize the thermodynamics of targeting reactions. These results are compared with those obtained indirectly from Hess cycles created from the DSC unfolding profiles of the

reactants and products of the targeting reactions. Surface Plasmon Resonance (SPR) was also used to measure the kinetics for these targeting reactions.

First, we postulate that the bases in the loop of a pseudoknot can alter the stability of the molecule, through interaction of the loop bases with the duplex stem if the loop is complementary to the stem to form base-triplet stacks. This hypothesis is addressed in Chapter 3, where we examine the stability of pseudoknots as a function of the loop length and stem and loop sequence to determine the formation of base-triplets in pseudoknots. In Chapter 3, we design a set of pseudoknots with different loop lengths increasing from 5 to 11 thymines. We also flip one AT base-pair in the stem to disrupt and triplet formation and finally we substitute TAT base-triplets for C⁺GC base-triplets and determine their standard thermodynamic profiles and ion and water binding. In Chapter 4, we study one of the pseudoknots in Chapter 3 along with a DNA pseudoknot containing a modified dU loop and a RNA pseudoknot all with loop lengths of 11 thymines, dUs, or uridines, respectively. We study the effects of buffer conditions on the overall stability of DNA, dU substitution and RNA oligos along with the effect of ion and water uptake in this chapter.

Next, we propose the use of a single stranded oligonucleotide for two reasons: first to act as a therapeutic reagent for the control of gene expression and also to confirm the formation of base-triplet stack formation in pseudoknots. This is addressed in Chapters 5 and 6. In Chapter 5, we studied reactions involving the targeting of two pseudoknots, one with loop length of 5 thymines and another with 9 thymines. It was found in Chapter 3 that a loop of 5 thymines isn't long enough to form base-triplets, however, a loop length of 9 thymines can form one TAT/TAT base-triplet stack. Knowing this the reaction of the

pseudoknot with base-triplets forming should be less favorable due to a more stable structure needing to be disrupted. In Chapter 6, we studied reaction rates of three pseudoknots two of which form base-triplets. In Chapter 7, we report preliminary investigations on the thermodynamic characterization of the class I preQ₁ aptamer in the unbound and bound states.

A summary of each chapter is given below:

- Chapter 2 contains a description of the experimental protocols used in this investigation.
- Chapter 3 focuses on the effect of loop length of the stability of DNA pseudoknots.
- Chapter 4 analyzes the effects of buffer conditions on DNA, dU and RNA pseudoknots.
- Chapter 5 studies the targeting reactions of pseudoknots with their complementary strands.
- Chapter 6 investigates the kinetics of the targeting reactions of DNA pseudoknots with their complementary strands using SPR
- Chapter 7 reports on the preliminary characterization of the preQ₁ riboswitch.
- Chapter 8 presents the overall conclusions of this dissertation and possible future investigations.

CHAPTER TWO

EXPERIMENTAL PROTOCOLS

2.1 MATERIALS

We have studied the energetics, ion, and hydration contributions of ~ 31 DNA/RNA pseudoknots and/or related oligonucleotides (ODNs). All ODNs were synthesized by Integrated DNA Technologies (IDT) (Coralville, IA). The ODNs were first purified using reverse phase HPLC and then size exclusion column chromatography. A concentrated solution of oligomer was loaded into a column packed with Sephadex G-10 gel and eluted with de-ionized and triple-distilled water. The void volume was generally 100 – 160 mL and the desalted ODN solution [~ 15-20 mL, to assure that the fraction collected was salt-free] was collected into a 50 mL ultracentrifuge plastic tube. The desalted oligomer solution was then frozen, lyophilized to dryness using a FreeZone Model 77510 freeze dry system from Labconco Co., (Kansas City, MO), and stored at ~ 4 °C. DNA stock solutions were prepared by dissolving lyophilized ODNs in appropriate buffers and their concentration was determined in water, spectrophotometrically, at 260 nm and high temperature where all oligomers were in the random coil state.

Their molar extinction coefficients, ϵ_{260} , were calculated as follows: First, we used the molar extinction values for monomers and dimers according to the relation: $\epsilon_{260} (25\text{ }^\circ\text{C}) = 2\sum_{\text{dimers}} - \sum_{\text{monomers}}$ to calculate ϵ_{260} at 25 °C (the summation of the monomers excludes the bases at the 5' and 3' ends for a given oligonucleotide) (96). Next, ϵ_{260} at high temperature, where the oligomer is in the single-stranded state, is obtained from ϵ_{260} at 25 °C and linearly extrapolated to this high temperature using the upper baseline of its melting curves (97). The molar extinction coefficients are summarized in Table 1.

Table 1. Extinction Coefficients of Oligonucleotides (mM⁻¹cm⁻¹).

<u>Oligonucleotide (5' → 3')</u>	<u>Name</u>	<u>ε₂₆₀</u> mM ⁻¹ cm ⁻¹	<u>Chapter</u>
<i>Pseudoknots</i>			
TCTCTT ₅ A ₈ GAGAT ₁₂	<i>PsK-5</i>	331	3
TCTCTT ₇ A ₈ GAGAT ₁₂	<i>PsK-7</i>	344	3
TCTCTT ₉ A ₈ GAGAT ₁₂	<i>PsK-9</i>	367	3
TCTCTT ₁₁ A ₈ GAGAT ₁₂	<i>PsK-11</i>	376	3
TCTCTdU ₁₁ A ₈ GAGAT ₁₂	<i>PsK-11dU</i>	360	6
UCUCUU ₁₁ A ₈ GAGAU ₁₂	<i>PsK-11RNA</i>	409	6
<i>Pseudoknot Stem Substitutions</i>			
TCTCTTCT ₃ A ₅ GAAGAGAT ₅ TCT ₅	<i>PsK-5-1CGC</i>	327	3
TCTCTTCTCTA ₃ GAGAAGAGAT ₅ TCTCT ₃	<i>PsK-5-2CGC</i>	327	3
TCTCTTCT ₇ A ₅ GAAGAGAT ₅ TCT ₅	<i>PsK-9-1CGC</i>	357	3
TCTCTTCTCT ₅ A ₃ GAGAAGAGAT ₅ TCTCT ₃	<i>PsK-9-2CGC</i>	347	3
TCTCTT ₉ A ₅ TAAGAGAT ₅ TAT ₅	<i>PsK-9-6TA</i>	363	3
TCTCTT ₁₁ A ₅ TAAGAGAT ₅ TAT ₅	<i>PsK-11-6TA</i>	374	3
<i>Control Molecules</i>			
TCTCTTTTTTTT	<i>5' Ctrl</i>	181	3
TTAAAAAAAAGAGATT	<i>3' Ctrl</i>	237	3
TCTCTT ₉ AGAGA	<i>TC HP</i>	174	3
A ₇ T ₉ T ₇	<i>AT HP</i>	219	3

<i>2-Amino Purine Substitutions</i>			
TCTCTT ₉ A ₅ A _p AAGAGAT ₁₂	<i>PsK-9-6AP</i>	341	3
TCTCTT ₁₁ A ₅ A _p AAGAGAT ₁₂	<i>PsK-11-6AP</i>	364	3
TCTCTT ₉ A ₃ A _p AAAAGAGAT ₁₂	<i>PsK-9-2AP</i>	343	3
TCTCTT ₁₁ A ₃ A _p AAAAGAGAT ₁₂	<i>PsK-11-2AP</i>	361	3
<i>Complementary Strands</i>			
A ₆ GAGA	<i>CS-5 Short</i>	122	5
T ₃ A ₆ GAGA	<i>CS-5 Mid</i>	146	5
CT ₈ A ₆ GAGA	<i>CS-5</i>	181	4, 5
A ₁₀ GAGA	<i>CS-9 Short</i>	170	5
T ₃ A ₁₀ GAGA	<i>CS-9 Mid</i>	194	5
CT ₈ A ₁₀ GAGA	<i>CS-9</i>	237	4, 5
A ₁₂ GAGA	<i>CS-11 Short</i>	194	5
T ₃ A ₁₂ GAGA	<i>CS-11 Mid</i>	218	5
<i>Riboswitch</i>			
G ₂ AGAG ₂ T ₂ CTAGCTACAC ₃ TCTATA ₆ CTA ₂	<i>PreQ₁</i>	376	7
G ₂ AGAG ₂ T ₂ CTAGCTACAC ₃ TCTAT	<i>PreQ₁ HP</i>	252	7
G ₂ AGAG ₂ T ₃ C ₂ TCTAT	<i>PreQ₁ T₅</i>	180	7

2.2 METHODS

2.2.1 Temperature-dependent UV Spectroscopy

Absorbance versus temperature profiles (melting curves) for the helix to coil transition of DNA complexes were measured with a thermoelectrically controlled Aviv 14-DS spectrophotometer (Lakewood, NJ), interfaced to a PC computer for acquisition and analysis of experimental data. Water condensation on the exterior of the cuvette, at low temperatures, was prevented by flushing the chamber with a constant stream of dry nitrogen gas. Nucleotide bases of DNA absorb light in the far UV region, and the absorbance was monitored at 260 nm, while the temperature was increased at a constant rate of 0.5 °C/min. The structure of pseudoknots, or the DNA double helical structure, is such that its aromatic bases are stacked while the sugar phosphate backbone is exposed to the solvent. Upon unfolding, the nucleotide bases are exposed to the solvent, yielding a hyperchromic effect, i.e., increase in absorbance at 260. Therefore, these melting curves allow us to directly monitor the helix-coil transition of a given pseudoknot or oligonucleotide. In general, an oligomer with dA-dT base pairs will have a higher hyperchromic effect at 260 nm. Figure 1A shows a typical UV-melting curve for standard duplex DNA, where we can observe the characteristic sigmoidal shape.

The melting curve begins at low temperature, where the oligomer is in a helical state, i.e., the bases are away from the solvent and therefore the absorbance is low. As the temperature is increased, the nucleotide bases are exposed to the solvent resulting in a hyperchromic effect for a typical duplex DNA. As we reach higher temperatures, the oligomer transitions to the random coil state i.e., all nucleotide bases are exposed to the solvent and thus a plateau in absorbance is observed at the end of the UV melt, Figure 2.

From these experiments we can obtain standard thermodynamic parameters such as, the thermal stability or T_M , as well as model dependent parameters (van't Hoff enthalpy, ΔH_{vH} , free energy, ΔG° ; and entropy, ΔS) (98).

If we define α as the total fraction of single strands in the helical state, and changes in the absorbance measure the progress of the helix \rightarrow coil transition, then an absorbance versus temperature profile (UV melt) can be translated to an α versus temperature profile. Assuming that the fractional change in absorbance at any temperature monitors the extent of reaction and taking the ratio at each temperature of the height between the upper baseline and the experimental curve (X) and the height between the lower and upper baselines ($X+Y$), we can construct the curve in Figure 1B, that communicates how an equilibrium property α , varies with temperature. The equilibrium constant (K) for the helix to coil transition can also be expressed in terms of α values. Using the temperature dependence of K we can calculate the transition enthalpy. For an intramolecular helix \rightarrow coil transition, K can be expressed in terms of α as follows:

$$K = \frac{[Coil]}{[Helix]} = \frac{\alpha}{1-\alpha} \quad (2.1)$$

Substituting the above expression in the van't Hoff equation, the model dependent van't Hoff enthalpy, ΔH_{vH} , is calculated from the shape of the melting curve.

$$\frac{\partial \ln K}{\partial T} = \frac{\Delta H_{vH}}{RT^2} \quad (2.2)$$

$$\Delta H_{vH} = (2 + 2n)RT_M^2 \left(\frac{\partial \alpha}{\partial T} \right)_{T=T_M} \quad (2.3)$$

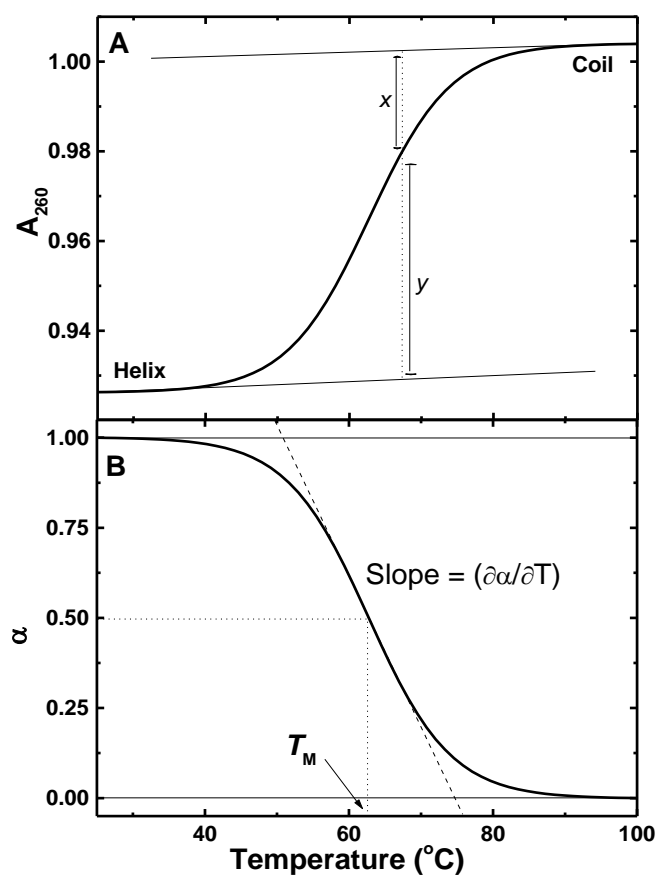


Figure 1. A) Typical absorbance versus temperature melting curves. X corresponds to the distance between an upper baseline and the curve, while Y represents the distance between the lower baseline and the curve. B) A plot of α versus temperature, where α equals the fraction of single strands in the duplex state. This curve is derived from the curve in (A) as described in the text.

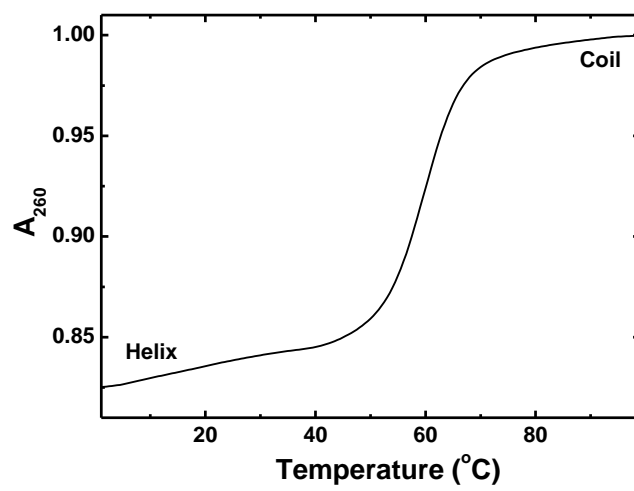


Figure 2. Typical UV melting curve for a pseudoknot.

The T_M is obtained from the midpoint of the helix \rightarrow coil transition for each oligonucleotide; n , is the molecularity of the reaction; α , is the total fraction of single strands in the duplex state; $d\alpha/dT$, is the slope around the T_M and obtained from an α versus temperature plots; and R is the gas constant (98).

Another method to quickly analyze a melting curve that provides the same information is as follows. First normalize the melting curve to 1, meaning that the largest absorbance on the curve is divided into all data points. This normalization makes the upper baseline of the melting curve at a value of 1 and the lower baseline at some fraction of 1. The next step is to draw an upper and lower baseline for the melting curve, similar to Figure 1A. The T_M will be the point equi-distant from the upper and lower baselines that lies on the melting curve, for monomolecular transitions. Draw a slope line perpendicular to the T_M , intersecting the upper and lower baselines similar to the dashed line in Figure 1B. Draw vertical lines down to the x-axis (temperature axis) from where the slope line intersects the upper and lower baselines, to find the temperature at which these intersections occur (T_2 and T_1 , respectively). The value for the slope in terms of α would be negative (0-1) but in this case the slope, m , is equal to $1/(T_2-T_1)$, because the slope is positive. As above, n is the molecularity of the reaction, R is the gas constant, and T_M is the value determined from the plot in Kelvin. The numbers can be inserted into equation 2.3b to quickly determine ΔH_{vH} .

$$\Delta H_{vH} = (2 + 2n)RT_M^2 m \quad (2.3b)$$

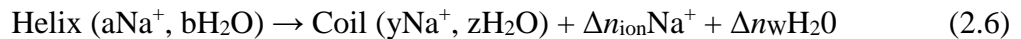
For intramolecular transitions, the free energy, ΔG° , at a given temperature can be calculated from the following equation:

$$\Delta G^\circ(T) = \Delta H_{vH} \left(1 - \frac{T}{T_M} \right) \quad (2.4)$$

The entropy, ΔS , can be obtained directly from the Gibbs equation:

$$\Delta G^\circ = \Delta H - T\Delta S \quad (2.5)$$

In addition, there is a release (or uptake) of counterions and water molecules during the helix \rightarrow coil transition because the amount of ions and water molecules associated with the helical and random coil states are different. We can calculate the release or uptake of ions and water from UV melting curves as a function of salt or osmolyte concentration, respectively. Given the general unfolding reaction:



Where, $\Delta n_{\text{ion}} = y - a$ and $\Delta n_{\text{w}} = z - b$; these terms correspond to the differential binding of counterions and water molecules, respectively. If a "release" takes place, the Δn parameter is written on the right hand side of this reaction, and if there is an "uptake" of any of these species, the Δn parameter should be written on the left hand side of the reaction. We can express the equilibrium constant of the previous reaction with the following equation:

$$K = \frac{[\text{Coil}]}{[\text{Helix}]} [\text{Na}^+]^{\Delta n_{\text{ion}}} [\text{H}_2\text{O}]^{\Delta n_{\text{w}}} \quad (2.7)$$

Since there are exponential terms, a logarithmic function can be used to simplify equation 2.7 to:

$$\ln K = \ln K(T, P, \ln[\text{Na}^+], \ln[\text{H}_2\text{O}]) \quad (2.8)$$

The total differential is equal to:

$$d \ln K = \left(\frac{\partial \ln K}{\partial T} \right)_{P, [Na^+], [H_2O]} dT + \left(\frac{\partial \ln K}{\partial P} \right)_{T, [Na^+], [H_2O]} dP \quad (2.9)$$

$$+ d \ln K = \left(\frac{\partial \ln K}{\partial \ln(Na^+)} \right)_{T, P, [H_2O]} d \ln(Na^+) + \left(\frac{\partial \ln K}{\partial \ln(H_2O)} \right)_{T, P, [Na^+]} d \ln(H_2O)$$

The last two partial differentials correspond to the desired quantities, which are called linking numbers. Linking numbers are measured experimentally with the assumption that the association of counterions and water molecules to the helical and coil states of the oligonucleotide takes place with a similar type of binding. Counterions bound to the negatively charged phosphate backbone in the helical and coil states are assumed to have similar binding. Furthermore, this assumption may not be correct for water molecules, because the helical state of DNA binds primarily electrostricted water (around charges) due to the exposure of the negatively charged phosphate groups to solvent, while the random coil state binds primarily structural (hydrophobic) water (around polar and non-polar atomic groups). These linking numbers are expressed as follows:

$$\Delta n_{Na^+} = \left(\frac{\partial \ln K}{\partial \ln(Na^+)} \right)_{T, P, [H_2O]} \quad (2.10)$$

$$\Delta n_w = \left(\frac{\partial \ln K}{\partial \ln(H_2O)} \right)_{T, P, [Na^+]} \quad (2.11)$$

Applying the chain rule to each linking number we obtain the following equations:

$$\Delta n_{Na^+} = \left(\frac{\partial \ln K}{\partial \ln(Na^+)} \right) = \left(\frac{\partial \ln K}{\partial T_M} \right) \times \left[\frac{\partial T_M}{\partial \ln(Na^+)} \right] = 1.11 \times \left(\frac{\Delta H}{RT_M^2} \right) \times \left[\frac{\partial T_M}{\partial \ln[Na^+]} \right] \quad (2.12)$$

$$\Delta n_w = \left(\frac{\partial \ln K}{\partial \ln(H_2O)} \right) = \left(\frac{\partial \ln K}{\partial T_M} \right) \times \left[\frac{\partial T_M}{\partial \ln a_w} \right] = \left(\frac{\Delta H}{RT_M^2} \right) \times \left[\frac{\partial T_M}{\partial \ln a_w} \right] \quad (2.13)$$

The terms Δn_{Na^+} and Δn_w represent the differential binding of counterions and water, respectively. In these equations, the terms in parentheses are constants that were obtained directly from differential scanning calorimetric experiments i.e., the enthalpy is model independent; while the terms in brackets are determined from UV melting curves by measuring the T_M dependence as a function of sodium concentration and water activity, respectively, and 1.11 is a constant for converting NaCl concentration into activity (99-104). Buffer solutions of various sodium concentrations were prepared by addition of NaCl to the desired salt concentration. Buffer solutions of various water activities are prepared by addition of osmolytes, to the desired activity of water. The final osmolality (Osm) of each solution is calculated by weight and further confirmed by vapor pressure osmometry using a UIC vapor pressure osmometer Model 830. (Joliet, IL), which was calibrated with standardized solutions of NaCl. These osmolalities were then converted into water activities (a_w) using the following equation (105):

$$a_w = -\frac{55.56}{55.56 + Osm} \quad (2.14)$$

Where Osm corresponds to the osmolality of the solution and the 55.56 is the molality of pure water equal to 55.56 mol/kg of H₂O. We used ethylene glycol as an osmolyte, which does not interact with DNA, to measure the release or uptake of water molecules in all of our experiments (101).

Melting curves can be followed by several kinds of experimental techniques, including, but not limited to UV-Vis spectroscopy, NMR, viscosity, gel electrophoresis, circular dichroism, and fluorescence spectroscopy. However, UV-spectroscopy is one of the most common and convenient techniques for this purpose because it provides a quick and convenient way to obtain accurate melting curves.

2.2.2 Differential Scanning Calorimetry

A Microcal VP-DSC (Northampton, MA) differential scanning calorimeter (DSC) was used to directly measure the total heat of the helix to coil transition of each pseudoknot or secondary structure. In general, the DSC measures the apparent molar heat capacity of a given macromolecule as a function of temperature (106), see Figure 3. A typical DSC instrument consists of two cells: the sample cell, containing the macromolecule dissolved in a particular buffer, and the reference cell, containing the matching buffer solution. Both cells are enclosed in an adiabatic compartment and heated at a constant rate (typically 45°C – 60°C per hour), while the differential temperature between the reference and the sample cells is maintained at zero. When a temperature induced process takes place in the sample cell, the instrument compensates by adding or subtracting electrical power (depending on whether the process is endothermic or exothermic) to the sample cell in order to maintain a differential temperature of zero. The instrument records this electric power difference, which is proportional to the difference in the apparent heat capacity between the sample and reference cells (ΔC_p^a), i.e., the changes in heat capacity that occur during a helix \rightarrow coil transition (98), (107). The resulting ΔC_p^a is plotted as a function of temperature and

normalized for the heating rate. A buffer versus buffer scan is then subtracted from the sample versus buffer scan, resulting in a typical bell shaped curve from which model-independent thermodynamic profiles are obtained. The T_M is obtained from the peak of the calorimetric curve and the enthalpy and entropy of unfolding are obtained from the area under the curve (98), (107), (108). ΔS is obtained from the area under the curve of plots of $\Delta C_p/T$ versus T . The resulting ΔH and ΔS are calculated at the T_M according to the following equations:

$$\Delta H_{cal} = \int \Delta C_p^a dT \quad (2.15)$$

$$\Delta S_{cal} = \int \frac{\Delta C_p^a}{T} dT \quad (2.16)$$

We can extrapolate these parameters to the temperature of interest (T) using the following equations:

$$\Delta H_T = \Delta H_{T_M} + \Delta C_p (T - T_M) \quad (2.17)$$

$$\Delta S_T = \Delta S_{T_M} + \Delta C_p \ln \left(\frac{T}{T_M} \right) \quad (2.18)$$

In these equations ΔC_p is the heat capacity change characterizing the unfolding process and can be calculated by subtracting the heat capacity of the folded state, C_f , from that of the unfolded state, C_u :

$$\Delta C_p = C_u - C_f \quad (2.19)$$

C_u and C_f can be obtained directly from the DSC plots, by measuring the ΔC_p values of the baselines at high and low temperature, respectively. Conversely, by measuring T_M

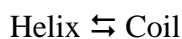
and ΔH_{cal} under multiple buffer conditions a plot of ΔH_{cal} versus T_M can be constructed. The slope of this plot can indirectly determine ΔC_p , of the oligonucleotide in question.

The free energy, ΔG°_T , is calculated using the Gibbs equation (99):

$$\Delta G_T = \Delta H_T - T\Delta S_T \quad (2.20)$$

However, the unfolding of many nucleic acids is accompanied by small heat capacity changes and they can be ignored without compromising the overall results. Thus, ΔH_{cal} and ΔS_{cal} can be considered independent of temperature and can be calculated directly from equations 2.15 and 2.16, when no heat capacity effects are involved.

For monomolecular transitions, ΔG° and ΔS can also be calculated according to the following derivation (98). For the following equilibrium:



At $T = T_M$, the fraction of random coils ($1 - \alpha$) is equal to the fraction of helical molecules (α). Thus:

$$K_{T=T_M} = \frac{(1-\alpha)}{\alpha} = 1 \quad (2.21)$$

$$\Delta G = -RT_M \ln K_{T=T_M} = 0 \quad (2.22)$$

$$\Delta G = \Delta H - T\Delta S = 0 \quad \text{and} \quad \Delta S = \frac{\Delta H}{T_M} \quad (2.23)$$

$$\Delta G = -\Delta H - T \frac{\Delta H}{T_M} = \Delta H \left(1 - \frac{T}{T_M} \right) \quad \text{and} \quad \Delta S = \frac{\Delta H - \Delta G}{T_M} \quad (2.24)$$

In addition, shape analysis of the DSC curves allows for the calculation of the model dependent van't Hoff enthalpies (98), which can be obtained from the full width at half the maximum height according to the relationship:

$$\Delta H_{vH} = \frac{A}{(1/T_1) - (1/T_2)} \quad (2.25)$$

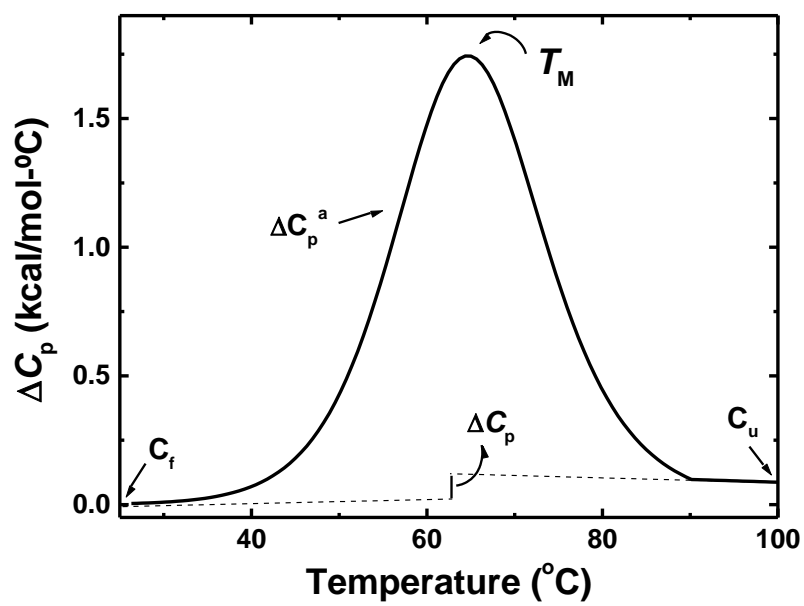


Figure 3. Typical DSC Melting Curve.

Where A is a constant that depends on the molecularity of the transition (A is equal to 7 and 10.14 for monomolecular and bimolecular transitions, respectively). T_1 and T_2 are the lower and upper temperatures that correspond to one half of the maximum height of ΔC_p^a , respectively.

Comparison between the calorimetric and van't Hoff enthalpies is used to evaluate the nature of each transition, or its cooperativity; whether the transition takes place in a two state manner ($\Delta H_{vH}/\Delta H_{cal} = 1$) or through the formation of intermediates ($\Delta H_{vH}/\Delta H_{cal} \neq 1$). A $\Delta H_{vH}/\Delta H_{cal}$ ratio smaller than one indicates that the size of the oligonucleotide is larger than the cooperative unit, i.e., the oligomer melts through the formation of partially unfolded intermediates; while a $\Delta H_{vH}/\Delta H_{cal}$ ratio larger than one indicates an aggregation of the oligonucleotide. A special case is observed in the melting of polynucleotides, where the $\Delta H_{vH}/\Delta H_{cal}$ ratio is greater than one. In this case, the ΔH_{cal} is determined per mole of base-pairs, and the value of the $\Delta H_{vH}/\Delta H_{cal}$ ratio yields the size of the cooperative unit, or the number of base-pairs melting simultaneously.

2.2.3 Temperature-dependent fluorescence spectroscopy

Fluorescence techniques have been used to study the physical properties of many biological macromolecules. While DNA itself does not fluoresce, a canonical base in a DNA molecule can be substituted by a synthetic fluorescent base. For example, 2-aminopurine (2AP) is a fluorescent analog of the purine bases with an amino group in the 2 position rather than 6 of adenine (7). Therefore, 2AP can be incorporated into DNA as a substitute for adenine or guanine, forming two and one hydrogen bonds when paired with thymine or cytosine, respectively (8). The absorption maximum of 2AP occurs at

longer wavelengths (~305 nm) than those of the purine bases, so it can be selectively excited even in the presence of a large excess of the other bases (109) (7). Moreover, the fluorescence quantum yield, lifetime and intensity decay kinetics of the incorporated 2AP in nucleic acids are affected by aromatic stacking, collisional interactions with neighboring bases and solvation (12). These properties make 2AP an ideal probe to follow the temperature-induced conformational transitions of a DNA molecule. In general, the fluorescence properties of 2AP depend on the local environment that it is experiencing, which includes effects of the solvent. When 2AP forms a base-pair and is embedded inside a helical structure, the fluorescence is quenched by the aromatic stacking interactions (12). In this case, the fluorescence will increase when the helical structure unfolds and 2AP is exposed to the solvent. Therefore, the fluorescence intensity of 2AP can be monitored as the whole DNA molecule undergoes a helix to coil transition.

The fluorescence emission spectra of each 2AP modified oligonucleotides, from 300 nm to 500 nm, were initially obtained at several temperatures using a Varian Cary Eclipse Fluorescence Spectrophotometer (Walnut Creek, CA) equipped with a peltier system for temperature control. The fluorescence was most often measured at a 90° angle relative to the excitation light. The emission spectrum was scanned at a fixed excitation wavelength of 307 nm, where the UV spectrum gives the maximum absorption, allowing us to select the wavelength of maximum fluorescence emission. Then, the excitation spectrum was taken at the maximum emission wavelength (370 nm). The excitation and emission spectra were taken at low and high temperature to obtain the optimum fluorescence parameters upon the conformational change, helping in the selection of excitation and emission wavelengths used in the fluorescence melting curve

and in studies of targeting reactions. Fluorescent melting curves were obtained by monitoring the emission fluorescence intensity changes at 370 nm (under excitation wavelength of 307 nm) from 15 °C to 90 °C, at a heating rate of ~1 °C/min. The resulting melting curve can be analyzed to yield model-dependent standard thermodynamic profiles using the procedures described in section 2.2.1.

2.2.4 Circular Dichroism Spectroscopy

We used an Aviv circular dichroism spectrometer Model 202SF equipped with a peltier temperature control system (Lakewood, NJ) to characterize the conformation of each oligomer. Typically, a sample solution is placed in a free-strain quartz cell and the spectrum is recorded from 200 nm to 320 nm every 1 nm. All the scans are recorded at 5°C to ensure the formation of the pseudoknot. Final spectra corresponded to an average of two scans; a buffer curve was subtracted and then normalized for the oligomer concentration and dilution effects. At low temperature the oligomers are in the helical state, therefore, the resulting spectrum indicates the overall conformation of each pseudoknot. In circularly polarized light, the magnitude of its electric component remains constant, but its direction is modulated. As a result, circularly polarized light can be used to describe the helical state of nucleic acids, proteins and other molecules that contain both chirality and an absorbing species (110). Circular dichroism is the difference in absorbance between left-handed circularly polarized light (A_L) and right-handed circularly polarized light (A_R) (111).

$$CD = A_L - A_R \quad (2.26)$$

Commercial spectrophotometers present CD as ellipticity. Ellipticity and CD describe a similar phenomenon and can be related to each other. The sum of the left and right-handed circularly polarized light results in a wave that is polarized in one plane, i.e., linearly polarized. CD involves the preferential absorption of left or right-handed circularly polarized light. Due to the preferential absorption of either the right or left-handed circularly polarized light, the sum of the polarized waves will no longer be plane polarized, but will describe an ellipse. Ellipticity (θ°) is defined as the arc-tangent of the ratio of the minor axis of the ellipse to the major axis of the ellipse and can be related to CD according to the following equation (96) (99):

$$\theta^\circ = \frac{2.303(A_L - A_R)180}{4\pi} \quad (2.27)$$

In order to compare the results of different samples, it is necessary to normalize the spectra i.e., express ellipticity on a molar basis. Ellipticity is converted into molar ellipticity $[\theta]$ using the following relationship (96) (99):

$$[\theta] = \frac{\theta}{Cl} \quad (2.27)$$

Where C is the molar concentration of the sample and l is the path length of the CD cell.

Symmetric molecules do not exhibit a CD signal because their magnetic dipoles are always perpendicular to their electric transition dipoles so their rotational strengths are identical to zero and, thus, no CD signal is observed. DNA is an optically active molecule and as such can alter the properties of transmitted light. The chromophores of DNA are symmetric, however, CD bands are observed due to the interaction between the

transition dipoles of the chromophores with the transition dipoles of other parts of the molecule. The asymmetric disposition of electric and magnetic dipoles in DNA arises from the intrinsic asymmetry of its chiral sugars and from the super asymmetry resulting from the formation of a helical structure. Since CD of DNA arises from the interaction of transition dipoles, the spectrum depends on the relative orientation of transition dipoles for the various groups in space and thus the technique is extremely sensitive to conformation of both DNA and RNA pseudoknots, see Figure 4. It should be noted that CD is a low resolution technique and does not provide the structure of a molecules, however; it can unequivocally provide the conformation present.

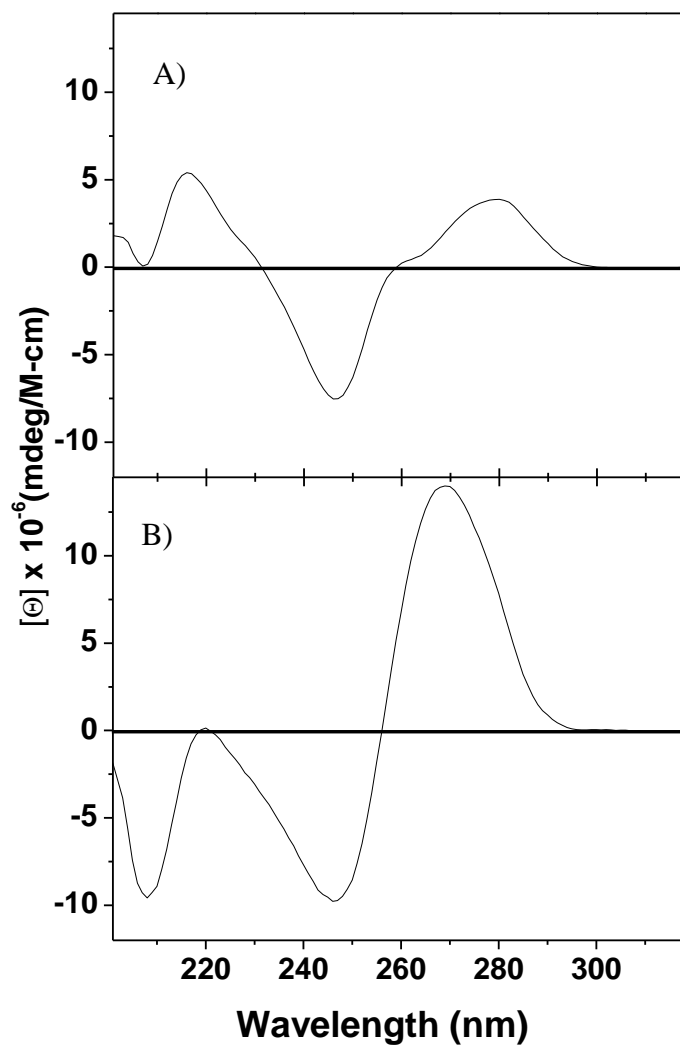


Figure 4. Typical CD spectra of pseudoknots. A) *PsK-11* DNA in the B-conformation
B) *PsK-11* RNA molecule in the A-conformation. 10mM Sodium Cacodylate, 10mM
MgCl₂ at pH 7.0 and 5°C

2.2.5 Pressure Perturbation Calorimetry

Pressure perturbation calorimetry (PPC) is used to determine the unfolding volume of macromolecules such as proteins, polymers, and DNA. This information sheds light on the hydration effects accompanying the unfolding of these molecules. However, molecules with smaller changes in hydration between the folded and unfolded states, such as smaller nucleic acids, need high concentrations in the reaction cell to evoke changes in the PPC curves. In addition, the exact nature of the type of water observed between in volume change between the folded and unfolded states is unknown. There may also be a compensation between structural water at lower temperatures and the formation of water around charges at higher temperatures, or the conversion of one type of water to bulk water upon unfolding. However, information gleaned from the magnitude and shape of the curves can provide insight into some of these issues.

In a PPC experiment, one follows the temperature dependence of the coefficient of thermal expansion (α) as a function of temperature. The magnitude of α and the values of the pre transition and post transition baselines, all provide insight on the type of groups (polar, nonpolar, aromatic) exposed to the solvent at a given point in the unfolding of a molecule. Aliphatic side chains in proteins, or hydrophobic groups, have a negative α value at low temperature, with a strong positive slope with negative curvature as the temperature is increased. Aromatic sidechains, or aromatic bases, have a positive α value at low temperature, with a slope near zero. The α value has little to no change as temperature is increased. Polar side chains, or hydrophilic groups, have a large positive α value at low temperature, but have a negative slope with positive curvature as the temperature is increased. Much of the work with PPC has been focused on proteins,

because the change in the volume of hydration is large for proteins, but not for DNA; however, similar rules can be applied.

The heat change (ΔQ) resulting from a pressure change (ΔP) above a solution is measured using the VP-DSC differential scanning calorimeter from Microcal (Northampton, MA) equipped with a PPC accessory. A complete description of this novel technique can be found elsewhere (112). Prior to the PPC scan, a DSC melt is carried out to determine the temperature range and temperature step to be used in the PPC experiment. A sample solution (sample cell, 0.35- 0.5 mM in strands) is allowed to equilibrate against the same buffer solution (reference cell) at constant temperature and external pressure. The external pressure is then increased by ~50 psi, causing heat to be absorbed differentially by the sample and reference cells. These heats, ΔQ , are obtained from integration of the compression and decompression peaks resulting from switching the external pressure on and off at particular temperatures determined by the DSC curve. The resulting values of ΔQ are then used to measure the apparent coefficient of thermal expansion, $\alpha(T)$, from integration of the relationship:

$$(\partial Q/\partial P)_T = -T(\partial V/\partial T)_P = -T\alpha(T)V \quad (2.28)$$

yielding: $\Delta Q = -TV\alpha(T)\Delta P$; where V is the apparent molar volume of the solute.

For a two component system:

$$\alpha(T) = \alpha_o - \Delta Q/(TV\Delta P) \quad (2.29)$$

where α_o is the thermal coefficient of the solvent. Integration of $\alpha(T)$ over the temperature range of the unfolding reaction, $\int \alpha(T)dT$, yields the relative volume changes of the solute, $\Delta V/V$, where ΔV is the unfolding volume of the macromolecule. The value of V is obtained from the equation (113):

$$V = M/\rho_0 - (\rho_0 - \rho)/\rho_0 C \quad (2.30)$$

where M is the molecular mass of a protein, ρ_0 and ρ are the densities of the solvent and solution, respectively. The density of the solutions used in the PPC experiment is measured with an Anton Paar (Graz, Austria) DMA densitometer in the differential mode, using two 602-M micro cells, each with a volume of $\sim 150 \mu\text{L}$. The reference cell is filled with water while the measuring cell is filled with solution or buffer. The density, ρ , is calculated from the oscillation period T of the cell using the following relationship: $\rho = AT^2 + B$, where A and B are constants determined from calibrating densities (and periods) of water and air.

2.2.6 Isothermal Titration Calorimetry

The thermodynamic profiles, binding enthalpy, stoichiometry (n) and binding affinity (K_b) for the interaction of a ligand with a macromolecule can be obtained using isothermal titration calorimetry (ITC). All reactions were measured with an ITC₂₀₀ isothermal titration calorimeter from Microcal (Northampton, MA). The reaction cell of the instrument has the same size as the reference cell, which is filled with double distilled water. In a typical ITC experiments the ligand solution is placed in the syringe and injected by a computer controlled step motor into the sample cell filled with the macromolecule solution. The heat absorbed or released in each injection is measured by a thermoelectric device, which increases or reduces the power input of the sample to keep the two cells at the same temperature (114), (115).

A $40 \mu\text{L}$ syringe was used to inject the titrant; mixing was effected by stirring this syringe at 1000 rpm. Typically, we used 5-7 injections of $2 \mu\text{L}$ of pseudoknot

solution with at least 2-fold lower concentration than the solution of the complementary strand in the cell, and over a time of 4-8 minutes between injections. The reaction heat of each injection is measured by integration of the area of the injection curve, corrected for the dilution heat of the titrant, and normalized by the moles of titrant added to yield the reaction enthalpy, ΔH_{ITC} (115-118). ITC experiments were designed to obtain the heat, ΔH_{ITC} , for each targeting reaction by averaging the reaction heat of at least five injections under unsaturated conditions. These ΔH_{ITC} terms correspond to the formation of duplex products. To determine the free energy, ΔG_{ITC} , for each targeting reaction, we use the following relationship, $\Delta G_{\text{ITC}} = \Delta G_{\text{HC}} (\Delta H_{\text{ITC}}/\Delta H_{\text{HC}})$ (116-118), while the Gibbs equation is used to determine the $T\Delta S_{\text{ITC}}$ parameter, where T is the temperature of the ITC experiments.

ITC can also be used to determine the heat of DNA duplex formation at constant temperature. Comparing the heat of duplex formation obtained from ITC to the temperature induced unfolding heat obtained from DSC provides extra information about the reaction, such as heat capacity effects and the contributions from base-base stacking of the single strands. In these experiments, the solution of the strand placed in the titrating syringe is ~10-fold more concentrated than the solution of its complementary strand in the reaction cell to produce peaks of titrant under unsaturated conditions.

2.2.7 Surface Plasmon Resonance

Surface plasmon resonance is a biophysical technique that can characterize the interactions between a varieties of molecules based on the Kretschmann configuration model (119). The method is based on a light source that passes through a prism and off

the back of the sensor surface and into a detector, Figure 5A. At a certain incidence angle, known as the resonance angle, light is absorbed by the electrons in the metal film of the sensor chip causing them to resonate. These resonating electrons are also known as surface plasmons which are sensitive to the surrounding environment. When there is a change in the surface the result is an intensity loss in the reflected beam which appears as a dark band and can be seen as a dip in the SPR inflection intensity curve. The shape and location of the dip can then be used to convey information about the sensor surface. It is this change in reflection that is measured to determine the amount of binding that is taking place. Once the analyte is no longer flown through the cell the bound analyte will begin to dissociate and again the change in reflected light is measured to determine the dissociation rate (119). Some of the SPR-machines convert the actual measured values (angle or wavelength) into an arbitrary one, which is easy to display and interpret. The BIACORE machine for instance uses the Resonance Unit (RU), which is converted from the actual angle shift in reflected light.

The equilibrium constants for targeting reactions of DNA pseudoknots were determined using a Biacore3000. In a typical experiment the streptavidin chip was docked in the instrument at 20°C or 25°C and flow cell one or three was primed with 10 μ L of Bionorm solution at 10 μ L/min. The needle and IFC was then washed 3xs before injecting 50 mM NaOH to normalize the chip surface to reach a steady baseline followed by washing the needle and IFC. Flow cell one was then injected with a control ligand until ~400 RUs was bound on the chip surface, followed by washing the needle and IFC. The flow cell was then injected with 1 mM HCl (regeneration buffer) and the total response units were recorded. This procedure was repeated for flow cell two or four with

the ligand under investigation. To determine the binding constants an analyte was flown through the cells at 10 $\mu\text{L}/\text{min}$ ranging in concentration from 100 μM to 377 pM until reaching a plateau indicating an equilibrium had been reached in 2X SSC buffer at pH 7.0. The binding curves of flow cell one was subtracted from flow cell two resulting in the binding curve used for analysis. Curves were analyzed using the Bioevaluation software using a 1:1 langmuir model as well as a steady state model to obtain the binding equilibrium constant, Figure 5B (120), (121).

In summary, the association occurs first during any bimolecular interaction and occurs when the analyte and ligand collide at the correct orientation and energy level and the rate of association equals:

$$[\text{Ligand}] [\text{Analyte}] \cdot k_a \quad (2.31)$$

The analyte and ligand will stay bound together for a random amount of time and the dissociation rate is equal to:

$$[\text{Ligand-Analyte}] \cdot k_d \quad (2.32)$$

Assuming the reaction follows a pseudo first order kinetics the following equation can be used:

$$\frac{d[\text{LA}]}{dt} = k_a[\text{L}][\text{A}] - k_d[\text{LA}] \quad (2.33)$$

The observed RU signal of the experiment corresponds to the complex formed and the R_{max} is proportional to the surface concentration of the pure ligand, therefore the following equation can be written:

$$\frac{dR}{dt} = k_a(R_{\text{max}} - RU) \cdot c - k_d(RU) \quad (2.34)$$

where c is the analyte concentration. If you take the natural logarithm:

$$\ln \frac{dR}{dt} = \ln(k_a \cdot R_{\text{max}} \cdot c) - (k_a \cdot c + k_d) \cdot t \quad (2.35)$$

and substituting

$$k_s = k_a \cdot c + k_d \quad (2.36)$$

results in the final equation:

$$\ln \frac{dR}{dt} = \ln(k_a \cdot R_{\max} \cdot c) - k_s \cdot t \quad (2.37)$$

By plotting dR/dt vs t the linear function gives a slope equal to the k_s and the association constant, k_a , can be determined by plotting k_s vs c .

To determine the dissociation rate constant, k_d , the following equation is used:

$$\frac{dR}{dt} = -k_d \cdot RU \quad (2.38)$$

The linearized form is equal to:

$$\ln \frac{R_0}{R_t} = k_d(t - t_0) \quad (2.39)$$

Where R_0 is the response at t_0 and plotting $\ln R_0/R_t$ vs $(t-t_0)$ gives a linear function with a slope equal to the k_d .

A steady state is reached when there is an equilibrium and the net rate of binding equals zero. There are two ways to calculate the equilibrium dissociation constant K_D . The first being using the k_d and k_a obtained from the kinetic analysis:

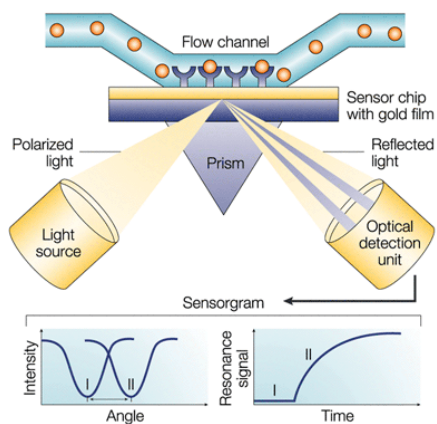
$$K_D = \frac{k_d}{k_a} \quad (2.40)$$

The second way is to reach equilibrium at different analyte concentrations and the resulting saturation curve is analyzed by a nonlinear regression to extract the dissociation constant:

$$\frac{dR}{dt} = k_a(R_{\max} - R_{eq}) \cdot c - k_d \cdot R_{eq} = 0 \quad \rightleftharpoons \quad R_{eq} = \frac{(R_{\max} - R_{eq}) \cdot c}{c + k_d/k_a} = \frac{(R_{\max} - R_{eq}) \cdot c}{c + K_D} \quad (2.41)$$

Where R_{eq} is the observed steady state response and c is the concentration of the analyte.

A)



Nature Reviews | Drug Discovery

B)

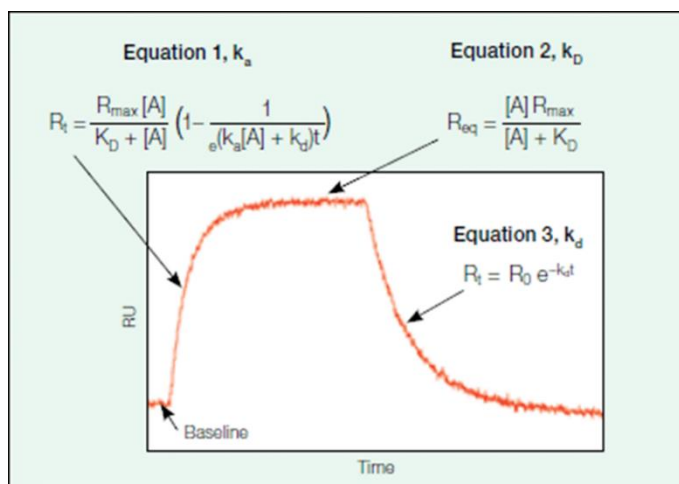


Figure 5. How SPR Works. A) Principle of SPR experiment (Image taken from: Nature Review (122) B) Typical Binding Curve and Equations (Image taken from: bio-rad.com)

CHAPTER THREE

STABILITY OF PSEUDOKNOTS CONTAINING TAT AND C⁺GC

BASE-TRIPLETS: EFFECT OF STEM-LOOP

COMPLEMENTARITY

3.1 SUMMARY

We report on the effects resulting from increasing the loop length of a pseudoknot which is complementary to the one of the core duplex stem with sequence: d(TCTCTT_nAAAAAAAAAGAGAT₅TTTTTTT), where “T_n” is the thymine loop which increases in length from 5 to 11 thymines in increments of two. All four oligonucleotides (*PsK-5*, *PsK-7*, *PsK-9*, and *PsK-11*) form intramolecular pseudoknots and show the increase in length of this loop yields more stable pseudoknots due to higher transition temperatures (53–59°C) and higher unfolding enthalpies (60-110 kcal/mol). This indicates formation of one and three TAT/TAT stacks in *PsK-9* and *PsK-11*, respectively. We determined unfolding volumes ranging from -18 cm³-mol⁻¹ (*PsK-5*) to -23 cm³-mol⁻¹ (*PsK-11*). An increase in temperature produced a volume contraction of the system, which means in the absence of cavities the unfolding is accompanied by an increase in the immobilization of water.

We have also flipped one AT for a TA base-pair in the core stem of these pseudoknots, preventing the formation of these base-triplet stacks. The DSC curves of these pseudoknots yielded lower melting temperatures and also unfolding enthalpies compared to their parent pseudoknots, confirming the formation of local base-triplets in

PsK-9 and *PsK-11*. Furthermore, to determine the actual location of the base-triplets, we replaced two adenines, independently, with 2-aminopurine in *PsK-9* and *PsK-11*. The fluorescence curves showed a sigmoidal shape between the folded and unfolded states, which were larger when 2-aminopurine was placed near the stem-junction than at the distal end. This suggests the base-triplets are forming at or close to the junction of the two core stem motifs. In addition, we also investigated four pseudoknots containing one and two TAT \rightarrow CGC substitutions and found these pseudoknots also formed C⁺GC base-triplets.

3.2 INTRODUCTION

The formation and prediction of secondary structures such as: hairpins, triplexes, and pseudoknots are sequence-dependent, for example: a single-stranded DNA molecule is able to form an intramolecular structure if it has a sequence that is partially complementary to itself. It is essential to understand how this folding takes place to fully understand its biological function. A complete physical description of a particular DNA complex depends on the contributions from base pairing, base stacking, as well as ion binding and hydration. The formation and biological functions of these structures are well documented (5) (21-36). In particular, pseudoknots are an interesting and diverse RNA structural motif. This is due to the variation in their stem sequence, the fluctuation of loop length and sequence, as well as, their interactions among themselves. Pseudoknots have been found to be involved in a variety of biological functions including: telomerase (38), (37), riboswitches (45), ribosomal frameshifting (43), (44), self-splicing introns (39), and forming the catalytic core of various ribozymes (40-42). In ribosomal frameshifting, a

common mechanism found in viruses, a pseudoknot and its slippery sequence are involved to change the reading frame allowing for different mRNAs to be translated (43). The high efficiency of frameshifting could be due to the formation of a local base-triplet stack within the pseudoknot to increase the stability of the terminal stem and its interaction with the ribosome (44).

Currently, our laboratory is interested in both the putative structure and overall physical properties for the folding (and unfolding) of nucleic acid stem-loop motifs. Our current understanding has been enhanced by thermodynamic investigations of the helix-coil transitions of model oligonucleotide compounds of known sequence, on both the stability and structure of DNA and RNA (124-128). Our laboratory is primarily focused on understanding the folding/unfolding of single-stranded DNA oligomers that are designed specifically to adopt intramolecular structures (116), (117), (129). Intramolecular complexes unfold with transition temperatures higher than the bimolecular counterparts due to a lower entropy penalty (117), this allow for the investigation of their physical properties of their folded states over a wider temperature range.

In this work, we have determined the unfolding thermodynamics of a set of DNA pseudoknots as a function of the number of thymines in one of their loops. The increase in the length of this loop yielded pseudoknots with higher transition temperatures and higher unfolding enthalpies, indicating the formation of local TAT/TAT stacks in *PsK-9* and *PsK-11*. This observation is further confirmed in three different ways: 1) by comparing the thermodynamics obtained from the pseudoknots to a variety of control molecules including a duplex of the core stem and also two hairpins of the individual

stems that comprise the pseudoknot stems, 2) by flipping one AT for a TA base pair in the core stem of these pseudoknots, which prevents the formation of base-triplet stacks, and 3) by investigating the fluorescence of modified pseudoknots with 2-amino purine placed in different places among the stem in which we believe the base-triplets are forming. Furthermore, pseudoknots with sequences that have potential to form 1 or 2 C⁺GC base-triplets were investigated.

3.3 MATERIALS AND METHODS

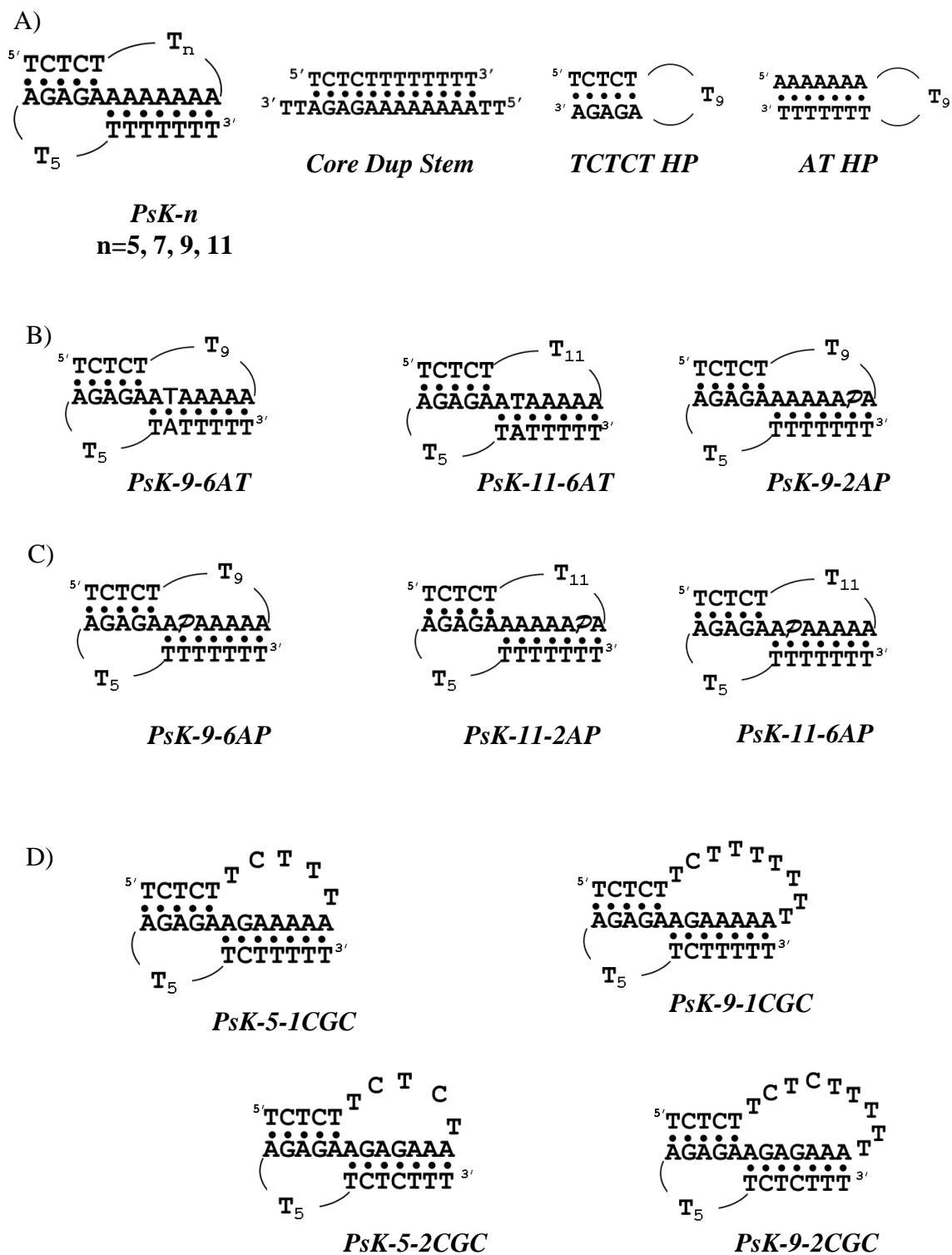
Materials. All oligonucleotides were synthesized by the Integrated DNA Technologies (IDT) (Coralville, IA), HPLC purified, and desalted by column chromatography using G-10 Sephadex exclusion chromatography. The sequences of oligonucleotides used in this work and their designation are shown in Figure 1. The concentrations of the oligomer solutions were determined at 260 nm and 90°C using an Aviv Spectrophotometer Model 14DS UV-Vis using the molar extinction coefficients listed previously: 331 mM⁻¹ cm⁻¹ (PsK-5), 344 mM⁻¹ cm⁻¹ (PsK-7), 367 mM⁻¹ cm⁻¹ (PsK-9), 376 mM⁻¹ cm⁻¹ (PsK-11), 145 mM⁻¹ cm⁻¹ (Core Stem Dup), 174 mM⁻¹ cm⁻¹ (TCTCT HP), 219 mM⁻¹ cm⁻¹ (AT HP), 327 mM⁻¹ cm⁻¹ (PsK-5-1CGC), 327 mM⁻¹ cm⁻¹ (PsK-5-2CGC), 357 mM⁻¹ cm⁻¹ (PsK-9-1CGC), 347 mM⁻¹ cm⁻¹ (PsK-9-2CGC) 363 mM⁻¹ cm⁻¹ (PsK-9-6TA), 374 mM⁻¹ cm⁻¹ (PsK-11-6TA). These values were obtained by extrapolation of the tabulated values for dimers and monomeric bases (96), (130) at 25°C to 90°C using procedures reported previously (97), (129). The extinction coefficients of the non-self-complementary duplex is simply calculated by averaging the molar extinction coefficients of its component complementary single strands. Inorganic salts from Sigma were reagent grade, and used

without further purification. Typical measurements were made in appropriate buffer solutions: 10 mM sodium phosphate with and without 100 mM NaCl at pH 7.0. All oligonucleotide solutions were prepared by dissolving the dry and desalted ODNs in buffer.

Temperature-Dependent UV Spectroscopy. Absorbance versus temperature profiles were measured at 260 nm with a thermoelectrically controlled Aviv Spectrophotometer Model 14DS UV-Vis (Lakewood, NJ). The temperature was scanned at a heating rate of 0.6 °C/min, and shape analysis of the melting curves yielded transition temperatures, T_{MS} (98). The transition molecularity for the unfolding of a particular complex was obtained by monitoring T_M as a function of the strand concentration. Intramolecular complexes show a T_M -independence on strand concentration, while the T_M of intermolecular complexes does depend on strand concentration (129).

Differential Scanning Calorimetry. The total heat required for the unfolding of each oligonucleotide was measured with a VP-DSC differential scanning calorimeter from Microcal (Northampton, MA). Standard thermodynamic profiles and T_{MS} are obtained from the DSC experiments using the following relationships (98), (129): $\Delta H_{cal} = \int \Delta C_p(T) dT$; $\Delta S_{cal} = \int \Delta C_p(T) / T dT$, and the Gibbs equation, $\Delta G^\circ(T) = \Delta H_{cal} - T \Delta S_{cal}$; where ΔC_p is the anomalous heat capacity of the ODN solution during the unfolding process, ΔH_{cal} and ΔS_{cal} are the unfolding enthalpy and entropy, respectively, assumed to be temperature-independent. $\Delta G^\circ(T)$ is the free energy at temperature T , normally 5 °C.

Fluorescence Spectroscopy. Fluorescent spectra for the 2-amino purine substituted pseudoknots were obtained at 15°C and 90°C ranging from 307 nm to 500 nm on a thermoelectrically controlled Cary Eclipse Fluorescence Spectrophotometer from Varian



(Walnut Creek, CA). Fluorescent melting curves were obtained by scanning the emission wavelength from 15 to 90°C at a heating rate of ~1 °C/min.

Determination of the Differential Binding of Counterions and Water. Additional UV melting curves, as a function of salt and osmolyte concentrations, were performed to determine the differential binding of counterions, Δn_{Na^+} , and water molecules, Δn_{W} , between the folded and coil states. The Δn_{Na^+} and Δn_{W} linking numbers represent the uptake (or release) of counterions and water, respectively, for the helix-coil transition of each complex, and are measured experimentally using the equations previously described in chapter two:

$$\Delta n_{\text{Na}^+} = 1.11 \left[\frac{\Delta H_{\text{cal}}}{RT_{\text{M}}^2} \right] \left(\frac{\partial T_{\text{M}}}{\partial \ln [\text{Na}^+]} \right) \quad (1)$$

$$\Delta n_{\text{W}} = \left[\frac{\Delta H_{\text{cal}}}{RT_{\text{M}}^2} \right] \left(\frac{\partial T_{\text{M}}}{\partial \ln [a_{\text{W}}]} \right) \quad (2)$$

The terms in brackets of Eqs 1 and 2 are determined directly from DSC experiments while the ones in parentheses from UV melting curves. The latter correspond to the slopes of the plots of T_{M} as a function of the concentration of sodium and water activity respectively (99). The value 1.11 in Eq. 1 is a constant which is used to convert activity into concentration terms. The activity of water is varied by using different concentrations of a co-solute, ethylene glycol, which does not interact with the ODN (101). The osmolality of these solutions were obtained using a UIC vapor pressure osmometer Model 830, calibrated with standardized NaCl solutions.

Pressure Perturbation Calorimetry. The heat change (ΔQ) resulting from a pressure change (ΔP) above a solution is measured using the VP-DSC differential scanning calorimeter from Microcal (Northampton, MA) equipped with a PPC accessory. A

complete description of this novel technique can be found elsewhere in Chapter 2. Prior to the PPC scan, a DSC melt is carried out to determine the temperature range and temperature step to be used in the PPC experiment.

3.4 RESULTS

3.4.1 UV Unfolding of Complexes

The melting curves for each pseudoknot and control molecules are shown in Figure 2A. All curves are sigmoidal and show a hypochromic effect at 260 nm. Pseudoknots with loops of 5 to 11 thymines show monophasic transitions with T_M s ranging from 53°C to 59°C (Figure 2A). These pseudoknots also have similar hyperchromicities of 16-17% at 260 nm. The main observation is there is an increase in the T_M as the loop length of the pseudoknots increases, which is the opposite effect that is normally seen with increasing the loop length of straight hairpin loops (128). This can be rationalized by the helical stems becoming less accessible to the solvent due to the loop thymines constituting the ceiling of the nearby major groove; thereby, making the pseudoknots more temperature stable. The control hairpin with sequence: d(TCTCTT₉AGAGA) has a T_M of 30°C while the other control hairpin d(AAAAAAAT₉TTTTTTT) has a T_M of 48°C, Figure 2B. Next, we follow the T_M as a function of strand concentration to determine the transition molecularity of each molecule and we find that the pseudoknots (Figure 2C) and control hairpins (Figure 2D) form intramolecularly due to similar T_M s over a 10-fold increase in strand concentration, however, the control duplex, which forms the core stem of the pseudoknot forms a bimolecular structure as expected and shows an increase in T_M as the strand concentration increases.

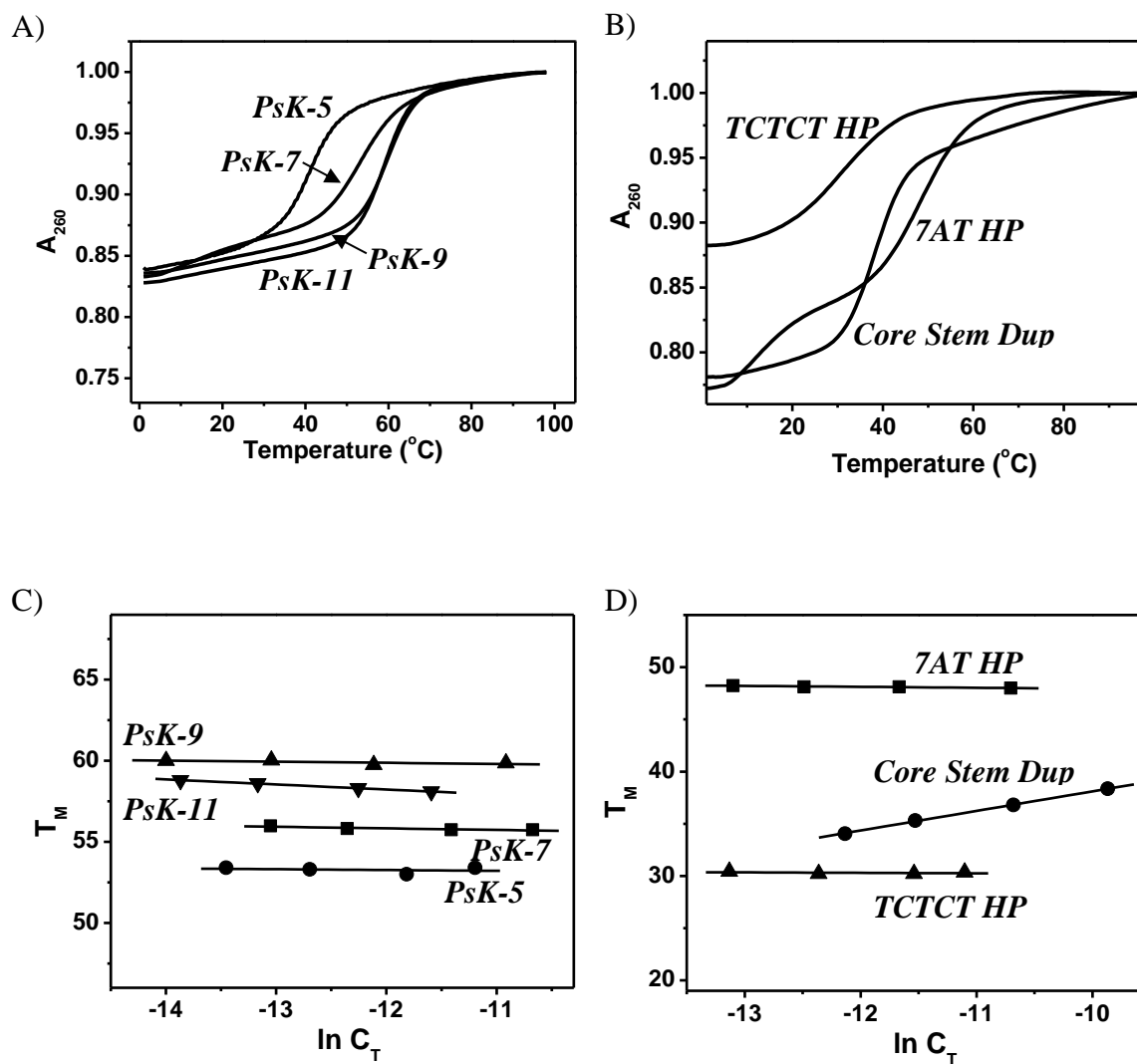


Figure 2. UV Melting Curves and Concentration Dependence. All experiments were carried out in 10 mM Phosphate buffer at pH 7.0 and 100 mM NaCl; T_M (± 0.5 $^{\circ}\text{C}$). Concentrations used ranged between 52-1 μM .

3.4.2 DSC Unfolding

The DSC unfolding for these pseudoknots and control molecules are shown in Figure 3, most of the pseudoknots unfold through asymmetric monophasic transitions due to the similar T_{MS} of the two adjacent stems; however, *PsK-11* unfolds through a biphasic transition. The increase in the length of the right side loop (Figure 3A) from 5 to 11 thymines yielded total ΔH_{calS} of 60.1 (*PsK-5*), 86.4 (*PsK-7*), 87.5 (*PsK-9*), and 110 kcal/mol (*PsK-11*), Table 1. The predicted enthalpies from N-N parameters are 87.3 (131) and 90.5 kcal/mol (124) for the duplex stem of this set of pseudoknots, however, we obtained experimentally a ΔH_{cal} of 69.4 kcal/mol in 116 mM Na⁺ for this stem duplex, d(TCTCTTTTTTTT/TTAAAAAAAAGAGATT), with two dangling thymines at each end in order to prevent fraying (132) (Figure 3B). We use a value of 65.2 instead of the 69.4 kcal/mol for the unfolding of the core stem of the pseudoknots; this assumes the middle AA/TT of each pseudoknot is considered as partially stacked. This result was confirmed using two control hairpins with the same stems as within the pseudoknot. The first hairpin d(TCTCTT₉AGAGA) unfolds with an enthalpy of 27.8 kcal/mol, while the second hairpin d(AAAAAAAT₉TTTTTTT) unfolds with an enthalpy of 35.5 kcal/mol, which is the second transition occurring in the DSC spectra shown in Figure 3B. The first transition can be attributed to either a duplex with dangling ends or a duplex with a bulge. With the combined enthalpies the calculated unfolding enthalpy is 63.3 kcal/mol, which is in excellent agreement with the *Core Stem Dup* once the partially stacked AA/TT within the pseudoknot is considered. *PsK-5* unfolds with a ΔH_{cal} of 60.1 kcal/mol, 5.1 kcal/mol lower than the *Core Stem Dup*, due to the constrained loops inducing unstacking of the stem and/or fraying at the 3' end of the AT base-pairs. It is important to emphasize

that the loop is complementary to the corresponding stem, nearby the major groove of this stem, and the increase in the length of the loop on the right side (Figure 1) yielded higher enthalpy terms. Relative to the *Core Stem Dup* ($\Delta H_{\text{cal}} = 65.2$ kcal/mol), we obtained enthalpy increases of 21.2 (*PsK-7*), 22.3 (*PsK-9*), and 44.8 kcal/mol (*PsK-11*), respectively. These enthalpies can be attributed to improving base-pair stacking of the stem by removing loop induced strain, closing the fraying of the ends, and the local formation of TAT base-triplets. We have estimated an enthalpy of 5.1 kcal/mol for the first two contributions (132), yielding excess enthalpies of 16.1 (*PsK-7*), 17.2 (*PsK-9*), and 39.7 kcal/mol (*PsK-11*). The enthalpy of a TAT/TAT base-triplet stack has been determined to be equal to 24.0 kcal/mol (24) and the enthalpy of the AA/TT base-pair stack is considered to be ~ 8.5 kcal/mol (124), (133), (131). This means, that an enthalpy of 15.5 kcal/mol is needed to form a single base-triplet stack from the addition of the third strand (thymine loop) to complement the A_7/T_7 duplex stem. By dividing the excess enthalpy of each pseudoknot by 15.5 kcal/mol, we estimate *PsK-7* and *PsK-9* form one TAT base-triplet stack, while *PsK-11* forms ~ 2.5 TAT/TAT base-triplet stacks.

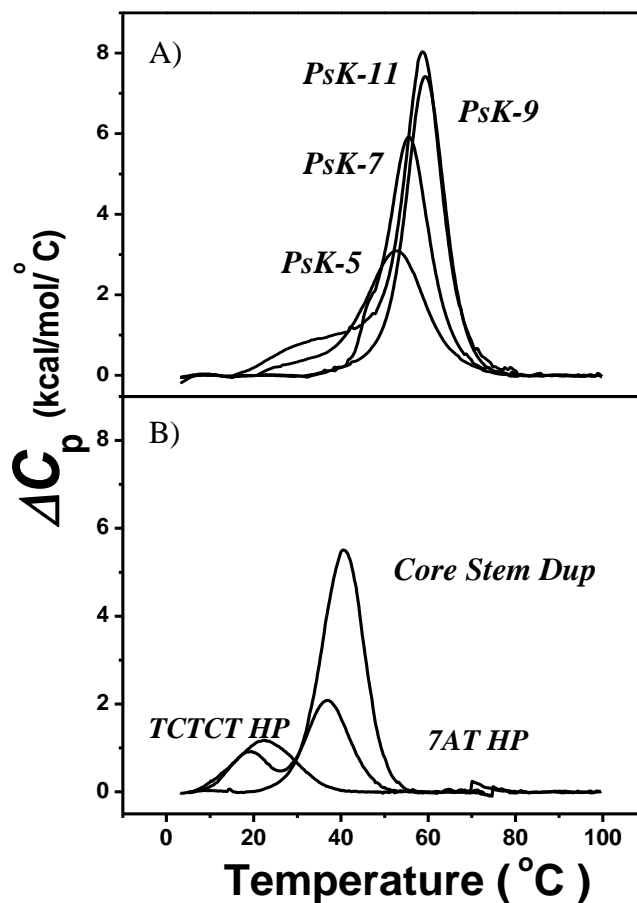


Figure 3. Unfolding of Pseudoknots. A) DSC unfolding of pseudoknots, concentrations used: 126 μM (*PsK-5*), 73 μM (*PsK-7*), 120 μM (*PsK-9*), 53 μM (*PsK-11*) B) DSC unfolding of control molecules: *Core Stem Dup* (120 μM), *7AT HP* (106 μM), *TCTCT HP* (104 μM). All experiments were carried out in 10 mM Phosphate buffer at pH 7.0 and 100 mM NaCl.

Table 1. Thermodynamic Folding Profiles for DNA Pseudoknots and Controls.

Molecule	T_M	ΔH_{cal}	$T\Delta S_{cal}$	ΔG°_5	Δn_{Na^+}	Δn_w^*	ΔV^*
	(°C)	(kcal/mol)	(kcal/mol)	(kcal/mol)	(mol Na ⁺)	(mol H ₂ O)	(cm ³ ·mol ⁻¹)
<i>PsK-5</i>	52.8	-60.1	-51.6	-8.5	-2.5	-11	18
<i>PsK-7</i>	56.2	-86.4	-73.2	-13.2	-3.1	-19	18
<i>PsK-9</i>	59.3	-87.5	-73.3	-14.2	-3.0	-23	22
<i>PsK-11</i>	31.6	-26.4	-23.4	-3.0	-1.1		
	58.7	-83.6	-70.0	-13.6	-3.0		
		-110	-93.4	-16.6	-4.1	-24	23

Control	T_M	ΔH_{cal}	$T\Delta S_{cal}$	ΔG°_5
Molecules	(°C)	(kcal/mol)	(kcal/mol)	(kcal/mol)
<i>Core Stem Dup</i>	40.5	-69.4	-61.5	-7.9
<i>7AT HP</i>	22.8	-27.2	-12.8	-0.8
	47.6	-35.5	-30.8	-4.7
<i>TCTCT HP</i>	28.6	-27.8	-25.6	-2.2

Experiments were carried out in 10 mM sodium phosphate buffer at pH 7.0 and 100 mM NaCl. * ΔV and Δn_w measurements were carried out in 10 mM sodium phosphate buffer at pH 7.0 Experimental errors are as follows: T_M (± 0.5 °C), ΔH_{cal} (± 5 %), $T\Delta S_{cal}$ (± 5 %), $\Delta G^{\circ}_{(5)}$ (± 7 %), Δn_{Na^+} (± 7 %), Δn_w (± 7 %), ΔV (± 12).

3.4.3 Differential Binding of Na⁺ and Water

We obtained UV melting curves as a function of salt concentration, 16–216 mM of Na⁺, to determine the slope of the T_M -dependences on salt concentration (Figure 4A). This data in combination with the DSC thermograms allows us to determine the differential binding of ions according to Eq. 1. Generally, as the concentration of sodium increases, the helical-coil transitions are shifted to higher temperatures. This is consistent with the stabilizing effect of cations on nucleic acid duplexes due to their larger charge density parameter (134). The resulting Δn_{Na^+} values are summarized in the last column of Table 1. These values were then calculated in terms of the total number of phosphates. We obtained differential ion binding of 0.073 (*PsK-5*), 0.085 (*PsK-7*), 0.079 (*PsK-9*), and 0.10 mol of Na⁺/mol of phosphate (*PsK-11*) these values are small but consistent with counterion uptake by short DNA duplexes of 4 to 10 base pairs (135), (136). In general, the Δn_{Na^+} values increase with the increased in the length of the thymine loop. However, a better assessment for the differential binding of counterions is to consider just the phosphates associated with the helical stems, this will include two extra loop phosphates for each molecule and considers the other loop phosphates to behave like random coil phosphates i.e., 22 helical phosphate groups. This yielded 0.11 (*PsK-5*), 0.14 (*PsK-7*), 0.14 (*PsK-9*), and 0.20 mol of Na⁺/mol of helical phosphate (*PsK-11*). Figure 4B shows their dependence on loop length. The increase in the loop length yielded a net uptake of, in mol Na⁺ per helical phosphate-per thymine: 0.014. The molecules begin to approach polymer behavior. Furthermore, the molecules with larger loops: *PsK-11*, shows a higher counterion uptake of 0.18. *PsK-11* shows the largest uptake of ions, a value in excess when compared to a phosphate in the duplex state of a DNA polymer, ~0.17 mol Na⁺/mol

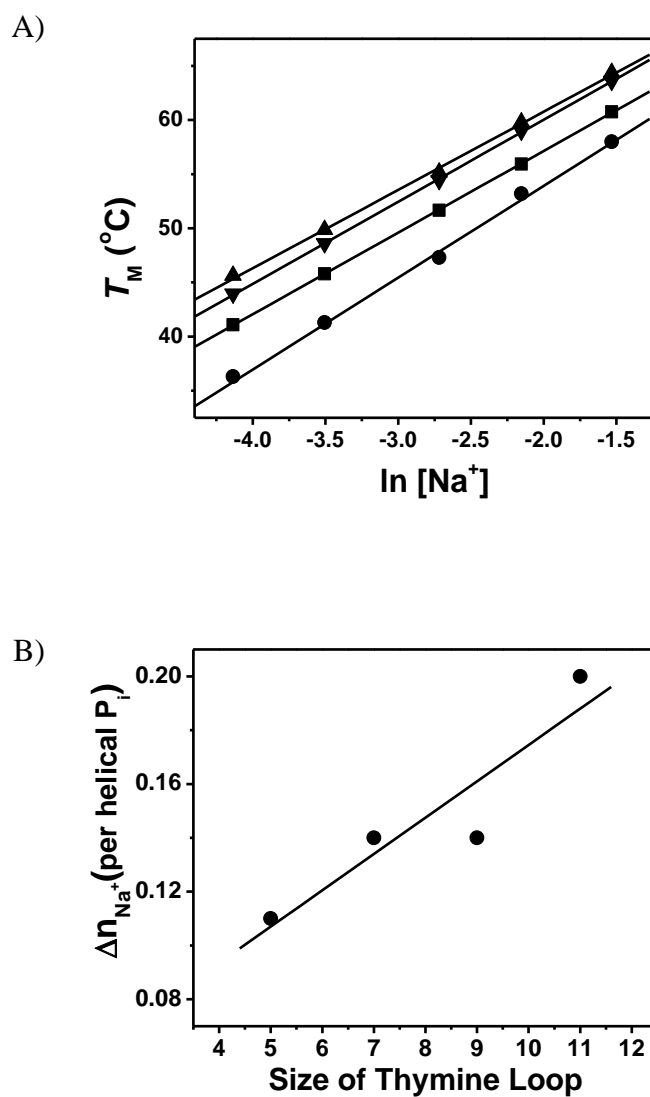


Figure 4. A) T_M dependence on salt concentration. B) Δn_{Na^+} as a function of the size of the thymine loop. All experiments were done in 10 mM sodium phosphate buffer with increasing salt concentrations, pH 7.0, with concentration of pseudoknots between 1-2 μM ; T_M (± 0.5 °C), Δn_{Na^+} ($\pm 7\%$).

Pi. This can be rationalized in terms of some loop thymines forming Hoogsteen base-pairing with the stem, which positions their phosphates in a triple helical state. This speculation is consistent with the formation of base-triplet stacks that was observed from the analysis of the folding enthalpies, in spite of ion binding being a long range interaction as oppose to the short range interactions of base-pair stacking.

We also obtained UV melting curves as a function of osmolyte concentration, in this case ethylene glycol concentration was used with concentrations ranging from 0-2.5 M, to change water activity and to determine in this way the slope of the T_M -dependences on water activity (Figure 5A). This data in combination with the DSC thermograms allows us to determine the differential binding of water according to Eq. 2. Generally, as the water activity decreases, the helical-coil transitions are shifted to lower temperatures. This is consistent with the stabilizing effect of water on nucleic acid duplexes. The resulting Δn_w values are summarized in the last column of Table 1. Specifically, we determined water uptakes of 11 mol of H₂O/mol (*PsK-5*), 19 mol of H₂O/mol (*PsK-7*), 23 mol of H₂O/mol (*PsK-9*), and 24 mol of H₂O/mol (*PsK-11*). In general, the Δn_w values increase with the increased in the length of the thymine loop. Figure 5B shows their dependence on loop length. The increase in the loop length yielded a net uptake of 2.2 mol H₂O/per thymine. This effect can be explained in two ways. The first being, as the loop length increases the loop becomes more flexible and starts to behave in a random coil state becoming more exposed to the solvent. The second explanation is due to triplet formation because with the thymine strand in the major groove the methyl group would be able to interact with the solvent yet it would still be protected resulting in the increase in stability of the molecules we are observing with the increase in loop length.

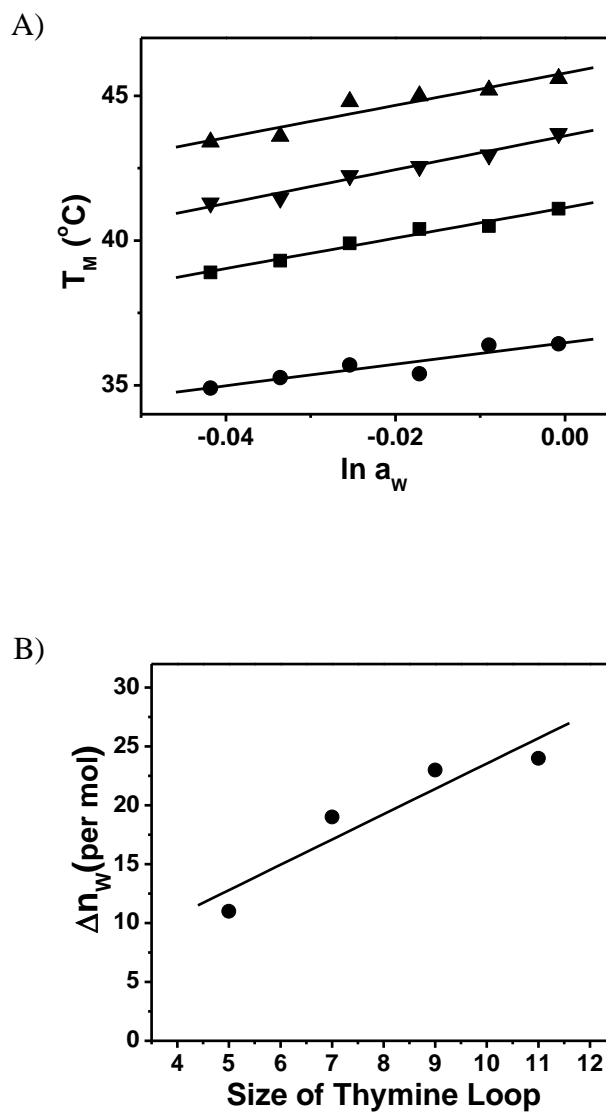


Figure 5. A) T_M dependence on water activity. B) Δn_w as a function of the size of the thymine loop. All experiments were done in 10 mM sodium phosphate buffer with increasing osmolyte concentration with concentration of pseudoknots between 1-2 μM , pH 7.0; $T_M (\pm 0.5 \text{ }^\circ\text{C})$, $\Delta n_w (\pm 7\%)$.

3.4.4 Pressure Perturbation Calorimetry to Measure Unfolding Volumes, ΔV_u

We have used the PPC technique to determine the unfolding volume of *PsK-5*, *PsK-7*, *PsK-9*, and *PsK-11*; this in turn may help with the interpretation of the hydration properties of pseudoknots. Initially, we obtained DSC melts of each pseudoknot to determine the temperature range and temperature steps for the subsequent PPC experiments. In these experiments, we used higher oligonucleotide concentrations, 0.35 mM (*PsK-5*), 0.50 mM (*PsK-7*), 0.45 mM (*PsK-9*), 0.27 mM (*PsK-11*), in 10 mM NaPi at pH 7.0. Analysis of the DSC melting curves (data not shown) yielded T_{MS} and ΔH_{calS} of 36.5 °C and 53.2 kcal/mol (*PsK-5*), 40.4 °C and 81.2 kcal/mol (*PsK-7*), 44.3 °C and 84.9 kcal/mol (*PsK-9*), 43.6 °C and 86.1 kcal/mol (*PsK-11*), respectively. These experiments were carried out in 10 mM NaPi buffer at pH 7.0 and do not correspond with the values reported in Table 1, which are higher salt concentrations.

The PPC melting curves, α as a function of T, for each pseudoknot are shown in Figure 6. More positive values of α and the negative slope of the baselines indicate the exposure of the hydrophilic groups (sugar-phosphate backbone) to the solvent in their folded states. At higher temperatures α is decreased and the slope becomes less negative due to the additional exposure of the aromatic groups of the nucleobases to the solvent in the random coil state. The transitions of each pseudoknot in these curves are monophasic and show T_{MS} , or transition minima, of 35.0 °C (*PsK-5*), 40.0 °C (*PsK-7*), 43.3 °C (*PsK-9*), 42.1 °C (*PsK-11*), these values are in good agreement from previous DSC melting curves. Integration of these negative peaks yielded $\Delta V/\Phi_V$ values of -2.5×10^{-3} (*PsK-5*), -2.4×10^{-3} (*PsK-7*), -2.8×10^{-3} (*PsK-9*), -3.1×10^{-3} (*PsK-11*), after determination of the Φ_V s from density measurements, we obtained ΔV s of $-18 \text{ cm}^3\text{-mol}^{-1}$ (*PsK-5*), $-18 \text{ cm}^3\text{-mol}^{-1}$

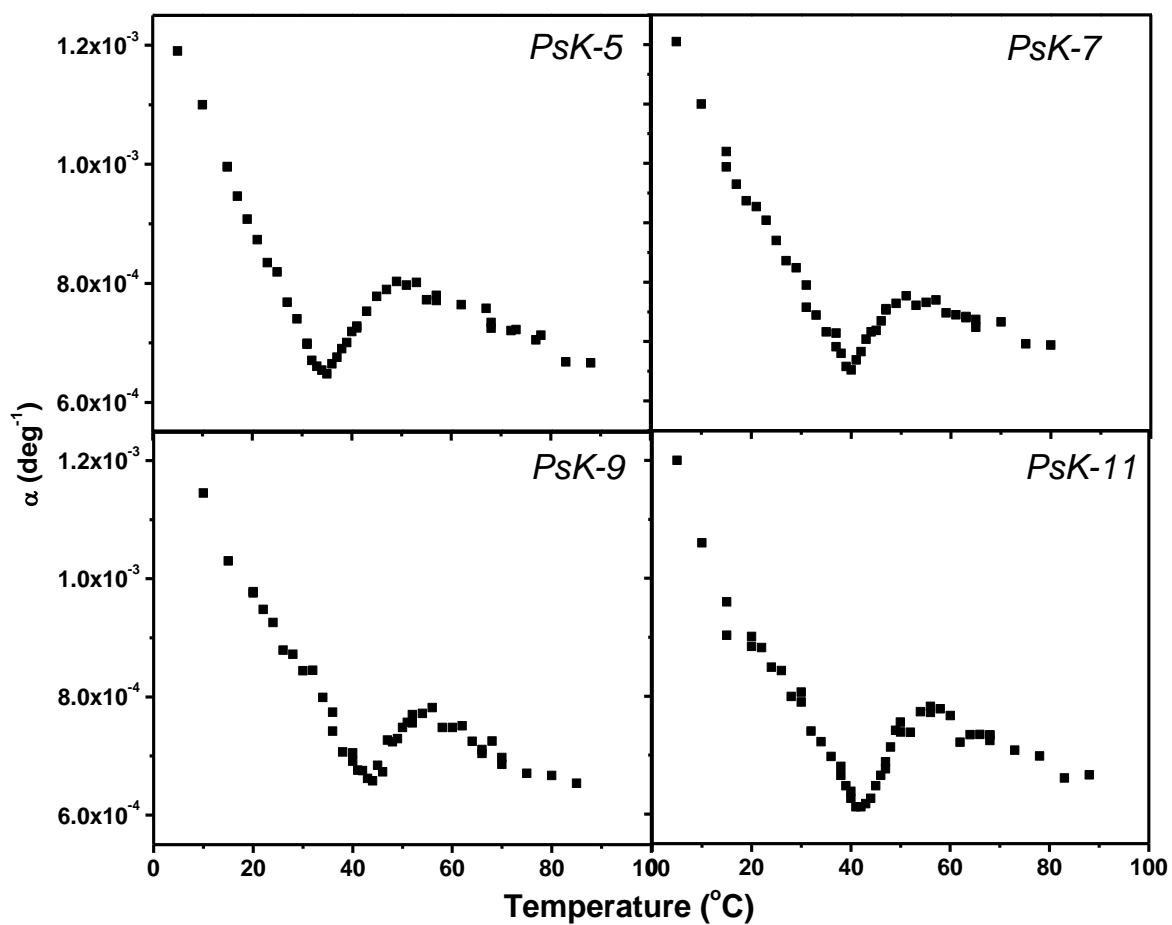


Figure 6. PPC curves of *PsK-5*, *PsK-7*, *PsK-9*, and *PsK-11* in 10 mM NaPi buffer pH 7.0, and at oligonucleotide concentrations of 0.35 mM (*PsK-5*), 0.50 mM (*PsK-7*), 0.45 mM (*PsK-9*), 0.27 mM (*PsK-11*).

(*PsK-7*), $-22 \text{ cm}^3\text{-mol}^{-1}$ (*PsK-9*), and $-23 \text{ cm}^3\text{-mol}^{-1}$ (*PsK-11*), Table 1. These negative values indicate that the increase in temperature produces a volume contraction of the system, if cavities do not exist, then these volume contractions correspond to changes in the hydration state upon unfolding of the solute. Meaning, the unfolding of a pseudoknot is accompanied by an increase in the uptake of water, i.e., an increase in the hydration state. This result contradicts the Δn_w where we see an uptake of water in the folded state. This apparent contradiction may be explained in terms of the removal of electrostricted water by the binding of counterions, which is compensated by the immobilization of structural water, measured by the osmotic stress technique.

3.4.5 Confirming the Formation of TAT Base-Triplets

To confirm the formation of TAT base-triplets in *PsK-9* and *PsK-11*, the sequence of the core stem of these pseudoknots (Figure 1) was changed by flipping one AT base-pair of the homopurine/homopyrimidine stretch ($5'\text{-A}_7/\text{T}_7$ to $5'\text{-A}_5\text{TA}/\text{TAT}_5$) on the right side of this stem, yielding the *PsK-9-6TA* and *PsK-11-6TA* pseudoknots. This disrupts a triplex helix because the shift of the third strand thymine to the other side of the major groove by $\sim 10 \text{ \AA}$ s (137) causes a triplex destabilization that spans 5 base triplets on either side (51). The melting curves of *PsK-9-6TA* and *PsK-11-6TA* are monophasic with T_{MS} around 46°C and similar hyperchromicities of 16-17% at 260 nm (Figure 7A). This indicates that the flip of an AT base pair causes a 13°C decrease in their T_{M} relative to *PsK-9* and *PsK-11*. This can be rationalized in terms of a higher exposure to the solvent of both the loop and stem bases. Furthermore, the T_{MS} remain the same for each pseudoknot over a 10-fold increase in strand concentration, indicating their

intramolecular folding/unfolding. *PsK-9-6TA* and *PsK-11-6TA* unfold through monophasic transitions, Figure 7B. The DSC experiments, shown in Figure 8, yielded total ΔH_{calS} of 72.1 (*PsK-9-6TA*) and 86.2 kcal/mol (*PsK-11-6TA*) when increasing the length of the right side loop from 9 to 11 thymines, Table 2. These are significant drops, 15.4 and 23.8 kcal/mol, relative to the enthalpies of the wild type pseudoknots, respectively. The decrease in enthalpy can be attributed to the disruption of the base-triplet stacks due to the instability cause by the AT flipped base pair in this stem. Since the destacking of a third strand thymine reduces the total enthalpy by 15.5 kcal/mol (24), we can confirm that *PsK-9* is forming one TAT/TAT stack. Similar calculation indicates *PsK-11* forms 1.5 TAT/TAT stacks, lower than suggested earlier. This apparent contradiction may be explained in terms of additional stacking contributions in the 11-thymine loop of *PsK-11-6TA* and lower enthalpy of its core stem (replacement of 2 AA/TT base pair stacks for 1 AT/AT & 1 TA/TA base pair stacks) and higher flexibility of this pseudoknot.

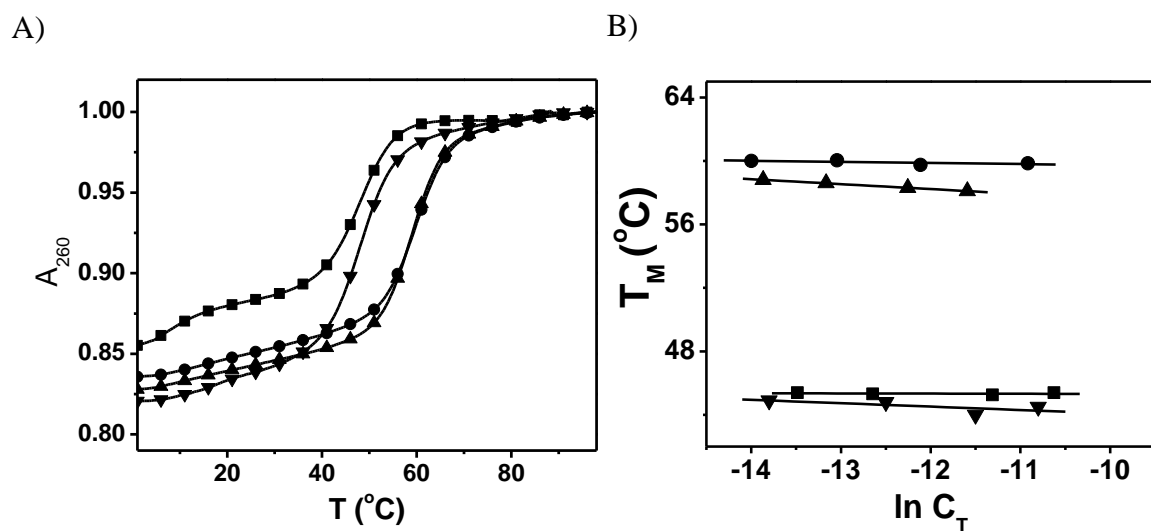


Figure 7. Unfolding of Pseudoknots with a Flipped AT Base Pair in the Core Stem.

A) UV melting curves of pseudoknots (● PsK-9, ■ *PsK-9-6TA*, ▲ PsK-11, ▼ *PsK-11-6TA*) B) T_M vs. Concentration. All experiments were carried out in 10 mM NaPi, 100 mM NaCl at pH 7.0. Concentrations ranged from 20-1 μ M.

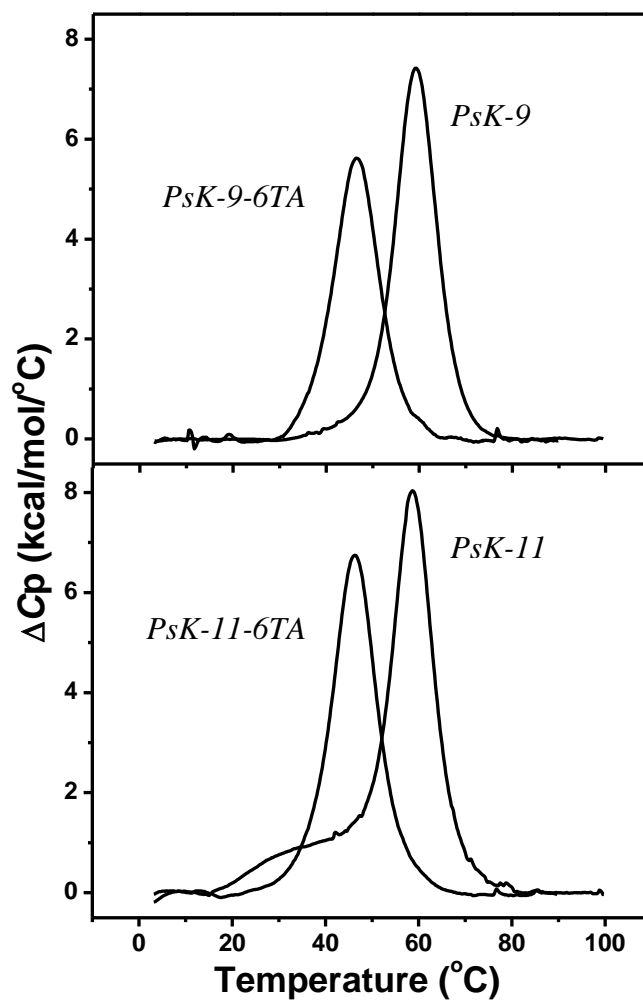


Figure 8. Unfolding of Pseudoknots with a Flipped AT Base Pair in the Core Stem. DSC curves of *PsK-9* (120 μ M) and *PsK-9-6TA* (26 μ M) (top); *PsK-11* (52 μ M) and *PsK-11-6TA* (43 μ M) (bottom). All experiments were carried out in 10 mM NaPi, 100 mM NaCl at pH 7.0.

Table 2. Thermodynamic Folding Profiles of Pseudoknots with a Flipped AT Base

Molecule		T_M (°C)	ΔH_{cal} (kcal/mol)	$T\Delta S_{cal}$ (kcal/mol)	ΔG°_5 (kcal/mol)
<i>PsK-9</i>		59.3	-87.5	-73.3	-14.2
<i>PsK-9-6TA</i>		46.6	-72.1	-62.7	-9.4
<i>PsK-11</i>	1 st	31.6	-26.4	-23.4	-3.0
	2 nd	58.7	-83.6	-70.0	-13.6
<i>Total</i>			-110	-93.4	-16.6
<i>PsK-11-6TA</i>		46.3	-86.2	-75.1	-11.1

All experiments were carried out in 10 mM Phosphate buffer at pH 7.0 and 100 mM NaCl. Experimental errors are as follows: T_M (± 0.5 °C), ΔH (± 5 %), $T\Delta S$ (± 5 %), $\Delta G^\circ_{(5)}$ (± 7 %)

3.4.6 Fluorescence Spectroscopy

Another method used to confirm whether base-triplets are forming within the pseudoknot was substitution of dA for 2-aminopurine. The rationale behind this is if the thymine of the loop is forming a base-triplet with the substituted adenine of the core stem of the pseudoknot then the fluorescent signal should be decreased significantly from that of the random coil because 2-AP is flanked by thymines in the major groove preventing its exposure to the solvent (138). As shown in Figure 9A, this was observed when 2-AP was substituted at either position 6 or 2 in the AT portion of the core stem. When comparing the spectra between the folded and unfolded states the pseudoknots with 2-AP at the position located in close proximity to the core stem junction shows the greatest change in fluorescent signal. This indicates the base-triplets are most likely occurring at the junction of the two stems of the pseudoknots.

The fluorescent melting curves, Figure 9B, were also obtained and all curves show a true sigmoidal shape indicating cooperative unfolding. The T_M s are also very similar to those obtained for the parent pseudoknots: 55.9°C (*PsK-9-6-AP*) 58.5°C (*PsK-9-2-AP*) 55.8°C (*PsK-11-6-AP*) 57°C (*PsK-11-2-AP*), however, there is a slight decrease by 2-3°C. This decrease is consistent with previous findings when substituting dA for 2-AP and shows that 2AP substitution does not hinder the formation of the pseudoknot (138). The large magnitude of the fluorescent changes of each pseudoknot suggests that 2-AP is forming T(2-AP)T base-triplets.

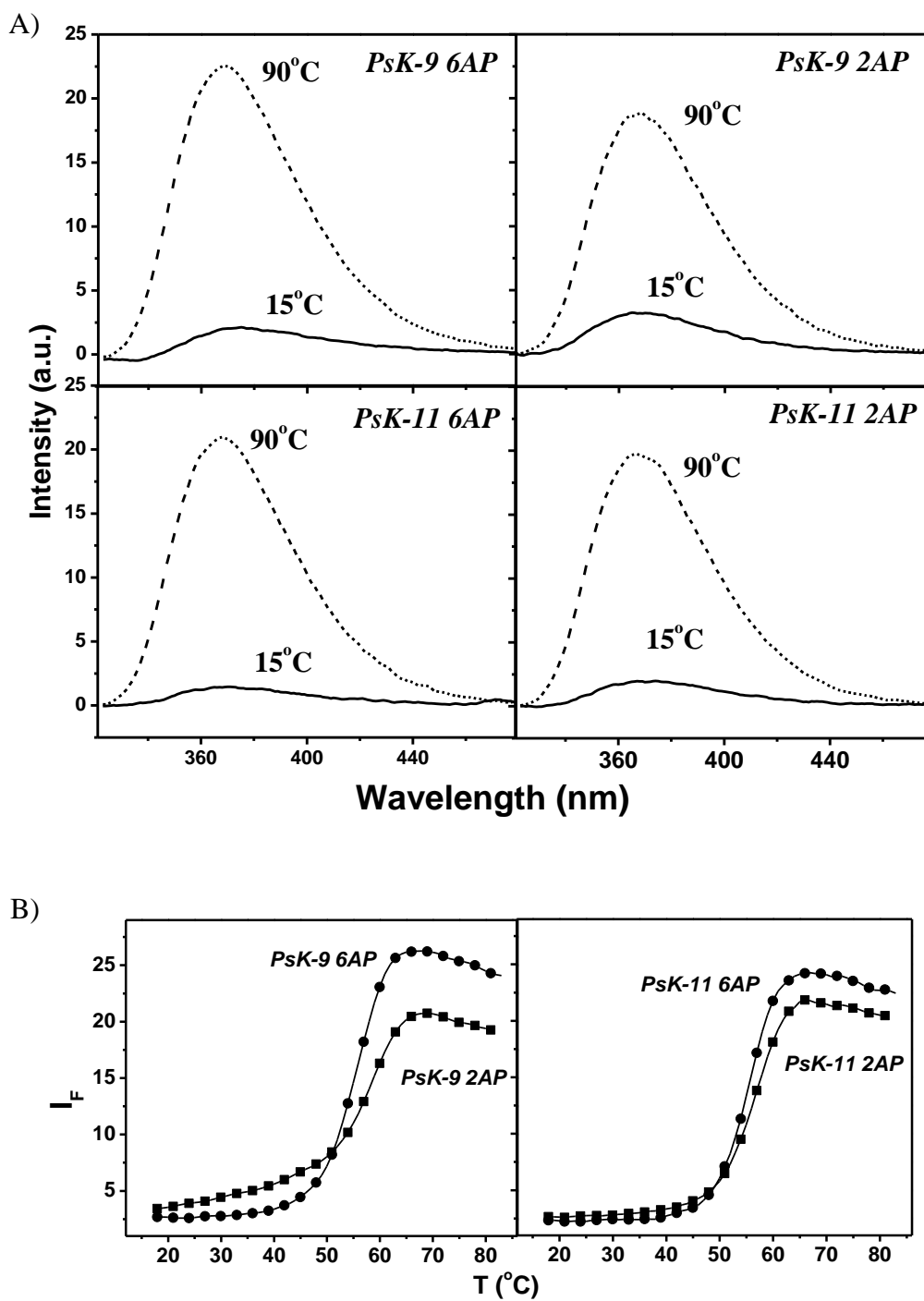


Figure 9. Fluorescence Spectra of 2-AP Modified Pseudoknots. A) Wavelength and B) Melting curves. All experiments were carried out in 10 mM NaPi, 100 mM NaCl at pH 7.0.

3.4.7 Pseudoknots Containing CGC Sequences with Potential to form C⁺GC Base-Triplets

We substituted a TAT triplet for a C⁺GC triplet in *PsK-9* and also at the same position in *PsK-5*, which has previously been shown not to form base-triplets. C⁺GC triplexes are pH dependent, meaning the cytosine must be protonated to in order for the base-triplet to form. The sequence of the core stem of these pseudoknots (Figure 1) was changed by substituting one or two GC base-pairs of the homopurine/homopyrimidine stretch ($5^{\prime}\text{-A}_7/\text{T}_7$ to $5^{\prime}\text{-A}_5\text{GA}/\text{TCT}_5$ or $5^{\prime}\text{-A}_3\text{GAGA}/\text{TCTCT}_3$) on the right side of this stem, yielding the *PsK-5-1CGC* and *PsK-9-1CGC* and *PsK-5-2CGC* and *PsK-9-2CGC* pseudoknots.

The DSC experiments are shown in Figures 10 and 11 with ΔH_{cat} s summarized in Table 3. The pseudoknots with CGC substitutions should produce a lower enthalpy due to the base-pair stacking contributions of AG/CT and GA/TC rather than two AA/TT (126). However, *PsK-5-1CGC* and *PsK-5-2CGC* have higher enthalpies than *PsK-5*. When decreasing the pH of the buffer there is a decrease in both the T_M and the ΔH of these pseudoknots, Table 3. The reason for this effect can be attributed to the destabilization of the base-pair stacking of the pseudoknot's core stem. It's important to note the protonation of the cytosine in the loop of this pseudoknot is not expected to form a base-triplet due to constrain of the loop as previously reported in this chapter. So, an increase in stability is not expected with an increase in pH.

PsK-9-1CGC and *PsK-9-2CGC* show a decrease in the enthalpy compared to *PsK-9*, Table 3, as expected due to the base-pair stacking contributions. Both of these pseudoknots showed a reduced enthalpy with a decrease in pH, which was opposite of

what was expected because the protonation of cytosines in this loop should strengthen the formation of C⁺GC base-triplets and increase the enthalpy and overall stability of the pseudoknot if base-triplets are forming. If the rest of the molecule is being destabilized with the lowering of the pH there could still be base-triplets forming. But, the triplet formation would be hard to detect by just considering the pH dependence experiments. Therefore, the best way to compare this data is between the *PsKn-5* and *PsK-9* molecules since these destabilizing effects should cancel themselves out as they would be observed with both molecules. When doing this *PsKn-9-1CGC* has an enthalpy difference of -12.6 kcal/mol (pH 7.0) and -18.6 kcal/mol (pH 6.2) indicating there is one base-triplet stack occurring under both buffer conditions, but is stabilized at lower pH conditions. When comparing the pseudoknots with two C⁺GC substitutions in low pH there is an enthalpy difference of -13.9 kcal/mol indicating the presence of one base-triplet stack in *PsK-9-2CGC*. These substitutions confirm the ability of local base-triplets to form within pseudoknots.

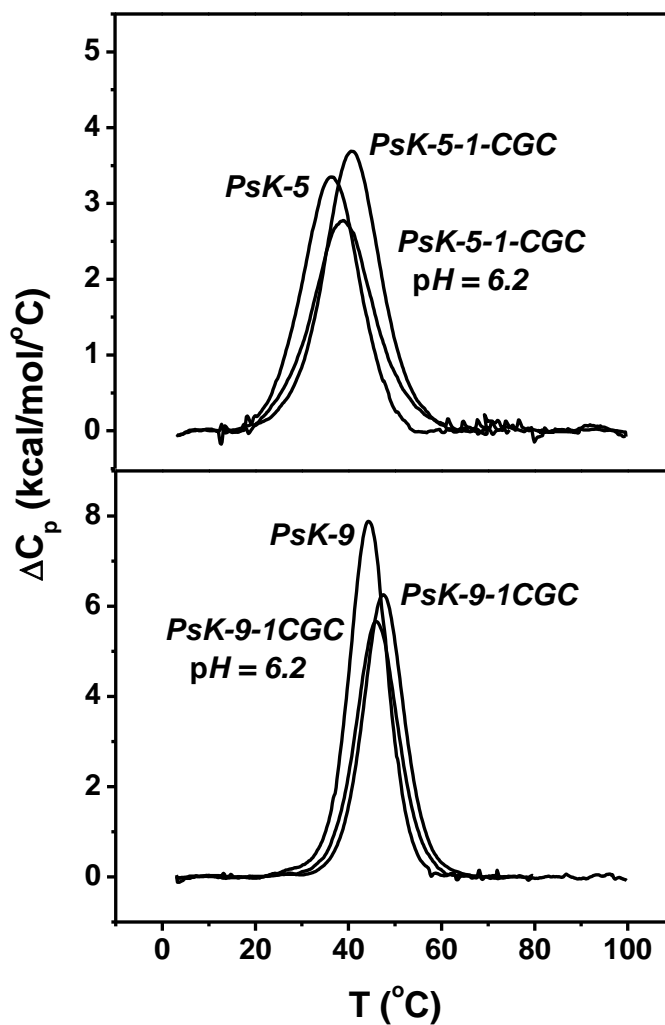


Figure 10. Unfolding of Pseudoknots with C⁺GC substitution. DSC curves of *PsK-5* (84 μM), *PsK-5-1CGC* (88 μM), *PsK-5-1CGC pH 6.2* (56 μM) (top); *PsK-9* (31 μM), *PsK-9-1CGC* (116 μM), *PsK-9-1CGC pH 6.2* (45 μM) (bottom). All experiments were carried out in 10 mM NaPi, at pH 7.0 unless indicated.

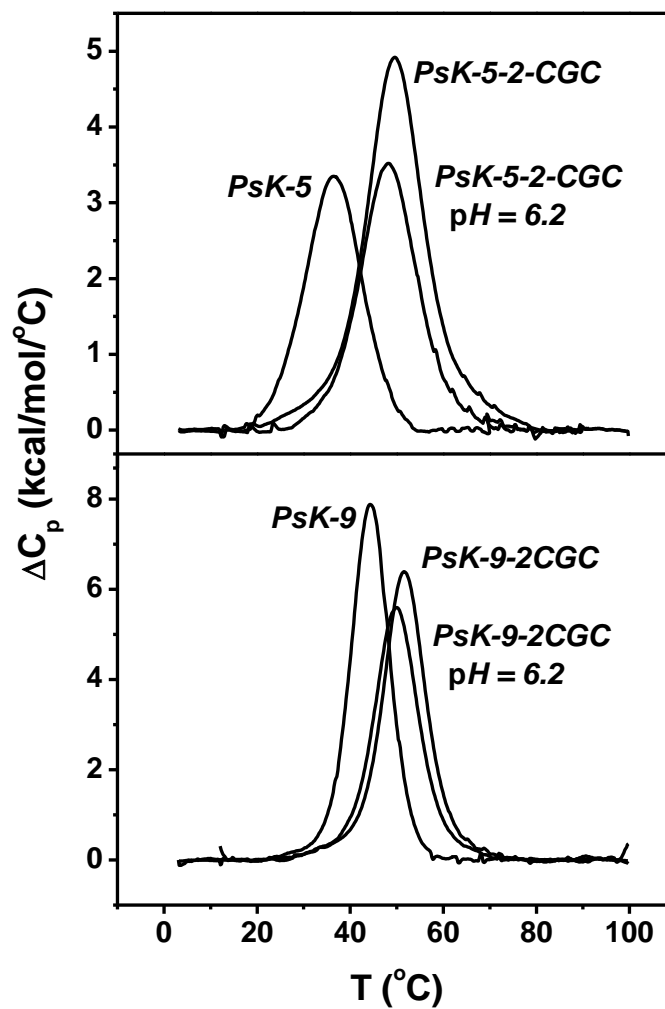


Figure 11. Unfolding of Pseudoknots with C⁺GC substitution. DSC curves of *PsK-5* (84 μ M), *PsK-5-2CGC* (113 μ M), *PsK-5-2CGC pH 6.2* (68 μ M) (top); *PsK-9* (31 μ M), *PsK-9-2CGC* (123 μ M), *PsK-9-2CGC pH 6.2* (53 μ M) (bottom). All experiments were carried out in 10 mM NaPi, at pH 7.0 unless indicated.

Table 3. Thermodynamic Folding Profiles of Pseudoknots with a C⁺GC Triplets

Molecule	pH	T_M (°C)	ΔH_{cal} (kcal/mol)	$T\Delta S_{cal}$ (kcal/mol)	ΔG°_5 (kcal/mol)
<i>PsK-5</i>		36.5	-53.2	-47.8	-5.4
<i>PsK-5-1CGC</i>		41.0	-58.2	-51.6	-6.7
<i>PsK-5-1CGC</i>	pH 6.2	39.1	-48.2	-42.9	-5.3
<i>PsK-5-2CGC*</i>		49.7	(-81.1)	-69.9	-11.2
<i>PsK-5-2CGC</i>	pH 6.2	48.2	-56.5	-48.9	-7.6
<i>PsK-9</i>		44.3	-84.9	-74.4	-10.5
<i>PsK-9-1CGC</i>		47.6	-71.8	-62.3	-9.5
<i>PsK-9-1CGC</i>	pH 6.2	46.1	-66.8	-58.2	-8.6
<i>PsK-9-2CGC</i>		51.7	-77.6	-66.4	-11.2
<i>PsK-9-2CGC</i>	pH 6.2	50.0	-70.4	-60.6	-9.8

All experiments were done in 10 mM sodium phosphate buffer at pH = 7 (except where specified otherwise). Experimental errors are as follows: T_M (± 0.5 °C), ΔH_{cal} (± 5 %), $T\Delta S$ (± 5 %), $\Delta G^{\circ}_{(5)}$ (± 7 %). **PsK-5-2CGC* not included in analysis due to inconsistent results.

3.5 CONCLUSIONS

In this chapter, we used a set of DNA oligonucleotides to study the folding thermodynamics of pseudoknots, which is an important motif in the biology of RNA. We used DNA pseudoknots containing a variable number of thymines in one of the loops, complementary to the core sequence of the duplex stem. Our biological question is if this particular set of pseudoknots can illustrate the formation of local base-triplets and base-triplet stacks, explaining to some extent the high efficiency in ribosomal frameshifting.

Our experimental approach was to use a combination of temperature-dependent spectroscopy and calorimetry techniques to determine the formation of base-triplet stacks within the pseudoknot structure. The first observation is that DNA strands are able to form intramolecular pseudoknots; their transition temperatures remains the same with the 10-fold increase in strand concentration. This means that DNA strands are flexible and can mimic to some extent the tertiary structures formed by RNA molecules, which is important considering the cheaper cost of DNA strands. The unfolding DSC data showed that the increase in the length of the thymine loop yielded higher transition temperatures and higher unfolding enthalpies, this is contrary to the loop effects of straight hairpin loops and indicates that additional interactions are occurring within the pseudoknot as the loop length increases. Specifically, pseudoknots with longer thymine loops are thermodynamically more stable because the sequence complementarity of this loop with the stem (A₇T₇) allows them to form Hoogsteen base-pairs. In this particular system, the magnitude of the excess enthalpies indicates formation of one and three TAT/TAT stacks in, *PsK-9* and *PsK-11*, respectively. We also found that there is an increase in ion and water uptake as the loop length of the pseudoknot increases stabilizing the Hoogsteen base-pairing during triplet formation. However, ΔV measurements had an opposite effect

showing the folding of a pseudoknot is accompanied by a decrease in the uptake of water, i.e., a decrease in the hydration state. This result contradicts the Δn_w where we see an uptake of water in the folded state, but can be rationalized in terms of the removal of electrostricted water by the binding of counterions, which is compensated by the immobilization of structural water, measured by the osmotic stress technique. In other words, the higher volume of the folded state is consistent with both the immobilization of water and the uptake of counterions. Also, one AT base-pair was flipped for a TA base-pair in the A₇T₇ stem of these pseudoknots, which prevents the formation of base-triplets. This resulted in modified pseudoknots with lower unfolding enthalpies, confirming the formation of local base-triplets in *PsK-9* and *PsK-11*. Furthermore, fluorescent changes of 2-AP as a function of both wavelength and temperature indicated a much higher intensity in the unfolded state, which indicates the 2-AP in the folded state is less exposed to the solvent and the melting of these pseudoknots showed large changes in fluorescent signal which also suggest that 2-AP is forming T(2-AP)T base-triplets. Additionally, CGC substitutions were made to show triplet formation in pseudoknots with varying sequence and also to show a *pH* dependence on triplet formation. This resulted in the formation of local base-triplets in *PsK-9* with both one and two CGC substitutions.

Overall, this investigation confirms the flexibility of DNA oligonucleotides being able to form pseudoknots; therefore, they can be used to mimic known RNA secondary structures. In particular, we were able to show the formation of local base-triplets that explains ribosomal frameshifting, which allows for differences in the translation of mRNAs.

CHAPTER FOUR

INFLUENCE OF BUFFER OF ON THERMODYNAMIC STABILITY OF DNA, dU AND RNA PSEUDOKNOTS

4.1 SUMMARY

We report on the unfolding behavior of DNA, dU substituted, and RNA pseudoknots with stem loop complementarity. All three pseudoknots (*PsK-11dT*, *PsK-11dU* and *PsK-11RNA*) form intramolecularly pseudoknots with *PsK-11dT* and *PsK-11dU* forming in the “B” conformation and *PsK-11RNA* forming in the “A” conformation. The thermodynamic profiles of each pseudoknot were characterized under three buffer conditions: 10 mM Sodium Phosphate, 10 mM Sodium Cacodylate, and 10 mM Sodium Cacodylate with 10 mM MgCl₂. The general trend was that the pseudoknots were more thermodynamically stable in 10 mM Sodium Cacodylate with 10 mM MgCl₂ followed by 10 mM Sodium Phosphate and finally 10 mM Sodium Cacodylate. The overall thermodynamic stability of these pseudoknots takes place in the following order regardless of the buffer conditions used: *PsK-11dU* < *PsK-11dT* < *PsK-11RNA*. The unfolding thermodynamics as a function of salt yielded similar ion uptakes between the molecules of ~3.1 mol Na⁺/mol in 10mM Sodium Phosphate and 10 mM Sodium Cacodylate and ~0.1 mol of Na⁺/mol in 10 mM Sodium Cacodylate with 10 mM MgCl₂. The water uptakes decreased when comparing *PsK-11dT* and *PsK-11dU* by 7.5 mol of H₂O/mol in the 10 mM Sodium Phosphate with 10 mM Sodium Cacodylate. There was also a decrease in the 10 mM Sodium Cacodylate with 10 mM MgCl₂ by 22 mol of H₂O/mol. When comparing *PsK-11dT* to *PsK-11RNA* there was a decrease in the water

uptake of 4 mol of H₂O/mol in 10 mM Sodium Phosphate and a decrease of 13 mol of H₂O/mol in 10 mM Sodium Cacodylate with 1.0 mM MgCl₂.

4.2 INTRODUCTION

A complete physical description of a particular DNA or RNA complex depends on the contributions from base pairing, base stacking, as well as ion binding and hydration (5), (21-36). These contributions can all be affected by solution conditions used within the experiment. The most predominant buffers used in the past have been sodium phosphate and sodium cacodylate (126), (131), (139). The reason these buffers have been used are they have a pK_a around 7 where DNA is most stable and changes in pK_a with temperature are minor. Benight's laboratory has also shown that when comparing short DNA duplexes sodium phosphate is the preferred buffer over sodium cacodylate due to potential differences in the DNA hydration levels (140), however, when working with RNA sodium phosphate is not the preferred buffer to use due to the requirement of Mg²⁺ ions.

These previous studies have focused on duplexes and little work has been done at comparing different secondary structures of nucleic acids. We are particularly interested in pseudoknots, due to the variation in their stem sequence, the fluctuation of loop length and sequence, as well as, their interactions among themselves. Pseudoknots have been found to be involved in a variety of biological functions including: telomerase (38), (37), riboswitches (45), ribosomal frameshifting (43), (44), self-splicing introns (39), and forming the catalytic core of various ribozymes (40-42). As you can see they are an important and diverse structural motif and it is important to study the effects of buffer conditions on these molecules along with the effect on ion and water uptake.

In this work, we have determined the folding/unfolding thermodynamics of a set of pseudoknots which includes a DNA pseudoknot (*PsK-11dT*) previously studied (141), the same pseudoknot with a dU substituted loop (*PsK-11dU*), and the RNA equivalent pseudoknot (*PsK-11RNA*). The thermodynamic profiles of each pseudoknot were characterized under three buffer conditions: 10 mM Sodium Phosphate, 10 mM Sodium Cacodylate, and 10 mM Sodium Cacodylate with 10 mM MgCl_2 to determine the effect of the buffer conditions on the overall stability of DNA, dU substituted and RNA pseudoknots along with the effect of ion and water uptake.

4.3 MATERIALS AND METHODS

Materials. All oligonucleotides were synthesized by the Integrated DNA Technologies (IDT) (Coralville, IA), HPLC purified, and desalted by column chromatography using G-10 Sephadex exclusion chromatography. The sequences of oligonucleotides used in this work and their designation are shown in Figure 1. The concentrations of the oligomer solutions were determined at 260 nm and 90°C using an Aviv Spectrophotometer Model 14DS UV-Vis using the molar extinction coefficients listed previously: $376 \text{ mM}^{-1} \text{ cm}^{-1}$ (*PsK-11dT*), $360 \text{ mM}^{-1} \text{ cm}^{-1}$ (*PsK-11dU*), $409 \text{ mM}^{-1} \text{ cm}^{-1}$ (*PsK-11RNA*). These values were obtained by extrapolation of the tabulated values for dimers and monomeric bases (96), (130) at 25°C to 90°C using procedures reported previously (97), (129). Inorganic salts from Sigma were reagent grade, and used without further purification. Measurements were made in appropriate buffer solutions: 10 mM sodium phosphate (NaPi), 10 mM Sodium Cacodylate (NaCac), and 10 mM NaCac, 10 mM MgCl_2 (NaCac & Mg^{2+}) at pH 7.0. All oligonucleotide solutions were prepared by dissolving the dry and desalted ODNs in buffer.

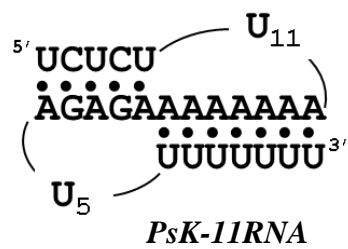
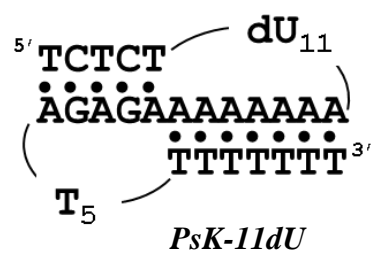
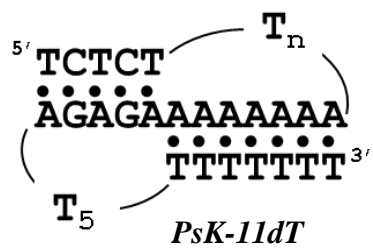


Figure 1. Sequences, structures and designation of the molecules investigated

Temperature-Dependent UV Spectroscopy. Absorbance versus temperature profiles were measured at 260 nm with a thermoelectrically controlled Aviv Spectrophotometer Model 14DS UV-Vis (Lakewood, NJ). The temperature was scanned at a heating rate of 0.6 °C/min, and shape analysis of the melting curves yielded transition temperatures, T_{MS} (98). The transition molecularity for the unfolding of a particular complex was obtained by monitoring T_M as a function of the strand concentration. Intramolecular complexes show a T_M -independence on strand concentration, while the T_M of intermolecular complexes does depend on strand concentration (129).

Differential Scanning Calorimetry. The total heat required for the unfolding of each oligonucleotide was measured with a VP-DSC differential scanning calorimeter from Microcal (Northampton, MA). Standard thermodynamic profiles and T_{MS} are obtained from the DSC experiments using the following relationships (98), (129): $\Delta H_{cal} = \int \Delta C_p(T) dT$; $\Delta S_{cal} = \int \Delta C_p(T) / T dT$, and the Gibbs equation, $\Delta G^\circ(T) = \Delta H_{cal} - T \Delta S_{cal}$; where ΔC_p is the anomalous heat capacity of the ODN solution during the unfolding process, ΔH_{cal} and ΔS_{cal} are the unfolding enthalpy and entropy, respectively, assumed to be temperature-independent. $\Delta G^\circ(T)$ is the free energy at temperature T , normally 5 °C.

Circular Dichroism. All CD spectra were obtained with an Aviv Circular Dichroism Model 202SF spectrometer (Lakewood, NJ) equipped with a peltier temperature control system. These CD spectra were taken from 320 nm to 200 nm in 1 nm increments with an averaging time of 3 seconds using 1.0 cm free-strained quartz cuvettes. The reported spectra correspond to the average of at least two scans. The particular conformation of each pseudoknot (10mM NaPi, 10mM NaCac, and 10mM NaCac, 10mM MgCl₂ all with 100mM NaCl) was determined from inspection of their CD spectra at 2°C.

Determination of the Differential Binding of Counterions and Water. Additional UV melting curves, as a function of salt and osmolyte concentrations, were performed to determine the differential binding of counterions, Δn_{Na^+} , and water molecules, Δn_{W} , between the folded and coil states and were determined using following equations:

$$\Delta n_{\text{Na}^+} = 1.11 \left[\frac{\Delta H_{\text{cal}}}{RT_{\text{M}}^2} \right] (\partial T_{\text{M}} / \partial \ln [\text{Na}^+]) \quad (1)$$

$$\Delta n_{\text{W}} = \left[\frac{\Delta H_{\text{cal}}}{RT_{\text{M}}^2} \right] (\partial T_{\text{M}} / \partial \ln [a_{\text{W}}]) \quad (2)$$

The terms in brackets of Eqs 1 and 2 are determined directly from DSC experiments while the ones in parentheses from UV melting curves. The latter correspond to the slopes of the plots of T_{M} as a function of the concentration of sodium and water activity respectively (99). The value 1.11 in Eq. 1 is a constant which is used to convert activity into concentration terms. The activity of water is varied by using different concentrations of a co-solute, ethylene glycol, which does not interact with the ODN (101). The osmolality of these solutions were obtained using a UIC vapor pressure osmometer Model 830, calibrated with standardized NaCl solutions.

4.4 RESULTS

4.4.1 UV Unfolding of Pseudoknots

The melting curves for each pseudoknot under different buffer conditions are shown in Figure 2A. The curves for *PsK-11dT*, *PsK-11dU*, and *PsK-11RNA* are all sigmoidal in shape and each pseudoknot has a monophasic transition under all buffer conditions. *PsK-11dT* has a T_M of 58°C in 10 mM NaPi, 59°C in 10 mM NaCac, and 67°C in 10 mM NaCac & Mg²⁺. *PsK-11dU* has a T_M of 51°C in 10 mM NaPi, 51°C in 10 mM NaCac, and 59°C in 10 mM NaCac & Mg²⁺. *PsK-11RNA* has a T_M of 62°C in 10 mM NaPi, 62°C in 10 mM NaCac, and 70°C in 10 mM NaCac and Mg²⁺. The main observation is there is a decrease in the T_M when the buffer condition is switched from 10 mM NaPi to 10 mM NaCac, but is then increased once the MgCl₂ is added to the solution due to the stabilizing effect of the magnesium. Also, the T_M decreases when dT is substituted for dU. This decrease in T_M is due to the stabilizing effect of the C5 methyl group in dT, which is absent in dU.

We follow the T_M as a function of strand concentration to determine the transition molecularity of each molecule in the three buffer conditions and we find that the pseudoknots (Figure 2B) form intramolecularly. The T_M of each pseudoknot in a particular buffer remains constant confirming their intramolecular formation.

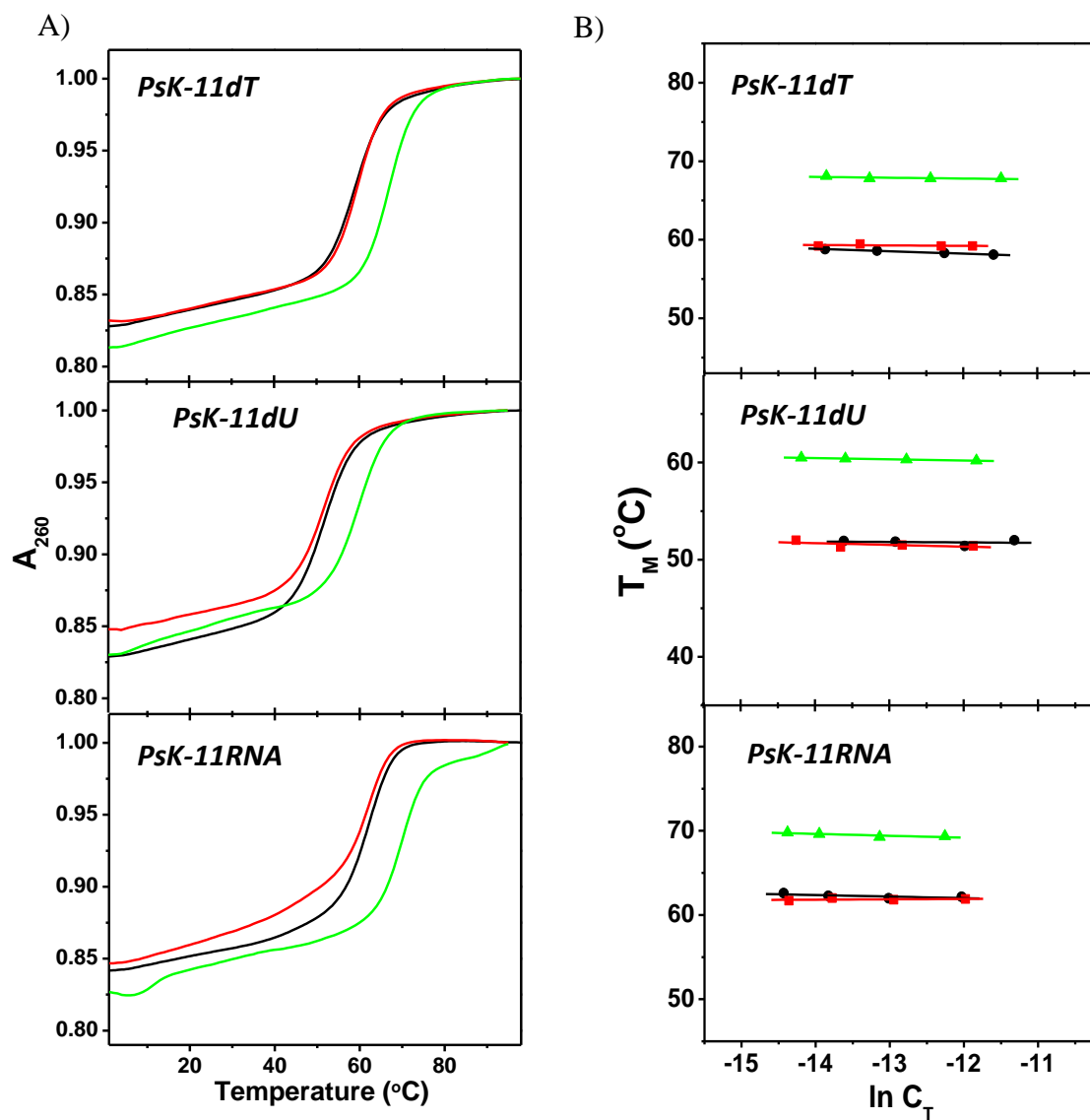


Figure 2. UV Melting Curves and Concentration Dependence. Experiments were carried out with the following salt concentrations: 10 mM NaPi (Black); 10 mM NaCac (Red); 10 mM NaCac, 10 mM MgCl_2 (Green) at pH 7.0; T_M (± 0.5 $^{\circ}\text{C}$).

4.4.2 Pseudoknot Conformation by Circular Dichroism

Circular dichroism experiments were ran in all three buffer conditions, Figure 3. When only considering the CD bands at wavelengths greater than 230 nms in these experiments, it was observed that *PsK-11dT* and *PsK-11dU* have very similar spectra with a minimum at 245 nm and a maximum at 278 nm with similar intensities in these bands. This is characteristic of “B” conformation with the two CD bands having equal areas. The conformation of both *PsK-11dT* and *PsK-11dU* do not show significant changes under the three different buffer conditions. The spectrum of *PsK-11RNA* is different, however, with a minimum at 243 nm and a maximum at 265 nm in 10 mM NaPi and 10 mM NaCac. The intensities of these peaks are not equal as seen with the other oligos, the peak at 265 nm has a much larger intensity than the peak at 243 nm which is characteristic of the “A” conformation. Another interesting observation is with the addition of Mg^{2+} we see shift and an increase in the intensity of the lower band to 247 nm which may be attributed to better base-pair stacking due to the stabilization of the Mg^{2+} . In each case the resulting spectra is characteristic of DNA and RNA molecules.

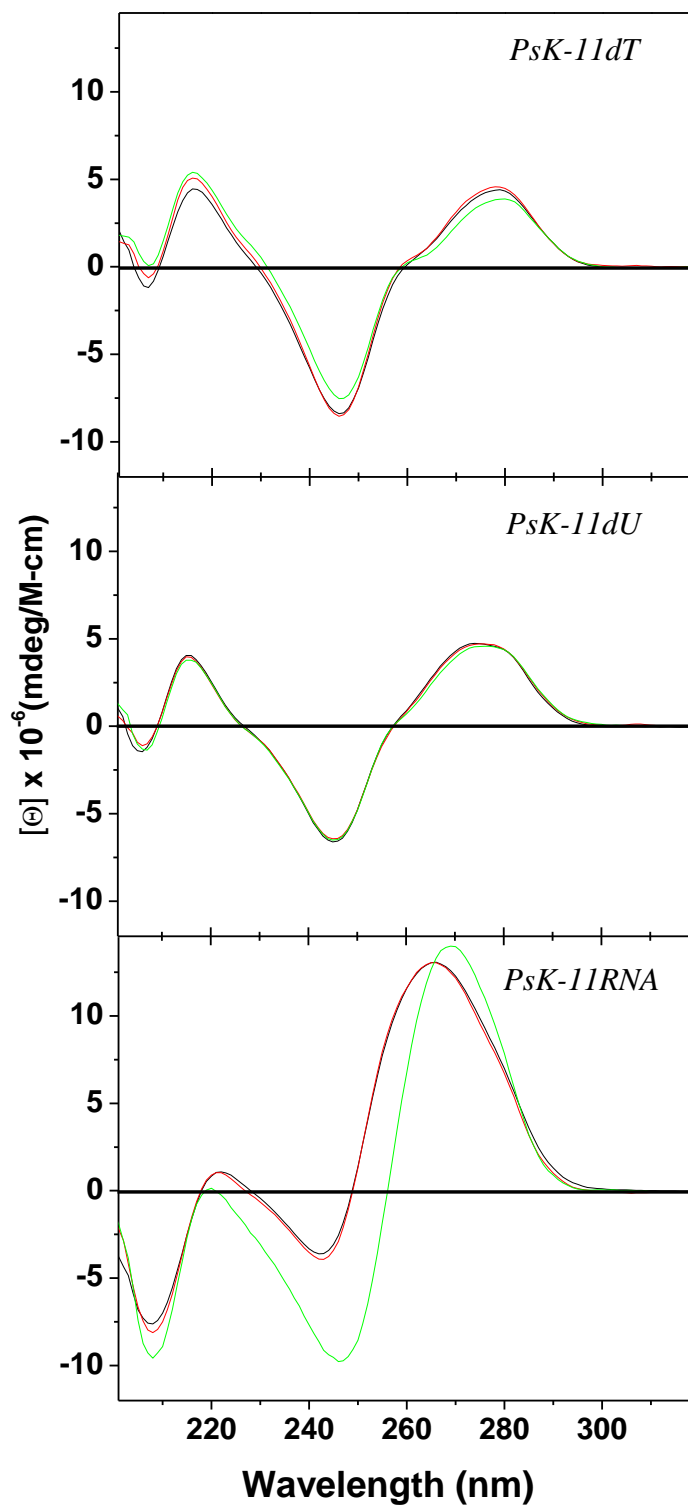


Figure 3. Circular Dichroism Spectra of Pseudoknots. 10 mM Sodium Phosphate (black), 10 mM Sodium Cacodylate (red), 10 mM Sodium Cacodylate, 10 mM MgCl₂ (green) at pH 7.0 and 5°C

4.4.3 DSC Unfolding

The calorimetric unfolding of *PsK-11dT* under different buffer conditions is shown in Figure 4. A similar trend is observed in all three buffers where there is an increase in T_M with an increase in salt concentration and a decrease in T_M with the addition of ethylene glycol, Table 1. The effect with the salt increase, however, is minimized with the NaCac & Mg^{2+} buffer due to the $MgCl_2$ stabilizing the complex. Specifically, in 10 mM NaPi increasing the salt concentration to 100 mM NaCl results in a ΔT_M of $15.7^\circ C$ and $\Delta\Delta H$ of -26 kcal/mol, but when adding ethylene there is a ΔT_M of $-1.7^\circ C$ and $\Delta\Delta H$ of 2.8 kcal/mol. In 10 mM NaCac increasing the salt concentration to 100 mM NaCl results in a ΔT_M of $18.1^\circ C$ and $\Delta\Delta H$ of -11.1 kcal/mol and when adding ethylene there is a ΔT_M of $-2.2^\circ C$ and $\Delta\Delta H$ of -1.8 kcal/mol. In 10 mM NaCac & Mg^{2+} increasing the salt concentration to 100 mM NaCl resulted in a ΔT_M of $-0.8^\circ C$ and $\Delta\Delta H$ of 5.5 kcal/mol, but when adding ethylene glycol there is a ΔT_M of $-4.2^\circ C$ and $\Delta\Delta H$ of 14.3 kcal/mol. When comparing the buffer condition for *PsK-11dT* with 100 mM NaCl specifically, we can observe that there is a decrease in stability by 2.4 kcal/mol when going from 10 mM NaPi to 10 mM NaCac, which is consistent with previous findings (140). The stability is then increased by 4.6 kcal/mol with the addition of $MgCl_2$. This observation could be due to differences in hydration levels around the oligos because due to cacodylate being larger than phosphate ions the steric difference can exclude water around the pseudoknot acting to dehydrate and as a result destabilizing the molecule (140). The addition of Mg^{2+} would help to cancel out these effects, stabilizing the pseudoknot.

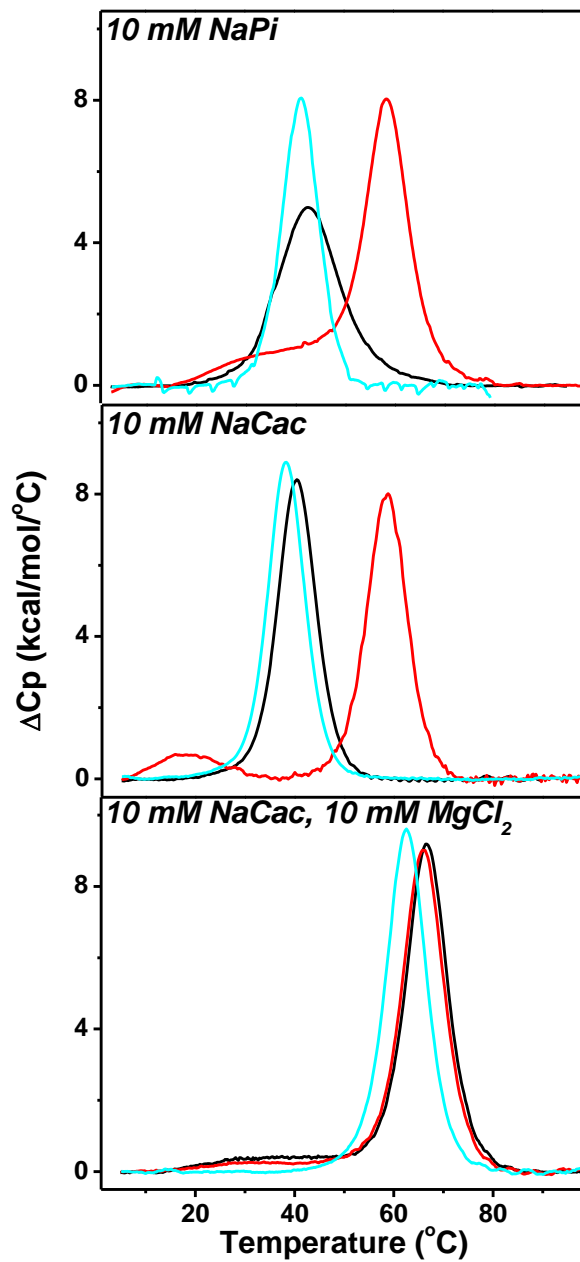


Figure 4. DSC Unfolding of *PsK-11dT*. 10 mM NaPi, 10 mM NaCac, 10 mM NaCac 10 mM MgCl₂ (Black) with additional 100 mM NaCl (Red) or 2M Ethylene Glycol (Cyan). All experiments were ran at pH 7.0.

Table 1. Thermodynamic Folding Profiles for *PsK-11dT*

Buffer	T_M (°C)	ΔH_{cal} (kcal/mol)	$T\Delta S_{cal}$ (kcal/mol)	ΔG°_5 (kcal/mol)
10mM NaPi				
10mM NaPi	43	-84.0	-75.1	-10.1
100mM NaCl	31.6	-26.4	-23.4	-3.0
	58.7	-83.6	-70.0	-13.6
		-110	-93.4	-16.6
2M EG	41.3	-81.2	-71.8	-9.4
10mM NaCac				
10mM NaCac	40.3	-85.8	-76.1	-9.7
100mM NaCl	18.7	-11.6	-11.1	-0.5
	58.4	-85.3	-71.6	-13.7
		-96.9	-82.7	-14.2
2M EG	38.1	-87.6	-78.3	-9.3
10mM NaCac & Mg²⁺				
10mM NaCac & Mg²⁺	43.5	-18.2	-16.0	-2.2
	66.7	-98.1	-80.3	-17.8
		-116.3	-96.3	-19.9
100mM NaCl	29.6	-11.1	-10.2	-0.9
	65.9	-99.7	-81.8	-17.9
		-110.8	-92	-18.8
2M EG	62.5	-102	-84.7	-17.5

Experimental errors: T_M ($\pm 0.5^\circ\text{C}$), ΔH_{cal} ($\pm 5\%$), $T\Delta S_{cal}$ ($\pm 5\%$), $\Delta G^\circ_{(5)}$ ($\pm 7\%$)

Similar experiments were ran for the pseudoknot with dU substitutions for the thymine loop that is complementary to the core stem (*PsK-11dU*), Figure 5. The same general trend is observed where there is an increase in stability with an increase in salt concentration, however a slight change was observed with the addition of ethylene glycol, these values are reported in Table 2. Specifically, in 10 mM NaPi increasing the salt concentration to 100 mM NaCl results in a ΔT_M of 15.1°C and $\Delta\Delta H$ of -28.7 kcal/mol, but when adding ethylene there is a ΔT_M of -2.2°C and $\Delta\Delta H$ of 0.3 kcal/mol. In 10 mM NaCac increasing the salt concentration to 100 mM NaCl results in a ΔT_M of 19.6°C and $\Delta\Delta H$ of -23.9 kcal/mol and when adding ethylene there is a ΔT_M of -0.4°C and $\Delta\Delta H$ of -9.2 kcal/mol. In 10 mM NaCac & Mg²⁺ increasing the salt concentration to 100 mM NaCl resulted in a ΔT_M of 2.8°C and $\Delta\Delta H$ of -31.6 kcal/mol, but when adding ethylene there is a ΔT_M of 0°C and $\Delta\Delta H$ of -22.1 kcal/mol. Comparing the buffer conditions for *PsK-11dU* with 100mM NaCl, we observe there is a decrease in overall stability by 0.5 kcal/mol when going from 10mM Napi to 10mM NaCac, but with the addition of MgCl₂ the stability is increased by 1.3 kcal/mol. This observation could still be due to differences in hydration levels around the oligos, but is minimized due to dU being less hydrated than dT. The addition of Mg²⁺ would help to cancel out these effects.

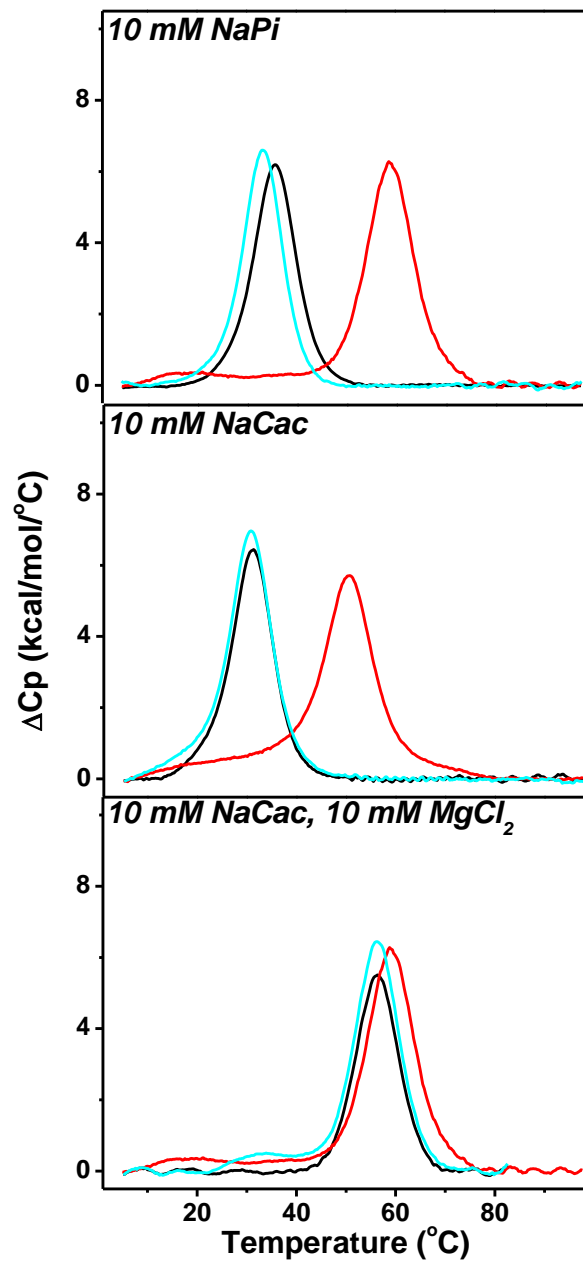


Figure 5. DSC Unfolding of *PsK-11dU*. 10 mM NaPi, 10 mM NaCac, 10 mM NaCac 10 mM MgCl₂ (Black) with additional 100 mM NaCl (Red) or 2M Ethylene Glycol (Cyan). All experiments were ran at pH 7.0.

Table 2. Thermodynamic Folding Profiles for *PsK-11dU*

Buffer	T_M	ΔH_{cal}	$T\Delta S_{cal}$	ΔG°_5
	(°C)	(kcal/mol)	(kcal/mol)	(kcal/mol)
10mM NaPi				
10mM NaPi	35.5	-70.3	-63.4	-7.0
100mM NaCl	33.0	-26.9	-24.4	-2.5
	50.6	-72.1	-61.9	-10.2
		-99	-86.3	-12.7
2M EG	33.3	-70	-53.5	-6.5
10mM NaCac				
10mM NaCac	30.9	-71.9	-65.8	-6.1
100mM NaCl	32.8	-25.4	-23.1	-2.3
	50.5	-70.4	-50.5	-9.9
		-95.8	-73.6	-12.2
2M EG	30.5	-81.1	-74.3	-6.8
10mM NaCac & Mg²⁺				
10mM NaCac & Mg²⁺	56.3	-61.2	-51.7	-9.5
100mM NaCl	20.5	-15.1	-14.3	-0.8
	59.1	-77.7	-65.0	-12.7
		-92.8	-79.3	-13.5
2M EG	35.7	-8.8	-7.9	-0.9
	56.3	-74.5	-62.9	-11.6
		-83.3	-70.8	-12.5

Experimental errors: T_M ($\pm 0.5^\circ\text{C}$), ΔH_{cal} ($\pm 5\%$), $T\Delta S_{cal}$ ($\pm 5\%$), $\Delta G^\circ_{(5)}$ ($\pm 7\%$)

The calorimetric unfolding of *PsK-IIRNA* under different buffer conditions is shown in Figure 6. A similar trend is observed in all three buffers where there is an increase in T_M with an increase in salt concentration and a decrease with the addition of ethylene glycol to the buffer, these values can be found in Table 1. The effect with the salt increase, however, is minimized with the NaCac & Mg^{2+} buffer due to the $MgCl_2$ stabilizing the complex. Specifically, in 10 mM NaPi increasing the salt concentration to 100 mM NaCl results in a ΔT_M of 11.2°C and $\Delta\Delta H$ of -15 kcal/mol, but when adding ethylene there is a ΔT_M of -2.5°C and $\Delta\Delta H$ of 9.9 kcal/mol. In 10 mM NaCac increasing the salt concentration to 100 mM NaCl results in a ΔT_M of 13.4°C and $\Delta\Delta H$ of -11 kcal/mol and when adding ethylene there is a ΔT_M of -2.6°C and $\Delta\Delta H$ of 10.8 kcal/mol. In 10 mM NaCac & Mg^{2+} increasing the salt concentration to 100 mM NaCl resulted in a ΔT_M of -0.9°C and $\Delta\Delta H$ of -16.5 kcal/mol, but when adding ethylene there is a ΔT_M of -3.7°C and $\Delta\Delta H$ of 15.7 kcal/mol. When comparing the buffer condition for *PsK-IIRNA* with 100 mM NaCl specifically, we can observe that there is a decrease in stability by 2.0 kcal/mol when going from 10 mM NaPi to 10 mM NaCac, but with the addition of $MgCl_2$ into the buffer there is an increase in stability by 3.5 kcal/mol. Again, this observation could be due to differences in hydration levels and Mg^{2+} would help to stabilize the pseudoknot canceling out the decreased stability observed in the 10 mM NaCac buffer.

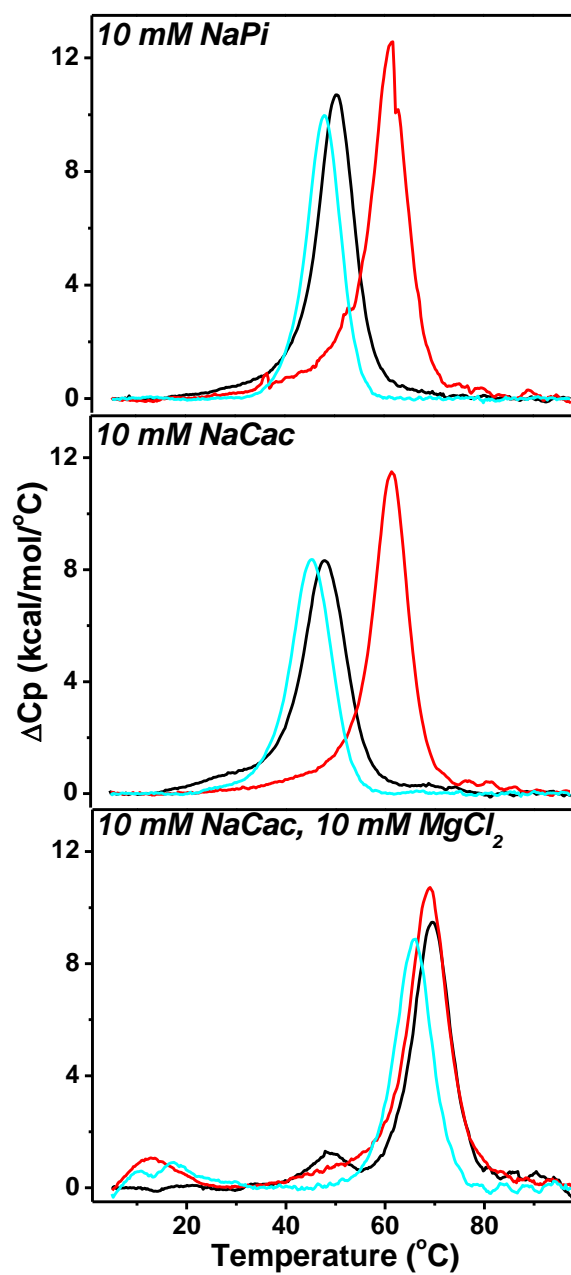


Figure 6. DSC Unfolding of *PsK-11RNA*. 10 mM NaPi, 10 mM NaCac, 10 mM NaCac 10 mM MgCl₂ (Black) with additional 100 mM NaCl (Red) or 2M Ethylene Glycol (Cyan). All experiments were ran at pH 7.0.

Table 3. Thermodynamic Folding Profiles for *PsK-IIRNA*

Buffer	T_M	ΔH_{cal}	$T\Delta S_{cal}$	ΔG°_5
	(°C)	(kcal/mol)	(kcal/mol)	(kcal/mol)
10mM NaPi				
10mM NaPi	50.2	-109	-93.8	-15.2
100mM NaCl	61.4	-124	-103.1	-20.9
2M EG	47.7	-99.1	-85.9	-13.2
10mM NaCac				
10mM NaCac	48.0	-101	-95.3	-14.7
100mM NaCl	61.4	-112	-93.1	-18.9
2M EG	45.4	-90.2	-78.8	-11.4
10mM NaCac, 10mM MgCl₂				
10mM NaCac, 10mM MgCl₂	49.6	-16.7	-14.4	-2.3
	69.4	-97.1	-78.8	-18.3
		-113.8	-93.2	-20.6
100mM NaCl	13.5	-12.3	-11.9	-0.4
	68.5	-118	-96.0	-22.0
		-130.3	-107.9	-22.4
2M EG	15.2	-11.5	-11.1	-0.4
	65.7	-86.6	-71.1	-15.5
		-98.1	-82.2	-15.9

Experimental errors: T_M ($\pm 0.5^\circ\text{C}$), ΔH_{cal} ($\pm 5\%$), $T\Delta S_{cal}$ ($\pm 5\%$), $\Delta G^\circ_{(5)}$ ($\pm 7\%$)

4.4.4 Differential Binding of Na⁺ and Water

We obtained UV melting curves as a function of salt concentration, 16–216 mM of Na⁺, to determine the slope of the T_M -dependences on salt concentration (Figure 7A). This data in combination with the DSC thermograms allows us to determine the differential binding of ions according to Eq. 1. Generally, as the concentration of sodium increases, the helical-coil transitions are shifted to higher temperatures. This is consistent with the stabilizing effect of cations on nucleic acid duplexes due to their larger charge density parameter (134). The resulting Δn_{Na^+} values are summarized in Table 4. When comparing the *PsK-11dT*, *PsK-11dU*, and *PsK-11RNA* we can see that there is an average uptake 3.1 mol Na⁺/mol of ions in the 10mM NaPi and 10mM NaCac buffer at pH 7.0. In the 10mM NaCac, 10mM MgCl₂ buffer there is an average uptake of 0.1 mol Na⁺/mol of ions among the three molecules which indicates that there are little to no uptake.

We also obtained UV melting curves as a function of osmolyte, in this case ethylene glycol concentration was used with concentrations ranging from 0-2.5 M, to determine the slope of the T_M -dependences on water activity (Figure 7B). This data in combination with the DSC thermograms allows us to determine the differential binding of water according to Eq. 2. Generally, as the water activity decreases, the helical-coil transitions are shift to lower temperatures. This is consistent with the stabilizing effect of water on nucleic acid duplexes. The resulting Δn_{W} values are summarized in Table 4. When comparing Δn_{W} in 10mM NaPi and 10mM NaCac for *PsK-11dT* there is a similar uptake of 25 mol H₂O/mol. *PsK-11dU* has a similar trend, but a lower uptake with an average of 17.5 mol H₂O/mol. This decrease in water immobilization can be due to the lack of the methyl group on the dU, which would in turn decrease the water interaction from the loop

in the major groove. In 10 mM NaCac & Mg²⁺ there is an increase in water uptake by 30 and 15.5 mol H₂O/mol in *PsK-11dT* and *PsK-11dU*, respectively. This can be rationalized by the addition of Mg²⁺ in the solvent having a larger hydration shell and interaction with the DNA increasing the hydration level. *PsK-11RNA* shows a different trend with an increasing uptake of water as the buffer changes going from 21 mol H₂O/mol to 42 mol H₂O/mol, Table 4. When comparing *PsK-11dT* and *PsK-11RNA*'s we observe that there is a decrease in water immobilization, similar to previous hydration studies (142).

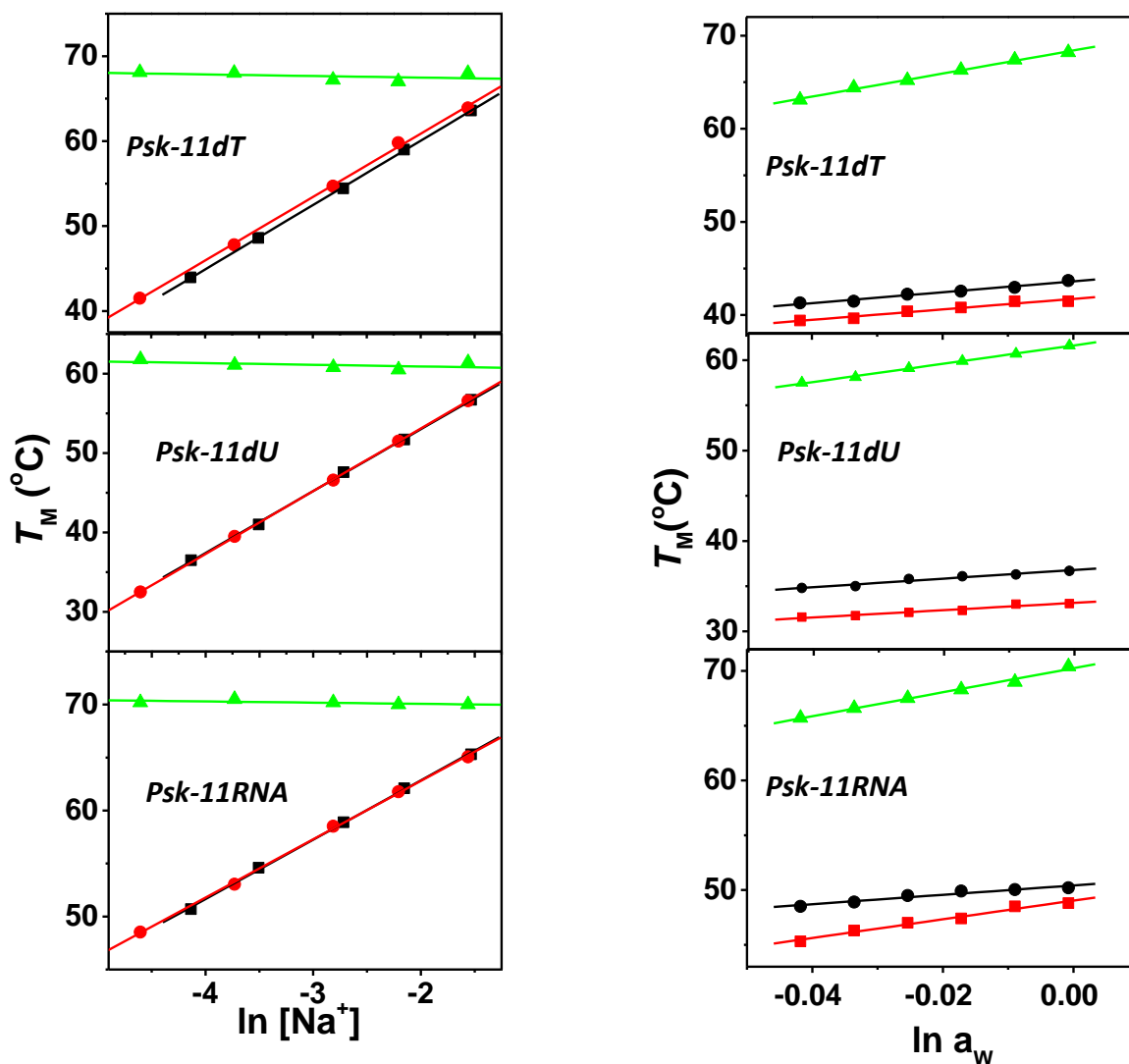


Figure 7. A) T_M dependence on salt concentration. All experiments were done in 10 mM sodium phosphate buffer with increasing salt concentrations, pH 7.0; T_M (± 0.5 °C), Δn_{Na^+} ($\pm 7\%$). B) T_M dependence on water activity. All experiments were done in 10 mM sodium phosphate buffer with increasing osmolyte concentration, pH 7.0; T_M (± 0.5 °C), Δn_w ($\pm 7\%$). ● 10 mM NaPi; ■ 10 mM NaCac; ▲ 10 mM NaCac, 10 mM MgCl₂

Table 4. Ion and Water Uptake for Pseudoknots

Buffer	Δn_{Na^+}	Δn_{W}
<i>PsK-11dT</i>		
NaPi	-3.1	-25
NaCac	-3.3	-25
NaCac & Mg²⁺	0.1	-55
<i>PsK-11dU</i>		
NaPi	-3.1	-18
NaCac	-3.0	-17
NaCac & Mg²⁺	0.1	-33
<i>PsK-11RNA</i>		
NaPi	-3.2	-21
NaCac	-3.0	-39
NaCac & Mg²⁺	0.1	-42

All experiments were done in 10 mM sodium phosphate buffer, pH 7.0 Δn_{Na^+} ($\pm 7\%$), Δn_{W} ($\pm 7\%$).

4.5 CONCLUSIONS AND FUTURE DIRECTIONS

In this chapter, we used a set of oligonucleotides to determine solvent effects between DNA, dU substituted, and RNA molecules. We used a pseudoknot containing a loop complementary to the core sequence of the duplex stem which we previously found the DNA sequence to form base-triplets to increase the stability of the pseudoknot. Our question is if this particular set of pseudoknots can still form base-triplets stacks with the dU substitutions and with the RNA equivalent sequence and if solvent conditions will have an overall effect on the stability of the molecule.

The first observation is that all molecules are able to form intramolecular pseudoknots and their transition temperatures remain constant under each buffer condition. Also, *PsK-11dT* and *PsK11dU* form in the “B” conformation and *PsK-11RNA* forms in the “A” conformation, which is typical for DNA and RNA molecules. We did find for *PsK-11RNA* the addition of Mg^{2+} to the buffer improved the base-pair stacking, which was confirmed by an increase in the intensity of the lower CD band. In all of the buffer conditions used *PsK-11dU* was the most unstable molecule followed by *PsK-11dT* and *PsK-11RNA* was the most stable molecule. The higher enthalpy contributions observed in 100 mM NaCl correspond to the formation of ~2 base-triplet stacks. The destabilizing effect observed from the dU loop substitution is due to the formation of weaker TAU/TAU base-triplet stacks and the higher stability of *PsK-11RNA* is explained in terms AA/UU base-pair stacking being less stable than AA/TT, therefore stronger UAU base-triplets would form and *PsK-11RNA* (143) also has a higher predicted ΔG based on nearest-neighbor calculations due to the other stem of the pseudoknot. We did find the thermodynamic contributions are buffer dependent. There was a decrease in the stability

of all of the molecules when going from 10 mM NaPi to 10 mM NaCac and the addition of Mg^{2+} is an important factor because there is an increase in stability when compared with both 10 mM NaPi and 10 mM NaCac buffers.

Overall, this investigation confirms oligos with DNA sequences are flexible enough to form pseudoknots; therefore, they can be used to mimic known RNA secondary structures. In particular, we were able to show the formation of local base-triplets in both the DNA and RNA pseudoknots under three buffer conditions and that it is important to consider the buffer you run experiments when working with nucleic acids. It is also very important to consider the buffer that has been used when comparing data in the field because based on these results there is a significant differences in the overall thermodynamic profiles depending on the solvent conditions of the experiment. To give additional insight into the hydration levels between the buffers conditions and DNA/RNA it would be important to run experiments investigating the volume changes between *PsK-11dT*, *PsK-11dU*, and *PsK-11RNA*.

CHAPTER FIVE

CONTRIBUTIONS OF THE LOOPS ON THE TARGETING OF DNA PSEUDOKNOTS

5.1 SUMMARY

We have investigated the targeting of two pseudoknots with loops complementary to the core stem. We have used a combination of ITC and DSC to determine thermodynamic profiles for the reaction of two pseudoknots with their complementary strands. The reaction enthalpy was first measured directly by isothermal titration calorimetry and then compared with the reaction enthalpy measured indirectly using differential scanning calorimetry by creating thermodynamic (Hess) cycles that correspond to each of the targeting reactions. These thermodynamic profiles indicate favorable reaction free energy contributions that were enthalpy driven. However, the disruption reaction of *PsK-9* took place with a less favorable free energy term, by 0.7 kcal/mol, and less favorable enthalpy term, by 4.5 kcal/mol. Analysis of the differential scanning calorimetry curves shows *PsK-9* to be more stable, by -5.7 kcal/mol, and unfolds with a higher enthalpy of 27.4 kcal/mol due to the involvement of two loop thymines forming one TAT/TAT base-triplet stack, in the stem of this pseudoknot. Again, when examining the targeting reactions indirectly by DSC each reaction was favorable and enthalpy driven; disruption of *PsK-9* took place with a less favorable free energy term by 1.6 kcal/mol and a less favorable enthalpy term by 11.5 kcal/mol. The main observation is that that each complementary strand is able to disrupt the pseudoknots. However, the disruption of *PsK-9* takes place with a less favorable free energy contribution, confirming the formation of local base-triplets.

5.2 INTRODUCTION

Oligonucleotides (ODNs) may be used for the control of gene expression due to their exquisite selectivity and their ability to discriminate targets that differ by a single base (27), (28), (123), (144). In the successful targeting of nucleic acids it is important that the structure of the target is known. This, however, is usually not the case, but if the sequence is known the secondary structure can be predicted (145). From this secondary structure the target strands can be designed to target the structures within with unpaired bases to drive the reaction forward because the strand must be able to invade and disrupt the secondary structure forming to form a larger number of base-pair stacks in the duplex products. Our laboratory is using DNA oligonucleotides to mimic the secondary structures of RNA molecules and their targeting with complementary strands to create a library of thermodynamic targeting data (116-118). The novelty of this approach is several fold, DNA oligonucleotides are less expensive than RNA oligonucleotides and more stable against hydrolysis, and most important the resulting DNA-DNA thermodynamic data is similar to the DNA-RNA thermodynamic data, in terms of nearest-neighbor contributions (98), (129), (130), which is obtained in the targeting of RNA molecules with DNA complementary strands.

A specific stem-loop motif worth investigating is pseudoknots due to the fact that they are an interesting and diverse RNA structural motif, due to variation in their loop lengths and stems and the types of interactions between them. Pseudoknots also have diverse roles in biological function; examples include forming the catalytic core of various ribozymes (40-42), self-splicing introns (39), telomerase (37), (38), riboswitches (45), and ribosomal frameshifting (43), (44). The targeting of pseudoknots with nucleic

acid ODNs may also stop their biological regulation (65), (116-117), (144), (146). Pseudoknots are an important structure with various roles as listed above which is why they are an important structure to understand the targeting reaction properties. However, there are some disadvantages in their targeting that could arise: they are very compact molecules; the loops could be interacting with other molecules; and they could be hard to reach sometimes being located in the center of a structure (147), (148). These are all important things to consider, but first it is important to understand the physio-chemical properties of pseudoknots and their targeting reactions.

In this work, we have designed a pair of DNA pseudoknots with different length in one of the loops to mimic the formation of a local triple helix shown within RNA pseudoknots. We have used ITC and DSC to determine thermodynamic profiles to investigate the targeting reaction of these pseudoknots with their complementary strands. The results show that the pseudoknot with the longer loop is more stable, due to the lower free energy obtained in the targeting of this pseudoknot by both techniques. This also confirms the formation of local base-triplets in *PsK-9* due to the stem-loop complementarity.

5.3 METHODS

The 5'-3' sequences of oligonucleotides (ODNs) are as follows: d(TCTCT- T_5 AAAAAAAAAGAGAT T_5 TTTTTTT) and d(TCTCTT T_9 AAAAAAAAAGAGAT T_5 -TTTTTTT), T_5 and T_9 are loops of 5 and 9 thymines, respectively; and complementary strands, d(CTTTTTTTTAAAAAAGAGA) and d(CTTTTTTTTAAAAAAAAAAGAGA). ODNs were synthesized by Integrated DNA Technologies, Inc. (Coralville, IA), purified by reverse-phase HPLC, and desalted by gel permeation chromatography using a G-10 Sephadex column. Figure 1 shows the putative secondary structures and designations of pseudoknots, complementary strands and resulting duplexes. The ODN concentrations were determined at 260 nm and 90°C using the following molar extinction coefficients ($\text{mM}^{-1}\text{cm}^{-1}$), obtained from the nearest-neighbor model (96) (130): 331.1 (*PsK-5*), 180.6 (*CS-5*), 255.9 (*PsKDup-5*), 366.6 (*PsK-9*), 236.9 (*CS-9*) and 301.8 (*PsKDup-9*). All experiments were carried out in 10 mM sodium phosphate, 100 mM NaCl buffer at pH 7.0. All oligonucleotides were prepared by dissolving dry and desalted ODNs in buffer.

Isothermal titration calorimetry (ITC). The heat for the reaction of a pseudoknot with its complementary strand was measured directly by isothermal titration calorimetry using the ITC₂₀₀ from GE Microcal (Northampton, MA). A 40 μL syringe was used to inject the titrant; mixing was effected by stirring this syringe at 1000 rpm. Typically, we used 5-7 injections of 2 μL of pseudoknot solution with at least 2-fold lower concentration than the solution of the complementary strand in the cell, and over a time of 4-8 minutes between injections. The reaction heat of each injection is measured by integration of the area of the injection curve, corrected for the dilution heat of the titrant,

and normalized by the moles of titrant added to yield the reaction enthalpy, ΔH_{ITC} (115-118). ITC experiments were designed to obtain the heat, ΔH_{ITC} , for each targeting reaction by averaging the reaction heat of at least five injections under unsaturated conditions. These ΔH_{ITC} terms correspond to the formation of duplex products. To determine the free energy, ΔG_{ITC} , for each targeting reaction, we use the following relationship, $\Delta G_{ITC} = \Delta G_{HC} (\Delta H_{ITC}/\Delta H_{HC})$ (116-118), while the Gibbs equation is used to determine the $T\Delta S_{ITC}$ parameter, where T is the temperature of the ITC experiments.

Temperature-Dependent UV Spectroscopy. Absorbance versus temperature profiles were measured at 260 nm with a thermoelectrically controlled Aviv Spectrophotometer Model 14DS UV-Vis (Lakewood, NJ). The temperature was scanned at a heating rate of 0.6 °C/min, and shape analysis of the melting curves yielded transition temperatures, T_{MS} (98). The transition molecularity for the unfolding of a particular complex was obtained by monitoring T_M as a function of the strand concentration. Intramolecular complexes show a T_M -independence on strand concentration, while the T_M of intermolecular complexes does depend on strand concentration (129).

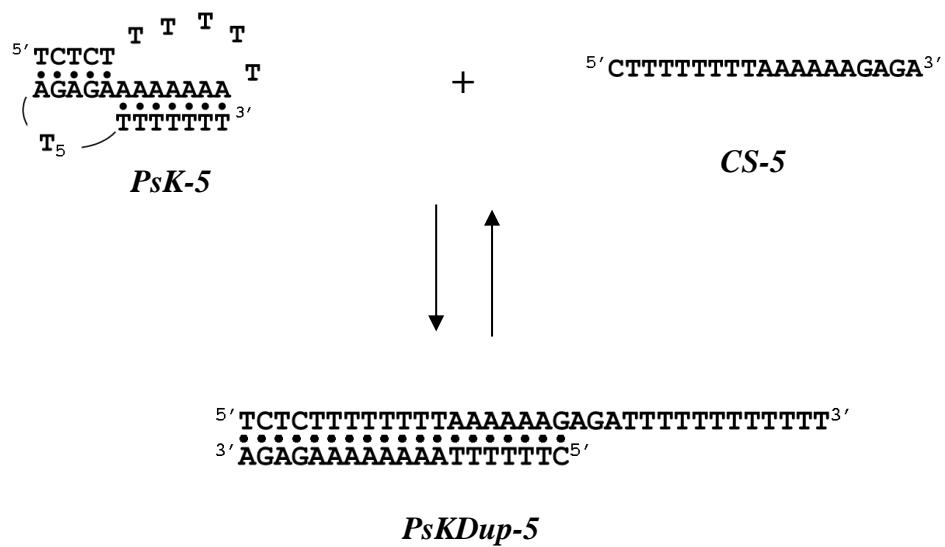
Differential scanning calorimetry (DSC). The total heat required for the unfolding of each oligonucleotide (pseudoknot, single strand or duplex product) was measured with a VP-DSC differential scanning calorimeter from Microcal (Northampton, MA). Standard thermodynamic profiles and T_{MS} are obtained from the DSC experiments using the following relationships (Marky L. a., 1987), (Marky L. M., 2007): $\Delta H = \int \Delta C_p(T) dT$; $\Delta S = \int \Delta C_p(T)/T dT$, and the Gibbs equation, $\Delta G^\circ_{(T)} = \Delta H - T\Delta S$; where ΔC_p is the anomalous heat capacity of the ODN solution during the unfolding process, ΔH and ΔS are the

unfolding enthalpy and entropy, respectively, assumed to be temperature-independent.

$\Delta G^\circ(T)$ is the free energy at a temperature T .

Overall experimental protocol. ITC titrations are used to measure directly the heat (ΔH_{ITC}) of each targeting reaction. We then characterized the helix-coil transition of each pseudoknot as a function of strand concentration. DSC experiments were carried out to determine T_{MS} and unfolding thermodynamic profiles for each reactant (pseudoknot and complementary strand) and product (duplex) of the targeting reaction (98, 129). The DSC data is used to set up Hess cycles, Figure 2, to yield thermodynamic profiles for these reactions and to compare the enthalpies (ΔH_{HC}) with those obtained from ITC (ΔH_{ITC}). This enthalpic ratio, $\Delta H_{\text{HC}} / \Delta H_{\text{ITC}}$, is used to determine ΔG_{ITC} (116-118).

Reaction 1:



Reaction 2:

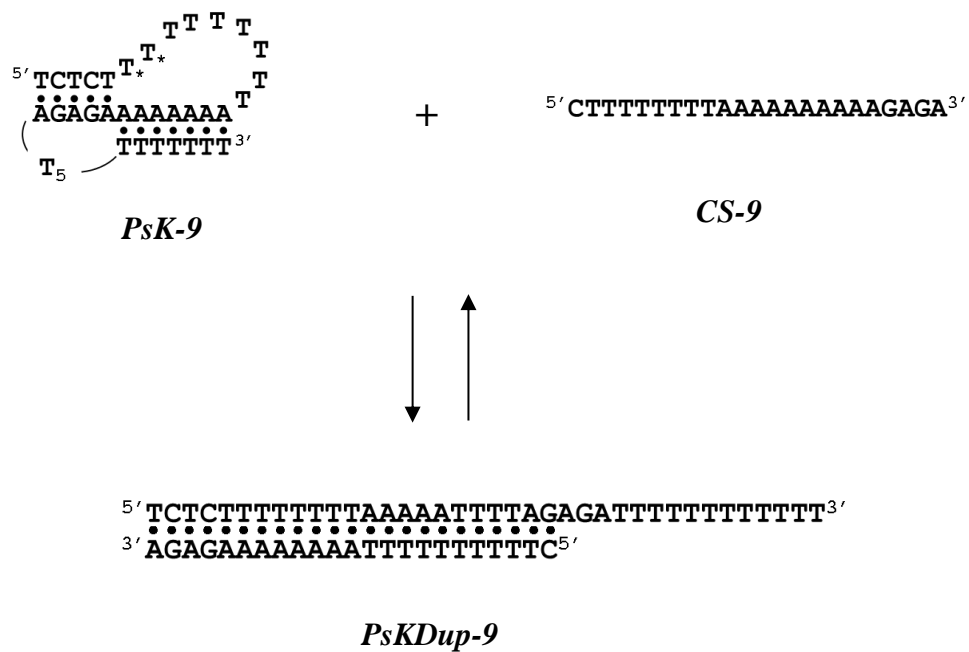


Figure 1. Reactions Investigated

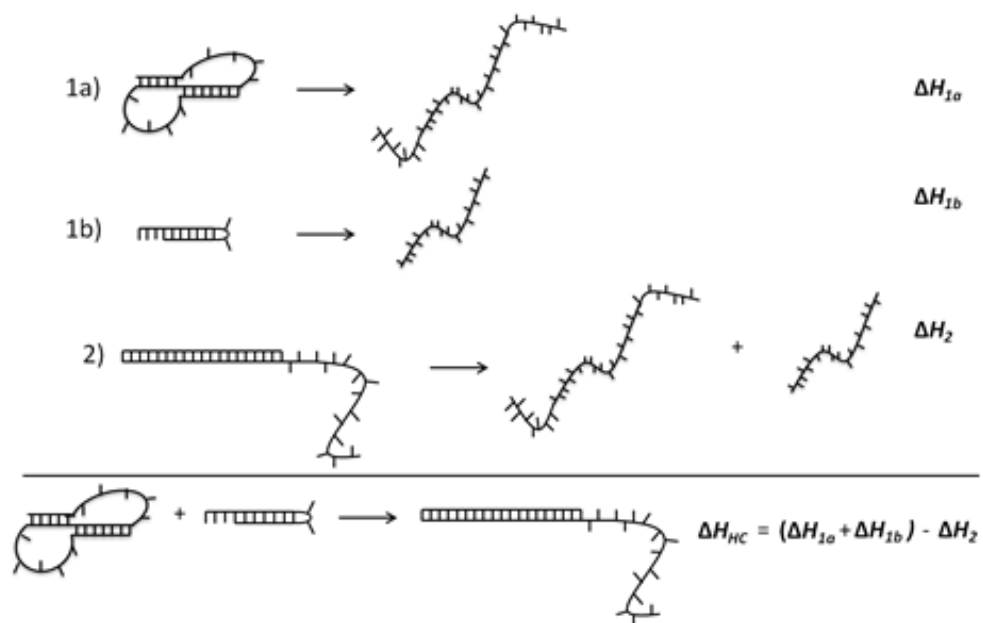


Figure 2. Hess Cycle

5.4 RESULTS

5.4.1 Targeting of Pseudoknots with Complementary Strands

To confirm *PsK-9* is forming a more compact pseudoknot, we investigated the reaction of each pseudoknot with its corresponding complementary strand to form duplex products with dangling ends:



Each reaction was investigated in two ways: a) directly by measuring reaction enthalpies using ITC techniques, and b) indirectly by determining unfolding thermodynamic profiles for the reactants and products of each targeting reaction.

5.4.2 Targeting Reactions Measured Directly by ITC Techniques

The heat for each targeting reaction was measured by ITC under unsaturated conditions, using ODN concentrations and temperatures that guaranteed 100% formation of the final duplex products. ITC titrations were carried out at 5°C, the heat of each injection was corrected for its dilution heat and normalized by the concentration of the limiting reagent to yield reaction enthalpies, ΔH_{ITC} . The ITC titrations are shown in Figure 3A (*PsK-5*) and Figure 3B (*PsK-9*), the shape of these curves show that the initial enthalpies are more exothermic, -32.0 kcal/mol and -33 kcal/mol, and gradually reaching a plateau at -27.3.0 kcal/mol and -21.2 kcal/mol, respectively. The net exothermicity of these enthalpy values corresponds to a complete override of the endothermic heat contributions (disruption of the base-pair stacks of both pseudoknot and hairpin loop) by the exothermic heat contributions (formation of base-pair stacks of the duplex product). An extra exothermic/endothermic term should be included due to hydration changes from

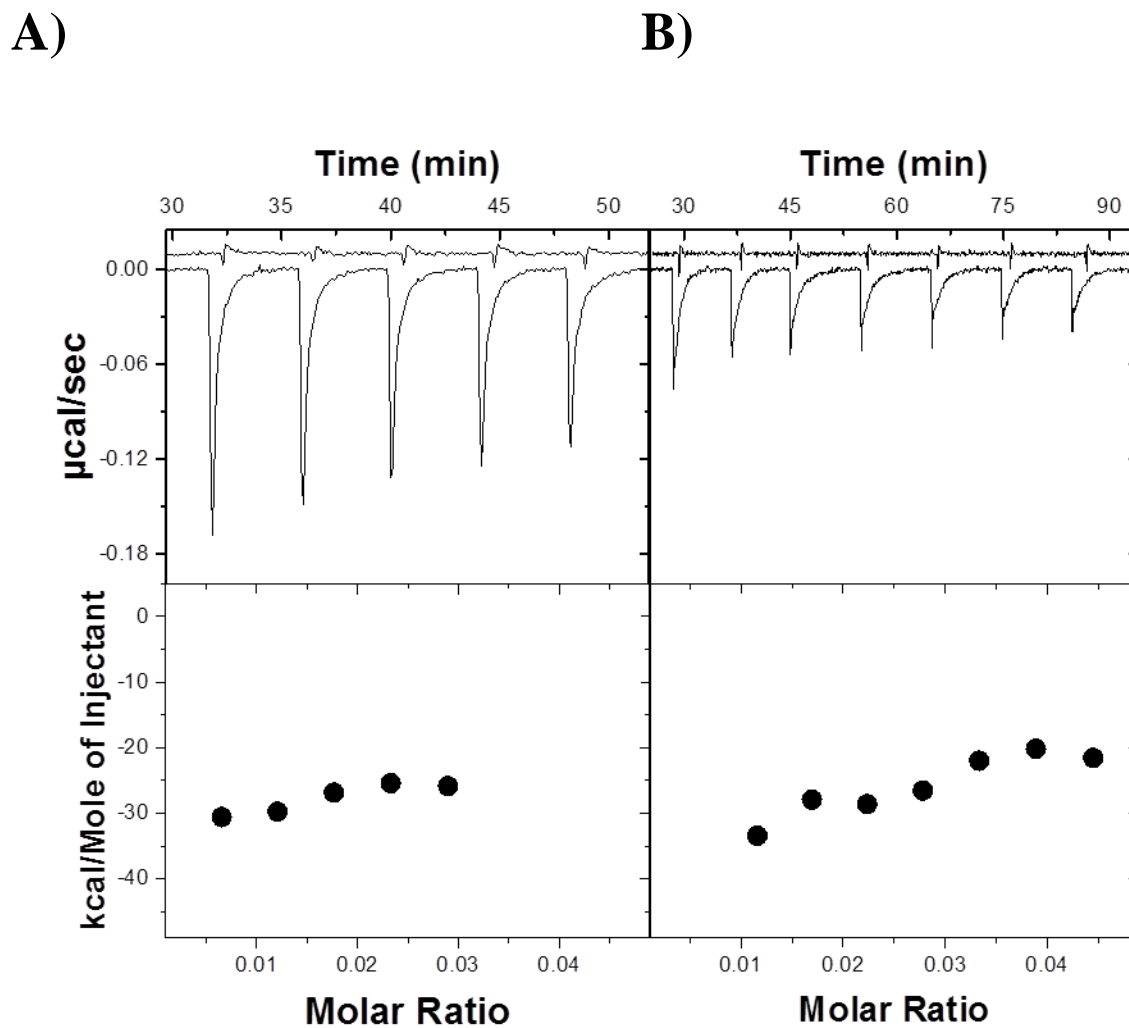


Figure 3. Targeting Reactions. A) ITC injections of *PsK-5* (0.065 mM) into *CS-5* (0.123 mM). Also shown are the dilution heats of *PsK-5* into buffer. B) ITC injections of *PsK-9* (0.067 mM) into *CS-9* (0.128 mM). Also shown are the dilution heats of *PsK-9* into buffer. All experiments performed in 10 mM NaPi, 100 mM NaCl at pH 7.0.

the participating reaction species, which may be accounted for the variability of the reaction enthalpies in these titrations. The resulting ΔH_{ITCS} for these injections are -28.2 ± 1.4 kcal/mol (*PsKDup-5*) and -23.7 ± 1.2 kcal/mol (*PsKDup-9*). These values will be later compared with enthalpies obtained indirectly by DSC, Table 2.

5.4.3 Unfolding Thermodynamics of Pseudoknots

Figure 4A shows typical UV melting curves for the helix-coil transition of each pseudoknot, their sigmoidal behavior is characteristic of the temperature-induced unfolding of a nucleic acid oligonucleotide. The T_M dependences on strand concentration are shown in Figure 4B, the T_M remains constant for each pseudoknot, indicative of their intramolecular formation at low temperatures. The DSC curves of each pseudoknot are shown in Figure 4C and the resulting thermodynamic profiles are shown in Table 1. Each curve shows slightly asymmetric peak, which is not consistent with the unfolding of an intramolecular complex. This observation may be explained in terms of loop constraints on the pseudoknot stems, which reduces favorable stacking contributions. The overall effect is most noticeable with *PsK-5*, which actually shows a small shoulder at around 37°C. We obtained unfolding enthalpies of 60.1 kcal/mol (*PsK-5*) and 87.5 kcal/mol (*PsK-9*), while an unfolding enthalpy of 69.4 kcal/mol was obtained for a duplex (^{5'}-TCTCTTTTTTTT/^{5'}-TTAAAAAAAGAGATT) with sequence similar to their stem and with two thymines flanking each end. This enthalpy comparison shows that the loops of *PsK-5* are constrained while the longer loop of *PsK-9* is actually releasing this tension. However, the main observation is *PsK-9* unfolds with a higher T_M , by 6.5 °C, and higher

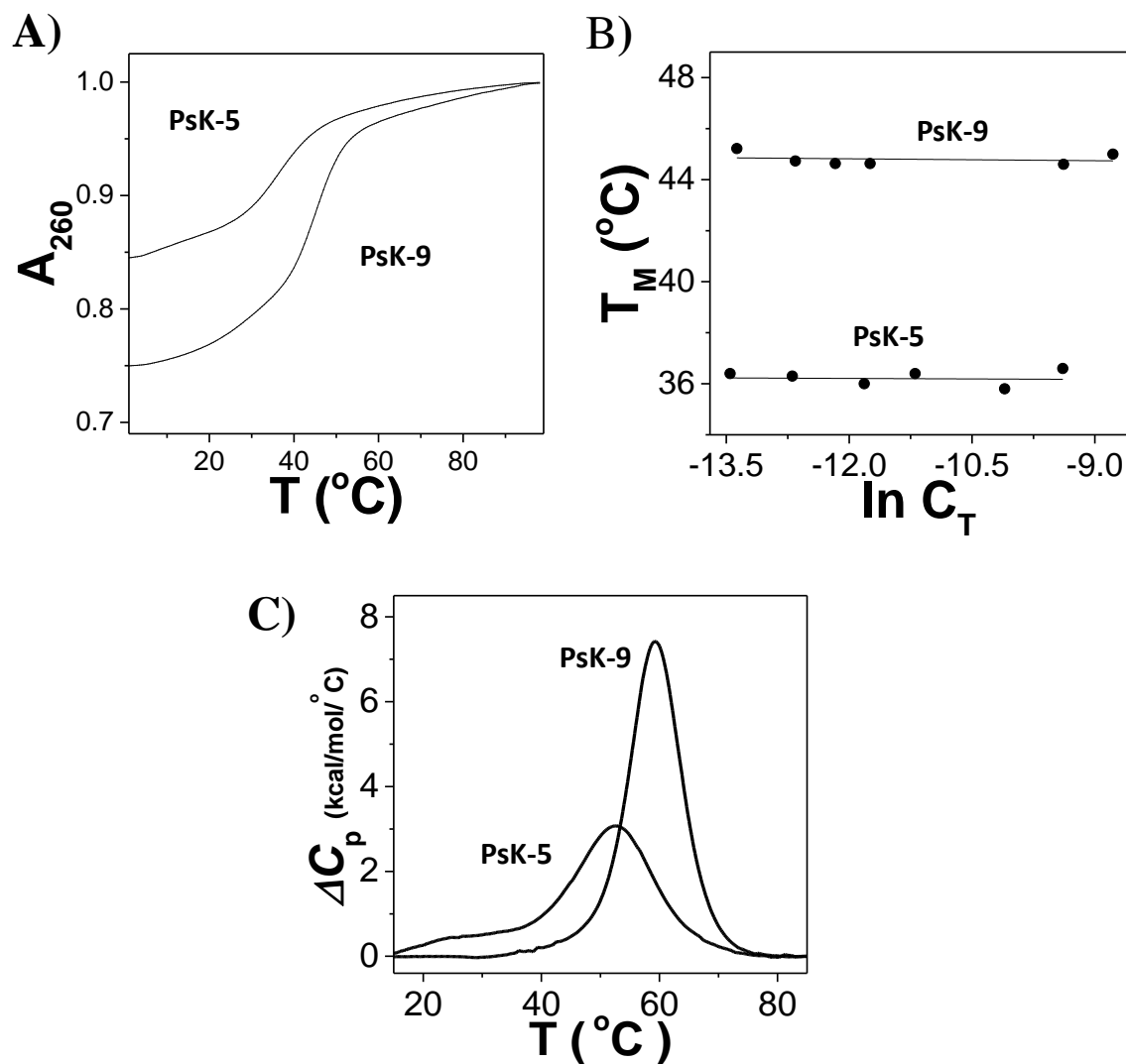


Figure 4. Melting curves for pseudoknots. A) UV curves showing concentration independence for *PsK-5* and *PsK-9*. B) $\ln C_T$ plots to determine concentration dependence on T_M . C) DSC curves for *PsK-5* (0.126 mM) and *PsK-9* (0.120 mM). UV experiments were carried out in 10mM NaPi and DSC experiments were carried out in 10mM NaPi, 100mM NaCl buffer at pH 7.0.

Table 1. Unfolding Thermodynamic profiles.

Transition		T_M (°C)	ΔH_{cal} (kcal/mol)	$T\Delta S_{cal}$ (kcal/mol)	ΔG°_5 (kcal/mol)
<i>PsK-5</i>		52.8	60.1	51.6	8.5
<i>CS-5</i>		47.9	38.4	33.3	5.1
<i>PsKDup-5</i>		49.6	135	116	18.7
<i>PsK-9</i>		59.3	87.5	73.3	14.2
<i>CS-9</i>		48.6	48.5	41.9	6.6
<i>PsKDup-9</i>	1 st	47.7	59.2	51.3	7.9
	2 nd	58.3	102	85.6	16.4
Total			161	137	24.3

All experiments were done in 10 mM sodium phosphate buffer and 100 mM NaCl at pH 7.0. Experimental errors are as follows: T_M (± 0.5 °C), ΔH° (± 5 %), $T\Delta S$ (± 5 %), $\Delta G^\circ_{(5)}$ (± 7 %). Thermodynamic profiles for the unfolding of the putative structures of the targeting single strands are included.

unfolding enthalpy, by 27.4 kcal/mol when compared to *PsK-5* (Table 1) and 18.1 kcal/mol when compared to the control duplex. This indicates that *PsK-9* is more stable with improved base-pair stacks. This additional heat suggests that the 9 thymine loop of *PsK-9* being located in the ceiling of the major groove of its 7 A•T stem, and two of the thymines are involved in the formation of two T•A•T base-triplets (or one T•AT/T•AT base-triplet stack) (24), (149). Overall, the unfolding of each pseudoknot takes place through the typical unfavorable enthalpy-favorable entropy compensation. Unfavorable enthalpy contributions correspond to energy needed to break base pairing and base-pair stacking interactions, while favorable entropy contributions correspond to the higher disorder state of the single strand at high temperature and the putative release of ions and water molecules (116-118), (150). In summary, the folding of *PsK-9* is thermodynamically more stable than *PsK-5* (reverse signs of Table 1), by -5.7 kcal/mol, resulting in a more compact molecule.

5.4.4 Unfolding Thermodynamics for the Species of Each Targeting Reaction

Figure 5 shows the DSC thermograms of each pseudoknot, complementary strand, and duplex product, and Table 3 has the resulting thermodynamic profiles from the analysis of these thermograms. The DSC of each pseudoknot was discussed earlier; their unfolding curves are included in this figure for clarity and for explaining the unfolding of each product duplex. The DSC of each single strand shows monophasic transitions with T_{MS} and ΔH_s of 47.9°C, 38.4 kcal/mol (*CS-5*) and 48.6°C, 48.5 kcal/mol (*CS-9*), respectively. UV melting experiments as a function of strand concentration (data not shown) show their

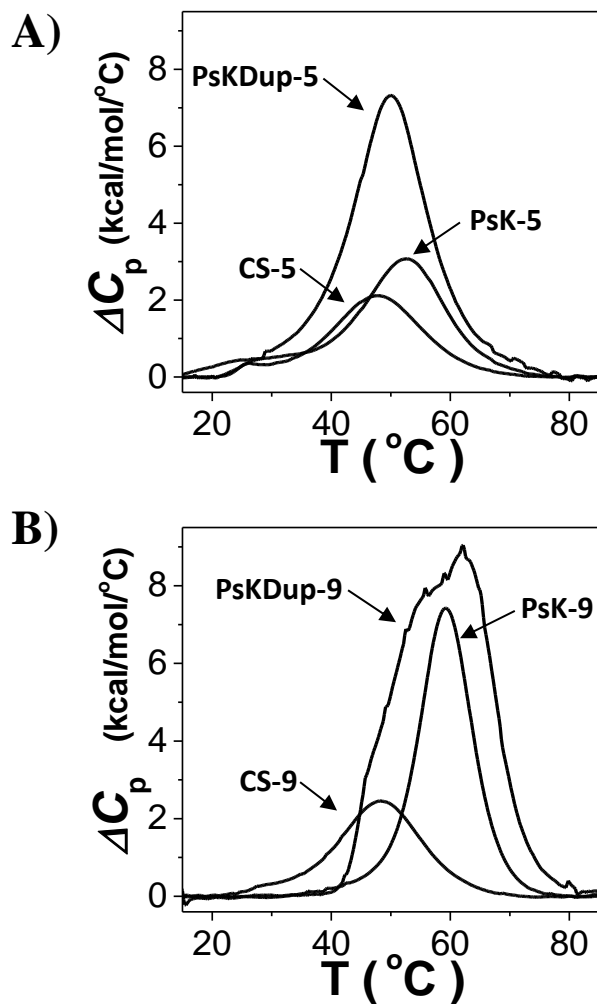


Figure 5. DSC curves for pseudoknots, complementary strands and duplexes. A) DSC curves of *PsK-5* (0.126 mM), *CS-5* (0.182 mM) and *PsKDup-5* (0.039 mM). B) DSC curves for *PsK-9* (0.120 mM), *CS-9* (0.136 mM) and *PsKDup-9* (0.025 mM). All experiments were carried out in 10mM NaPi, 100mM NaCl at pH 7.0.

T_{MS} remain constant, indicating their intramolecular formation. Based on their sequence, magnitude of their enthalpies, and assuming an enthalpy of 7-8 kcal per mol of base-pair stack, these single strands are forming hairpin loops with dangling ends and with 5 (*CS-5*) and 6 (*CS-9*) base-pair stacks in their stems.

The DSC curves of each product duplex (Figure 5) show *PsKDup-5* unfolds in an apparent monophasic transition with a T_M of 49.6°C and ΔH of 135 kcal/mol, while *PsKDup-9* unfolds in a biphasic transition with T_{MS} of 47.7 °C and 58.3 °C and total ΔH of 161 kcal/mol. Each DSC profile corresponds to the unfolding of the duplex followed by the folding and sequential unfolding of the corresponding pseudoknot and hairpin (single strands). For instance, the monophasic unfolding of *PsKDup-5* is due to the similar T_{MS} of the structures formed by the reactants and product of this reaction, which are within 5°C. On the other hand, *PsKDup-9* shows a biphasic transition (Figure 5B), the first transition corresponds to the unfolding of the duplex into partially folded *PsK-9* and *CS-9*, followed by the simultaneous unfolding of molecules. The higher ΔH term of *PsKDup-9*, by 26 kcal/mol, corresponds to the formation of three additional base-pair stacks.

We created Hess cycles with this unfolding data to generate indirectly thermodynamic profiles for each targeting reaction i.e., we added the thermodynamic profiles of the pseudoknot and single strand (hairpin), and subtracted the thermodynamic profiles of the duplex. The resulting data is shown in Table 2. This exercise yielded ΔG°_{HC} and ΔH_{HC} of -5.1 kcal/mol & -37 kcal/mol (*PsK-5*), and -3.5 kcal/mol & -25 kcal/mol (*PsK-9*), respectively. Both reactions are favorable and enthalpy driven. However, the targeting of *PsK-9* is less favorable, which is consistent with the higher

Table 2. Thermodynamic Profiles for the Targeting Reactions: Formation of Duplex Products

	ΔH_{HC} (kcal/mol)	$\Delta G^{\circ}_{\text{HC}}$ (kcal/mol)	$T\Delta S_{\text{HC}}$ (kcal/mol)	ΔH_{ITC} (kcal/mol)	$\Delta G^{\circ}_{\text{ITC}}$ (kcal/mol)	$T\Delta S_{\text{ITC}}$ (kcal/mol)
<i>PsKDup-5</i>	-36.5	-5.1	-31.4	-28.2	-3.9	-24.3
<i>PsKDup-9</i>	-25.0	-3.5	-21.7	-23.7	-3.2	-20.5

All experiments were done in 10 mM sodium phosphate buffer and 100 mM NaCl at pH 7.0. Experimental errors are as follows: ΔH_{HC} ($\pm 10\%$), $T\Delta S_{\text{HC}}$ ($\pm 10\%$), $\Delta G^{\circ}_{\text{HC}}$ ($\pm 14\%$), ΔH_{ITC} ($\pm 5\%$), $\Delta G^{\circ}_{\text{ITC}}$ ($\pm 7\%$).

stability of this pseudoknot. Furthermore, we obtained unfavorable $T\Delta S_{\text{HC}}$ terms of -31.4 (*PsK-5*), and -21.7 kcal/mol (*PsK-9*), which correspond to the net uptake of ions and water molecules by the duplex products of each reaction, since the conformational entropy change is considered similar for each reaction. When comparing these ΔH_{HC} s with those obtained directly from ITC we observe an enthalpy difference of -8 kcal/mol (*PsKDup-5*) and -1.3 kcal/mol (*PsKDup-9*). While these values are in good agreement, potential differences could come from the exclusion of heat capacity effects and/or base-base interactions in the complementary strand (151).

5.4.5 Determination of Targeting Free Energy

The ΔG°_{ITC} at 5°C for each targeting reaction were obtained from the ΔG°_{HC} values by using an enthalpy factor ($= \Delta H_{ITC}/\Delta H_{HC}$), that comes from temperature differences, which assumes ΔH_{HCS} to be independent of temperature i.e., $\Delta C_p = 0$. The $T\Delta S_{ITC}$ parameters were calculated using the Gibbs equation. We obtained favorable ΔG°_{ITC} contributions for each targeting reaction, i.e. each complementary strand is able to invade and disrupt the pseudoknot structure. *PsKDup-5* and *PsKDup-9* having a ΔG°_{ITC} of -3.9 and -3.2 kcal/mol, respectively. These values are in good agreement with those obtained indirectly from DSC, Table 2. The reaction for the targeting of *PsK-9* is less favorable in spite of forming a more stable duplex, by 0.7 kcal/mol. This result is consistent with the higher stability *PsK-9* and confirms the formation local base-triplets in the stem of *PsK-9* consistent of two T*A•T base-triplets (or one T*AT/T*AT base-triplet stack).

5.5 CONCLUSIONS AND FUTURE DIRECTIONS

We have investigated the thermodynamic stability of two pseudoknots to determine the formation of local base-triplets in the pseudoknot with a longer thymine loop. Specifically, we used a combination of ITC and DSC techniques to thermodynamically characterize the targeting reaction of two pseudoknots with their complementary strands. The favorable folding of DNA pseudoknots results from the typical favorable enthalpy-unfavorable entropy compensation, confirming the flexibility of DNA strands being able to form pseudoknots that can be used to mimic known RNA secondary structures. The folding data shows that *PsK-9* is more stable due to a more

favorable enthalpy. This enthalpy value corresponds to the partial folding of the thymine loop (third strand) on the major groove of the duplex, yielding a net formation of one T*AT/T*AT base-triplet stack at the middle of its stem. The targeting thermodynamic data indicated that each complementary strand is able to disrupt the pseudoknots. However, the disruption of *PsK-9* takes place with a less favorable free energy contribution, confirming the formation of local base-triplets.

The main observation from this study is that local base-triplets are able to form in the pseudoknot if the loop length and sequence are appropriate. The favorable targeting of these pseudoknots depends on the length and sequence of the complementary strand. However, the favorable free energy term of these targeting reactions may well be increased by improving the stability of the duplex products, by using longer single strands with complementary sequences and/or DNA intramolecular structures with loops containing a larger number of un-paired bases. In general, the higher the number of base-pairs and base-pair stacks that are formed in the duplex product, the higher the free energy term; specifically, if a larger number of unpaired bases are involved in this base-pairing. This investigation of the targeting of DNA pseudoknots has enabled us to improve our method, based on physico-chemical principles, to determine the thermodynamics of the targeting of nucleic acid secondary structures that can be used to control the expression of genes.

Future Directions of this work would include the targeting reactions of the pseudoknots discussed in Chapter One including: *PsK-9-6AT* along with *PsK-5-1CGC*, *PsK-5-2CGC*, *PsK-9-1CGC*, *PsK-9-2CGC* which have TAT→CGC substitutions.

CHAPTER SIX

KINETIC CHARACTERIZATION OF DNA PSEUDOKNOT TARGETING BY SURFACE PLASMON RESONANCE

6.1 SUMMARY

We have investigated kinetic parameters, k_{on} and k_{off} , for the reactions of pseudoknots with complementary strands. Specifically, we have used SPR to measure these kinetic rates as a function of target strand length. The kinetic results $K_{D\ app.} = k_{off}/k_{on}$ are compared with DSC profiles. *PsK-5* with 5 free thymines in its loop was targeted with three target strands with 10, 13, and 19 nucleotides and had k_{on} rates of 7.49×10^5 , 1.67×10^3 and 1.42×10^3 1/Ms at 20°C, respectively. Their k_{off} rates were 3.37×10^{-3} , 8.02×10^{-3} , and 1.11×10^{-2} 1/s. For *PsK-5* there is a decrease in the association rate as the length of the target strand increases and also an increase in the dissociation rate, based on this and the $K_{D\ app.}$ values becoming less favorable from 4.5×10^{-9} to 4.5×10^{-7} M. Overall, the targeting reaction becomes less favorable as the target strand increases in length. This same trend was observed with *PsK-9* when targeted with strands of 14, 17, and 23 nucleotides in length. The k_{on} rates decreased from 7.76×10^4 to 6.29×10^3 1/Ms and the k_{off} rates also increased from 5.4×10^{-4} to 1.67×10^{-3} 1/s when increasing the target strand length from 14 to 23 nucleotides. These $K_{D\ app.}$'s ranged from 6.7×10^{-9} to 2.3×10^{-7} M. *PsK-11* followed this trend when it came to k_{on} rates with target strands lengths of 16 and 19 nucleotides having rates of 1.26×10^6 and 6.97×10^5 1/Ms. The k_{off} rates remained similar, but increased slightly, 1.88×10^{-3} to 1.26×10^{-3} 1/s. This resulted in $K_{D\ app.}$ values of 1.5 - 1.8×10^{-9} M. We also found an average activation energy of 12 kcal/mol for *PsK-11*'s targeting reactions by running this reaction at two different temperatures.

The DSC unfolding for the targeting reactions showed a similar trend for all of the pseudoknot's reactions where there is an increase in the $K_{D \text{ DSC}}$, meaning a decrease in the affinity of the targeting strand with an increase in the strand length. For *PsK-5*, we see an increase in the $K_{D \text{ DSC}}$ values from 7.6×10^{-2} to 1.73×10^2 . *PsK-9*'s reactions show a similar trend increasing from 1.5×10^{-2} to 6.4×10^{-2} due to the reaction becoming less favorable as the targeting strand length increases. This same trend was confirmed for *PsK-11* with $K_{D \text{ DSC}}$ values increasing from 1.2×10^{-3} to 3.5×10^{-3} as a function of strand length indicating a higher affinity for the shorter complementary strand. These values do not correspond to the values obtained from SPR and one reason for this could be due to measuring two different types of reactions, i.e., SPR may be measuring the initial rates of binding and dissociation while DSC is measuring the equilibrium interaction between the two oligos.

6.2 INTRODUCTION

The formation of DNA structures, such as hairpin loops, triplexes, G-quadruplexes, i-motifs and pseudoknots is well documented (5), (21). These non-canonical DNA secondary structures have been postulated to be involved in a variety of biological functions (26), (27), (30-36), (123) and may also be important causal factors in human diseases such as cancer and the aging of the cell (33), (38), (144), (146). The secondary structure we are interested in targeting is pseudoknots due to the fact that they are an interesting and diverse RNA structural motif, due to variation in their loop lengths and stems and the types of interactions between them. The targeting of pseudoknots with nucleic acid ODNs may also stop their biological regulation (65), (116-118), (144), (146).

Pseudoknots are an important structure with various roles as listed above which is why it's important to understand their targeting reaction properties.

The kinetics of hybridization reactions is not very well understood due to rarely visited intermediated states (152). Association rate constants have been previously measured for bimolecular interactions for DNA and RNA to be $\sim 10^6$ - 10^7 1/Ms (153-156). Hairpin formation has been found to be closer to 10^4 1/Ms (157) and the association reaction of distamycin has a reaction rate of 10^7 1/Ms (158). It is important to understand the kinetic rates for DNA/DNA interactions because they can be used to mimic DNA/RNA targeting. The rate of this reaction is important when designing targeting strands because a targeting strand needs to be able to interact with its target in a timely fashion. There are many factors that would come into play for example it would need to interact with its target before getting degraded.

From a thermodynamic point of view, successful control of gene expression depends on the effective binding of a DNA sequence to its target with tight affinity and specificity. We plan on measuring the kinetics for the targeting reactions of pseudoknots with various targeting strand lengths to determine the on and off rates of each reaction to calculate the affinity their respective pseudoknot. To do this we will be using surface plasmon resonance (SPR). This technique is very popular for the kinetics of nucleic acids and proteins binding small molecules, protein/protein interactions, protein/nucleic acid interactions, and for DNA/DNA hybridization (159-161). The goal of this study is to determine the on and off rates to compare these values as a function of target strand length. We also will be discussing the unfolding of the pseudoknots, reactants, and products and comparing the K_D DSC values determined.

6.3 METHODS

All oligonucleotides were synthesized by Integrated DNA Technologies, Inc. (Coralville, IA), purified by reverse-phase HPLC, and desalted by gel permeation chromatography using a G-10 Sephadex column. The 5'-3' sequences of oligonucleotides (ODNs) are as follows: d(Biotin-TCTCT- T_5 AAAAAAAAAGAGAT T_5 TTTTTTT), d(Biotin-TCTCT T_9 AAAAAAAAAGAGAT T_5 TTTTTTT), and d(Biotin-TCTCT T_{11} AAAAAAAAAGAGAT T_5 TTTTTTT) T_5 , T_9 and T_{11} are loops of 5, 9, and 11 thymines, respectively; and complementary strands, d(AAAAAAGAGA), d(TTTAAAAAAGAGA), d(CTTTT-TTTTAAAAAAGAGA) and d(AAAAAAAAAGAGA), d(TTTAAAAA-AAAAGAGA), d(CTTTTTTTTAAAAAAAAGAGA) and d(AAAAA-AAAAAAGAGA), d(TTTAAAAAAAAGAGA). The ODN concentrations were determined at 260 nm and 90°C using the following molar extinction coefficients ($\text{mM}^{-1}\text{cm}^{-1}$), obtained from the nearest-neighbor model (96), (130): 331 (*PsK-5*), 367 (*PsK-9*), 376 (*PsK-11*), 122 (*CS-5 Short*), 146 (*CS-5 Mid*), 181 (*CS-5*), 170 (*CS-9 Short*), 194 (*CS-9 Mid*), 237 (*CS-9*), 194 (*CS-11 Short*), 218 (*CS-11 Mid*). All experiments were carried out in 2X Sodium Citrate, buffer at pH 7.0 + 0.005% P20. All oligonucleotides were prepared by dissolving dry and desalted ODNs in buffer.

Surface Plasmon Resonance (SPR). The equilibrium constant for each targeting reaction was determined using a Biacore3000. A detailed description can be found in Chapter 2. In a typical experiment the streptavidin chip was docked in the instrument at 20°C or 25°C and flow cell one or three was primed with 10 μ L of Bionorm solution at 10 μ L/min. The needle and IFC was then washed 3xs before injecting 50 mM NaOH to normalize the chip surface to reach a steady baseline followed by washing the needle and

IFC. Flow cell one was then injected with a control ligand until ~400 RUs was bound on the chip surface, followed by washing the needle and IFC. The flow cell was then injected with 1mM HCl (regeneration buffer) and the total response units were recorded. This procedure was repeated for flow cell two or four with the ligand under investigation. To determine the binding constants an analyte was flown through the cells at 10 $\mu\text{L}/\text{min}$ ranging in concentration from 100 μM to 377 μM until reaching a plateau indicating an equilibrium had been reached in 2X SSC buffer at pH 7.0. The binding curves of flow cell one was subtracted from flow cell two resulting in the binding curve used for analysis. Curves were analyzed using the Bioevaluation software using a 1:1 langmuir model as well as a steady state model to obtain the binding equilibrium constant (120).

Differential scanning calorimetry (DSC). The total heat required for the unfolding of each reactant and product of a particular reaction (pseudoknot, single strand or duplex product) was measured with a VP-DSC differential scanning calorimeter from Microcal (Northampton, MA). A full description of this method can be found in Chapter 2. Standard thermodynamic profiles and T_{MS} are obtained. These experiments were ran in 2X Sodium Citrate (2X SSC) buffer at pH 7.0, with 0.005% P20.

Overall Experimental Protocol. We use SPR to measure the association and dissociation rates, k_{on} and k_{off} , respectively. This gives the $K_{\text{D app}}$ from the equation $K_{\text{D app}} = k_{\text{off}}/k_{\text{on}}$. The SPR experiments were also ran until reaching a steady state to confirm the K_{D} calculated from the k_{on} and k_{off} values. To determine the predicted ΔG° of each targeting reaction, we use the DNA nearest-neighbor parameters to estimate the $\Delta G^{\circ}_{\text{pred}}$ from the targeting reaction using $\Delta G^{\circ}_{\text{pred}} = \Delta G^{\circ}_{\text{products}} - \Delta G^{\circ}_{\text{reactants}}$. In particular cases the $\Delta G^{\circ}_{\text{products}}$ includes the formation of a hairpin due to the complementarity of the dangling

end of the duplex product. To directly compare dissociation constants, we use unfolding profiles to obtain our $\Delta G^\circ_{\text{pred}}$. With this in mind, $\Delta G^\circ_{\text{pred}} = -RT \ln K_{\text{D pred}}$. These values are compared with $K_{\text{D app}}$ from the SPR experiments. Then, we measured the unfolding thermodynamics for each targeting reaction, i.e. we determined unfolding profiles for each product and reactant by DSC. Using thermodynamic cycles, as in chapter 5, we measure the $\Delta G^\circ_{\text{HC}}$, which will give us the $K_{\text{D DSC}}$ from the relationship: $\Delta G^\circ_{\text{HC}} = -RT \ln K_{\text{D DSC}}$. Again, it's important to note using the unfolding values for $\Delta G^\circ_{\text{HC}}$ will give the K_{D} directly to compare with the $K_{\text{D app}}$ obtained from SPR.

6.4 RESULTS

6.4.1 Targeting Reaction of PsK-5

The targeting reaction of *PsK-5* was examined first by SPR at 20°C in 2X SSC buffer at pH 7.0 with 0.005% P20 using three target strands of different lengths, Figure 1. The first strand was designed to target the first stem of the pseudoknot plus the unpaired bases of the first loop (*CS-5 Short*). The second target strand was extended to include three bases in the second stem (*CS-5 Mid*) and the final target strand was designed to target both of the stems of the pseudoknot and the first loop (*CS-5 Full*). In the first reaction (*PsK-5 + CS-5 Short*) concentrations ranging from 750 pM to 780 nM were needed in order to start seeing a response until a steady state was achieved in the binding curve, respectively (Figure 2A). A k_{on} of 7.49×10^5 1/Ms was obtained with a k_{off} of 3.37×10^{-3} 1/s. Using the equation of $K_{\text{D}} = k_{\text{off}}/k_{\text{on}}$ we obtained an apparent K_{D} ($K_{\text{D app}}$) of 4.5×10^{-9} M, Table 1. Running these experiments until a steady state equilibrium was reached also produced a K_{D} of 4.5×10^{-9} M, Figure 2B. Looking at the structure of the

pseudoknot and the targeting reaction the product formed is most likely a short duplex with a hairpin from the AT stem of the pseudoknot that is not targeted. Using this information we can calculate the predicted equilibrium constant ($K_{D \text{ pred.}}$) using the equation $\Delta G^\circ = -RT \ln K_{\text{pred.}}$. With a predicted unfolding ΔG° of 7.02 kcal/mol a $K_{D \text{ pred.}}$ of 5.8×10^{-6} is expected. This value is larger than the experimental indicating a tighter interaction is occurring experimentally.

In the second reaction (*PsK-5 + CS-5 Mid*) concentrations ranging from 1.5 nM to 12.5 μ M were needed in order to start seeing a response until a steady state was achieved in the binding curve, respectively (Figure 3A). A k_{on} of 1.67×10^5 1/Ms was obtained with a k_{off} of 8.02×10^{-3} 1/s resulting in a $K_{D \text{ app.}}$ of 4.8×10^{-8} M, Table 1. Using the data when reaching equilibrium a $K_{D \text{ app.}}$ of 4.8×10^{-8} M was also obtained confirming the $K_{D \text{ app.}}$ obtain in the kinetic experiment, Figure 3B. This targeting reaction product is likely to form a short duplex with a hairpin from the AT stem of the pseudoknot that is not targeted. Using this information we calculate the $K_{D \text{ pred}}$ using a predicted unfolding ΔG° of 6.9 kcal/mol to be 7.1×10^{-6} . Again, we are seeing a tighter interaction experimentally.

The third reaction (*PsK-5 + CS-5 Full*) required concentrations ranging from 48.8 nM to 298 μ M in order to start seeing a response, but a true steady state still wasn't fully achieved in the binding curve (Figure 4A). A k_{on} of 1.42×10^3 1/Ms was obtained with a k_{off} of 1.11×10^{-3} 1/s resulting a $K_{D \text{ app.}}$ of 7.8×10^{-7} M, Table 1. Using this experiment when reaching equilibrium a $K_{D \text{ app.}}$ of 7.8×10^{-7} M was also obtained confirming the $K_{D \text{ app.}}$ obtain from the kinetic rates, Figure 4B. The product to form in this reaction is likely a duplex with a dangling end and has predicted ΔG° of 1.62 kcal/mol and a $K_{D \text{ pred.}}$ of 6.2

$\times 10^{-2}$. However, this value is not in good agreement with the experimental value obtained.

In the reaction of *PsK-5* with its complementary strands it appears that based on the $K_{D \text{ app.}}$ and $K_{D \text{ pred.}}$ differences there is the potential other interactions are occurring other than the one that is predicted based on nearest-neighbor calculations to be the most stable. Another possibility is there could be multiple products forming making the data hard to interpret. The main observation that can be drawn is there is an increase in the $K_{D \text{ app.}}$ value indicating as the strand length increases there is a decrease in affinity for the complementary strand. The $K_{D \text{ pred.}}$ predicts that this decrease in affinity should take place with the increase in strand length and it has to do with more bonds needing to be broken in the pseudoknot for the resulting products to form, meaning it's becoming less favorable for the reaction to take place.

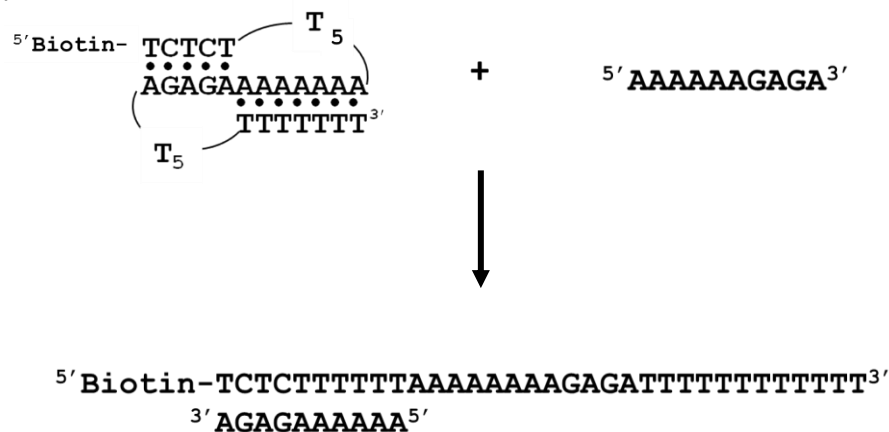
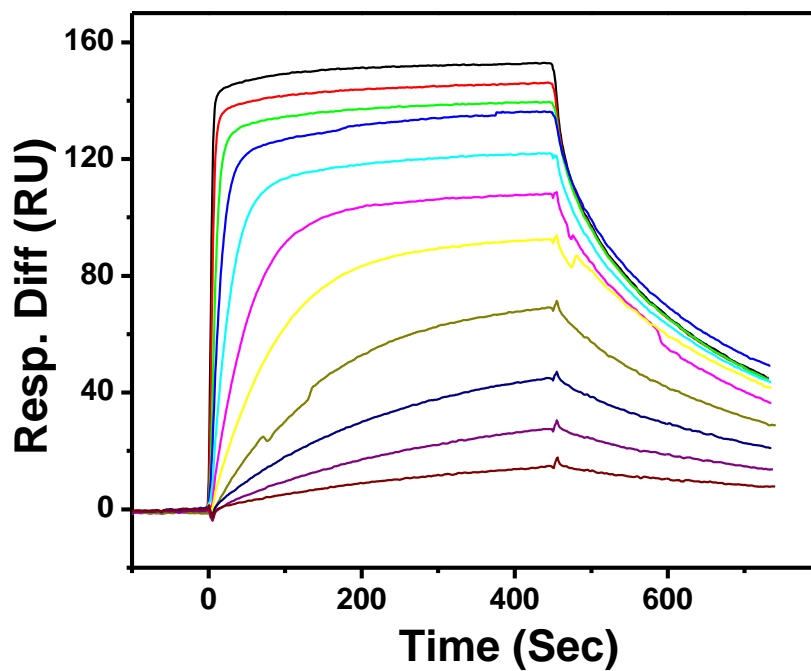
Reaction 1:**Reaction 2:****Reaction 3:**

Figure 1. Targeting Reactions of *PsK-5* with Complementary Strands. Reaction 1: *PsK-5* + *CS-5 Short*. Reaction 2: *PsK-5* + *CS-5 Mid*. Reaction 3: *PsK-5* + *CS-5 Full*.

A)



B)

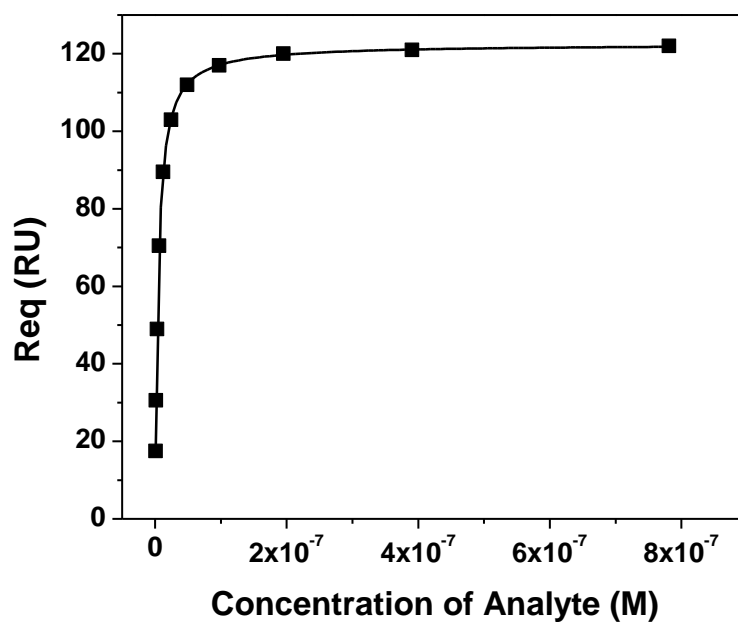


Figure 2. Sensograms and steady state fitting. A) The concentrations CS-5 Short used from bottom to top are 750pM, 1.5 nM, 3 nM, 6 nM, 12 nM, 24 nM, 48 nM, 98 nM, 196 nM, 391 nM, 781 nM. B) Steady state fitting of the sensogram in (A) was converted to Req vs. Conc of analyte. All experiments were carried out in 2X SSC, 0.005% P20 buffer at pH 7.0 at 20°C

Table 1. Kinetic Rates and Equilibrium Constants for *PsK-5* Targeting Reactions

	k_{on} (1/Ms)	k_{off} (1/s)	K_D app. (M)	K_D Pred
Reaction 1				
<i>CS-5 Short Duplex 20 °C</i>	7.49 x 10 ⁵	3.37 x 10 ⁻³	4.5 x 10 ⁻⁹	7.02 x 10 ⁻⁶
<i>CS-5 Mid Duplex 20 °C</i>	1.67 x 10 ⁵	8.02 x 10 ⁻³	4.8 x 10 ⁻⁸	7.1 x 10 ⁻⁶
<i>CS-5 Full Duplex 20 °C</i>	1.42 x 10 ³	1.11 x 10 ⁻³	7.8 x 10 ⁻⁷	6.2 x 10 ⁻²

Experiments were carried out in 2X SSC buffer at pH 7.0, 0.005% P20. Experimental errors are as follows: k_{on} (± 5 %), k_{off} (± 5 %), K_D app. (± 5 %), K_D pred. (± 7%).

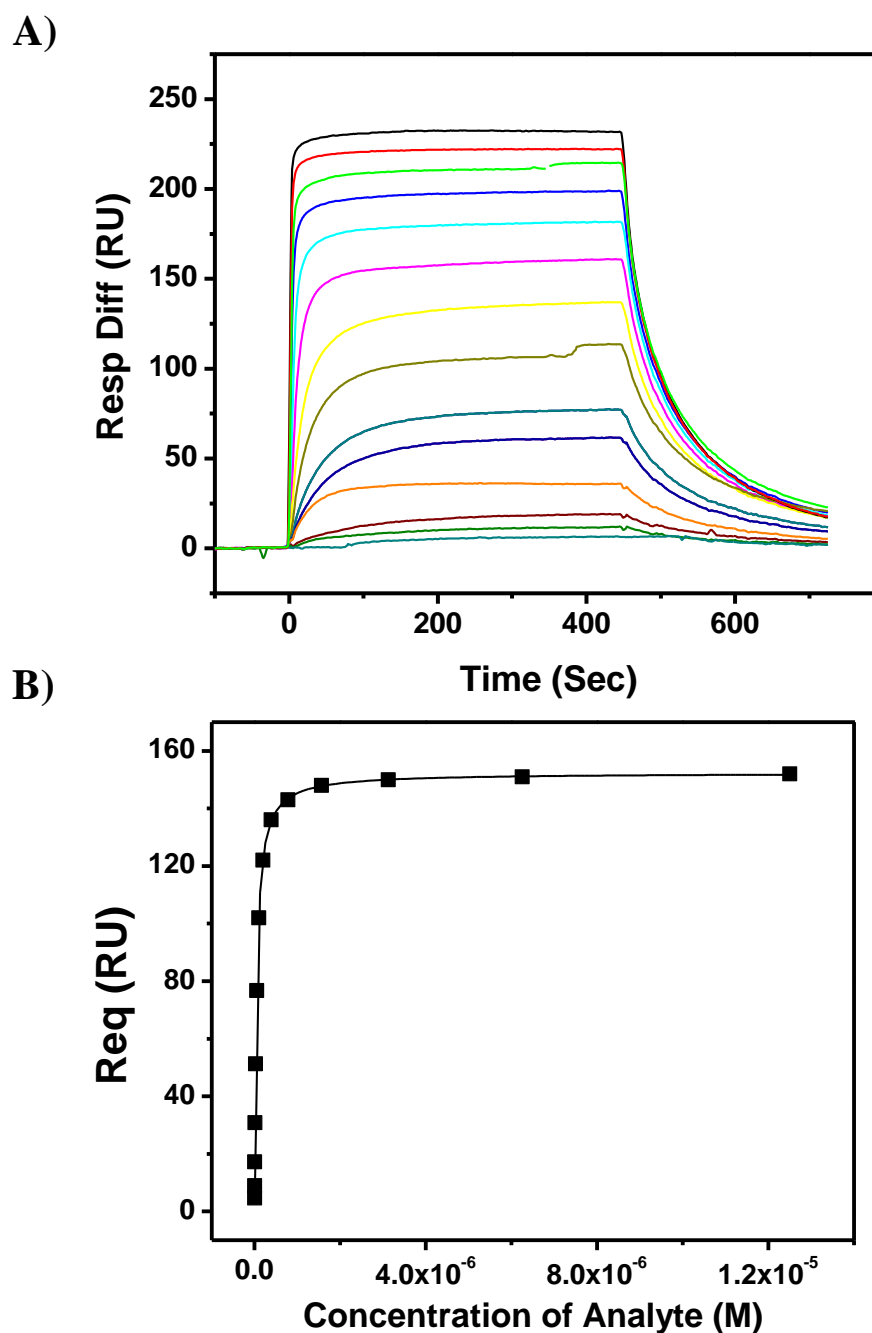


Figure 3. Sensograms and steady state fitting. A) The concentrations *CS-5 Mid* used from bottom to top are: 1.5 nM, 3 nM, 6 nM, 12 nM, 24 nM, 48 nM, 98 nM, 196 nM, 391, nM, 781 nM, 1.6 μ M, 3.1 μ M, 6.3 μ M, and 12.5 μ M. B) Steady state fitting of the sensogram in (A) was converted to Req vs. Conc of analyte. . All experiments were carried out in 2X SSC, 0.005% P20 buffer at pH 7.0 at 20°C

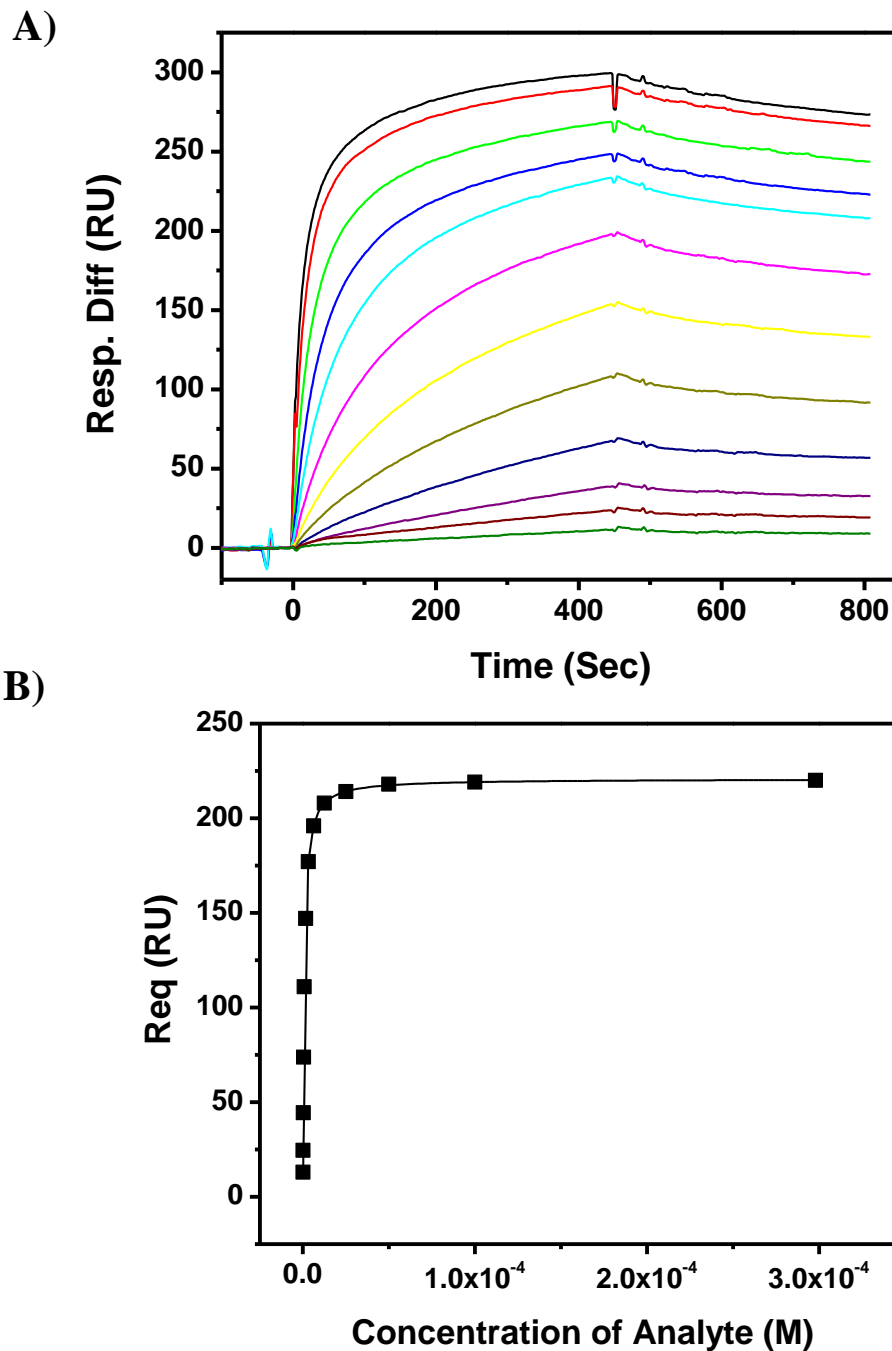


Figure 4. Sensograms and steady state fitting. A) The concentrations CS-5 Full used from bottom to top are: 48 nM, 98 nM, 196 nM, 391 nM, 781 nM, 1.6 μ M, 3.1 μ M, 6.3 μ M, and 12.5 μ M, 25 μ M, 50 μ M, 100 μ M, 298 μ M. B) Steady state fitting of the sensogram in (A) was converted to Req vs. Conc of analyte. All experiments were carried out in 2X SSC, 0.005% P20 buffer at pH 7.0 at 20°C

6.4.2 Targeting Reactions of *PsK-9*

The targeting reaction of *PsK-9* was examined first by using SPR at 25°C in 2X SSC buffer at pH 7.0 with 0.005% P20 using three target strands of different lengths, Figure 5. The first strand was designed to target the first stem of the pseudoknot plus the unpaired bases of the first loop (*CS-9 Short*). The second target strand was extended to include three bases in the second stem (*CS-9 Mid*) and the final target strand was designed to target both of the stems of the pseudoknot and the first loop (*CS-9 Full*). In the first reaction (*PsK-9 + CS-9 Short*) concentrations ranging from 48.8 nM to 12.5 μM were needed in order to start seeing a response until a steady state was achieved in the binding curve, respectively (Figure 6A). A k_{on} of 7.76×10^4 1/Ms was obtained with a k_{off} of 5.4×10^{-4} 1/s resulting in a K_D app. of 6.96×10^{-9} M, Table 2. Using the data when reaching a steady state equilibrium a K_D of 7.0×10^{-9} M was also obtained confirming the K_D app. obtain in the kinetic experiment, Figure 6B. *PsK-9* when targeted with *CS-9 Short* is most likely to form a short duplex with a hairpin from the AT stem which is not targeted in this reaction. This reaction has a predicted unfolding ΔG° of 11.1 kcal/mol resulting in a K_D pred. of 7.2×10^{-9} . This value is in excellent agreement to what we are obtaining experimentally indicating what we are predicting is likely to be forming in the SPR reactions.

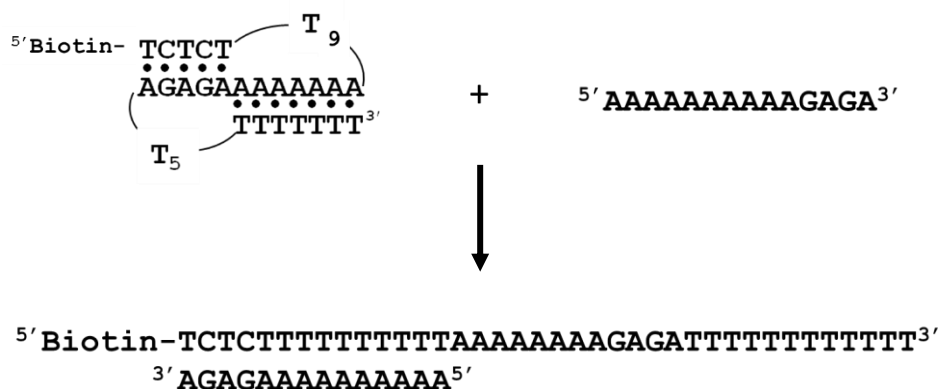
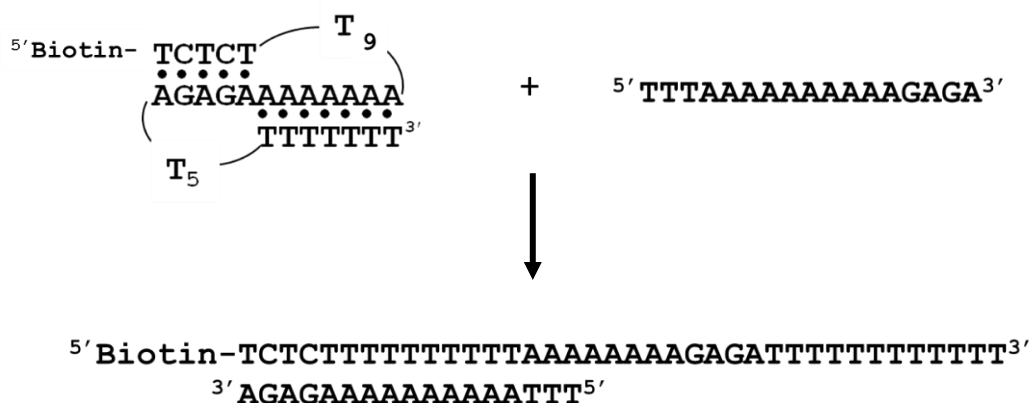
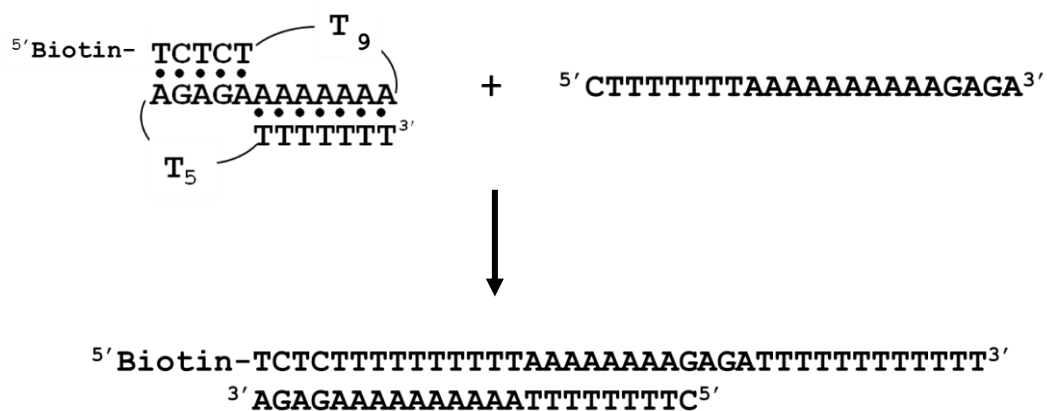
Reaction 1:**Reaction 2:****Reaction 3:**

Figure 5. Targeting Reactions of *PsK-9* with Complementary Strands. Reaction 1: *PsK-9* + CS-9 Short. Reaction 2: *PsK-9* + CS-9 Mid. Reaction 3: *PsK-9* + CS-9 Full.

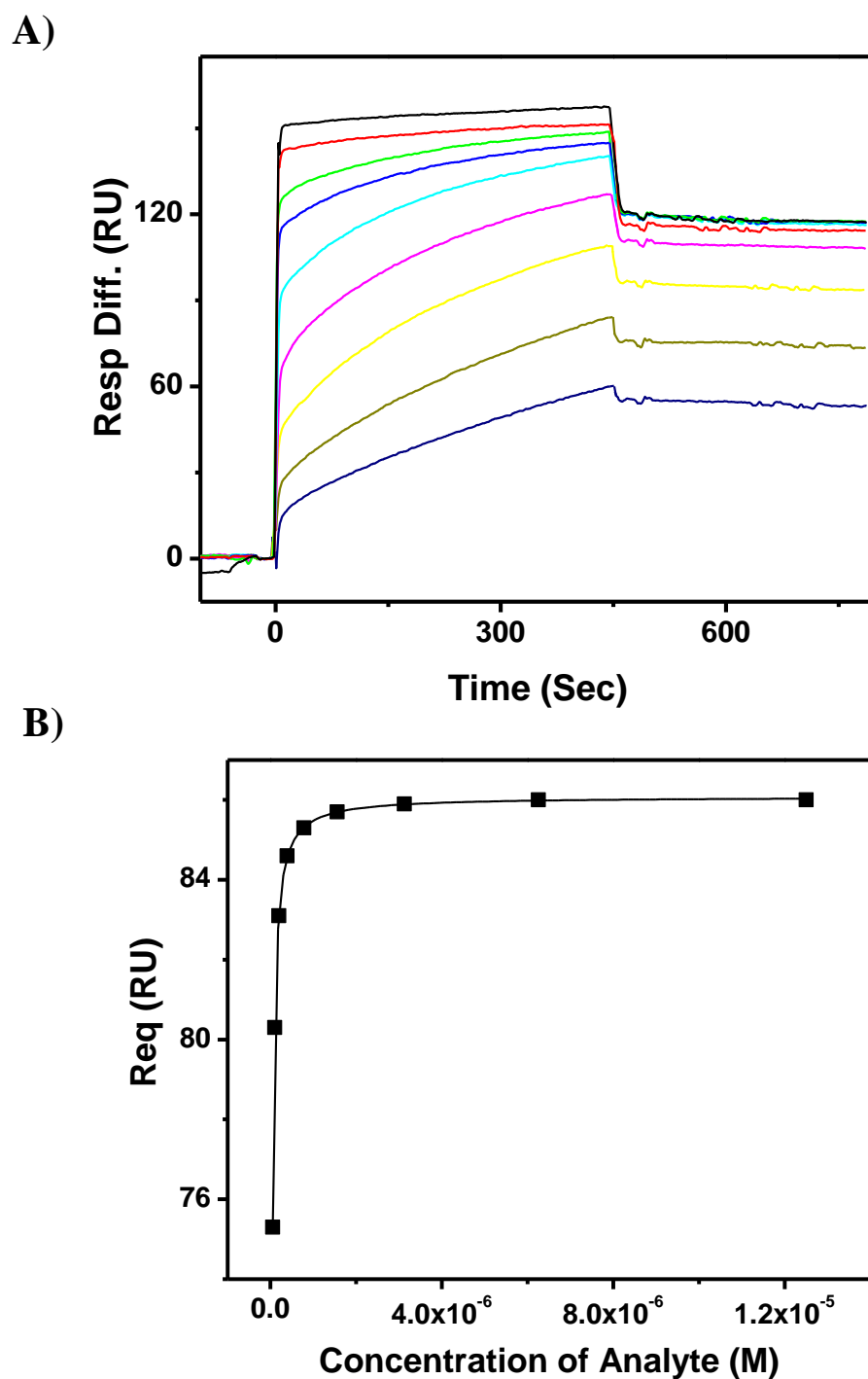


Figure 6. Sensograms and steady state fitting. A) The concentrations *CS-9 Short* used from bottom to top are: 48 nM, 98 nM, 196 nM, 391 nM, 781 nM, 1.6 μ M, 3.1 μ M, 6.3 μ M, and 12.5 μ M. B) Steady state fitting of the sensogram in (A) was converted to Req vs. Conc of analyte. All experiments were carried out in 2X SSC, 0.005% P20 buffer at pH 7.0 at 25°C

Table 2. Kinetic Rates and Equilibrium Constants for *PsK-9* Targeting Reactions

	k_{on} (1/Ms)	k_{off} (1/s)	K_D app. (M)	K_D Pred
<i>CS-9 Short Duplex</i> 25 °C	7.76 x 10 ⁴	5.4x 10 ⁻⁴	6.96 x 10 ⁻⁹	7.2 x 10 ⁻⁹
<i>CS-9 Mid Duplex</i> 25 °C	1.05 x 10 ⁵	2.46 x 10 ⁻³	2.35 x 10 ⁻⁸	8.9 x 10 ⁻⁹
<i>CS-9 Full Duplex</i> 25 °C	6.29 x 10 ³	1.67 x 10 ⁻³	2.66 x 10 ⁻⁷	3.7 x 10 ⁻⁴

Experiments were carried out in 2X SSC buffer at pH 7.0, 0.005% P20. Experimental errors are as follows: k_{on} (± 5 %), k_{off} (± 5 %), K_D app. (± 5 %), K_D pred. (± 7%).

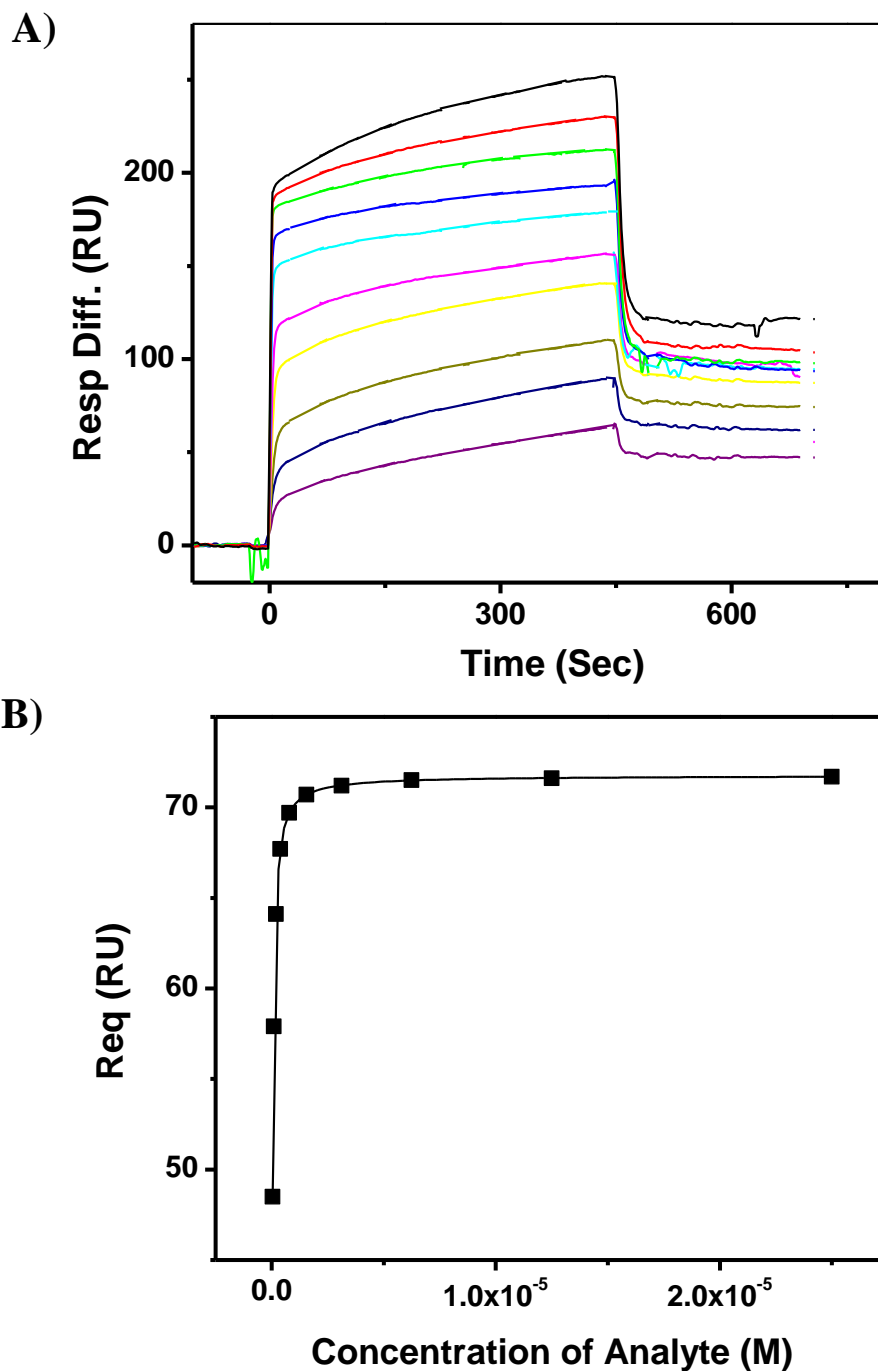


Figure 7. Sensograms and steady state fitting. A) The concentrations CS-9 Mid used from bottom to top are: 48 nM, 98 nM, 196 nM, 391 nM, 781 nM, 1.6 μ M, 3.1 μ M, 6.3 μ M, and 12.5 μ M, 25 μ M. B) Steady state fitting of the sensogram in (A) was converted to Req vs. Conc of analyte. All experiments were carried out in 2X SSC, 0.005% P20 buffer at pH 7.0 at 25°C

In the second reaction (*PsK-9 + CS-9 Mid*) concentrations ranging from 48.8 nM to 25 μM were needed in order to start seeing a response until a steady state was achieved in the binding curve, respectively (Figure 7A). A k_{on} of 1.05×10^5 1/Ms was obtained with a k_{off} of 2.46×10^{-3} 1/s with a $K_{\text{D app.}}$ of 2.35×10^{-8} M, Table 2. Using the data when reaching a steady state equilibrium a K_{D} of 2.3×10^{-8} M was also obtained confirming the $K_{\text{D app.}}$ obtain in the kinetic experiment. Again, looking at the targeting reaction the product most likely to form is a short duplex with a hairpin from the AT stem of the pseudoknot that is not completely targeted. Using this information, we predict an unfolding ΔG° of 10.98 kcal/mol and a $K_{\text{D pred.}}$ of 8.9×10^{-9} for this reaction. This value is close to what we are obtaining experimentally, but there is an increase in the experimental value indicating a decrease in the overall affinity of the complementary strand to the pseudoknot.

In the third reaction (*PsK-9 + CS-9 Full*) concentrations ranging from 48.8 nM to 50 μM were needed in order to start seeing a response but a steady state still wasn't fully achieved in the binding curve, (Figure 8A). A k_{on} of 6.29×10^3 1/Ms was obtained with a k_{off} of 1.67×10^{-3} 1/s resulting in a $K_{\text{D app.}}$ of 2.66×10^{-7} M, Table 2. Using this experiment when reaching steady state equilibrium a K_{D} of 2.7×10^{-7} M was also obtained confirming the $K_{\text{D app.}}$ obtained from the kinetic rates. The product to form in this reaction is likely a duplex with a dangling end and has a predicted unfolding ΔG° of 4.7 kcal/mol resulting in a $K_{\text{D pred.}}$ of 3.7×10^{-4} . However, this value is not in good agreement with the experimental value obtained.

In the reaction of *PsK-9* with its complementary strands it appears that based on the $K_{\text{D app.}}$ and $K_{\text{D pred.}}$ as the complementary strand length increases there is the potential

other interactions are occurring other than the one that is predicted based on nearest-neighbor calculations to be the most stable. Another possibility is there could be multiple products forming making the data hard to interpret. The main observation that can be drawn is there is an increase in the $K_{D \text{ app.}}$ value indicating as the strand length increases there is a decrease in affinity for the complementary strand. The $K_{D \text{ pred.}}$ predicts that this decrease in affinity should take place with the increase in strand length and it has to do with the reaction becoming less favorable.

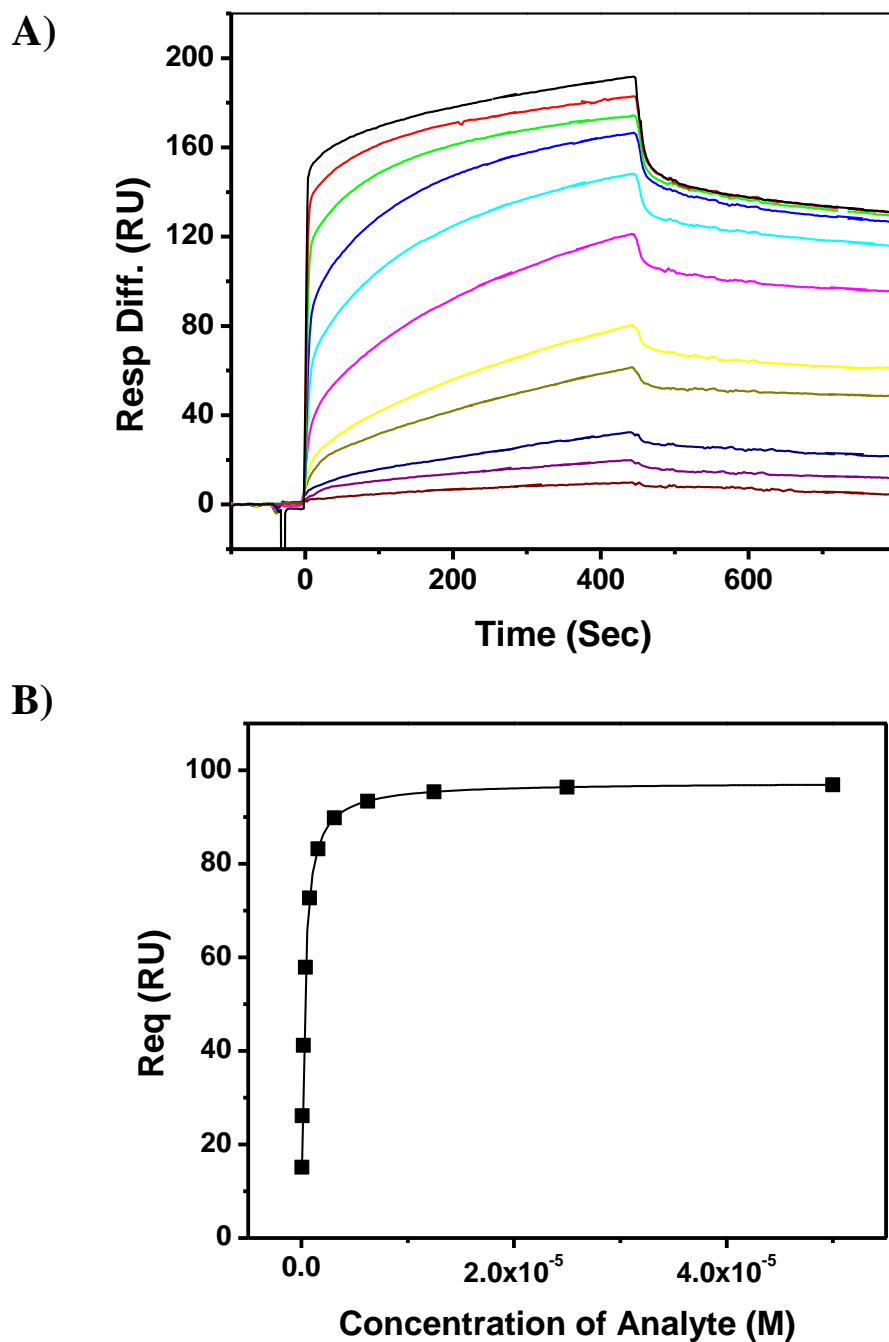


Figure 8. Sensograms and steady state fitting. A) The concentrations CS-9 Full used from bottom to top are: 48 nM, 98 nM, 196 nM, 391 nM, 781 nM, 1.6 μ M, 3.1 μ M, 6.3 μ M, 12.5 μ M, 25 μ M, 50 μ M. B) Steady state fitting of the sensogram in (A) was converted to Req vs. Conc of analyte. All experiments were carried out in 2X SSC, 0.005% P20 buffer at pH 7.0 at 25°C

6.4.3 Targeting Reactions of *PsK-11*

The targeting reaction of *PsK-11* was examined first by using SPR at 20 and 25°C in 2X SSC buffer at pH 7.0 using two target strands of different lengths, Figure 9. The first strand was designed to target the first stem of the pseudoknot plus the unpaired bases of the first loop (*CS-11 Short*). The second target strand was extended to include three bases in the second stem (*CS-11 Mid*). In the first reaction at 20°C concentrations ranging from 375 pM to 391 nM were needed in order to start seeing a response until a steady state was achieved in the binding curve, respectively (Figure 10A). A k_{on} of 1.26×10^6 1/Ms was obtained with a k_{off} of 1.88×10^{-3} 1/s resulting in a $K_{D\ app.}$ of 1.49×10^{-9} M, Table 3. Using the data when reaching a steady state equilibrium K_D of 1.5×10^{-9} M was also obtained confirming the $K_{D\ app.}$ obtain in the kinetic analysis, Figure 10B. A similar product is predicted as the other short targeting strands producing a duplex with a hairpin from the AT stem of the pseudoknot that is not targeted. With this structure in mind a predicted unfolding ΔG° of 13.14 kcal/mol was calculated and a $K_{D\ pred.}$ of 1.6×10^{-10} is expected from the targeting reaction. The experimental value is larger than predicted indicating a lower binding affinity is occurring when this reaction is taking place.

The same reaction at 25°C concentrations ranging from 188 pM to 391 nM were needed in order to start seeing a response until a steady state was achieved in the binding curve, respectively (Figure 11A). A k_{on} of 8.62×10^5 1/Ms was obtained with a k_{off} of 3.62×10^{-3} 1/s resulting in a $K_{D\ app.}$ of 4.2×10^{-9} M, Table 3. Using this experiment when reaching equilibrium a K_D of 4.2×10^{-9} M was also obtained confirming the $K_{D\ app.}$ obtain from the kinetic rates, Figure 11B. When comparing this value with the one obtained at 20°C we can see that there is a decrease in the k_{on} rate and an increase and in k_{off} rate

making this reaction less favorable at higher temperatures which is reflected in the $K_{D \text{ app.}}$ values, Table 1. The Arrhenius energy, i.e., enthalpy of activation, for this reaction was calculated to be 11.1 kcal/mol using the following equation: $\ln(k_{\text{on}1}/k_{\text{on}2}) = -E_a/R (1/T_2 - 1/T_1)$. This indicates the activation enthalpy is around 2 base-pair stacks.

In the second reaction (*PsK-11 + CS-11 Mid*) concentrations ranging from 375 pM to 391 nM were needed in order to start seeing a response until a steady state was achieved in the binding curve, respectively (Figure 12A). A k_{on} of 6.97×10^5 1/Ms was obtained with a k_{off} of 1.26×10^{-3} 1/s resulting in a $K_{D \text{ app.}}$ of 1.81×10^{-9} M. Using this experiment when reaching equilibrium a K_D of 1.82×10^{-9} M was obtained confirming the $K_{D \text{ app.}}$ from the kinetic rates, Figure 12B. Again, the targeting reaction the product formed is most likely a short duplex with a hairpin from the AT stem of the pseudoknot that is not targeted. With a predicted unfolding ΔG° of 13.02 kcal/mol, a $K_{D \text{ pred.}}$ of 1.94×10^{-10} is expected. The experimental value is larger than predicted indicating a lower binding affinity is occurring when this reaction is taking place.

The same reaction at 25°C concentrations ranging from 780 pM to 391 nM were needed in order to start seeing a response until a steady state was achieved in the binding curve, respectively (Figure 13A). A k_{on} of 5.06×10^5 1/Ms was obtained with a k_{off} of 3.41×10^{-3} 1/s resulting in a $K_{D \text{ app.}}$ of 6.74×10^{-9} M, Table 3. This was confirmed by using the data when reaching equilibrium producing a K_D of 6.7×10^{-9} M, Figure 13B. When comparing this value with the one obtained at 20°C, we can see that there is a slight decrease in the k_{on} rate and an increase in the k_{off} rate. These together with the lower K_D value make this reaction less favorable at higher temperatures. The Arrhenius energy for this reaction was calculated to be 13.2 kcal/mol. This values is in good

agreement with the previous reaction of *PsK-11* with *CS-11 Short* and shows the activation enthalpy corresponds to around 2 base-pair stacks.

In the reaction of *PsK-11* with its complementary strands it appears that based on the $K_{D \text{ app.}}$ and $K_{D \text{ pred.}}$ as the complementary strand length increases there is the potential other interactions are occurring other than the one that is predicted based on nearest-neighbor calculations to be the most stable, due to the experimental value being larger than predicted. Another possibility is there could be multiple products forming making the data hard to interpret. The main observation that can be drawn is there is an increase in the $K_{D \text{ app.}}$ value indicating as the strand length increases there is a decrease in affinity for the complementary strand. The $K_{D \text{ pred.}}$ predicts that this decrease in affinity should take place with the increase in strand length and it has to do with more bonds needing to be broken in the pseudoknot for the resulting products to form, meaning it's becoming less favorable for the reaction to take place.

There is a big difference between the $K_{D \text{ app.}}$ and $K_{D \text{ pred.}}$ for the majority of the targeting reactions investigated by SPR, so we wanted to compare these $K_{D \text{ app.}}$ values with the $K_{D \text{ DSC}}$ values that can be obtained from DSC ($K_{D \text{ DSC}}$). We have previously determined the thermodynamic profiles for two of the reactions studied in this chapter, *PsK-5* and *PsK-9* with *CS-5 Full* and *CS-9 Full*, respectively, which are reported in Chapter 5. Using the unfolding $\Delta G^{\circ}_{\text{HC}}$ at 20°C (3.3 kcal/mol) for *PsK-5*'s reaction a $K_{D \text{ DSC}}$ of 3.3×10^{-3} was measured. This is a very large discrepancy with the $K_{D \text{ app.}}$ of 7.8×10^{-7} M measured by SPR. When comparing *PsK-9*'s reaction a $K_{D \text{ DSC}}$ of 5.0×10^{-2} was measured which is much weaker than the $K_{D \text{ app.}}$ of 2.66×10^{-7} M measured by SPR. This could mean two things, either the buffer conditions between the SPR and DSC data

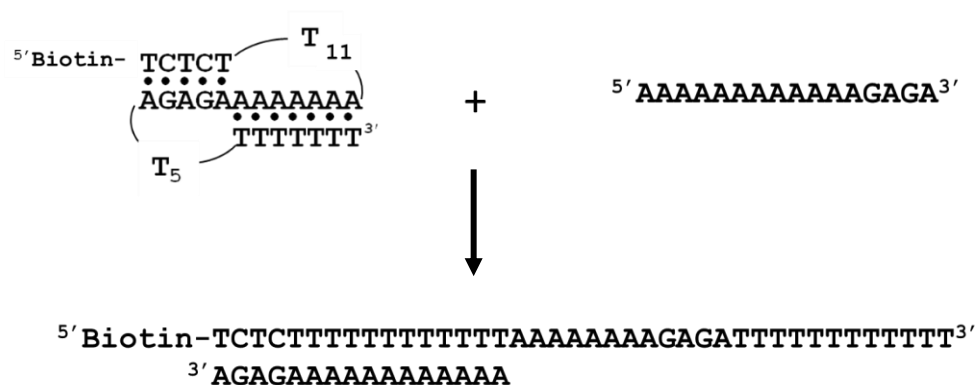
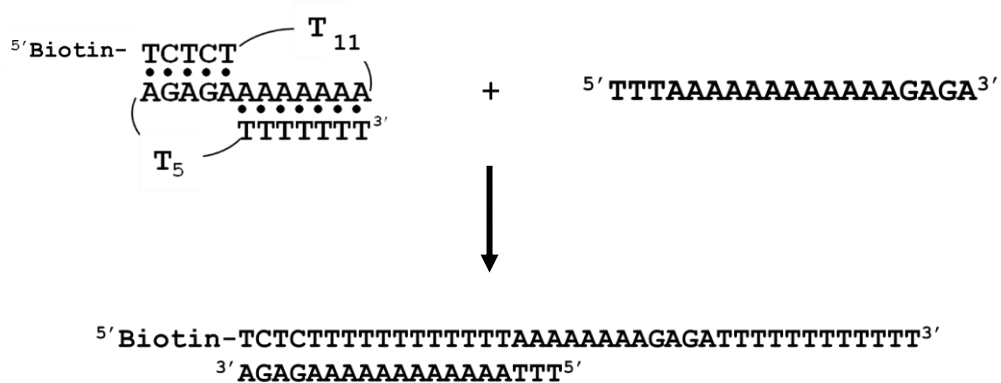
Reaction 1:**Reaction 2:**

Figure 9. Targeting Reactions of *PsK-11* with Complementary Strands.
Reaction 1: *PsK-11* + *CS-11 Short*. Reaction 2: *PsK-11* + *CS-11 Mid*.

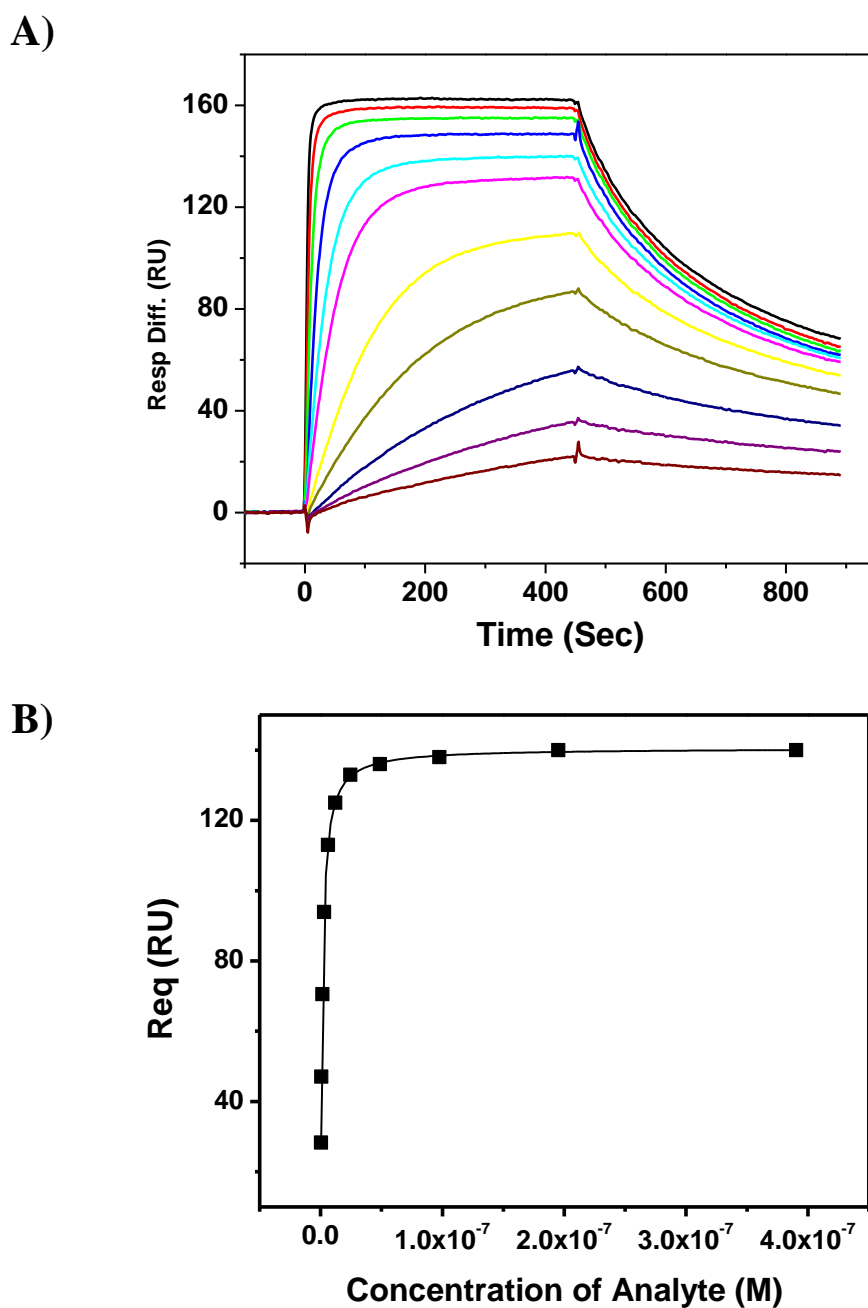


Figure 10. Sensograms and steady state fitting. A) The concentrations *CS-11 Short* used from bottom to top are: 375 pM, 750pM, 1.5 nM, 3 nM, 6 nM, 12 nM, 24 nM, 48 nM, 98 nM, 196 nM, 391, nM, 781 nM. B) Steady state fitting of the sensogram in (A) was converted to Req vs. Conc of analyte. All experiments were carried out in 2X SSC, 0.005% P20 buffer at pH 7.0 at 20°C

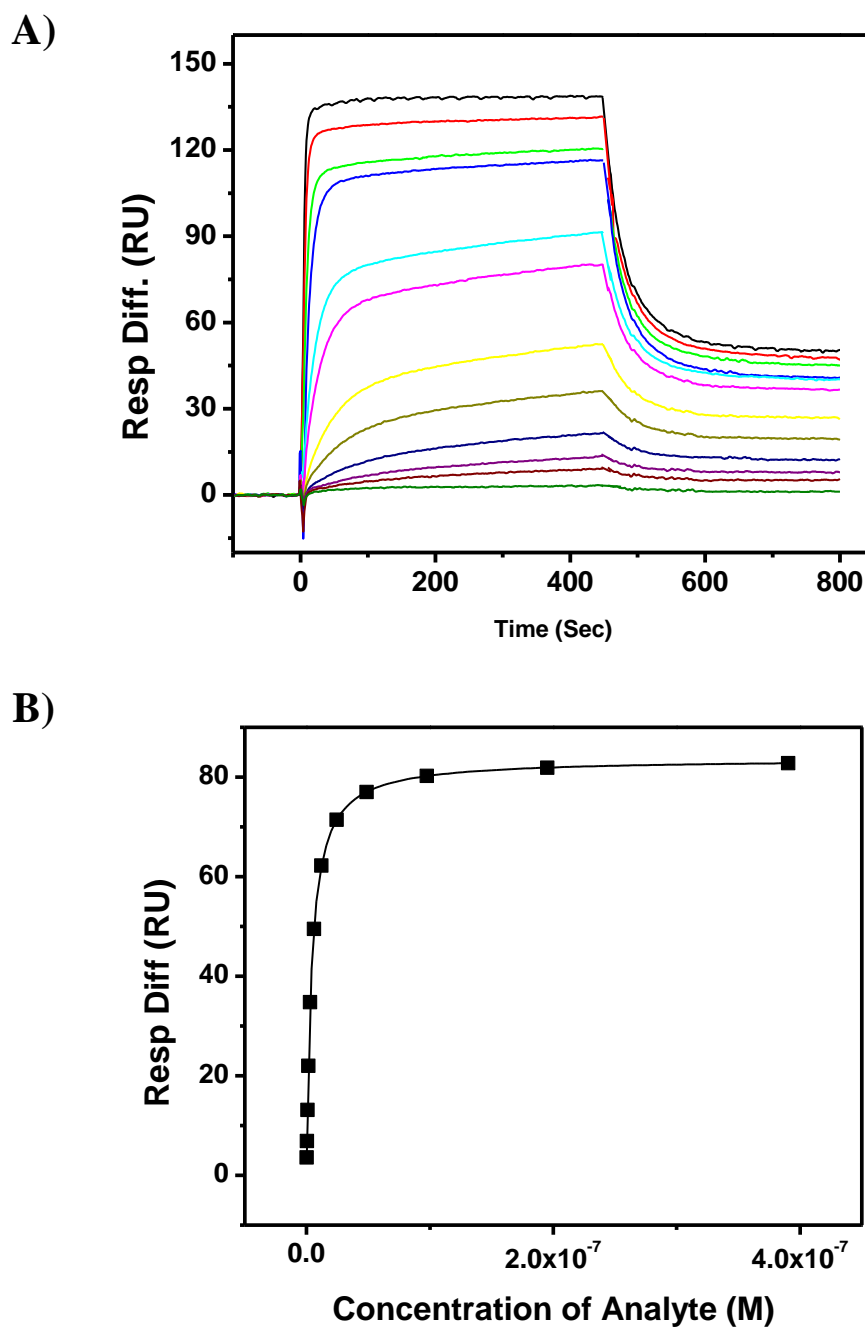


Figure 11. Sensograms and steady state fitting. A) The concentrations *CS-11 Short* used from bottom to top are: 188 pM, 375 pM, 750pM, 1.5 nM, 3 nM, 6 nM, 12 nM, 24 nM, 48 nM, 98 nM, 196 nM, 391, nM,. B) Steady state fitting of the sensogram in (A) was converted to Req vs. Conc of analyte. All experiments were carried out in 2X SSC, 0.005% P20 buffer at pH 7.0 at 25°C

Table 3. Kinetic Rates and Equilibrium Constants for *PsK-11* Targeting Reactions

	k_{on} (1/Ms)	k_{off} (1/s)	K_{D app.} (M)	K_{D Pred}
<i>CS-11 Short Duplex 20 °C</i>	1.26x 10 ⁶	1.88 x 10 ⁻³	1.49 x 10 ⁻⁹	1.6 x 10 ⁻¹⁰
<i>CS-11 Short Duplex 25 °C</i>	8.62 x 10 ⁵	3.62 x 10 ⁻³	4.2 x 10 ⁻⁹	2.3 x 10 ⁻¹⁰
<i>CS-11 Mid Duplex 20 °C</i>	6.97 x 10 ⁵	1.26 x 10 ⁻³	1.81 x 10 ⁻⁹	1.94 x 10 ⁻¹⁰
<i>CS-11 Mid Duplex 25 °C</i>	5.06 x 10 ⁵	3.41 x 10 ⁻³	6.74 x 10 ⁻⁹	2.82 x 10 ⁻¹⁰

Experiments were carried out in 2X SSC buffer at pH 7.0, 0.005% P20. Experimental errors are as follows: k_{on} (± 5 %), k_{off} (± 5 %), K_{D app.} (± 5 %), K_{D pred.} (± 7%).

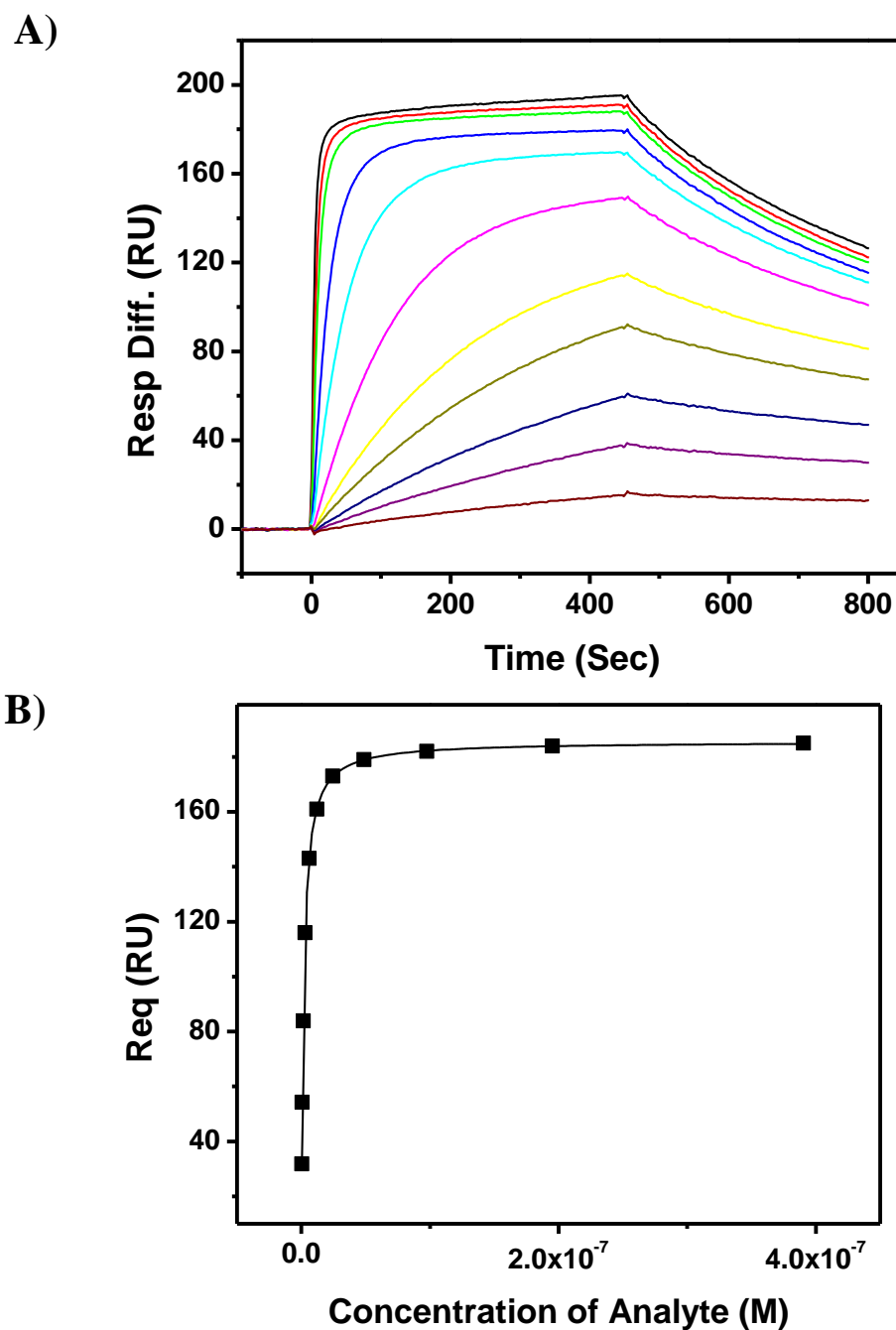


Figure 12. Sensograms and steady state fitting. A) The concentrations *CS-11 Mid* used from bottom to top are: 375 pM, 750pM, 1.5 nM, 3 nM, 6 nM, 12 nM, 24 nM, 48 nM, 98 nM, 196 nM, 391, nM. B) Steady state fitting of the sensogram in (A) was converted to Req vs. Conc of analyte. All experiments were carried out in 2X SSC, 0.005% P20 buffer at pH 7.0 at 20°C

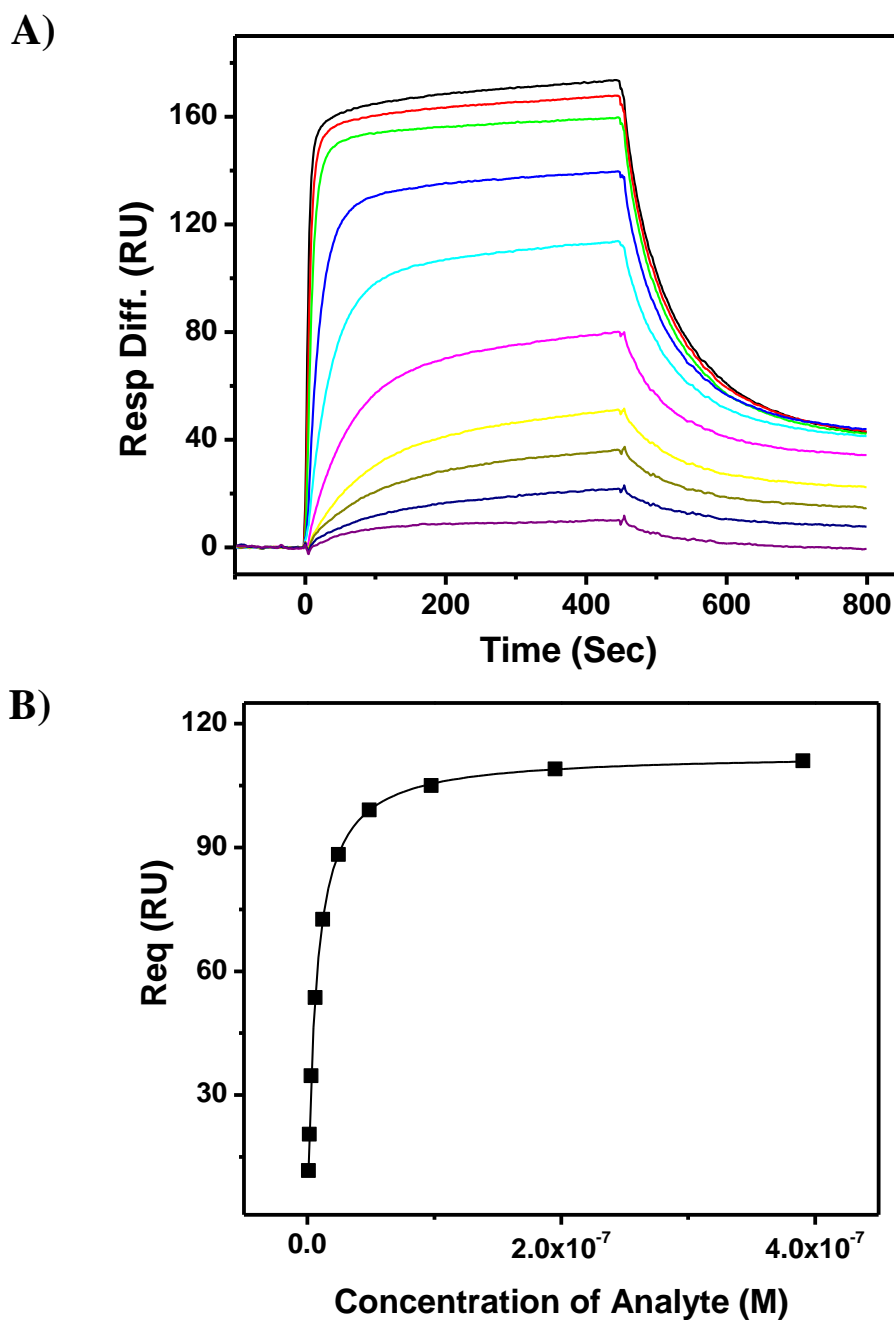


Figure 13. Sensograms and steady state fitting. A) The concentrations *CS-11 Mid* used from bottom to top are: 750pM, 1.5 nM, 3 nM, 6 nM, 12 nM, 24 nM, 48 nM, 98 nM, 196 nM, 391, nM. B) Steady state fitting of the sensogram in (A) was converted to Req vs. Conc of analyte. All experiments were carried out in 2X SSC, 0.005% P20 buffer at pH 7.0 at 25°C

compared here are causing a discrepancy in the values or two different types of reactions are being measured between the techniques. To get a better insight into what is happening we measured the thermodynamic profiles for each targeting reaction in the same buffer conditions as used in the SPR experiments to directly compare the K_D values.

6.4.4 DSC Unfolding of *PsK-5* with Complementary Strands

The reaction of *PsK-5* with its complementary strands was characterized by DSC to determine the thermodynamic profiles for the reactants and products for each targeting reaction. *PsK-5* unfolds in a monophasic transition with a T_M of 61.7°C and an enthalpy of 61.4 kcal/mol and the product of the reaction with *CS-5 Short* unfolds with a biphasic transition, Figure 14A. We first observe the unfolding of the duplex product with a T_M of 38.4°C and ΔH of 34.4 kcal/mol and then it refolds back into the pseudoknot which has a T_M of 62.4°C and ΔH of 56.1 kcal/mol. Using the ΔG_{20}° obtained from the DSC experiment, Table 4, after subtracting the ΔG° of the pseudoknot a $K_{D \text{ DSC}}$ of 7.6×10^{-2} was calculated. *PsK-5* with its complementary strand, *CS-5 Mid*, showed similar trends as the short complementary strand having two transitions indicating the unfolding of the duplex followed by the folding and unfolding of the pseudoknot, Figure 14B. We observed that the melting of the duplex takes place with a T_M of 34.3°C and ΔH of 35.1 kcal/mol and the pseudoknot unfolds at a T_M of 62.3°C and has a ΔH of 52.0 kcal/mol, Table 4. Using the ΔG_{20}° from the DSC we obtained a $K_{D \text{ DSC}}$ after subtracting the ΔG° of the pseudoknot of 0.3. Again, this value is not in good agreement with the value of 4.8×10^{-8} M from the SPR study. In the final reaction of *PsK-5* with *CS-5 Full* the DSC unfolding, Figure 14C, shows one peak attributed to the unfolding of the duplex with a

T_M of 58.7°C and ΔH of 76.3 kcal/mol, Table 4. Using the ΔG°_{20} obtained from the DSC experiment after subtracting the ΔG°_{20} of the pseudoknot and target strand a $K_{D \text{ DSC}}$ of 1.73×10^2 was calculated.

The $K_{D \text{ DSC}}$ values are not in good agreement with the experimental obtained from the SPR experiments, Table 5. One reason for this difference could be due to the buffer conditions used in the SPR experiment might not be optimal for measurement by calorimetric techniques. Also, the addition of surfactant in the buffer could cause additional complications or interactions making interpretation of the data complicated. The same targeting reaction for *PsK-5* with *CS-5 Full* was previously determined (Chapter 5) in 10 mM NaPi, 100 mM NaCl at pH 7.0. The unfolding ΔG°_{HC} for this reaction at 20°C would be 3.3 kcal/mol which would result in a $K_{D \text{ DSC}}$ of 3.3×10^{-3} compared to 173 which was obtained from this study. This indicates that the reaction under different buffer conditions results in the possibility of different interactions occurring between the pseudoknot and complementary strand and/or the surfactant in the buffer could be responsible for some of the disagreement we are observing between the techniques. Also, the addition of surfactant in the buffer could potentially increase the chance for error in the enthalpy calculation due to unsteady baselines and potential interaction with the DNA. It's also possible DSC is measuring the reaction at true equilibrium, while SPR is measuring just the initial association and dissociation rates.

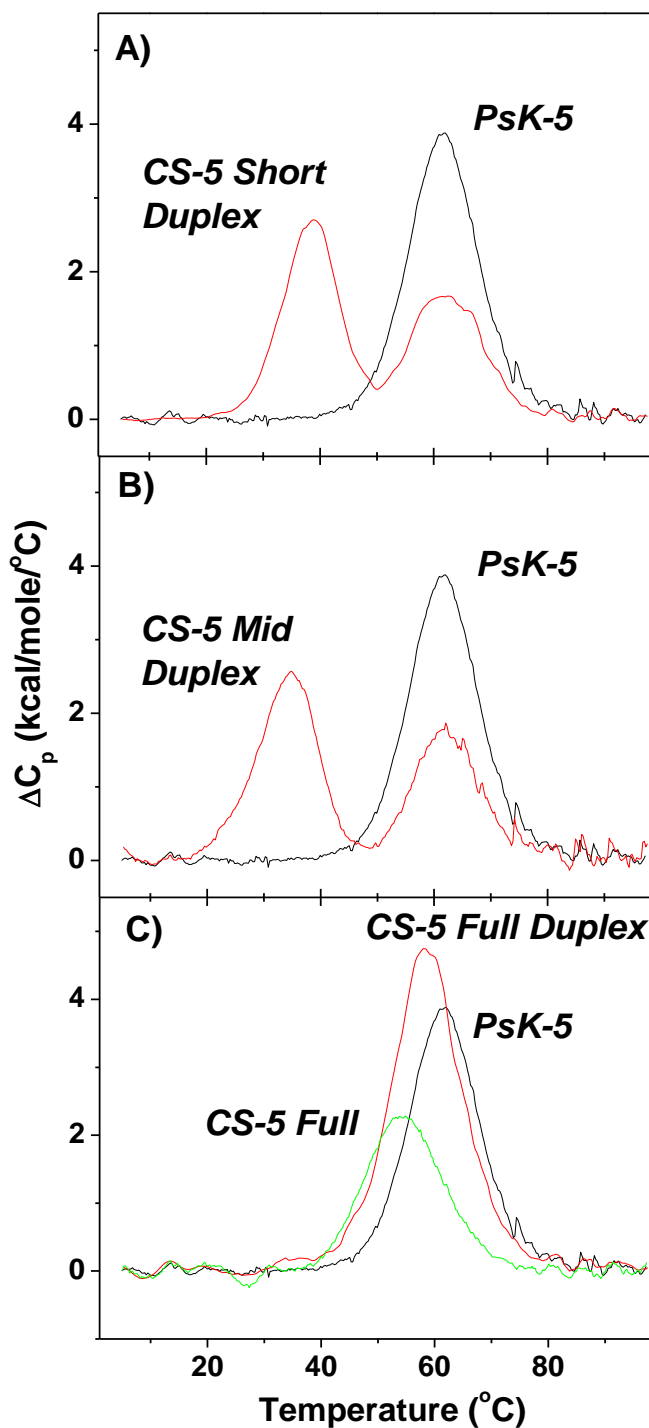


Figure 14. DSC Unfolding of *PsK-5* and Its Reaction Products. A) *PsK-5* (30 μM) and *CS-5 Short Duplex* (30 μM). B) *PsK-5* (30 μM) and *CS-5 Mid Duplex* (30 μM). C) *PsK-5* (30 μM) and *CS-5 Full Duplex* (30 μM). All experiments were carried out in 2X SSC buffer at pH 7.0, 0.005% P20.

Table 4. Unfolding Thermodynamic Profiles for *PsK-5*, Target Strands, and Duplex Products.

	Transition	T_M (°C)	ΔH (kcal/mol)	$T\Delta S$ (kcal/mol)	$\Delta G^\circ_{(20)}$ (kcal/mol)
<i>PsK-5</i>		61.7	61.4	53.8	7.6
<i>CS-5 Short Duplex</i>	1 st	38.4	34.4	32.4	2.0
	2 nd	62.4	56.1	49.0	7.1
	Total		90.5	81.4	9.1
<i>CS-5 Mid Duplex</i>	1 st	34.3	35.1	33.5	1.6
	2 nd	62.3	53.0	46.3	6.7
	Total		88.1	79.8	8.3
<i>CS-Full</i>		54.6	40.4	36.1	4.3
<i>CS-5 Full Duplex</i>		58.7	76.3	67.4	8.9

Experiments were carried out in 2X SSC buffer at pH 7.0, 0.005% P20. Experimental errors are as follows: T_M (± 0.5 °C), ΔH (± 5 %), $T\Delta S$ (± 5 %), $\Delta G^\circ_{(20)}$ (± 7 %).

Table 5. DSC and SPR Equilibrium Constants for *PsK-5* Targeting Reactions

	$\Delta G^{\circ}_{\text{HC}}$ (kcal/mol)	$K_{\text{D, DSC}}$	$K_{\text{D, app.}}$ (M)
Reaction 1			
<i>CS-5 Short Duplex</i> 20 °C	1.5	7.6×10^{-2}	4.5×10^{-9}
<i>CS-5 Mid Duplex</i> 20 °C	0.7	0.3	4.8×10^{-8}
<i>CS-5 Full Duplex</i> 20 °C	-3.0	173	7.8×10^{-7}

Experiments were carried out in 2X SSC buffer at pH 7.0, 0.005% P20. $\Delta G^{\circ}_{\text{HC}}$ is calculated from unfolding thermodynamic profiles. Experimental errors are as follows: $\Delta G^{\circ}_{\text{HC}}$ (± 14 %), $K_{\text{D DSC}}$ (± 7 %), $K_{\text{D app.}}$ (± 5 %).

6.4.5 DSC Unfolding of *PsK-9* with Complementary Strands

The reaction of *PsK-9* with its complementary strands was characterized by DSC to determine the thermodynamic profiles for the reactants and products for each targeting reaction, Figure 15A. We observed that the melting of the duplex is taking place first with a T_M of 40.7°C and ΔH of 41.2 kcal/mol followed by the refolding back into the pseudoknot which unfolds with a T_M of 67.7°C and a ΔH of 88.4 kcal/mol, Table 6. Using the ΔG_{25}° obtained from the DSC experiment after subtracting the ΔG° of the pseudoknot a $K_{D \text{ DSC}}$ of 1.5×10^{-2} was calculated. The melting of *PsK-9* with *CS-9 Mid* showed a similar melting curve with the unfolding of the duplex first with a T_M of 39.1°C and a ΔH of 32.6 kcal/mol and then the oligo refolds back into the pseudoknot which unfolds with a T_M of 67.8°C and a ΔH of 93.4 kcal/mol. Using the ΔG_{25}° obtained from the DSC experiment after subtracting the ΔG° of the pseudoknot a $K_{D \text{ DSC}}$ of 1.5×10^{-2} was calculated. *PsK-9*'s reaction with its full complementary strand unfolded with T_M s of 58.7 and 67.9°C and ΔH s of 39.5 and 87.9 kcal/mol, Table 6. Using the ΔG_{25}° of the duplex obtained from the DSC experiment after subtracting the ΔG° of the pseudoknot and target strand a $K_{D \text{ DSC}}$ of 6.4×10^{-2} was calculated.

The $K_{D \text{ DSC}}$ values are not in good agreement with the experimental obtained from the SPR experiments, Table 7. One reason for this is it's possible that SPR is measuring initiation rates, while DSC is measuring true equilibrium of the duplex. This can be rationalized because the same targeting reaction for *PsK-9* with *CS-9 Full* was previously determined (Chapter 5) in 10 mM NaPi, 100 mM NaCl at pH 7.0. The unfolding $\Delta G_{\text{HC}}^\circ$ for this reaction at 25°C would be 1.8 kcal/mol which would result in a $K_{D \text{ DSC}}$ of 5.0×10^{-2} . This confirms the $K_{D \text{ DSC}}$ value of 6.4×10^{-2} we are observing in the 2X SSC buffer.

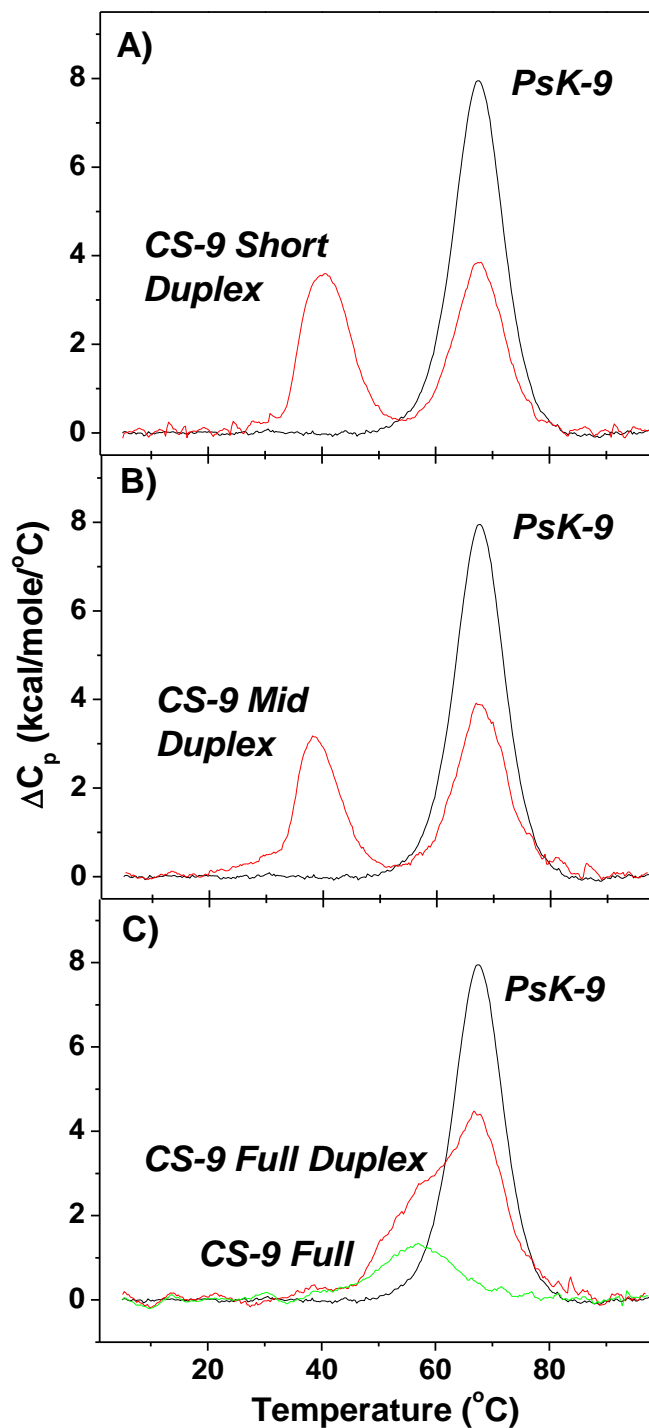


Figure 15. DSC unfolding of *PsK-9* and Reaction Products. A) *PsK-9* (22.7 μM) and *CS-9 Short Duplex* (22.7 μM). B) *PsK-9* (22.7 μM) and *CS-9 Mid Duplex* (22.7 μM). C) *PsK-9* (22.7 μM) and *CS-9 Full Duplex* (22.7 μM). All experiments were carried out in 2X SSC buffer at pH 7.0, 0.005% P20.

Table 6. Unfolding Thermodynamic Profiles for *PsK-9* and Duplex Products.

	Transition	T_M (°C)	ΔH (kcal/mol)	$T\Delta S$ (kcal/mol)	$\Delta G^\circ_{(25)}$ (kcal/mol)
<i>PsK-9</i>		67.5	90.1	77.5	12.6
<i>CS-9 Short Duplex</i>	1 st	40.7	41.2	38.5	2.7
	2 nd	67.7	88.4	76.0	12.4
	Total		129.6	114.5	15.1
<i>CS-9 Mid Duplex</i>	1 st	39.1	32.6	30.6	2.0
	2 nd	67.8	93.4	80.3	13.1
	Total		126	110.9	15.1
<i>CS-9 Full</i>		56.9	23.3	20.7	2.6
<i>CS-9 Full Duplex</i>	1 st	57.6	39.5	35.0	4.5
	2 nd	67.9	87.9	75.6	12.3
	Total		127.4	110.6	16.8

Experiments were carried out in 2X SSC buffer at pH 7.0, 0.005% P20. Experimental errors are as follows: T_M (± 0.5 °C), ΔH (± 5 %), $T\Delta S$ (± 5 %), $\Delta G^\circ_{(20)}$ (± 7 %).

Table 7. DSC and SPR Equilibrium Constants for *PsK-9* Targeting Reactions

	$\Delta G^{\circ}_{\text{HC}}$ (kcal/mol)	$K_{\text{D DSC}}$	$K_{\text{D app.}}$ (M)
<i>CS-9 Short Duplex 25 °C</i>	2.5	1.5×10^{-2}	6.96×10^{-9}
<i>CS-9 Mid Duplex 25 °C</i>	2.5	1.5×10^{-2}	2.35×10^{-8}
<i>CS-9 Full Duplex 25 °C</i>	1.6	6.4×10^{-2}	2.66×10^{-7}

Experiments were carried out in 2X SSC buffer at pH 7.0, 0.005% P20. $\Delta G^{\circ}_{\text{HC}}$ is calculated from unfolding thermodynamic profiles. Experimental errors are as follows: $\Delta G^{\circ}_{\text{HC}}$ (± 14 %), $K_{\text{D DSC}}$ (± 7 %), $K_{\text{D app.}}$ (± 5 %).

6.4.6 *PsK-11* DSC Unfolding with Complementary Strands

The reaction of *PsK-11* with its complementary strands was characterized by DSC to determine the thermodynamic profiles for the reactants and products for each targeting reaction. *PsK-11* unfolds in a monophasic transition with a T_M of 67.4°C and an enthalpy of 91.9 kcal/mol and the product of the reaction with *CS-11 Short* unfolds with a biphasic transition, Figure 16A. We first observe the unfolding of the duplex product with a T_M of 46.1°C and ΔH of 45.1 kcal/mol and then it refolds back into the pseudoknot which has a T_M of 67.6°C and ΔH of 93.4 kcal/mol, Table 8. Using the unfolding ΔG°_{20} obtained from the DSC experiment, Table 2, after subtracting the ΔG° of the pseudoknot a $K_{D \text{ DSC}}$ of 1.2×10^{-3} was calculated. *PsK-11* with its complementary strand, *CS-11 Mid*, showed similar trends as the short complementary strand having two transitions indicating the unfolding of the duplex followed by the folding and unfolding of the pseudoknot, Figure 16B. We observed that the melting of the duplex takes place with a T_M of 44.1°C and ΔH of 44.2 kcal/mol and the pseudoknot unfolds at a T_M of 67.5°C and has a ΔH of 90.8 kcal/mol, Table 8. Using the ΔG°_{20} from the DSC we obtained a $K_{D \text{ DSC}}$ after subtracting the ΔG° of the pseudoknot of 3.5×10^{-3} .

The $K_{D \text{ DSC}}$ values are not in good agreement with the experimental obtained from the SPR experiments, Table 9. One reason for this difference could be due to different structures forming between the techniques. It's possible that SPR is measuring initiation rates, while DSC is measuring true equilibrium between the formation of the duplex products when there is a 1:1 ratio between the reactants.

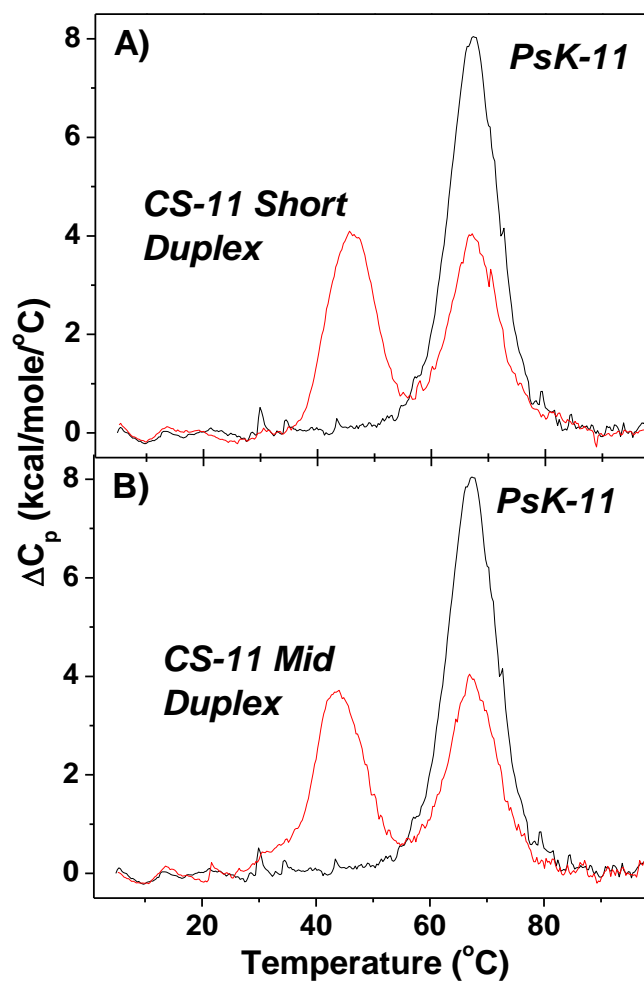


Figure 16. DSC unfolding of *PsK-11* and Reaction Products. A) *PsK-11* (30 μ M) and *CS-11 Short Duplex* (30 μ M). B) *PsK-11* (30 μ M) and *CS-11 Mid Duplex* (30 μ M). All experiments were carried out in 2X SSC buffer at pH 7.0, 0.005% P20.

Table 8. Unfolding Thermodynamic Profiles for *PsK-11* and Duplex Products.

	Transition	T_M (°C)	ΔH (kcal/mol)	$T\Delta S$ (kcal/mol)	$\Delta G^\circ_{(20)}$ (kcal/mol)
<i>PsK-11</i>		67.4	91.9	79.1	12.8
<i>CS-11 Short Duplex</i>	1 st	46.1	45.1	41.4	3.7
	2 nd	67.6	93.4	80.4	13.0
	Total		138.5	121.8	16.7
<i>CS-11 Mid Duplex</i>	1 st	44.1	44.2	40.8	3.4
	2 nd	67.5	90.8	78.1	12.7
	Total		135	118.9	16.1

Experiments were carried out in 2X SSC buffer at pH 7.0, 0.005% P20. Experimental errors are as follows: T_M (± 0.5 °C), ΔH (± 5 %), $T\Delta S$ (± 5 %), $\Delta G^\circ_{(20)}$ (± 7 %).

Table 9. DSC and SPR Equilibrium Constants for *PsK-11* Targeting Reactions

	$\Delta G^{\circ}_{\text{HC}}$ (kcal/mol)	$K_{\text{D DSC}}$	$K_{\text{D app.}}$ (M)
<i>CS-11 Short Duplex 20 °C</i>	3.9	1.2×10^{-3}	1.49×10^{-9}
<i>CS-11 Short Duplex 25 °C</i>	3.9	1.4×10^{-3}	4.2×10^{-9}
<i>CS-11 Mid Duplex 20 °C</i>	3.3	3.5×10^{-3}	1.81×10^{-9}
<i>CS-11 Mid Duplex 25 °C</i>	3.3	3.8×10^{-3}	6.74×10^{-9}

Experiments were carried out in 2X SSC buffer at pH 7.0, 0.005% P20. $\Delta G^{\circ}_{\text{HC}}$ is calculated from unfolding thermodynamic profiles. Experimental errors are as follows: $\Delta G^{\circ}_{\text{HC}}$ ($\pm 14\%$), $K_{\text{D DSC}}$ ($\pm 7\%$), $K_{\text{D app.}}$ ($\pm 5\%$).

6.5 CONCLUSIONS

The targeting reactions of three pseudoknots were characterized by surface plasmon resonance to determine the kinetic on and off rates to give dissociation constant for each reaction. This is a very common technique for the characterization for the binding constants for the interaction of ligand binding to nucleic acids and proteins, protein/protein interactions, protein/nucleic acid interactions, and DNA/DNA duplex formation. However, there hasn't been much work done in the field exploring the targeting of different nucleic acid secondary structures with complementary strands using this technique, so our main objective was to develop the technique for this type of interaction.

The main observation that can be drawn from this study is that as the targeting strand increases in length the rate of association, k_{on} , decreases and the rate of dissociation, k_{off} , increases. This reflects in the $K_{D\ app}$ values, the affinity of the target strand towards the pseudoknot decreases as the length of the target strand increases. This can be rationalized when looking at the DSC unfolding of the duplex products because as the targeting strand length increases the ΔG° of the reaction decreases, resulting in less favorable K_D values. Also, as the loop length of the pseudoknot increases, when comparing *PsK-5* and *PsK-11*, there is an increase in affinity for its targeting strand and this is due to the unpaired bases in the loop driving the reaction forward. We also find with *PsK-11*'s reactions there is an average activation enthalpy of 12 kcal/mol, which corresponds to 2 base-pair stacks. The most important thing to note here is that the $K_{D\ app}$ measured by SPR appears to be only measuring the initial association and dissociation rates and this could be a huge reason as to why these values are not matching those measured by DSC which would be at true equilibrium in a 1:1 ratio. Also, it's important

to note previous studies looking at DNA/DNA interaction have looked at single strands without complex secondary structures. This is the first time investigating the targeting of a pseudoknot with complementary strands using SPR to obtain the kinetic rates for its reaction.

The future directions of this work would be to conduct isothermal titration calorimetry (ITC) experiments to estimate the K_D to compare the binding affinities obtained from SPR and DSC since there is some discrepancy between the values. We also plan to conduct an experiment looking at the formation of short duplexes as a function of target strand length to compare the results obtained here. We will then expand this study to include different secondary structures including but not limited to: pseudoknots with varying sequences, 3 arm junctions and 4 arm junctions.

CHAPTER SEVEN

THERMODYNAMIC CHARACTERIZATION OF *PREQ*₁ RIBOSWITCH IN BOUND AND UNBOUND STATES

7.1 SUMMARY

We report on preliminary studies for the structural changes of the *preQ*₁ riboswitch DNA analog using DSC with different salt conditions in the bound and unbound states. The unfolding data suggests different structures are forming in the unbound state based on the results obtained and further analysis of the sequence. Under low salt conditions *PreQ*₁ has two transitions with a maximum T_M of 22°C and an overall ΔH of -39.0 kcal/mol, increasing the salt to a total concentration of 116 mM gave rise to what appeared as a possible third transition. The max T_M under these conditions is 38.9°C yielding a total ΔH of -69.1 kcal/mol. However, increasing the salt to 216mM still gave rise to three transitions with a max T_M of 43.7°C and a total ΔH of -68.2 kcal/mol. *PreQ*₁ *HP* had similar results to *PreQ*₁ under these same conditions. Based on the sequence, the additional transition could be due to a duplex with mismatches and wobble base-pairs. The duplex would unfold first resulting in the unfolding of the hairpin based on the observed enthalpies when compared to the control *PreQ*₁ *T*₅ (-41 kcal/mol). In the ligand bound state there are changes in the structure due to the observed differences in the T_M and enthalpies, but are most noticeable under low salt conditions. This could mean that in higher salt conditions some of the *PreQ*₁ is already in a pseudoknot like structure, so the

observed changes upon the addition of the ligand are minimized compared to the low salt conditions. More studies will need to be done to confirm this finding.

7.2 INTRODUCTION

Riboswitches are noncoding RNA elements that control gene expression and monitor the cellular environment (52). They are composed of a highly conserved aptamer domain and an expression platform which controls the genetic on/off switch (53). Riboswitches are cis-acting mRNA sequences that provide a well-designed solution to the problem of bacterial gene regulation. By directly sensing small molecules via an aptamer domain, riboswitches can adapt quickly to fluctuations in intracellular ligand concentration to establish a feedback loop that controls the production or import of metabolites, or the response to second messengers (54). Several ligands have been identified that are recognized by multiple, structurally unrelated riboswitch classes; this group includes: SAM, cyclic-di-GMP, and preQ₁ (55), (56).

The riboswitch of interest due to its size and structure is preQ₁. The preQ₁ riboswitch is responsive to preq₁ which is the final metabolite on the biosynthetic pathway that produces the hypermodified nucleotide queuosine (Q). Q is an important modification that enhances translational accuracy (57-59) by incorporating Q at the wobble position of specific anticodons in several eukaryotic and bacterial tRNAs (58). Q deficiency in bacteria can lead to reduced growth in the stationary phase (59) and reduced virulence (60). To meet regulatory needs, riboswitches responsive to preq₁ evolved into two phylogenetically distinct riboswitch classes. The preQ₁-I (class 1) aptamer is distributed widely and is 34 nucleotides (61). The preQ₁-II riboswitch is 80 nucleotides

and it regulates expression at the translational level (62), while the preQ₁-III is 120 nucleotides and much more complex in structure (63).

There have been a number of structural studies done on the class I preQ₁ aptamer and there is still some discrepancy on the bound and unbound states of the riboswitch, particularly the unbound structure (53), (162). In one study it suggests that the 3' tail is already in a pre-folded like state similar to that of the H-type pseudoknot (162), (163). There was another study done which suggests there is a possibility of kissing hairpins occurring between the loops of the hairpin structure (53). Since our laboratory is interested in both the putative structure and overall physical properties for the folding (and unfolding) of nucleic acid stem-loop motifs, we want to investigate what is occurring from a physio-chemical point of view.

In this work, we have determined the unfolding thermodynamics of a DNA oligomer with sequence of the preQ₁ riboswitch (*PreQ₁*). We have found that the unbound state is likely to form a kissing hairpin and/or duplex with the flanking 3' tail. It also forms a duplex with mismatches and wobble base-pairs which unfolds forming into a hairpin structure. This observation was confirmed by using control molecules without the 3' tail (*PreQ₁ HP*) which forms a pseudoknot upon binding of preq₁ and also a PreQ₁ hairpin with a T₅ loop (*PreQ₁ T₅*) which would minimize any loop interaction to avoid any kissing hairpin formation. To avoid confusion it's important to note the oligos are capitalized and the ligand in lowercase.

7.3 MATERIALS AND METHODS

Materials. All oligonucleotides were synthesized by the Integrated DNA Technologies (IDT) (Coralville, IA), HPLC purified, and desalted by column chromatography using G-10 Sephadex exclusion chromatography. The sequences of oligonucleotides used in this work and their designation are shown in Figure 1. The concentrations of the oligomer solutions were determined at 260 nm and 90°C using an Aviv Spectrophotometer Model 14DS UV-Vis using the molar extinction coefficients listed previously: 376 mM⁻¹ cm⁻¹ (*PreQ_I*), 252 mM⁻¹ cm⁻¹ (*PreQ_I HP*), 180 mM⁻¹ cm⁻¹ (*PreQ_I T₅*). These values were obtained by extrapolation of the tabulated values for dimers and monomeric bases (96), (130) at 25°C to 90°C using procedures reported previously (97), (129). Inorganic salts from Sigma were reagent grade, and used without further purification. All oligonucleotide solutions were prepared by dissolving the dry and desalted ODNs in buffer.

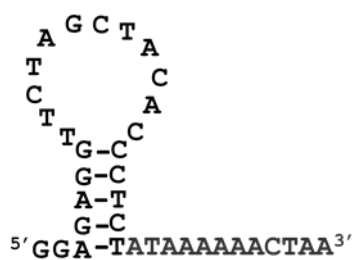
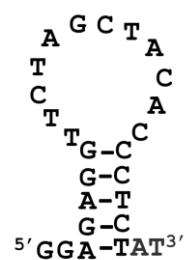
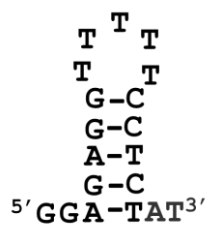
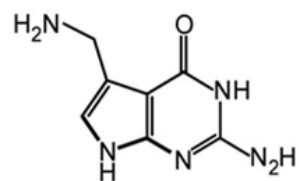
*PreQ₁**PreQ₁ HP**PreQ₁ T₅**peq₁ (ligand)*

Figure 1. Sequences, structures and designation of the molecules investigated.

Temperature-Dependent UV Spectroscopy. Absorbance versus temperature profiles were measured at 260 nm with a thermoelectrically controlled Aviv Spectrophotometer Model 14DS UV-Vis (Lakewood, NJ). The temperature was scanned at a heating rate of 0.6 °C/min, and shape analysis of the melting curves yielded transition temperatures, T_{MS} (98). The transition molecularity for the unfolding of a particular complex was obtained by monitoring T_M as a function of the strand concentration. Intramolecular complexes show a T_M -independence on strand concentration, while the T_M of intermolecular complexes does depend on strand concentration (129).

Differential Scanning Calorimetry. The total heat required for the unfolding of each oligonucleotide was measured with a VP-DSC differential scanning calorimeter from Microcal (Northampton, MA). Standard thermodynamic profiles and T_{MS} are obtained from the DSC experiments using the following relationships (98), (129): $\Delta H_{cal} = \int \Delta C_p(T) dT$; $\Delta S_{cal} = \int \Delta C_p(T) / T dT$, and the Gibbs equation, $\Delta G^\circ_{(T)} = \Delta H_{cal} - T \Delta S_{cal}$; where ΔC_p is the anomalous heat capacity of the ODN solution during the unfolding process, ΔH_{cal} and ΔS_{cal} are the unfolding enthalpy and entropy, respectively, assumed to be temperature-independent. $\Delta G^\circ_{(T)}$ is the free energy at temperature T , 5 °C.

7.4 RESULTS

7.4.1 UV Unfolding of Complexes

Typical UV melting curves for *PreQ₁* and control molecules at 260 nm are shown in Figure 2A. All three curves are sigmoidal and show T_{MS} ranging from 20°C to 44°C (Figure 2A) with similar hyperchromicities of 20%. The main observation is there is an increase in the T_M as the loop length of the hairpins decreases, which is a similar effect that is normally seen with decreasing the loop length of straight hairpin loops (128). Next, we follow the T_M as a function of strand concentration (Figure 2B) to determine the transition molecularity of each molecule and we find that each molecule forms an intramolecular structure due to similar T_{MS} over a 10-fold increase in strand concentration.

7.4.2 DSC Unfolding of *Preq₁* in Unbound State

The DSC unfolding for *PreQ₁* and control molecules are shown in Figure 3 under three different salt conditions. The same general trend is observed for all molecules, increasing the salt concentration stabilizes the structures by increasing the T_M and enthalpy of the molecule, Table 1. Under low salt conditions *PreQ₁* has two transitions one with a T_M of 15.1°C and an observed enthalpy of -9.1 kcal/mol and the second transition with a T_M of 22°C with an enthalpy of -29.9 kcal/mol, Table 1. Increasing the salt to 116 mM gave rise to what appeared as a possible third transition. The first transition has a T_M of 22.3°C, ΔH of -5.6 kcal/mol, the second transition has a T_M of 28.7°C, ΔH of -16.7 kcal/mol, and the third transition a T_M of 38.9°C, ΔH of -46.8 kcal/mol, Table 1.

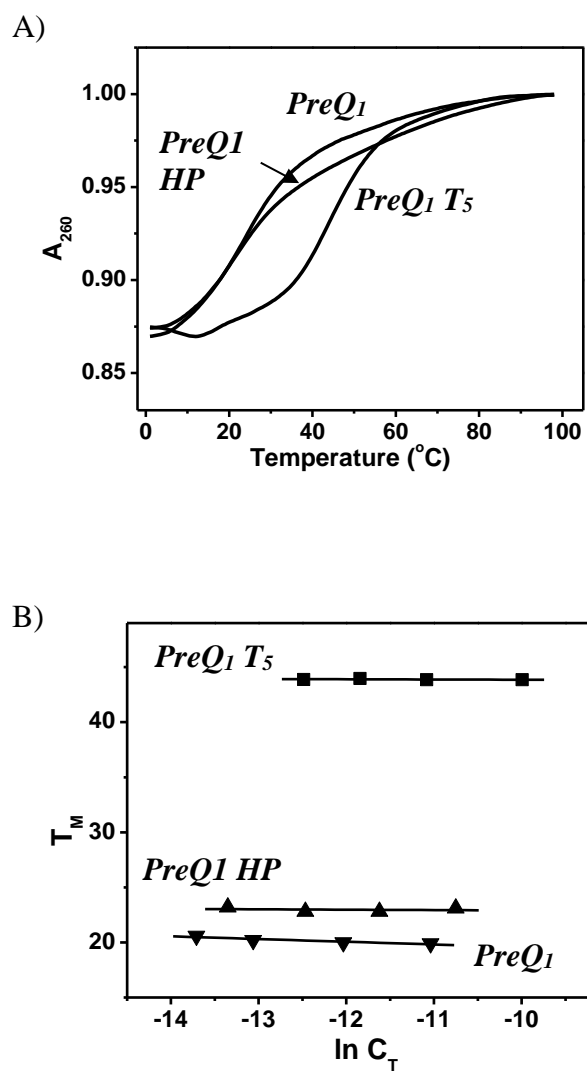


Figure 2. UV Melting Curves and T_M Dependence on Concentration. All experiments were carried out in 10 mM Phosphate buffer at pH 7.0; T_M ($\pm 0.5^{\circ}\text{C}$). Concentrations used ranged between 1-46 μM .

Increasing the salt to even higher concentration, 216 mM, still gave rise to three transitions with the first having a T_M of 24.7°C, ΔH of -5.4 kcal/mol, the second transition having a T_M of 32.4°C, ΔH of -6.8 kcal/mol, and the third transition a T_M of 43.7°C, ΔH of -56.8 kcal/mol, Table 1. When predicting the structure based on the previous structures of the preQ₁ riboswitch we were expecting only one transition from a hairpin formation in the DSC melting curve and a predicted enthalpy of -31.8 kcal/mol based on nearest-neighbor calculations (124), (126), (127). To get a better idea of what was happening we created a control molecule without the 3' tail and characterized the hairpin of the preQ₁ riboswitch. The rationale behind this was the tail under metabolite bound conditions interacts with the loop of the hairpin to form a pseudoknot structure, Figure 4A. We wanted to confirm the 3' tail was not interacting with the loop under unbound conditions. This hairpin, however, resulted in very similar melting curves, Figure 3B, indicating that it's possible the 3'tail is not interacting with the loop of the preQ₁ riboswitch. *PreQ₁ HP* had total observed enthalpies of -49 kcal/mol (16mM Na⁺), -61.6 kcal/mol (116mM Na⁺), and -60.0 kcal/mol (216mM Na⁺), Table 1. The final control hairpin was the same stem as *PreQ₁ HP* with a T₅ loop which would also factor out any loop interactions. We observed a single transition with increasing T_M s from 42.9 to 58.6°C and enthalpies increasing from -40.2 to -41.9 kcal/mol with increasing salt concentrations, Table 1. This helps in when deciphering what could be happening in the melting of the *PreQ₁* and *PreQ₁ HP* sequence. So, when looking at the melting of both *PreQ₁* and *PreQ₁ HP* there could be many possible scenarios occurring. The first being, the first transition could be due to bimolecular interactions between the complementary of the loops known as “kissing hairpins” (Figure 4C) or a duplex forming due to the complementary of the flanking

residues of the hairpins (Figure 4D). This duplex, however would not be extremely stable due to the AA mismatches occurring in the center of the duplex. The second transition is the unfolding of the hairpin structure (Figure 4B) at low salt. Upon increasing the salt concentration another structure is being stabilized in *PreQ₁ HP* which based on the sequence it is believed to be duplex with mismatches and wobble base-pairs, Figure 4E. The duplex would unfold first followed by the unfolding of the hairpin based on the observed enthalpies when compared to the control *PreQ₁ T₅*. DSC was ran at different concentrations and it appears the first (16 mM, 116 mM, 216 mM Na⁺) and second (116 mM and 216 mM Na⁺) transitions show a decrease in T_M with a decrease in concentration, if the first and second transitions are due to intermolecular interaction the enthalpies listed in Table 1 would then be doubled in value.

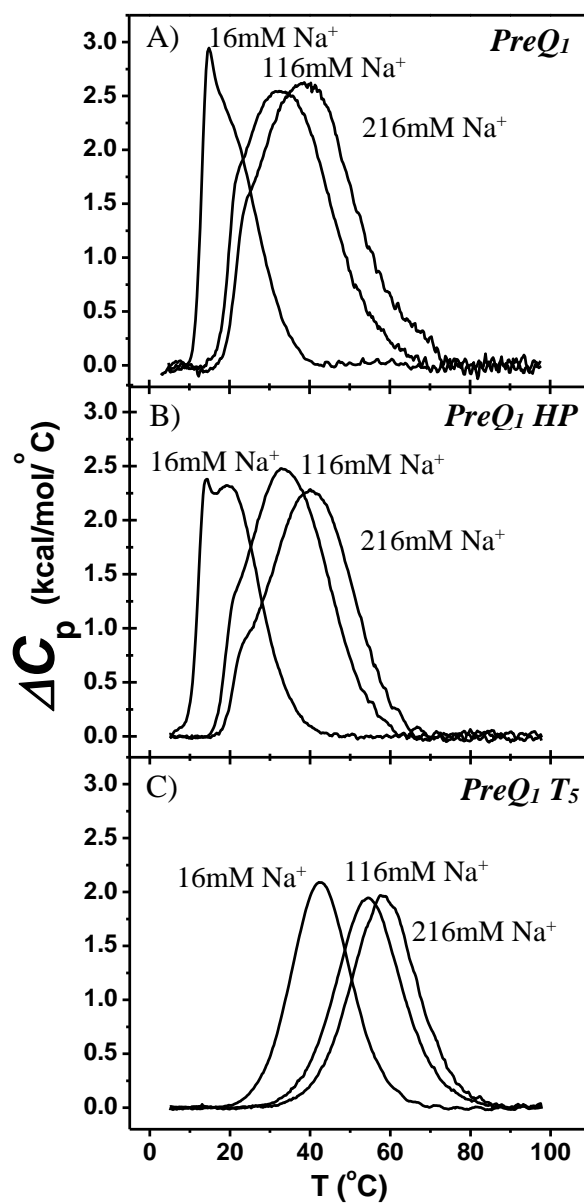


Figure 3. Unfolding of *Preq₁* and Controls. A) DSC unfolding of *PreQ₁*: concentrations used: 72 μM (16mM Na⁺), 41 μM (116mM Na⁺), 42 μM (216mM Na⁺). B) DSC unfolding of *PreQ₁ HP*: 74 μM (16mM Na⁺), 74 μM (116mM Na⁺), 67 μM (216mM Na⁺). C) DSC unfolding of *PreQ₁ T₅*: 135 μM (16mM Na⁺), 130 μM (116mM Na⁺), 125 μM (216mM Na⁺). All experiments were carried out in 10 mM Phosphate buffer at pH 7.0 with adjusted salt concentrations listed.

Table 1. Folding Thermodynamic Profiles for DNA PreQ₁ and Control Molecules.

[Na ⁺]	T_M (°C)	ΔH_{cal} (kcal/mol)	$T\Delta S_{cal}$ (kcal/mol)	ΔG°_5 (kcal/mol)
<i>PreQ₁</i>				
16 mM	15.1	-9.1	-8.7	-0.3
	22.0	-29.9	-28.1	-1.7
		-39.0	-36.8	-2.0
116 mM	22.3	-5.6	-5.3	-0.3
	28.7	-16.7	-15.4	-1.3
	38.9	-46.8	-41.7	-5.1
		-69.1	-62.4	-6.7
216 mM	24.7	-5.4	-5.0	-0.4
	32.4	-16.8	-15.3	-1.5
	43.7	-56.8	-49.7	-6.9
		-68.2	-70.0	-8.8
<i>PreQ₁ HP</i>				
16 mM	14.3	-14.0	-13.6	-0.4
	21.8	-35.0	-33.0	-2.0
		-49.0	-46.6	-2.4
116 mM	21.8	-5.0	-4.8	-0.3
	29.6	-20.1	-18.5	-1.6
	39.4	-36.5	-32.5	-4.0
		-61.6	-55.8	-5.9
216 mM	24.5	-4.0	-3.7	-0.3
	34.8	-23.2	-21.0	-2.2
	45.4	-32.8	-28.6	-4.2
		-60.0	-53.3	-6.7
<i>PreQ₁ T₅</i>				
16 mM	42.9	-40.2	-35.4	-4.8
116 mM	54.8	-41.4	-35.1	-6.3
216 mM	58.6	-41.9	-35.1	-6.8

All experiments were carried out in 10 mM Phosphate buffer at pH 7.0 and varying salt conditions. Experimental errors are as follows: T_M (± 0.5 °C), ΔH_{cal} (± 5 %), $T\Delta S_{cal}$ (± 5 %), $\Delta G^{\circ}_{(5)}$ (± 7 %).

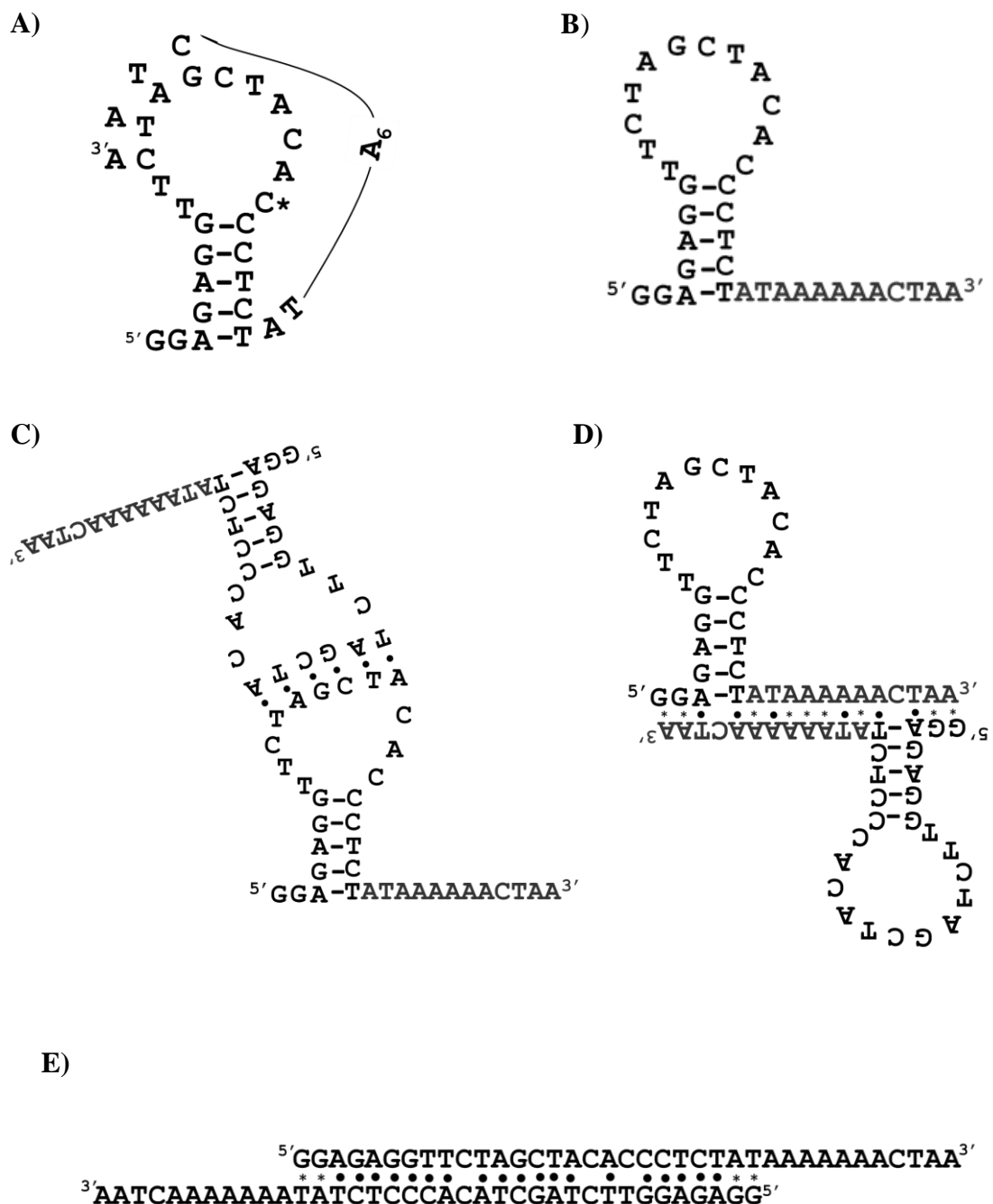


Figure 4. Possible Structures of *PreQ1* Based on Sequence. *Site where *preq1* binds.

7.4.3 DSC Unfolding of PreQ₁ in Bound State

The preQ₁ riboswitch has been previously found to bind the metabolite preq₁ in a 1:1 binding ratio using ITC (164), therefore the following DSC experiments were carried out under these conditions, Figure 5. *PreQ₁* in the metabolite bound state in low salt conditions still showed two transitions, however, the transitions were both shifted to higher temperatures 23.6 and 26.3°C, respectively. There was also an increase in the total observed enthalpy being measured at -50.9 kcal/mol compared to -39.0 kcal/mol in the unbound state, meaning the ligand is stabilizing the structure and the 3' tail is likely interacting with the loop of the hairpin forming the pseudoknot structure, Figure 4A. In salt conditions of 116 mM three peaks are still present in the melting curve and all T_M 's are shifted to higher temperatures and the total observed enthalpy is increased by -6.8 kcal/mol, indicating more stable structures are forming with ligand binding by 1 kcal/mol, Table 2. Upon additional salt added into the solution the effects of the ligand binding to the *PreQ₁* molecule is minimized. There aren't huge changes in the overall observed enthalpies between the 116 mM Na⁺ and the 216 mM Na⁺ when the ligand is bound to *PreQ₁*, Table 2. Also, when compared with the unbound state in this salt condition there is a shift in the T_{MS} of all three transitions, but there is a decrease in the observed enthalpy by 5.4 kcal/mol. This could mean that in higher salt condition some of the *PreQ₁* is already in a pseudoknot like structure (Figure 4A), so the observed changes upon the addition of the ligand are minimized compared to the low salt conditions.

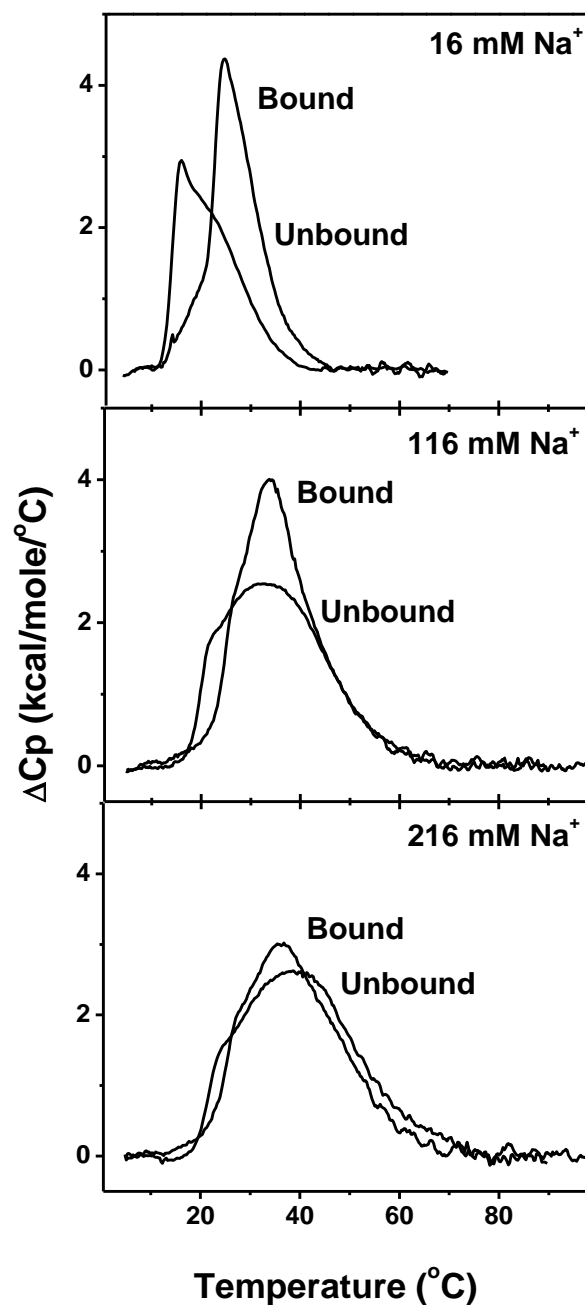


Figure 5. Unfolding of *PreQ1* in Bound and Unbound States. A) DSC unfolding of *PreQ1* bound (30 μ M) and unbound (72 μ M) in 16mM Na⁺. B) DSC unfolding of *PreQ1* bound (34 μ M) and unbound (41 μ M) in 116mM Na⁺. C) DSC unfolding of *PreQ1* bound (34 μ M) and unbound (42 μ M) in 216mM Na⁺. All experiments were carried out in 10 mM Phosphate buffer at pH 7.0 with adjusted salt concentrations listed.

Table 2. Folding Thermodynamic Profiles for DNA PreQ₁ in Bound State

[Salt]	T_M	ΔH_{cal}	$T\Delta S_{cal}$	ΔG°_5
	(°C)	(kcal/mol)	(kcal/mol)	(kcal/mol)
16 mM	23.6	-5.8	-5.4	-0.4
	26.3	-45.0	-41.8	-3.2
		-50.8	-47.2	-3.6
116 mM	26.6	-3.7	-3.4	-0.3
	33.0	-30.2	-27.4	-2.8
	39.4	-42.0	-37.4	-4.6
		-75.9	-68.2	-7.7
216 mM	27.3	-3.3	-3.1	-0.2
	34.8	-39.7	-35.9	-3.9
	45.7	-30.6	-26.7	-3.9
		-73.6	-65.7	-8.0

All experiments were carried out in 10 mM Phosphate buffer at pH 7.0 and varying salt conditions. Experimental errors are as follows: T_M (± 0.5 °C), ΔH_{cal} (± 5 %), $T\Delta S_{cal}$ (± 5 %), $\Delta G^\circ_{(5)}$ (± 7 %).

7.5 CONCLUSIONS AND FUTURE DIRECTIONS

In this chapter, we used a DNA oligonucleotide to model the folding of the preQ₁ riboswitch, which is an important structure in biology. We used this sequence along with two control molecules during this study to answer an important question where there is still some debate in the field even after structural data has been obtained. Our questions is whether or not the preQ₁ riboswitch is able to form into a pseudoknot-like structure before the binding of its response mediated ligand, preq₁.

Our experimental approach was to use a combination of temperature-dependent spectroscopy and calorimetry techniques to determine the formation of pseudoknot within the preQ₁ riboswitch. The first observation is that DNA strands are able to form an intramolecular structure. The unfolding DSC data showed that there is the potential for different structures to be forming based on the sequence. For example, in the unbound state the first small transition observed in the majority of the curves could be due to either kissing hairpins (Figure 4C) forming or a duplex between the flanking residues of the hairpins (Figure 4D). Under low salt conditions *PreQ₁* is forming a hairpin structure (Figure 4B). Upon increasing the salt in the buffer conditions another structure is being stabilized in *PreQ₁* and *PreQ₁ HP* which based on the sequence it is believed to be duplex with mismatches and wobble base-pairs (Figure 4E). The duplex would unfold first resulting in the unfolding of the hairpin (Figure 4B) based on the observed enthalpies when compared to the control *PreQ₁ T₅*. So, in the unbound state depending on the salt conditions *PreQ₁* is likely to form either a hairpin or duplex structure. In the ligand bound states there were definitely changes in the structure due to the observed differences in the T_M and enthalpies of the melts, but most noticeable under low salt conditions. This

could mean that in higher salt conditions some of the *PreQ_I* is already in a pseudoknot like structure (Figure 4A), so the observed changes upon the addition of the ligand are minimized compared to the low salt conditions. More studies will need to be done to confirm this finding.

Future directions of this study would include studying the unfolding of another control hairpin with a similar sequence as the *PreQ_I HP*, but without the flanking side residues (^{5'}AGAGGTTCTAGCTACACCCTCT^{3'}). This would confirm if there is a formation of any hairpins with short flanking duplexes forming. We will also repeat these experiments with the *preQ_I* riboswitch RNA sequence. It will be interesting to see if similar results are obtained and if the RNA sequence is likely to form into an equilibrium between a duplex state and hairpin state like the DNA sequence. Another suggestion is to target this molecule with a short single stranded DNA sequence that would target the loop of the hairpin structure to prohibit the binding of *preq_I*. This could potentially have influence at a biological level to control the production of queuosine because queuosine deficient bacteria can lead to reduced virulence (60).

CHAPTER EIGHT

CONCLUSIONS AND FUTURE STUDIES

In this dissertation we report on the energy contributions for the formation of DNA and RNA pseudoknots, the targeting reaction of DNA pseudoknots with their complementary strands, and the characterization of a biologically relevant pseudoknot riboswitch. A combination of spectroscopic, calorimetric, and kinetic techniques were used to investigate: (1) Local base-triplet formation in pseudoknot secondary structures and the effect of buffer conditions on DNA, dU, and RNA pseudoknots; (2) energetic contribution for the association of pseudoknots with their complementary strands, including the kinetic rates as a function of targeting strand length; and (3) characterization of the preQ₁ riboswitch DNA analog in its unbound and ligand bound states. In the following sections, we summarize our conclusions for each of the foregoing projects and offer ideas for future work.

8.1. LOCAL BASE-TRIPLET FORMATION IN PSEUDOKNOT SECONDARY STRUCTURES AND THE EFFECT OF BUFFER CONDITIONS ON DNA, DU, AND RNA PSEUDOKNOTS

We used a set of pseudoknots to study the unfolding thermodynamics of pseudoknots which are an important motif in the biology of RNA. This is due to their wide spread functional roles and variation in their stem sequence, the fluctuation of loop length and sequence, as well as, their interactions among themselves. The triplet formation in pseudoknots is believed to be involved in the mechanism of ribosomal frameshifting which lead to the development of this study. Our question was whether or

not base-triplet formation is possible if stem-loop complementarity is present in the pseudoknot's structure.

Our findings showed that base-triplet formation was dependent on loop length and complementarity between the stem and loop. In this particular set of pseudoknots the stem length of 7 A•T require at least 7 thymines in the loop in order to see the formation of base-triplets. Based on the enthalpy observed, a loop length of 5 thymines constrained the molecule too much and formation of base-triplets did not take place. As the length of the thymine loop is increased from 5 to 11, additional base-triplet stacks are formed, indicating that triplet formation is loop length dependent. This formation was indicated by the increase in the T_M and a more favorable ΔH in the folded state which resulted in an increase in the overall stability of the molecule. Also, $T\Delta S$ decreased due to the intramolecular folding of the pseudoknots and the uptake of water and counterions resulting in the typical enthalpy/entropy compensation. There was also an increase in the ΔV of the folded pseudoknots which may be explained in terms of the observed uptake of water and ions. This together confirms the formation of base-triplets with an increase in loop length of the pseudoknots. The base-triplets formed were disrupted when the sequence of the stem was mutated, disrupting the complementarity of the stem and loop. This confirms that it's important for the stem and loop to show complete complementarity in order to form base-triplets, at least in the case of this particular set of pseudoknots. With our 2-AP studies, we also showed these base-triplets are likely to form at the junction of the two stems in the core of the pseudoknot and the thymine loop most likely follows the major groove of the 7 A•T duplex stem. We also found that C⁺GC

triplets are capable of forming in pseudoknots and lowering the pH increased the strength of this triplet.

We used a set of oligonucleotides based on *PsK-11*, which was found to form three base-triplet stacks, to determine solvent effects between DNA, dU substituted, and RNA molecules. The following buffers: 10 mM NaPi, 10 mM NaCac, and 10 mM NaCac with Mg^{2+} were compared. In all of the buffer conditions used *PsK-11dU* was the most unstable molecule followed by *PsK-11dT*. *PsK-11RNA* was the most stable molecule. The destabilizing effect observed from the dU loop substitution is due to the formation of weaker TAU/TAU base-triplet stacks and the higher stability of *PsK-11RNA* is explained in terms of AA/UU base-pair stacking being less stable than AA/TT, therefore stronger UAU base-triplets would form and *PsK-11RNA* also has a higher predicted ΔG based on nearest-neighbor calculations due to the other stem of the pseudoknot. Comparing the buffers, there was a decrease in the stability of all of the molecules when going from 10 mM NaPi to 10 mM NaCac which may be due to hydration effects.

The addition of Mg^{2+} to the 10 mM NaCac buffer showed an increase in stability when compared with both 10 mM NaPi and 10 mM NaCac buffers for all of the molecules, due to electrostatic stabilization. In particular, we were able to show the formation of local base-triplets in both the DNA and RNA pseudoknots under three buffer conditions. However, it is important to consider the buffer you are running your experiments with when working with nucleic acids. It is also very important to consider the buffer that has been used when comparing data in the field because based on these results there are significant differences in the overall thermodynamic profiles depending on the solvent conditions of the experiment. Overall, this investigation confirms oligos

with DNA sequences are flexible enough to form pseudoknots; therefore, they can be used to mimic known RNA secondary structures.

One thing that is not 100% clear in the effects of buffer on DNA, dU substitution, and RNA pseudoknots, is if hydration differences can be the main cause for the decrease in stability when comparing 10 mM NaPi with 10 mM NaCac. This could be due to cacodylate being larger than phosphate ions the steric difference could exclude water around the pseudoknot. This is why we propose to carry out PPC experiments in all three buffer conditions to confirm if this effect can be attributed to hydration levels.

8.2. ENERGETIC CONTRIBUTION FOR THE ASSOCIATION OF PSEUDOKNOTS WITH THEIR COMPLEMENTARY STRANDS, INCLUDING THE KINETIC RATES AS A FUNCTION OF TARGETING STRAND LENGTH

We used a set of pseudoknots which we found to form zero to two/three base-triplet stacks to target with complementary strands to mimic the targeting of RNA secondary structures with DNA oligos. From this secondary structure the target strands can be designed to target the structures with unpaired bases to drive the reaction forward. The novelty of this approach is several fold, DNA oligonucleotides are less expensive than RNA oligonucleotides and more stable against hydrolysis, and most important the resulting DNA-DNA thermodynamic data is similar to the DNA-RNA thermodynamic data, in terms of nearest-neighbor contributions, which is obtained in the targeting of RNA molecules with DNA complementary strands.

Our findings showed that each targeting strand was able to disrupt *PsK-5* and *PsK-9*, respectively. However, the disruption of *PsK-9* takes place with a less favorable free energy contribution in 10 mM NaPi, 100 mM NaCl at pH 7.0. This is due to *PsK-9*

having a larger free energy than *PsK-5*, resulting from the formation of base-triplets that need to be broken in order to form the final duplex product. This results in less favorable free energy contributions. The results from this set of targeting reactions confirms our previous finding of *PsK-9* forming local base-triplets.

From the kinetic studies we found that as the targeting strand increases in length the rate of association, k_{on} , decreases and the rate of dissociation, k_{off} , increases in 2X SSC at pH 7.0 with 0.005% P20. This reflects in the $K_{D\ app}$ values, the affinity of the target strand to the pseudoknot decreases as the length of the target strand increases for each pseudoknot. This can be rationalized when looking at the unfolding of the reactants and duplex products. The ΔG°_{HC} becomes less favorable for each targeting reaction as the targeting strand length increases resulting in a less favorable $K_{D\ DSC}$. We observed very different values between the $K_{D\ app}$ measured by SPR and $K_{D\ DSC}$ calculated from ΔG° obtained from Hess cycles for each targeting reaction. The most important thing to note is that the $K_{D\ app}$ measured by SPR appears to be only measuring the initial association and dissociation rates and this could be a huge reason as to why these values are not matching those measured by DSC which would be at true equilibrium.

The favorable targeting of these pseudoknots depends on the length and sequence of the complementary strand. The general rule in targeting reactions is, the higher the number of base-pairs and base-pair stacks that are formed in the duplex product, the higher the free energy term; specifically, if a larger number of unpaired bases are involved in this base-pairing. This investigation of the targeting of DNA pseudoknots has enabled us to improve our method, based on physico-chemical principles, to determine

the thermodynamics of the targeting of nucleic acid secondary structures that can be used to control the expression of genes.

Future directions of these studies would include the targeting on additional pseudoknots including those studied in Chapter 1: *PsK-9-AT*, *PsK-5-1CGC*, *PsK-5-2CGC*, *PsK-9-1CGC*, *PsK-9-2CGC* which have TAT \rightarrow CGC substitutions directly by ITC and indirectly by DSC. Also, with the kinetic studies the K_D values need to be confirmed by another technique, for example ITC, to compare the binding affinities obtained from SPR and DSC since there are big discrepancies between the values potentially due to the measurement of different reactions, i.e., SPR is measuring initial association and dissociation rates and DSC is measuring true equilibrium between the two reactants. To better understand the differences between SPR and DSC it's best to work with a short duplex before using complicated secondary structures. Eventually we will also expand this study to include different secondary structures including but not limited to: pseudoknots with varying sequences, 3 arm junctions and 4 arm junctions.

8.3. CHARACTERIZATION OF THE PREQ₁ RIBOSWITCH DNA ANALOG IN ITS UNBOUND AND LIGAND BOUND STATES

Pseudoknots are also secondary structures found in riboswitches, which are noncoding RNA elements that control gene expression and monitor the cellular environment. The preQ₁ riboswitch, which forms a type H-pseudoknot when bound to its response ligand preq₁ regulates expression at the translational level. In this preliminary study, we provide insight in potential structures forming in the unbound and bound states of preq₁ using the DNA analog of this sequence.

The unfolding data showed that there is the potential for different structures to be forming based on the sequence and the results obtained. For example, in the unbound state the first small transition observed in the majority of the curves could be due to either the formation of dimers due to complementarity of the loops (kissing hairpins) or of the flanking ends (duplex). Under low salt conditions *PreQ1* forms a hairpin structure. Upon increasing the salt in the buffer conditions another structure is being stabilized in *PreQ1* and *PreQ1 HP* which based on the sequence it is believed to be duplex with mismatches and wobble base-pairs. The duplex would unfold first resulting in the unfolding of the hairpin when compared to the control *PreQ1 T5*, based on the unfolding enthalpies observed. So, in the unbound state depending on the salt conditions *PreQ1* is likely to form either a hairpin or duplex structure. In the ligand bound states there were changes in the structure due to the observed differences in the T_M and enthalpies of the melts, but most noticeable under low salt conditions. This could mean that in higher salt conditions some of the *PreQ1* is already in a pseudoknot like structure, so the observed changes upon the addition of the ligand are minimized compared to the low salt conditions.

Future directions of this study would include studying the unfolding of another control hairpin with a similar sequence as the *PreQ1 HP*, but without the flanking side residues. This would confirm if there is a formation of any hairpins with short flanking duplexes forming. We will also repeat these experiments with the *preQ1* riboswitch RNA sequence. It will be interesting to see if similar results are obtained and if the RNA sequence is likely to form an equilibrium between a duplex and a hairpin-state. Another suggestion is to target this molecule with a short single-stranded DNA sequence that would target the loop of the hairpin structure to prohibit the binding of *preq1*.

References

1. *Friedrich Miescher and the Discovery of DNA*. **Dahm, R.** 2005, *Dev. Biol.*, Vol. 278, pp. 274-288.
2. *Studies on the Chemical Nature of the Substance Inducing Transformation of Pneumococcal Types*. **Avery, O.T., MacLeod, C.M. and McCarty, M.** 1944, *The Journal of Experimental Medicine*, Vol. 79, pp. 137-158.
3. *Independent Functions of Viral Protein and Nucleic Acid in Growth of Bacteriophage*. **Hershey, A.D. and Chase M.** 1952, *The Journal of General Physiology*, Vol. 36, pp. 39-56.
4. *Molecular Structure of Nucleic Acids. A Structure For Deoxyribose Nucleic Acid*. **Watson, J.D. and Crick F.H.C.** 1953, *Nature*, Vol. 171, pp. 737-738.
5. *DNA comes in many forms*. **Rich, A.** 1993, *Gene*, Vol. 135, pp. 99-109.
6. *A Novel RNA Pentaloop Fold Involved in Targeting ADAR2*. **Stefl, R. and Allain, F.H.** 2005, *RNA*, Vol. 11, pp. 592-597.
7. *Fluorescence Studies of Nucleotides and Polynucleotides. I. Formycin, 2-aminopurine riboside, 2,6-diaminopurine riboside, and their derivatives*. **Ward, D.C., Reich, E. and Stryer, L.** 1969, *Journal of Biological Chemistry*, Vol. 244, pp. 1228-37.
8. *Structure and Dynamics of a Fluorescent DNA Oligomer Containing the EcoRI Recognition Sequence: Fluorescence, Molecular Dynamics, and NMR Studies*. **Nordlund, T.M., Andersson, S., Nilsson, L., Rigler, R., Graeslund, A. and McLaughlin L.W.** 1989, *Biochemistry*, Vol. 28, pp. 9095-9103.
9. *Synthesis and Properties of Defined DNA Oligomers Containing Base Mispairs Involving 2-Aminopurine*. **Eritja, R., Kaplan, B.E., Mhaskar, D., Sowers, L.C., Petreska, J. and Goodman, M.F.** 1986, *Nucleic Acids Research*, Vol. 25, pp. 5869-5884.
10. *2-Aminopurine Optical Spectra: Solvent, Pentose Ring, and DNA Helix Melting Dependence*. **Evans, K., Xu, D., Kim Y. and Nordlund, T.M.** 1992, *Journal of Fluorescence*, Vol. 2, pp. 209-216.
11. *Spectroscopic and Calorimetric Characterizations of DNA Duplexes Containing 2-Aminopurine*. **Law, S.M., Eritja, R., Goodman, M.F. and Breslauer K.J.** 1996, *Biochemistry*, Vol. 35, pp. 12329-12337.

12. *Probing Structure and Dynamics of DNA with 2-Aminopurine: Effects of Local Environment on Fluorescence.* **Rachosfsky, E.L., Osman, R. and Ross, J.B.A.** 2001, *Biochemistry*, Vol. 40, pp. 946-956.
13. *Dynmaics of the IRE RNA Hairpin Loop Probed by 2-Aminopurine Fluorescence and Stochastic Dynamics Simulations.* **Hall, K.B. and Williams, D.J.** 2004, *RNA*, Vol. 10, pp. 34-47.
14. *Fluorescence Properties of 2-Aminopurine in Human Telomeric DNA.* **Kimura, T., Kawai, K., Fujitsuka, M. and Majima, T.** 2004, *Chemical Communications*, Vol. 12, pp. 1438-1439.
15. *Recombination R-Triplex: H-Bonds Contribution to Stability as Revealed with Minor Base Substitutions for Adenine.* **Shchvolkina, A.K., Kaluzhny, D.N., Amdt-Jovin, D.J., Jovin, T.M. and Zhurkin, V.B.** 2006, *Nucleic Acids Research*, Vol. 34, pp. 3239-3245.
16. *Monitoring G-Quadruplex Structures and G-Quadruplex-Ligand Complex Using 2-Aminopurine Modified Oligonucleotides.* **Kimura, T., Kawai, K., Fujitsuka, M. and Majima, T.** 2007, *Tetrahedron*, Vol. 63, pp. 3585-3590.
17. *The Preparation of Site-Specifically Modified Ribo-Switch Domains as an Example For Enzymatic Ligation of Chemically Synthezied RNA Fragments.* **Lang, K. and Micura, R.** 2008, *Nature Protocols*, Vol. 3, pp. 1457-1466.
18. *On the Use of 2-Aminopurine as a probe for base pair opening during transcription initiation.* **Roy, S.** 2003, *Methods in Enzymology*, Vol. 370, pp. 568-578.
19. *2-Aminopurine Fluorescence Studies of Base Stacking Interactions at Abasic Sites in DNA: Metal-Ion and Base Sequence Effects.* **Stivers, J.T.** 1998, *Nucleic Acid Research*, Vol. 26, pp. 3837-3844.
20. *Hydrogen Bonding, Base Stacking, and Steric Effects in DNA Replication.* **Kool, E.T.** 2001, *Annu. Rev. Biophys. Biomol. Struct.*, Vol. 30, pp. 1-22.
21. *A tetrameric DNA structure with protonated cytosine base pairs.* **Gehring, K., Leroy, J.L. and Gueron, M.** 1993, *Nature*, pp. 561-565.
22. *Calorimetric unfolding of the bimolecular and i-motif complexes of the human telomere complementary strand, d(C(3)TA(2))(4).* **Kaushik, M., Suehl, N. and Marky, L.A.** 2007, *Biophys. Chem.*, pp. 154-164.
23. *Folding of the Thrombin Aptamer into a G-Quadruplex with Sr²⁺: Stability, Heat and Hydration.* **Kankia, B.I. and Marky L.A.** 2001, *J. Am. Chem. Soc.*, Vol. 123, pp. 10799-10804.
24. *Energetic Contribution for the Formation of TAT/TAT, TAT/CGC⁺, and CGC⁺/CGC⁺ Base Triplet Stacks.* **Soto, A. M., Loo, J., and Marky, L. A.** 2002, *J. Am. Chem. Soc.*, pp. 14355-14363.

25. *DNA Complexes Containing Joined Triplexed and Duplex Motifs: Melting Behavior of Intramolecular and Bimolecular Complexes with Similar Sequences.* **Lee, H-T., Khutsishbili, I. and Marky, L.A.** 2010, *J Phys Chem B.*, Vol. 114, pp. 541-548.
26. *Macromolecular therapeutics: emerging strategies for drug discovery in the postgenome era.* **Juliano, R.L., Astriab-Fisher, A. and Falke, D.** 2001, *Mol. Interv.*, pp. 40-53.
27. *Molecular mechanisms of action of antisense drugs.* **Crooke, S.T.** 1999, *BBA-Gene Struct Expr*, pp. 31-43.
28. *Rational design of sequence-specific oncogene inhibitors based on antisense and antigene oligonucleotides.* **Helene, C.** 1991, *Eur. J. Cancer*, pp. 1466-1471.
29. *Control of Oncogene Expression by Antisense Nucleic Acids.* **Helen, C.** *Eur. J. Cancer*, Vol. 30A, pp. 1721-1726.
30. *Triplex forming ability of a c-myc promoter element predicts promoter strength.* **Firulli, A.B., Maibenco, D.C. and Kinniburgh, A.J.** 1994, *Arch. Biochem. Biophys.*, pp. 236-242.
31. *Long (dA)_n x (dT)_n tracts can form intramolecular triplexes under superhelical stress.* **Fox, K.R.** 1990, *Nucleic Acid Res.*, pp. 5387-5391.
32. *A potential target for anti-cancer drug design.* **Han, H. and Hurley, L.H.** 2000, *Trends Pharmacol. Sci.*, pp. 136-142.
33. *Unusual DNA conformations: implications for telomeres.* **Mills, M., et al.** 2002, *Curr. Med. Chem.: Anti-Cancer Agents.*, pp. 627-644.
34. *Selection of single-stranded DNA molecules that bind and inhibit human thrombin.* **Bock, L.C., et al.** 1992, *Nature*, pp. 564-566.
35. *The tertiary structure of a DNA aptamer which binds to and inhibits thrombin determines activity.* **Wang, K.Y., et al.** 1993, *Biochemistry*, pp. 11285-11292.
36. *Suppression of human immunodeficiency virus type 1 activity in vitro by oligonucleotides which form intramolecular tetrads.* **Rando, R.F., et al.** 1995, *J. Biol Chem*, pp. 1754-60.
37. *Structure of the Human Telomerase RNA Pseudoknot Reveals Conserved Tertiary Interactions Essential for Function.* **Theimer, C.A., Blois, C.A., Feigon, J.** 2005, *Mol Cell*, Vol. 17, pp. 671-682.
38. *Targeting Human Telomerase in Cancer Therapy.* **Huard, S., and Autexier, C.** 2002, *Current Medicinal Chemistry: Anti-Cancer Agents*, Vol. 2, pp. 577-587.
39. *Crystal Structure of a Self-Splicing Group I Intron with Both Exons.* **Adams, P.L., Stahley, M.R., Kosek, A.B., Wang, J. and Strobel, S.A.** 2004, *Nature*, Vol. 430, pp. 45-50.

40. *A Long-Range Pseudoknot is Required for Activity of the Neurospora VS Ribozyme.* **Rastogi, T., Beattie, T.L., Olive, J.E., Collins, R.A.** 1996, EMBO J, Vol. 15, pp. 2820-2825.
41. *A Conformational Switch Controls Hepatitis Delta Virus Ribozyme Catalysis.* **Ke, A., Zhou, K., Ding, F., Cate, J.H., Doudna, J.A.** 2004, Nature, Vol. 429, pp. 201-205.
42. *Modeling RNA folding paths with pseudoknots: application to hepatitis delta virus ribozyme.* **Isambert, H. and Siggia, E.D.** 2000, Proc Natl Acad Sci USA, pp. 6516-20.
43. *Highly Conserved RNA Pseudoknots at Gag-pol Junction of HIV-1 Suggest a Novel Mechanism for -1 Ribosomal Frameshifting.* **Huang, X., Yang, Y., Wang, G., Cheng, Q., Du, Z.** 2014, RNA, Vol. 20, pp. 587-593.
44. *Triplex Structures in an RNA Pseudoknot Enhance Mechanical Stability and Increase -1 Ribosomal Frameshiftity.* **Chen, G., Chang, K.Y., Chou, M.Y., Bustamante, C., and Tinoco, I. Jr.** 2009, PNAS, Vol. 106, pp. 12706-12711.
45. *Tuning a Riboswitch Response Through Structural Extension of a Pseudoknot.* **Souliere, M.F., Altman, R.B., Micura, R.** 2013, PNAS, Vol. 110, pp. 3256-3264.
46. *Structural and Sequence Elements Required for the Self-Cleaving Activity of the Hepatitis Delta Virus Ribozyme.* **Thill, G. Vasseur, M., Tanner, N.K.** 1993, Biochemistry, Vol. 32, pp. 4254-4262.
47. *A Pseudoknot in the 3' Non-Core Region of the glmS Ribozyme Enhances Self-Cleavage Activity.* **Wilkinson, S.R. and Been, M.D.** 2005, RNA, Vol. 11, pp. 1788-1794.
48. *On Programmed Ribosomal Frameshifting the Alternative Proteomes.* **Kettler, R.** 2012, Frontiers in Genetics, Vol. 3.
49. *Enhancement of Ribosomal Frameshifting by Oligonucleotides Targeted to the HIV gag-pol Region.* **Vickers, T.A. and Ecker, D.J.** 1992, Nucleic Acid Research, Vol. 20, pp. 3945-3953.
50. *A Mechanical Explanation of RNA Pseudoknot Function in Programmed Ribosomal Frameshifting.* **Namy, O., Moran, S.J., Stuart, D.I., Gilbert, R.J. and Brierley, I.** 2006, Nature, Vol. 441, pp. 244-247.
51. *Calorimetric Unfolding of Intramolecular Triplexes: Length Dependence and Incorporation of Single AT-TA Substitutions in the Duplex Domain.* **Shikiya, R. and Marky, L.A.** 2005, J. Phys. Chem. B., Vol. 109, pp. 18177-18183.
52. *The Distributions, Mechanisms, and Structures of Metabolite-Binding Riboswitches.* **Barrick, J.E. and Breaker, R.R.** 2007, Genome Biolog, Vol. 8.
53. *Single Transcriptional and Translational PreQ1 Riboswitches Adopt Similar Pre-Folded Ensembles That Follow Distinct Folding Pathways Into The Same Ligand-Bound*

Structure. **Suddala, K.C., Rinaldi, A.J., Feng, J., Mustoe, A.M., Eichhorn, C.D., Liberman, J.A., Wedekind, J.E., Al-Hashimi, H.M., Brooks III, C.L. and Walter, N.G.** 2013, *Nucleic Acids Research*, Vol. 41, pp. 1042-10475.

54. *New Insights Into Riboswitch Regulation Mechanisms*. **Bastet, L., Dube A., Masse, M. and Lafontaine, D.A.** 2011, *Mol Microbiol*, Vol. 80, pp. 1148-1154.

55. *Recognition of S-adenosylmethionine by Riboswitches*. **Batey, R.T.** 2011, *Rev RNA*, Vol. 2, pp. 299-231.

56. *Structure and Mechanism of Purine-Binding Riboswitches*. **Batey, R.T.** 2012, *Q. Rev Biophys*, Vol. 45, pp. 345-81.

57. *Wild-Type tRNA TyrG Reads the TMV RNA Stop Codon, But Q Base-Modified tRNA TyrQ Does Not*. **Bienz, M. and Kubli, E.** 1981, *Nature*, Vol. 294, pp. 188-190.

58. *Three-Dimensional Structure of Hyper-Modified Nucleoside Q Located In The Wobble Position of tRNA*. **Yokoyama, S., Miyazawa, T., Iitaka, Y., Yamaizumi, Z., Kasai, H. and Nishimura, S.** 1979, *Nature*, Vol. 282, pp. 107-109.

59. *Isolation and Characterization of an Escherichia coli Mutant Lacking tRNA-Guanine Transglycosylase: Function and Biosynthesis of Gueuosine in tRNA*. **Noguchi, S., Nishimura, Y., Hirota, Y. and Nishimura S.** 1982, *J Biol Chem*, Vol. 257, pp. 6544-6550.

60. *vavC, A Virulence-Associated Chromosomal Locus of Shigella flexneria, is Homologous to tgt, A Gene Encoding tRNA-Guanine Transglycosylase (Tgt) of Escherichia coli K-12*. **Durand, J.M., Okada, N., Tobe, T., Watarai, M., Fukuda, I, Suzuki, T., Nakata, N., Komatsu, K., Yoshikawa, M. and Sasakawa C.** 1994, *J Bacteriol*, Vol. 176, pp. 4627-4634.

61. *A Riboswitch Selective For The Queuosine Precursor PreQ1 Contains An Unusually Small Aptamer Domain*. **Roth, A., Winkler, W.C., Regulski, E.E., Lee, B.W.K., Lim, J., Jona, L, Barrick, J.E., Ritwik, A., Kim, J.N., Welz, R., Iwata-Reuyl, D. and Breaker R.R.** 2007, *Nat Struct Mol Biol*, Vol. 14, pp. 308-317.

62. *Confirmation Of A Second Natural PreQ1 Aptamer Class in Streptococcaceae Bacteria*. **Meyer, M.M., Roth, A., Chervin, S.M., Garcia, G.A. and Breaker R.R.** 2008, *RNA*, Vol. 14, p. 2008.

63. *Structural, Functional, and Taxonomic Diversity of Three PreQ1 Riboswitch Classes*. **McCown, P.J., Liang, J.J., Weinberg, Z. and Breaker, R.R.** 2014, *Cell Press*, Vol. 21, pp. 880-889.

64. *Ethidium Derivatives Bind to G-Quartets, Inhibit Telomerase and Act as Fluorescent Probes for Quadruplexes*. **Koeppl, F., Riou J-F., Laoui, A., Mailliet, P., Arimondo, P.B., Labit, D., Petitgenet, O., Helene C. and Mergny, J-L.** 2001, *Nucleic Acid Res.*, Vol. 29, pp. 1087-1096.

65. *Targeting Human Telomerase by Antisense Oligonucleotides and Ribozymes.* **Folini, M., Pennati, M and Zaffaroni N.** 2002, *Curr. Med. Chem.: Anti-Cancer Agents.*, Vol. 5, pp. 605-612.
66. *Drug-DNA Interactions and Novel Drug Design.* **Gibson, D.** 2002, *Pharmacogenomics Journal*, Vol. 2, pp. 275-276.
67. *Selective Binding of Small Molecules to DNA.* **Wang, B., Tan, J. and Zhu, L.** 2010, *Application and Perspectives Colloids and Surfaces, B: Biointerfaces*, Vol. 79, pp. 1-4.
68. *Nuclear DNA Content and Genome Size of Trout and Human.* **Doleel, J., Voglmayr, H. and Greilhuber, J.** 2003, *Cytometry Part A.*, Vol. 51, pp. 127-128.
69. *Modulation of Gene Expression by Antisense and Antisense Oligodeoxynucleotides and Small Interfering RNA.* **Mahato, R.I., Cheng, K. and Guntaka, R.V.** 2005, *Experin Opin. Drug Delivery*, Vol. 2, pp. 3-28.
70. *Triplex DNA Structures.* **Frank-Kamenetskii, M.D. and Mirkin, S.M.** 1995, *Annu. Rev. Biochem.*, Vol. 64, pp. 65-95.
71. **Soyfer, V.N. and Potaman, V.N.** *Triple-Helical Nucleic Acids.* New York : Springer-Verlag, 1996. Vol. 360.
72. *Stabilities of Double and Triple Strand Helical Nucleic Acids.* **Cheng, Y.K. and Pettitt, B.M.** 1992, *Prog. Biophys. Mol. Bio.*, Vol. 58, pp. 225-257.
73. *Inhibition of DNA Binding Proteins by Oligonucleotide-Directed Triple Helix Formation.* **Maher, L.J. III, Wold, B., and Dervan P.B.** 1989, *Science*, Vol. 245, pp. 725-730.
74. *Specific Inhibition of Transcription by Triple Helix-Forming Oligonucleotides.* **Duval-Valentin, G., Thuong, N.T. and Helene, C.** 1992, *Proceedings of the National Academy of Sciences of the USA*, Vol. 89, pp. 504-508.
75. *Chromosome Targeting at Short Polypurine Sites by Cationic Triplex-Forming Oligonucleotides.* **Vasquez, K.M., Dagle, J.M., Weeks, D.L. and Glazer, P.M.** 2001, *J. Biol. Chem.*, Vol. 276, pp. 38536-38541.
76. *Triple-Helix Formation at Different Positions on Nucleosomal DNA.* **Brown, P.M., Madden, C.A. and Fox, K.R.** 1998, *Biochemistry*, Vol. 37, pp. 16139-16151.
77. *Role for a Bidentate Ribonuclease in the Inhibition Step of RNA Interference.* **Bernstein, E., Caudy, A.A., Hammond, S.M. and Hannon, G.J.** 2001, *Nature*, Vol. 409, pp. 363-366.
78. *The Microprocessor Complex Mediates the Genesis of microRNAs.* **Gregory, R.I., Yan, K-P., Amuthan, G., Chendrimada, T., Doratotaj, B., Cooch, N. and Shiekhattar, R.** 2004, *Nature*, Vol. 432, pp. 235-240.

79. *The Drosha-DGCR8 Complex in Primary microRNA Processing.* **Han, J., Lee, Y., Yeom, K-H., Kim, Y-K., Jin, H. and Kim, V.N.** 2004, *Genes & Development*, Vol. 18, pp. 3016-3027.
80. *The Nuclear RNase III Drosha Initiates microRNA Processing.* **Lee, Y., Ahn, C., Han, J., Choi, H., Kim, J., Yim, J., Lee, J., Provost, P., Radmark, O., Kim, S. and Kim, V.N.** 2003, *Nature*, Vol. 425, pp. 415-419.
81. *Exportin-5 Mediates the Nuclear Export of Pre-MicroRNAs and Short Hairpin RNAs.* **Yi, R., Qin, Y., Macara, I.G. and Cullen, B.R.** 2003, *Genes & Development*, Vol. 17, pp. 3011-3016.
82. *Human RISC Couples microRNA Biogenesis and Posttranscriptional Gene Silencing.* **Gregory, R.I., Chendrimada, T.P., Cooch, N. and Shiekhattar, R.** 2005, *Cell*, Vol. 23, pp. 631-640.
83. *An RNA-Directed Nuclease Mediates Post-Transcriptional Gene Silencing in Drosophila Cells.* **Hammond, S.M., Bernstein, E., Beach, D. and Hannon, G.J.** 2000, *Nature*, Vol. 404, pp. 293-296.
84. *Argonaute Proteins: Key Players in RNA Silencing.* **Hutvanger, G. and Simard, M.J.** 2008, *Nature Reviews Molecular Cell Biology*, Vol. 9, pp. 22-32.
85. *Exploring the Functions of RNA Interference Pathway Proteins: Some Functions Are More RISCy Than Others?* **Jaronczyk, K., Carmichael, J.B. and Hobman, T.C.** 2005, *Biochemical Journal*, Vol. 387, pp. 561-571.
86. *A Human, ATP-Independent, RISC Assembly Machine Fueled by Pre-miRNA.* **Maniataki, E. and Mourelatos, Z.** 2005, *Genes & Development*, Vol. 19, pp. 2979-2990.
87. *Functional siRNAs and miRNAs Exhibit Strand Bias.* **Khvorova, A., Reynolds, A. and Jayasena, S.D.** 2003, *Cell*, Vol. 115, pp. 209-216.
88. *Cleavage of the siRNA Passenger Strand During RISC Assembly in Human Cells.* **Leuschner, P.J.F., Ameres, S.L., Kueng, S and Martinez, J.** 2006, *EMBO Reports*, Vol. 7, pp. 314-320.
89. *Asymmetry in the Assembly of the RNAi Enzyme Complex.* **Schwartz, D.S., Hutvagner, G., Du, T., Xu, Z., Aronin, N.Z. and Philip, D.** 2003, *Cell*, Vol. 115, pp. 199-208.
90. *Passenger-Strand Cleavage Facilitates Assembly of siRNA into Ago2-Containing RNAi Enzyme Complexes.* **Matranga, C., Tomari, Y., Shin, C., Bartel, D.P. and Zamore, P.D.** 2005, *Cell*, Vol. 123, pp. 607-620.
91. *A Protein Sensor for siRNA Asymmetry.* **Tomari, Y., Matranga, C., Haley, B., Martinez, N. and Zamore, P.D.** 2004, *Science*, Vol. 306, pp. 1377-1380.

92. *Targeted mRNA Degradation by Double-Stranded RNA in vitro.* **Tuschl, T., Zamore, P.D., Lehmann, R., Bartel, D.P. and Sharp, P.A.** 1999, *Genes & Development*, Vol. 13, pp. 3191-3197.
93. *Specificity of microRNA Target Selection in Translational Repression.* **Doench, J.G. and Sharp, P.A.** 2004, *Genes & Development*, Vol. 18, pp. 504-511.
94. *Behind the Scenes of a Small RNA Gene-Silencing Pathway.* **Ku, G. and McManus, M.T.** 2008, *Human Gene Therapy*, Vol. 19, pp. 17-26.
95. *The C. elegans Heterochronic Gene lin-4 Encodes Small RNAs with Antisense Complementarity in lin-14.* **Lee, R.C., Feinbaum, R.L. and Ambros V.** 1993, *Cell*, Vol. 75, pp. 843-54.
96. *Oligonucleotide Interactions. 3. Circular Dichroism Studies of the Conformation of Deoxyoligonucleotides.* **Cantor, C.R., Warshaw, M.M. and Shapiro, H.** 1970, *Biopolymers*, Vol. 9, pp. 1059-1077.
97. *Salt-Dependent Conformational Transitions in the Self-Complementary Deoxydodocanucleotide d(CGCGAATTCGCG): Evidence for Hairpin Formation.* **Marky, L.A., Blumenfeld, K.S., Kozlowski, S., and Breslauer, K.J.** 1983, *Biopolymers*, Vol. 22, pp. 1247-1257.
98. *Calculating Thermodynamic Data for Transitions of Any Molecularity from Equilibrium Melting Curves.* **Marky, L.A. and Breslauer, K.J.** 1987, *Biopolymers*, Vol. 26, pp. 1601-1620.
99. **Cantor, C.R. and Schimmel P.R.** *Biophysical Chemistry*. San Francisco : W.H. Freeman and Company, 1980.
100. *Binding and Linkage.* **Wyman, J. and Gill, S.J.** Mill Valley, University Science Books : s.n., 1990.
101. *Effects of Hydration, Ion Release, and Excluded Volume on the Melting of Triplex and Duplex DNA.* **Spink, C.H. and Chaires, J.B.** 1999, *Biochemistry*, Vol. 38, pp. 496-508.
102. *Coupling of Sequential Transitions in a DNA Double Hairpin: Energetics, Ion Binding, and Hydration.* **Rentzeperis, D., Kharakoz, D.P. and Marky, L.A.** 1991, *Biochemistry*, Vol. 30, pp. 6276-6283.
103. *Na⁺ Effects on Transitions of DNA and Polynucleotides of Variable Linear Charge Density.* **Record, M.T.J., Woodbury, C.P. and Lohman, T.M.** 1976, *Biopolymers*, Vol. 15, pp. 839-915.
104. *Thermodynamics of an Intramolecular DNA Triple Helix: A Calorimetric and Spectroscopic Study of the pH and Salt Dependence of Thermally Induced Structural Transitions.* **Plum, G.E. and Breslauer, K.J.** 1995, *J. Mol. Biol.*, Vol. 248, pp. 679-695.

105. *Vapor Pressure Osmometry Studies of Osmolyte-Protein Interactions: Implications for the Action of Osmoprotectants in vivo and for the Interpretation of "Osmotic Stress" Experiments in vitro.* **Courtenay, E.S., Capp, M.W. Anderson, C.F. and Record, M.T.** 2000, *Biochemistry*, Vol. 39, pp. 4455-4471.
106. *Differential Scanning Calorimetry.* **Chowdhry, B.Z. and Cole, S.C.** 1989, *Trends Biochem. Sci.*, Vol. 7, pp. 11-18.
107. —. **Freire, E.** 1995, *Methods Mol. Biol.*, Vol. 40, pp. 191-218.
108. *Thermodynamic Analysis of Transfer RNA Unfolding.* **Privalov, P.L. and Filimiov, V.V.** 1978, *J. Mol. Biol.*, Vol. 122, pp. 447-464.
109. *Fluorescence Quenching of 2-Aminopurine in Dinucleotides.* **Somsen, O.J.G., Van Hoek, A. and Van Amerongen, H.** 2005, *Chemical Physics Letters*, Vol. 402, pp. 61-65.
110. **vanHolde, K.E., Johnson, W.C. and Ho, P.S.** *Principles in Physical Biochemistry.* s.l. : Upper Saddle River, Prentice-Hall, 1998.
111. **Rodger, A. and Norden, B.** *Circular Dichroism and Linear Dichroism.* New York : Oxford Press, 1997.
112. *Determinaiton of the Volumetric Properties of Proteins and Other Solutes Using Pressure Perturbation Calorimetry.* **Lin, L-N., Brandts, J.F. Brants, J.M. Plotnikov, V.** 2002, *Anal. Biochem.*, Vol. 302, pp. 144-160.
113. *Interaction of Alkaline-Earth Metal Ions with Calf Thymus DNA. Volume and Compressibility Effects in Diluted Aqueous Solutions.* **Kankia, B.I.** 2000, *Biophys. Chem*, Vol. 84, pp. 227-237.
114. *Theroretical Aspects of Isothermal Titration Calorimetry.* **Indyk, L. and Fisher, H.F.** 1998, *Methods Enzymol*, Vol. 295, pp. 350-364.
115. *Rapid Measurments of Binding Constants and Heats of Binding Using a New Titration Calorimeter.* **Wiseman, T., Williston, S., Brandts, J.F. and Lin L.N.** 1989, *Anal. Biochem.*, Vol. 159, pp. 131-137.
116. *Thermodynamic Contributions of the Reactions of DNA Intramolecular Structures with Their Complementary Strands.* **Lee, H-T., Olsen, C.M., Waters, L., Sukup., and Marky, L.A.** 2008, *Biochimie*, Vol. 90, pp. 1052-1063.
117. *A Thermodynamic Approach for the Targeting of Nucleic Acid Strucutres Using Their Complementary Single Strands.* **Lee, H-T., Carr, C., Siebler, H., Waters, L., Khutsishvili., Iseka, F., Domack, B., Olsen, C.M., and Marky, L.A.** 2011, *Methods in Enzymol*, Vol. 492, pp. 1-26.
118. **Khutsishvili, I., Johnson S.E., Reiling, C., Prislán, I., Lee, H-T. and Marky L.A.** *Interaction of DNA Intramolecular Structures with Their Complementary Strands: A*

Thermodynamic Approach for the Control of Gene Expression. [ed.] VA Erdmann et al. s.l. : RNA Technologies, 2014. pp. 367-383.

119. *Theory and Applications of Surface Plasmon Resonance, Resonant Mirror, Resonant Waveguide Grating, and Dual Polarization Interferometry Biosensors*. **Daghestani, H.N. and Day, B.W.** 2010, *Sensors*, Vol. 10, pp. 9630-9646.

120. **Tudos, A.J. and Schasfoort, R.B.M.** Introduction to Surface Plasmon Resonance. [ed.] R.B.M. and Tudos, A.J. Schasfoort. *Handbook of Surface Plasmon Resonance*. s.l. : RSC Publishing, 2008, pp. 1-14.

121. *Real-Time Analysis of Specific Protein-DNA Interactions with Surface Plasmon Resonance*. **Ritzefeld, M. and Sewald, N.** 2012, *Journal of Amino Acids*.

122. *Optical Biosensors in Drug Discovery*. **Cooper, M.A.** 2002, *Nature Reviews: Drug Discovery*, pp. 515-528.

123. *Control of Oncogene Expression by Antisense Nucleic Acids*. **Helen, C.** *Eur. J. Cancer*, Vol. 30A, pp. 1721-1726.

124. *Predicting DNA Stability from the Base Sequence*. **Breslauer, K.J., Frank, R., Blocker, H., and Marky, L.A.** 1986, *Proc. Natl. Acad. Sci. USA*, Vol. 83, pp. 3746-3750.

125. *Thermodynamic Parameters for an Expanded Nearest-Neighbor Model for Formation of RNA Duplexes with Watson-Crick Base Pairs*. **Xia, T., SantaLucia, J. Jr., Burkard, M.E., Kierzek, R., Schroeder, S.J., Jiao, X, Cox, C., Turner, D.H.** 1998, *Biochemistry*, Vol. 37, pp. 14719-14735.

126. *Improved Nearest-Neighbor Parameters for Predicting DNA Duplex Stability*. **SantaLucia, J. Jr., Allawi, H.T., and Seneviratne, P.A.** 1996, *Biochemistry*, Vol. 35, pp. 3555-3562.

127. *Thermodynamic Parameters to predict stability of RNA/DNA Hybrid Duplexes*. **Sugimoto, N., Nakano, S., Katoh, M., Matsumura, A, Nakamuta, H., Ohmichi, T. Yoneyama, M., Sasaki, M.** 1995, *Biochemistry*, Vol. 34, pp. 11211-11216.

128. *Differential Hydration of dA.dT Base Pairs in Parallel-Stranded DNA Relative to Antiparallel DNA*. **Rentzeperis, D., Kupke, D.W. and Marky, L.A.** 1994, *Biochemistry*, Vol. 33, pp. 9588-9591.

129. *Building Blocking of Nucleic Acid Nanostructures: Unfolding Thermodynamics of Intramolecular DNA Complexes*. **Marky, L.A., Maiti, S., Olsen, C.M., Shikiya, R., Johnson, S.E., Kaushik, M., and Khutsishvili, I.** [ed.] V. Labhasetwar and D. Leslie-Pelecky. s.l. : John Wiley & Sons, Inc., 2007, *Biomedical Applications of Nanotechnology*, pp. 191-225.

130. **Borer, P.N.** Optical Properties of Nucleic Acids, Absorptions and Circular Dichroism Spectra. [ed.] Fasman GD. *Handbook of Biochemistry and Molecular Biology*. 3rd. Cleveland : CRC Press, 1975, pp. 589-595.
131. *A Unified View of Polymer, Dumbbell, and Oligonucleotide DNA Nearest-Neighbor Thermodynamics.* **SantaLucia, J. Jr.** 1998, *Biochemistry*, Vol. 95, pp. 1460-1465.
132. *Influence of Dangling Thymine Residues on the Stability and Structure of Two DNA Duplexes.* **Senior, M., Jones, R.A. and Breslauer, K.J.** 1988, *Biochemistry*, Vol. 27, pp. 3879-3885.
133. **Alessi, K.** *Thermodynamic Contributions of Deoxyoligonucleotides Containing A-T Base-Pairs.* s.l. : PhD Dissertation, New York University, 1995.
134. *Nucleic Acid Duplex Stability: Influence of Base Composition on Cation effects.* **Nakano, S-I., Fujimoto, M., Hara, H. and Sugimoto, N.** 1999, *Nucleic Acids Research*, Vol. 27, pp. 2957-2965.
135. *The Molecular Theory of Polyelectrolyte Solutions with Applications to the Electrostatic Properties of Polynucleotides.* **Manning, G.S.** 1978, *Quart. Rev. Biophys.*, Vol. 11, pp. 179-246.
136. *Thermodynamic Analysis of Ion Effects on the Binding and Conformational Equilibria of Proteins and Nucleic Acids: The Roles of Ions Association or Release, Screening, and Ion Effects on Water Activity.* **Record, M.T. Jr., Anderson, C.F. and Lohman, T.M.** 1978, *Quart. Rev. Biophys.*, Vol. 11, pp. 103-178.
137. *Design of Triplex Helix Forming C-Glycoside Molecules.* **Li, J-S., Fan, Y-H., Zhang, Y., Marky, L.A. and Gold B.** 2003, *J. Am. Chem. Soc.*, Vol. 125, pp. 2084-2093.
138. *Probing the Temperature Unfolding for a Variety of DNA Secondary Structures Using the Fluorescence Properties of 2-Aminopurine.* **Lee, H-T., Waters, L., Olsen, C.M., Khutsishvili, I. and Marky, L.A.** 2012, *Acta Chim Slov*, Vol. 53, pp. 443-53.
139. *The Thermodynamics of DNA Structural Motifs.* **SantaLucia, J. Jr., Hicks, D.** 2004, Vol. 33, pp. 415-440.
140. *Influence of Buffer Species on the Thermodynamics of Short DNA Duplex Melting: Sodium Phosphate Versus Sodium Cacodylate.* **Alemayehu, S., Fish, D.J., Brewood, G.P., Horne, M.T., Manyanga, F., Dickman, R., Yates, I. and Benight, A.S.** 2009, *J. Phys. Chem. B*, Vol. 113, pp. 2578-2586.
141. *The Complementarity of the Loop to the Stem in DNA Pseudoknots Gives Rise to Local TAT Base-Triplets.* **Reiling-Steffensmeier, C. and Marky, L.A.** 2016, *Methods in Enzymology*, Vol. 567, pp. 414-432.

142. *DNA, RNA, and DNA/RNA Oligomer Duplexes: A Comparative Study of Their Stability, Heat, Hydration and Mg²⁺ Binding Properties.* **Kankia, B.I. and Marky L.A.** 1999, *J. Phys. Chem. B*, Vol. 103, pp. 8759-8767.
143. *Stability and Properties of Double and Triple Helices: Dramatic Effects of RNA and DNA Backbone Composition.* **Roberts, R.W. and Crothers, D.M.** 1992, *Science*, Vol. 258, pp. 1463-6.
144. *Second Structural Motif for Recognition of DNA by Oligonucleotide-Directed Triple-Helix Formation.* **Beal, P.A. and Dervan, P.B.** 1991, *Science*, Vol. 251, pp. 1360-1363.
145. **Zuker, M., Mathews, D.H. and Turner, D.H.** Algorithms and Thermodynamics for RNA Secondary Structure Prediction: A Practical Guide. [ed.] J. Barciszewski and B.F.C. Clark. *RNA Biochemistry and Biotechnology*. s.l. : Kluwer Academic Publishers, 1999, pp. 11-43.
146. *Inhibition of Telomerase by G-Quartet DNA Structures.* **Zahler, A.M., Williamson, J.R., Cech, T.R. and Prescott D.M.** 1991, *Nature*, Vol. 350, pp. 718-720.
147. *Folding a Stable RNA Pseudoknot Through Rearrangement of Two Hairpin Structures.* **Wu, Y-J., Wu, C-H., Yeh, AY-C. and Wen, J-D.** 2014, *Nucleic Acids Research*, Vol. 42, pp. 4505-4515.
148. *Secondary Structures of rRNAs from All Three Domains of Life.* **Petrov, A.S., Bernier, C.R., Gulen, B., Waterbury, C.C., Hershkovits, E., Hsiao, C., Harvey, S.C., Hud, N.V., Fox, G.E., Wartell, R.M. and Williams, L.D.** 2014, *PLOS ONE*, Vol. 9, p. e88222.
149. *DNA Intramolecular Triplexes Containing dT--> Substitutions: Unfolding energetics and Ligand Binding.* **Soto, A.M., Rentzeperis, D., Shikiya, R., Alonso, M. and Marky, L.A.** 2006, *Biochemistry*, Vol. 45, pp. 3051-3056.
150. *Enthalpy-Entropy Compensation in Nucleic Acids: Contributions of Electrostriction and Structural Hydration.* **Marky, L.A. and Kupke, D.W.** 2000, *Methods Enzymol*, Vol. 323, pp. 419-441.
151. *The Size of the Internal Loop in DNA Hairpins Influences Their Targeting with Partially Complementary Strands.* **Prislan, I., Lee, H-T., Lee, C. and Marky, L.A.** 2015, *J. of Phys. Chem. B*, Vol. 119, pp. 96-104.
152. *DNA Hybridization Kinetics: Zippering, Internal Displacement and Sequence Dependence.* **Ouldrige, T.E., Sulc, P., Romano, F., Doye, J.P.K., and Louis, A.A.** 2013, *Nucleic Acids Research*, pp. 1-10.
153. *Secondary Structure effects on DNA Hybridization Kinetics: A Solution Versus Surface Comparison.* **Gao, Y., Wolf, L.K. and Georgiadis, R.M.** 2006, *Nucleic Acid Res.*, Vol. 34, pp. 370-377.

154. *Sensitive Fluorescence-Based Thermodynamic and Kinetic Measurements of DNA Hybridization in Solution.* **Morrison, L.E. and Stols, L.M.** 1993, *Biochemistry*, Vol. 32, pp. 3095-3104.
155. *Relaxation Kinetics of Dimer Formation by Self-Complementary Oligonucleotides.* **Craig, M.E., Crothers, D.M. and Doty, P.** 1971, *J. Mol. Biol.*, Vol. 62, pp. 383-392.
156. *Implication of RNA Sequence on Antisense Oligonucleotide Hybridization Kinetics.* **Lima, W.F., Monia, B.P., Ecker, D.J. and Freir, S.M.** 1992, *Biochemistry*, Vol. 31, pp. 12055-12062.
157. *RNA Hairpin-Folding Kinetics.* **Zhang, W. and Chen, S-J.** 2001, *PNAS*, Vol. 99, pp. 1931-1936.
158. *On the Kinetics of Distamycin Binding to its Target Sites on Duplex DNA.* **Baliga, R. and Crothers, D.M.** 2000, *PNAS*, Vol. 97, pp. 7814-7818.
159. *Quantitative Analysis of Small Molecule-Nucleic Acid Interactions with a Biosensor Surface and Surface Plasmon Resonance Detection.* **Lui, Y. and Wilson, D.W.** 2010, *Methods Mol. Biol.*, Vol. 613, pp. 1-23.
160. *Real Time Measurements of Elongation by a Reverse Transcriptase Using Surface Plasmon Resonance.* **Buckle, M., Williams, R.M., Negroni, M. and Henri, B.** 1996, *Biochemistry*, Vol. 93, pp. 889-894.
161. *Analysis of Oligonucleotide Probe Affinities Using Surface Plasmon Resonance: A Means for Mutational Scanning.* **Persson, B., Stenhag, K., Nilsson, P., Larsson, A., Uhlen M. and Nygren, P-A.** 1997, *Analytical Biochemistry*, Vol. 246, pp. 34-44.
162. *Single Transcriptional and Translational PreQ1 Riboswitches Adopt Similar Pre-Folded Ensembles That Follow Distinct Folding Pathways Into The Same Ligand-Bound Structure.* **Suddala, K.C., Rinaldi A.J., Feng, J., Mustoe, A.M., Eichhorn, C.D., Liberman, J.A., Wedekind, J.E., Al-Hashimi, H.M.** 2013, *Nucleic Acids Research*, Vol. 41, pp. 10462-10475.
163. *Pseudoknot Preorganization of the PreQ1 Class I Riboswitch.* **Santner, T., Rieder, U., Kreutz, C. and Micura, R.** 2012, *JACS*, Vol. 134, pp. 11928-11931.
164. **Liberman, J.A., Bogue, J.T., Jenkins, J.L., Salim M. and Wedekind J.E.** ITC Analysis of Ligand Binding to PreQ1 Riboswitches. *Methods in Enzymology*. s.l.: Elsevier Inc, 2014, Vol. 549, pp. 435-450.